UNIVERSITY OF LONDON THESIS

Degree PhD Year 2008 Name of Author ROBERTS, JULIA, FLORENCE.

COPYRIGHT

This is a thesis accepted for a Higher Degree of the University of London. It is an unpublished typescript and the copyright is held by the author. All persons consulting the thesis must read and abide by the Copyright Declaration below.

COPYRIGHT DECLARATION

I recognise that the copyright of the above-described thesis rests with the author and that no quotation from it or information derived from it may be published without the prior written consent of the author.

LOAN

Theses may not be lent to individuals, but the University Library may lend a copy to approved libraries within the United Kingdom, for consultation solely on the premises of those libraries. Application should be made to: The Theses Section, University of London Library, Senate House, Malet Street, London WC1E 7HU.

REPRODUCTION

University of London theses may not be reproduced without explicit written permission from the University of London Library. Enquiries should be addressed to the Theses Section of the Library. Regulations concerning reproduction vary according to the date of acceptance of the thesis and are listed below as guidelines.

A. Before 1962. Permission granted only upon the prior written consent of the author. (The University Library will provide addresses where possible).

B. 1962 - 1974. In many cases the author has agreed to permit copying upon completion of a Copyright Declaration.

C. 1975 - 1988. Most theses may be copied upon completion of a Copyright Declaration.

D. 1989 onwards. Most theses may be copied.

This thesis comes within category D.

☐ This copy has been deposited in the Library of UCL

☐ This copy has been deposited in the University of London Library, Senate House, Malet Street, London WC1E 7HU.

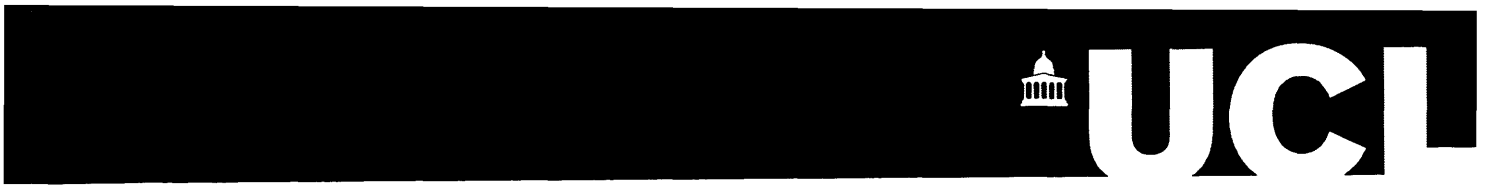

The Chemical Evolution of Low Mass Prestellar Cores and Young Stellar Objects

Julia Florence Roberts

Thesis submitted for the Degree of Doctor of Philosophy
of the University of London

Department of Physics & Astronomy
UNIVERSITY COLLEGE LONDON

October 2008

ProQuest LLC
789 East Eisenhower Parkway
P.O. Box 1346
Ann Arbor, MI 48106-1346

I, Julia Roberts, confirm that the work presented in this thesis is my own. Where information has been derived from other sources, I confirm that this has been indicated in the thesis.

To my family and friends.

ABSTRACT

In this thesis we develop models of the chemical kinetics of prestellar cores, so we can identify molecules which will be able to trace various physical processes, and therefore give us more understanding of how stars form from these objects.

First, we investigate non-thermal desorption mechanisms which can operate inside prestellar cores, and make estimates of the desorption efficiencies based on observational data, which before now were poorly constrained by theory. We then use our chemical models to predict molecular abundances during the collapse phase of a prestellar core. In particular we investigate the effect of different initial conditions and collapse models, so we can identify molecules which could be used to distinguish between slow and rapid star formation models.

We also generate line profiles for selected molecules using a radiative transfer code, using the abundances predicted from our chemical models. We find that for CS, a double peaked line profile with a blue asymmetry can only be produced for models of core collapse with extended inward motions. This contradicts many previous interpretations of line profiles, which have explained the infall signature by collapse models with a static envelope and temperature gradient.

We also explore deuterium chemistry in prestellar cores, to investigate whether core collapse by ambipolar diffusion can leave a signature on deuterium fractionation. We find that the fractionation is very sensitive to the density profile of the core, thus we propose that observations of the spatial distribution of deuterated molecules could be used to distinguish between different collapse models.

Finally, we investigate the chemistry in C-shock regions associated with outflows of young stellar objects, where we also include the analysis of some new observations of outflow L1448mm, which show very strong evidence for the presence of a magnetic precursor.

CONTENTS

LIST OF FIGURES

LIST OF TABLES

CHAPTER 1

INTRODUCTION

One of the more fundamental questions in astronomy is how stars form from the interstellar medium. It is well established that the birth places of stars are molecular clouds, composed of mainly molecular gas and dust, which fragment and collapse into smaller cores which go on to form protostars, but many of the details of this process are missing. For example, it is not known how important magnetic fields and turbulence are in star formation, and therefore there is currently debate on whether star formation is a slow process with magnetic fields providing support for cores and resisting their collapse (Shu *et al.* 1987), or whether star formation is rapid, with non-linear (turbulent) perturbations accelerating core evolution (Basu *et al.* 2008).

Part of the reason there is still so much to learn about star formation is that it occurs in such cold, dense, opaque regions, making it extremely difficult to observe. There is no optical emission so astronomers need to use observations of (i) extinction of background starlight by dust in the star forming cloud, (ii) emission by dust at infrared and submillimetre wavelengths, and (iii) emission and absorption from molecules, to deduce information about the star formation process.

In this thesis we explore the chemistry in molecular clouds using chemical kinetics models, so we can try to understand the observed abundances and spectra of molecules in star forming regions, and use them to interpret the physical processes that are occurring. We concentrate on the chemistry of low mass ($\sim 1 M_{\odot}$) pre-protostellar cores (which we refer to as 'prestellar cores' for brevity) and how they evolve into Class 0 protostars (which are defined in Section 1.2.2).

In section 1.1 we start by outlining the basic theory of how a molecular cloud fragments and forms stars to put this work into context, and then mention some of the problems in the current theory. In Section 1.2 we then talk about the observed properties of molecular clouds, dense

cores and young stellar objects, and how these fit into the evolutionary sequence of star formation. In Section 1.3 we discuss in more detail the debate over the timescale of star formation, and in Section 1.4 we talk about the work in this thesis and how it relates to star formation theory.

1.1 From molecular clouds to stars

To form a star from a molecular cloud, the material in the cloud must contract somehow, to become dense and hot enough to dissociate and ionise hydrogen, and eventually begin nuclear burning.

So what causes a cloud, or part of a cloud, to contract? In 1902, James Jeans considered the balance between the gravitational forces and internal thermal pressure of a cloud, to derive the maximum mass of a cloud stable against gravitational collapse (the *Jeans Mass*, $M_{\rm J}$). At this critical mass, the time taken for free-fall collapse, $t_{\rm ff}$, is equal to $2\sqrt{10}/\pi \sim 2\times$ the time taken for a sound wave to cross the cloud, $t_{\rm s} = R_c/c$, where R_c is the radius of the cloud and c is the sound speed (Dyson & Williams 1997). Physically this makes sense because, if the free-fall time is less than the sound crossing time, the cloud cannot restabilise itself if the density is perturbed, making it unstable to gravitational collapse.

The free-fall timescale, assuming a uniform density cloud, is given by (Dyson & Williams 1997):

$$t_{\rm ff} = \left(\frac{3\pi}{32 G \rho_c}\right)^{1/2}. \tag{1.1}$$

Setting this equal to $2t_{\rm s}$, and using $M_c = 4/3 R_c^3 \rho_c$, where M_c is the mass of the cloud and ρ_c is the mass density, gives the Jeans Mass as:

$$M_J = \left(\frac{3\pi^5}{32}\right)^{1/2} c^3 G^{-1/2} \rho_c^{-1/2}. \tag{1.2}$$

Assuming the cloud is isothermal, the sound speed is given by $c^2 = kT_c/\mu m_{\rm H}$, where T_c is the temperature of the cloud, μ is the mean molecular mass, and $m_{\rm H}$ is the mass of a hydrogen atom. The Jeans Mass can then be rewritten as:

$$M_{\rm J} = 5 \times 10^{34} \left(\frac{T}{\rm K}\right)^{3/2} \left(\frac{n}{\rm m^{-3}}\right)^{-1/2} \rm kg, \tag{1.3}$$

where n is the number density of the gas, and assuming that the mean molecular mass is 2 atomic mass units (appropriate for molecular hydrogen).

Molecular clouds, such as Taurus and Ophiuchus, which are examples of low mass star forming regions, have average temperatures of about 20 K, and number densities of $n_{\rm H} \sim 10^3$ cm^{-3} =

10^9 m^{-3} (where $n_{\rm H} = n({\rm H}) + 2n({\rm H_2})$, is the total hydrogen nucleon density; hereafter when we refer to the 'density' of a core or cloud, we specifically mean $n_{\rm H}$ unless otherwise stated). Putting these values into (1.3) gives $M_{\rm J} \sim 70$ M$_\odot$, which is less than the typical mass of such a region ($M_c = 10^3 - 10^4$ $M_\odot$, Bergin & Tafalla 2007). This means that such giant molecular clouds are prone to collapse.

As the cloud starts collapsing, both its temperature and density will increase. If the cloud cooling is inefficient, according to equation (1.3), $M_{\rm J}$ will increase and the cloud may regain its stability. If, however, the cooling is efficient enough such that the increase in density is not accompanied by an increase in temperature, $M_{\rm J}$ decreases, meaning that smaller regions within the cloud itself can now have $M > M_{\rm J}$. These smaller regions can themselves start to collapse, resulting in large density inhomogeneities within the cloud. This can continue until the cloud becomes highly fragmented, consisting of an ensemble of dense cores within a larger nebula. The smallest cores have masses in the solar range, and these are believed to be the precursors of protostars, known as *prestellar cores* (see Section 1.2.1).[1]

Eventually the cores become dense enough that they are opaque to their own radiation; cooling is inefficient, thermal pressure increases and so the collapse halts, forming a hydrostatic core. The protostar becomes opaque at mass densities of approximately $10^{-10} - 10^{-9}$ kg m^{-3} (number density $\sim 10^{10} - 10^{11}$ cm^{-3}) and a temperature of a few hundred Kelvin (Prialnik 2000). Once the temperature of the hydrostatic core becomes greater than about 2000 K, molecular hydrogen begins to dissociate (Aikawa *et al.* 2008). The energy from the infalling material now goes into hydrogen dissociation, rather than increasing the thermal pressure of the core, and so the core becomes gravitationally unstable again and collapses further until a second hydrostatic core forms (Masunaga *et al.* 1998). This is the point where the *protostar* is born, with its boundary defined by the photosphere.

The protostar still accretes mass from a surrounding infalling envelope, with the infalling gas being shocked as it hits the surface of the protostar, and giving rise to the infall luminosity of $L_{\rm inf} \sim GM_*(t)\dot{M}/R_*$ (Ward-Thompson 1996).

The opacity of the (partially ionised) hydrostatic core is initially very high, impeding radiation flow so the protostar is fully convective. On an Hertzsprung-Russell diagram, the protostar will follow the path of a Hayashi track, the evolutionary path of a fully convective object (Prialnik

[1] Strictly, cores are only classed as prestellar if the mean density of the core exceeds that of the parent cloud by a factor of $\gtrsim 5 - 10$ (André *et al.* 2008), to distinguish between cores which will disperse back into the interstellar medium rather than forming stars.

2000). Once ionisation is complete, the temperature increases, the opacity decreases and the star becomes partially radiative, leaving the Hayashi track and approaching the main sequence along the Henyey track (Henyey *et al.* 1988). Hydrogen burning begins at a temperature of $\sim 10^7$ K, first in the centre of the core, then spreading outwards. The star joins the main sequence once hydrogen burning is taking place throughout the core.

The timescales for the protostellar stages are estimated by the Kelvin-Helmholtz scale, $\tau_{\rm KH} = U/L \approx GM^2/RL$, where U is the internal energy of the protostar. $\tau_{\rm KH}$ is an estimate of the time it would take for a star to radiate away all its gravitational potential energy, and is approximately a few $\times 10^6$ yr for protostars in the Taurus molecular cloud (Tassis & Mouschovias 2004).

This simplified theory given above is useful for giving a broad understanding of star formation, and it introduces useful concepts such as the Jeans Mass, which is still used to estimate the stability of prestellar cores (e.g. Aguti *et al.* 2007), but there are many holes in the arguments and there is still much left to understand. Crucial factors have been left out, such as the importance of magnetic fields and turbulence. Magnetic fields can provide extra support for the cores against gravitational collapse, slowing down the star formation process, whereas turbulence can both provide support on large scales as well as generating density fluctuations on small scales, overall tending to decrease the timescale for star formation (André *et al.* 2008).

There is currently much debate on this, which has lead to four modes of star formation, depending on whether linear (gravitational) or non-linear (turbulent) perturbations initiate core formation, and whether magnetic fields are dynamically dominant or not. Table 1.1, adapted from André *et al.* (2008), summarises the four main types of star formation models.

In this thesis, we will refer to the traditional theory of star formation, whereby cores are supported by magnetic fields and can only collapse once the magnetic field has dissipated by the process of ambipolar diffusion with timescales of $\sim$ 10 Myr, as SSF (slow star formation; scenario C in Table 1.1), and the more recent theories of star formation (scenarios A, B and D in Table 1.1), which have timescales of $\lesssim$ a few Myr, as RSF (rapid star formation) models.

By not fully understanding the role of magnetic fields and turbulence, we therefore do not know the relative timescales of the prestellar phase and the protostellar stages, and how the core mass function (CMF) relates to the initial mass function (IMF). Details of the initial conditions (e.g. density and temperature profiles) of prestellar cores before they begin their final collapse into protostars are also subject to much debate. This issue is discussed more in Section 1.3.

The work in this thesis focuses on the evolution from the prestellar core phase to the Class 0 phase; we do not attempt to model the formation of the prestellar core from the more diffuse giant

Table 1.1: Summary of the four main types of star formation models (adapted from André *et al.* 2008).

molecular cloud. We consider the chemistry during this period, and how it can be used as a tool to answer some of the questions above; for example, whether the chemical abundances will be different in the RSF models to the SSF models.

1.2 Observed properties of star forming regions

Below we briefly summarise the observed properties of star forming regions, in particular prestellar cores, because these are the regions for which we model the chemistry in this thesis. We also give a short description of the observed classes of young stellar objects (YSOs), and how they fit into the evolutionary sequence of star formation.

Low mass star formation is observed to occur in nearby giant molecular clouds, such as Taurus, Ophiuchus, Scorpius and Perseus (Ward-Thompson *et al.* 2007). These clouds are all within a distance of 500 pc, and are composed of molecular gas and dust, with a mass ratio of gas:dust $\sim$100:1 (Williams & Viti 2002). The clouds have scales of $\sim$ 10 pc, densities of $n_{\rm H} \sim 50 - 500$ cm^{-3}, and masses of $\sim 10^3 - 10^4$ $M_{\odot}$, and have highly irregular structures, containing filaments and dense condensations on many scales. The smallest cores found in such clouds, some of which are possibly prestellar cores and others which harbour protostars and young stellar objects (YSOs), have scales of about 0.1 pc, $n_{\rm H} \sim 10^4 - 10^6$ cm^{-3} and masses $\sim$ 1 $M_{\odot}$. These objects are often found within larger *clumps*, which have scales $\sim$ 1 pc, $n_{\rm H} \sim 10^3 - 10^4$ cm^{-3} and masses 50-500 $M_{\odot}$ (Bergin & Tafalla 2007). Observations have shown that the dense material in molecular clouds makes up

only a small fraction of the total mass of the cloud. For example, Johnstone *et al.* (2004) found that only $\sim 2.5\%$ of of the mass of the Ophiuchus cloud was in dense substructures.

A dust extinction map of the Taurus Molecular Cloud, taken from Dobashi *et al.* (2005), is shown in Figure 1.1, to illustrate the clumpy nature of star forming regions. A few clumps identified from the Lynds (1962) survey are marked, as well as the filament L1495. The TMC1 clump is marked because this object has been well studied in star formation research, and is found to be made up of several sub-clumps, which themselves are made of smaller sub-stellar cores. TMC1-D, for example, is made up of three cores of masses $0.4 - 1.4\ M_{\odot}$ (Wolkovitch *et al.* 1997).

Isolated dense cores have also been found, and these are known as *Bok globules*. B68 is a well known example of a Bok globule, with properties very similar to the dense cores found inside larger molecular clouds, so it is also a candidate prestellar core. It has been proposed that Bok globules formed from larger molecular clouds, but some event such as ionisation from a nearby O star dispersed the original cloud, leaving only the densest structures.

The smallest cores inside molecular clouds, which have masses of the order 1 $M_{\odot}$, can be divided into those which are detected at infrared wavelengths and those which are not. Since the infrared emission is thought to arise from protostars, cores with no infrared emission are often termed *starless cores*, and if they have masses estimated above the Jeans Mass (see Section 1.1) or show signs of collapse, they are called *prestellar cores* (Kirk *et al.* 2007). The properties of prestellar cores, as derived from observations, are discussed below. Cores which do show infrared emission are classed as *young stellar objects* (YSOs), and are discussed further in Section 1.2.2.

1.2.1 Properties of prestellar cores

Understanding the properties or prestellar cores is vital for the theory of star formation, as they set the initial conditions for the final collapse into a protostar. The initial conditions used in the models in this thesis are based on the observed properties of prestellar cores, summarised below:

1.2.1.1 Density profile

Theoretical models of the collapse of prestellar cores often assume that the density profile is that of a singular isothermal sphere, i.e. $n_{\rm H} \propto r^{-2}$ (e.g. Shu 1977). Observations, however, have revealed that the densities of prestellar cores tend to flatten off in the centre. Ward-Thompson *et al.* (1999) observed 8 prestellar cores with 1.3mm dust continuum mapping, and found that the observed radial intensity profiles of the cores were better fitted with a dual power law, with $n_{\rm H} \propto r^{-2}$ for radii greater than $R_{\rm flat}$, and a flatter density profile within this radius. $R_{\rm flat}$ ranged from $2500 - 4200$

Figure 1.1: Extinction map of the Taurus molecular cloud. Panel (a) shows the distribution of the A_v at $6''$ resolution. The lowest contour is 0.5 mag, and the contour intervals are 0.5 mag for $A_v \leq 3.0$ mag and 1.0 mag for $A_v > 3.0$ mag. Panel (b) is the same as panel (a), but with the extended components removed. *Source: Dobashi* et al. *(2005).*

AU, and for the core L1689A the density profile within $R_{\rm flat}$ was well fitted with $n_{\rm H} \propto r^{-1.3}$. The estimated central densities of the cores ranged from 7.9×10^5 to 2.1×10^6 cm^{-3}. These flattened density profiles are qualitatively consistent with models of magnetically supported cores undergoing ambipolar diffusion, although the models of Basu & Mouschovias (1995) require a magnetic field much greater than the magnetic field strengths inferred from observations in order to reproduce the density profiles observed by Ward-Thompson *et al.* (1999). Furthermore, the analysis performed by Ward-Thompson *et al.* (1999) assumed that the dust temperature profiles were uniform throughout the core, which is unlikely to be the case (see Section 1.2.1.2).

Evans *et al.* (2001) modelled the emission from dust in prestellar cores using a self-consistent calculation of the dust temperature distribution, $T_{\rm d}$, for a given input density distribution, and found that using the calculated $T_{\rm d}$ (which ranged from $\sim$ 7 K in the core centre to $\sim$ 15 K at the core edge), rather than assuming a constant dust temperature, had a substantial impact on the conclusions. By fitting their models to submillimetre observations of the cores L1689B, L1512 and L1544 taken by Shirley *et al.* (2000), Evans *et al.* (2001) found that the models indicated smaller regions of relatively constant temperature (by factors of 0.5–0.9), and higher central densities (by factors of 3–10), than previous studies which assumed a constant $T_{\rm d}$ (Andre *et al.* 1996; Ward-Thompson *et al.* 1999). The observational data for all three of the cores could be well matched by models assuming unstable Bonner-Ebert sphere density profiles (described below), and for L1544, the observations even appeared to be consistent with the models of a singular isothermal sphere.

Bonner-Ebert spheres are the family of solutions to the equations for a pressure confined, self-gravitating, isothermal sphere. The fluid equations describing a self-gravitating, isothermal sphere in hydrostatic equilibrium can be summarised by the following variant of the Lane-Emden equation (Bonnor 1956):

$$\frac{1}{\xi^2}\frac{d}{d\xi}\left(\xi^2\frac{d\psi}{d\xi}\right) = e^{-\psi}, \tag{1.4}$$

where $\rho = \rho_{\rm c}e^{-\psi}$, $\xi = (r/a)\sqrt{4\pi G\rho_{\rm c}}$ is the non-dimensional radial parameter and $a = \sqrt{kT/m}$ is the isothermal sound speed. This equation can be solved subject to the boundary conditions $\psi(0) = 0$ (i.e. $\rho = \rho_{\rm c}$ at $r = 0$) and $d\psi(0)/d\xi = 0$ (i.e. $d\rho/dr = 0$ at $r = 0$). For such a sphere bounded by a fixed external pressure, there is a family of solutions characterised by

$$\xi_{\rm max} = \frac{R}{a}\sqrt{4\pi G\rho_{\rm c}}, \tag{1.5}$$

where $\xi_{\rm max}$ is the value of ξ at the outer boundary, R. For $\xi_{\rm max} > 6.5$, the core will be unstable to gravitational collapse.

Alves *et al.* (2001), who used extinction of background starlight to estimate the density profile of the Bok globule B68, found this core is also well fitted by a Bonner-Ebert sphere, with $\xi_{max} = 6.0 \pm 0.2$, making it just critical.

Since Bonnor-Ebert spheres neglect magnetic fields and turbulence, they may not be appropriate models for all prestellar cores. Nevertheless, it appears that prestellar cores can generally be described with density profiles that approach r^{-2} at large radii but flatten off towards the centre.

1.2.1.2 Temperature profile

Since cores are made up of both gas and dust, depending on the conditions, the gas and dust components can have different temperatures. Theoretical models predict that the gas and dust are coupled at densities greater than about 10^4 cm^{-3} through collisions (e.g. Burke & Hollenbach 1983), so for our models we assume that the gas and dust temperatures are equal.

Dust temperatures are difficult to determine observationally because the optical properties of the dust are very complex, especially at high densities, when they become covered in icy mantles (see Section 2.2.2). Nevertheless, attempts at estimating the dust temperature gradient have been made using colour measurements at FIR and submm wavelengths. Bianchi *et al.* (2003), for example, estimated the dust temperature distribution in B68 by modelling it as a Bonnor-Ebert sphere heated externally by the interstellar radiation field (hereafter ISRF) and cooling by emission at infrared and submillimetre wavelengths, and adjusting the external temperature to fit the observed spectral energy distribution. The best fit was an external temperature of 14 ± 2 K, with a central temperature of ~ 9 K.

As mentioned above, the models of Evans *et al.* (2001) also computed dust temperatures of Bonnor-Ebert spheres heated by the interstellar radiation field, and they found that the models which best reproduced the observations of Shirley *et al.* (2000) had dust temperatures of ~ 7 K in the centre and ~ 15 K at the edge. In general, models of the dust temperature predict central temperatures of $7 - 9$ K and external temperatures of $14 - 20$ K (Bergin & Tafalla 2007).

The gas is heated by cosmic ray ionisation and grain photoelectric heating, and cools by emission from molecules such as the $J = 1 \rightarrow 0$ line of CO ($\Delta E = 5.5$ K). At higher densities, CO and other heavy molecules freeze-out, inhibiting molecular cooling, but since the gas and dust are coupled, the dust regulates the gas temperature. Models of the gas temperature generally predict quite a shallow profile, because while at the edge of the core there will be extra heating by the interstellar radiation field, there is also less cooling in the centre of the core owing to freeze-out. Tafalla *et al.* (2004) used observations of NH_3 to estimate the gas temperatures of the cores L1498

and L1517B, and found the observations of both cores were well fitted using a constant temperature profile of 10 K. On the other hand, Bergin *et al.* (2006) found the temperature at the edge of the core B68, traced by $C^{18}O$ and ^{13}CO, was surprisingly low (6 – 7 K) compared to the central temperature estimated by NH_3 observations ($\sim$ 10 K). This increase could be due to the weakening of gas-grain coupling due to dust coagulation.

1.2.2 Observations of young stellar objects

A core is classed as a young stellar object (YSO) once it begins emitting at infrared wavelengths. If the source also emits at optical wavelengths then it is a *T Tauri star* [2]. In Chapter 8 of this thesis, we investigate the chemistry of the youngest protostars, Class 0 objects, whose properties are described below. For completeness, we also discuss the properties of Class I to III protostars, and the inferred sequence of protostellar evolution.

YSOs can be divided into subclasses depending on the shape of their spectral energy distribution (SED) and the value of their spectral index, a, for wavelengths greater than 2 μm [3].

The original classification scheme, involving only Class I, II and III protostars, was devised by Lada & Wilking (1984). The much fainter Class 0 protostars were discovered almost 10 yr afterwards (Andre *et al.* 1993). The properties of each class of protostar are described below:

Class 0 sources: Class 0 objects are defined as having more than half of their mass still in the form of an accreting envelope (André *et al.* 2008). Their observational characteristics are that they are not yet visible in the near or far infrared, they emit strongly at submillimetre wavelengths, and their SEDs can be modelled by a single temperature black body. An example SED of a Class 0 object is shown in Figure 1.2, for the first classified Class 0 object, VLA 1623. Class 0 objects have already formed molecular outflows, indicating that the 'switch on' for outflows occurs at a very early stage, and the presence of an outflow does not halt accretion as previously suggested (Lada 1987).

Class I sources: $0 < a \lesssim +3$ Their SEDs are broader than that of a black body, and rise for wavelengths greater than $\sim 2\mu$m. They are very deeply embedded and invisible in the optical. The SEDs fit models of objects accreting mass from circumstellar matter. They often have molecular outflows.

[2] T Tauri stars are pre-main sequence stars, descending the Hayashi track on a Hertzsprung-Russell diagram, and are characterised by variable optical emission, prominent emission lines and low surface temperatures (Shu *et al.* 1987).

[3] The SED of an object is a plot of $\log(\lambda F_\lambda)$ versus $\log \lambda$, and the spectral index is defined as $\frac{\mathrm{d}\log(\lambda F_\lambda)}{\mathrm{d}\log\lambda}$.

Class II sources: $-2 \lesssim a \lesssim 0$ Their SEDs are also broader than that of a black body, but they are flat or decreasing for wavelengths greater than $\sim 2\mu$m. They are visible in the optical and are mostly associated with T-Tauri stars with disks. Their SEDs are well fitted by models of photospheres surrounded by a circumstellar disk and they often have molecular outflows.

Class III sources: $-3 < a \lesssim -2$ Their SEDs can be modelled by reddened black bodies. They have little or no excess near infrared emission, but slight excess in the mid infrared caused by the cool dust grains which are responsible for the extinction. Their SEDs resemble model SEDs for reddened photospheres of stars very near to or on the zero age main sequence, with most of the envelope already dispersed ('naked' T-Tauri stars).

Example SEDs for Class I, II and III protostars are shown in Figure 1.2.2.

Figure 1.2: SED of the first identified Class 0 protostar, VLA1623. *Source: Andre* et al. *(1993).*

These observations led to the following theory for the evolution of prestellar cores into protostars (see Figure 1.4):

(a) Dense prestellar cores form from the more diffuse gas of molecular clouds. The duration of this phase depends on how much support the cores get from magnetic fields and turbulence (see the discussion of SSF and RSF models in Section 1.3).

Figure 1.3: The SEDs of Class I, II and III protostars. *Source: Lada (1987).*

(b) The core begins collapsing dynamically. Even if star formation is regulated by magnetic fields, there will come a point where the ambipolar diffusion increases the mass to flux ratio in the central regions of the core so that it can collapse dynamically. At this stage the object is a Class 0 protostar.

(c) Bipolar outflows form, driven by magnetic stresses in the protostar-disk system, but accretion still continues. Once the majority of the mass of the system has been accreted onto the protostar it becomes a Class I object.

(d) The outflow widens and eventually exposes the young stellar object surrounded by its accretion disk (a T-Tauri star). As the envelope disappears the object evolves through the Class II stage to the Class III stage. Eventually even the disk will disappear, as the young star evolves onto the main sequence.

Figure 1.4: Evolution of a prestellar core into a protostar. See text for a description of phases (a) to (d). *Source: Shu* et al. *(1987).*

1.3 Slow versus rapid star formation models

One of the largest problems facing star formation theory is the importance of magnetic fields in regulating the star formation timescale, and this is one of the problems we address in Chapters 4, 5 and 6 of this thesis. Traditionally it was believed that magnetic fields provided support for prestellar cores against gravity, since unlike turbulence, magnetic fields are not easily dissipated and can provide support on long timescales (Shu *et al.* 1987). The cores would then contract quasi-statically over a time period of about 10 Myr by the process of ambipolar diffusion. Ambipolar diffusion occurs when the ions and negatively charged dust grains within the core or cloud are tied to the magnetic field, but the neutral species are not and so drift past the ions as they try to collapse. The neutrals experience a drag force from the ions and so the overall collapse of the core or cloud is drastically slowed down. This theory leads to a low star formation efficiency which agrees with the observed low efficiency of Galactic star formation.

Recently, however, it has been suggested that the lifetimes of molecular clouds are actually shorter than the timescale for a subcritical core to become supercritical through ambipolar diffusion (e.g. Elmegreen 2007), casting doubt upon the traditional theory. The so called *T-Tauri problem*, as well as the problem of rapid dissipation of supersonic turbulence (explained below), prompted research into other mechanisms for star formation, and theories for rapid, dynamic star formation were proposed.

There are several versions of the dynamic picture of star formation (see Table 1.1), the most rapid of which is the super-Alfvénic turbulent fragmentation model, where star formation can occur on timescales < 1 Myr.

The debate over the star formation timescale is still unresolved. The current observational evidence is unclear; both sides of the argument can use the same piece of evidence, but with a different interpretation, to support their case. Below we mention some of the arguments for and against the SSF and RSF theories.

1.3.1 The post T-Tauri problem

It was originally thought that the sound crossing time of molecular clouds, which is about 10^7 yr, gives a lower estimate to their age. If this were the case, stars within a cloud should also be of a similar age. However, the average age of T-Tauri stars, as estimated from their position along the Hayashi track, is on average found to be less than 10^6 yr. This led to the conclusion that a population of older stars, with ages greater than ~ 5 Myr, were missing. It appeared that the theory

of long-lived molecular clouds was inconsistent with the ages of the stars contained within them. If, however, molecular clouds were short-lived ($\sim 10^6$ yr), and the star formation timescale was also of this order, the problem of the missing population of stars is resolved.

Some authors, however, argue that this is not a problem for ambipolar diffusion controlled star formation. Tassis & Mouschovias (2004) suggested that the young age of T-Tauri stars was because the age taken into consideration was only the time taken for the later stages of star formation, and that the potentially long initial phase, the contraction of a starless core, could significantly increase the 'age' of these stars. The situation as described by Tassis & Mouschovias (2004) is summarised in Figure 1.5. They propose that the age of T-Tauri stars is just the time for phase C, which is approximately the Kelvin-Helmholtz timescale. Phases A and B, which are, respectively, the evolution of the starless core and the accreting phase of the protostar once the hydrostatic core has formed, could be significantly longer than phase C, especially if the core evolves from a subcritical core to a supercritical core through ambipolar diffusion. The ages of T-Tauri stars offer no information on these earlier stages.

Figure 1.5: The star formation timeline, as given in Tassis & Mouschovias (2004).

1.3.2 The decay of supersonic turbulence

Since turbulence can both compress and support gas, it can be important in both models. Supersonic turbulence is widely observed in the interstellar medium (Heyer & Brunt 2007), and can provide non-thermal support for cores against gravitational collapse. If a core is initially in equilibrium with its surroundings, thermal pressure, magnetic pressure and turbulent pressure all contribute to the support of the core. However, turbulence is found to decay on a dynamical timescale (Stone *et al.* 1998), so if the support from turbulence is removed, it is possible that the core is not left

with enough support to withstand gravity, so the core becomes supercritical and collapses. Since the dynamical timescale is much shorter than the timescale for ambipolar diffusion, the core will become supercritical on a dynamical timescale, and the process of ambipolar diffusion is irrelevant (Elmegreen 2007).

Mouschovias *et al.* (2006), however, argued that since there is considerable evidence that molecular cloud lifetimes are long, and that turbulent decay is rapid and difficult to replenish, then the turbulence-induced RSF models are also unrealistic.

1.3.3 Lifetimes of molecular clouds

If the age of molecular clouds were well established, this could set an upper limit on the timescale for star formation. Unfortunately, the ages of molecular clouds are just as uncertain as the star formation timescale. The slow star formation model needs long molecular cloud lifetimes, greater than $\sim 10^7$ yr, whereas the rapid star formation model favours molecular cloud lifetimes of around $\sim 10^6$ yr.

Part of the evidence for long-lived molecular clouds comes from the sound crossing time and the fraction of atomic hydrogen remaining in the cloud. If a giant molecular cloud is in equilibrium (at least on a large scale), then its age must be at least the value of the sound crossing time, so that two points on opposite sides of the cloud can 'communicate' with each other. For the Taurus molecular cloud, the sound crossing time is $\sim 10^7$ yr (Hartmann *et al.* 1991), setting this as a lower limit on its age.

Goldsmith & Li (2005) derived the ages of several dark clouds by estimating the abundance of atomic hydrogen using HI narrow self-absorption observations. The small amount of atomic hydrogen detected implied that the clouds had had enough time to convert hydrogen from atomic to molecular form, which according to their model should take at least $10^{6.5} - 10^7$ yr, therefore setting a lower limit (because they believed their model to underestimate the conversion timescale) on the ages of these clouds.

There are estimates of molecular cloud ages even greater than 10^7 yr; early estimates of molecular clouds were often $\geq 10^8$ yr (e.g. Scoville *et al.* 1979), derived from estimates of the fraction of atomic to molecular interstellar hydrogen in the inner Milky Way, although these ages are now believed to be overestimates, even by supporters of SSF (Mouschovias *et al.* 2006).

Further estimates of the ages of molecular clouds have been made from the statistics of prestellar cores and protostars, discussed in the next section.

1.3.4 The statistics of prestellar cores

Since the protostellar phase of star formation must always be preceded by a prestellar core phase, it has been suggested that the ratio of the number of prestellar (starless) cores to the number of embedded protostars should be an indicator of the lengths of these phases (Tassis & Mouschovias 2004), i.e.,

$$\frac{\tau_{\text{starless cores}}}{\tau_{\text{embedded p.s.}}} = \frac{\text{No. of starless cores}}{\text{No. cores with embedded point sources}}. \tag{1.6}$$

This equation assumes that all prestellar cores will form protostars. Several different surveys have concluded different results employing this method. Lee & Myers (1999) found the right hand side of equation 1.6 to be approximately 1/0.3, and using a value of $\tau_{\text{embedded p.s.}} \sim 1 - 5 \times 10^5$ yr, this gives $\tau_{\text{starless cores}} \sim 10^6$ yr, which these authors conclude is too short for ambipolar diffusion. Ward-Thompson *et al.* (1994) and Jessop & Ward-Thompson (2000), on the other hand, found the ratio to be $\sim 10/1$, and using $\tau_{\text{embedded p.s.}} \sim 10^6$ yr they concluded that $\tau_{\text{starless cores}} \sim 10^7$ yr, consistent with ambipolar diffusion theory.

Tassis & Mouschovias (2004) made the point that the estimates of $\tau_{\text{starless cores}}$ are extremely unreliable because not only do they depend on the value of $\tau_{\text{embedded p.s.}}$, itself very uncertain, but also that the number of starless cores themselves is extremely unreliable. They make the argument that an object can only be identified as a core if its density enhancement is greater than 2-4 times the background density, and this can take up to 10^7 yr for a subcritical core.

1.3.5 Extra-galactic evidence

It has been suggested that shocks formed as a result of the rotation of galactic spiral arms relative to the gas can trigger star formation, and so the distance between the shock front of the spiral arm and the areas where the newly formed stars are found is an indicator of the star formation timescale (Roberts 1969). The newly formed stars are traced by Hα emission, and the galactic shock waves are traced by dust lanes and CO emission. Mouschovias *et al.* (2006) discussed observations of galaxies such as M81 and M51 which show a separation between the peak CO emission and/or dust lanes and the Hα emission consistent with a star formation timescale of $\sim$ 10 Myr.

Ballesteros-Paredes & Hartmann (2007) argued that these observations are also consistent with rapid, dynamic star formation. In their interpretation, a first generation of stars would form close to the triggering shock front, dispersing the surrounding gas to form concentrations downstream of the shock which could then form a second generation of stars. It could be that these later generations

of stars are responsible for the downstream Hα emission, and so the separation does not give any information on the timescale of forming a single star.

1.4 Outline of thesis

The above sections show that there is still clearly much to learn about star formation. In this thesis we explore the use of chemical models as a tool to help resolve some of these issues raised. In Chapter 2 we review the chemical processes in star forming regions, which are included in our chemical models. In Chapter 3 we investigate the non-thermal desorption mechanisms which can operate in dark cores, a process that is often neglected in such cores but needs to be considered to produce reliable chemical models.

The work in Chapters 4, 5, 6 and 7 relate to the discussion on SSF and RSF theories given above. In these chapters we try to find observational diagnostics which could be used to distinguish between these two paradigms of star formation. In Chapter 4 we look at the initial chemical conditions which might be appropriate for SSF and RSF models, and in Chapter 5 we generate line profiles for the chemical models introduced in Chapter 4.

In Chapter 6 we compare two different collapse models, to investigate whether the model of core collapse used can leave a signature on the chemical abundances inside the core and on the observed line profiles.

In Chapter 7 we study the deuterium chemistry in a core collapsing via ambipolar diffusion, to see if we can find any observational signatures in the abundances of deuterated species for this method of collapse.

In Chapter 8 we turn our attention to the protostellar stages of star formation, and present studies on the interaction of the molecular outflows of protostars with their surrounding medium. This Chapter is divided into an observational section, where we present observations of the magnetic precursor in the outflow associated with the Class 0 source L1448-mm, and a modelling section where we give the results of a chemical model of such a region.

CHAPTER 2

CHEMISTRY IN STAR FORMING REGIONS

Over the past thirty or so years, over 100 molecules have been discovered in the interstellar medium (Williams & Viti 2002). The appropriately named molecular clouds mentioned in Chapter 1 and the prestellar cores inside them, the regions which are the focus of this thesis, are particularly rich in molecular material, containing simple diatomic molecules such as H_2 and CO, as well as larger organic species such as methanol. In this chapter we briefly explain the importance of molecules in star formation, and give an overview of how such a rich chemistry can be produced in harsh interstellar environments. Finally we explain our approach to modelling the chemistry in molecular clouds and cores in order to be able to predict molecular abundances under various conditions.

2.1 The role of molecules in star formation

The basis of this thesis is that molecular abundances reflect the physical conditions of their environment, so we can use them to probe the conditions of star formation. However, it is important to note that molecular abundances can also *control* their physical environment and radically affect the process of star formation. For example, molecules such as CO are effective coolants at the cold temperatures of prestellar cores ($\sim$ 10 K). This is because the $J = 1 \rightarrow 0$ line of CO ($\Delta E = 5.5$ K) can be excited at such cold temperatures, and the photons produced are radiated away from the cloud causing it to lose energy (Dyson & Williams 1997). In this way, CO acts as a thermostat for dark interstellar clouds. Without CO, instead of the initial core collapse being isothermal, the core would heat up, increasing the thermal pressure earlier and therefore not allowing the core to collapse to as small a radius as it could do if CO were present. This is the case for Population III

stars in the early Universe, which were formed in metal free conditions with H_2 as the main coolant, and were therefore much more massive and short-lived than the stars we see today (Dalgarno 2006).

Another way that chemistry affects star formation is through the ionisation fraction of the gas, because this affects the degree of coupling of the gas to the magnetic field and therefore how much support the magnetic field gives the gas against gravitational collapse. The ambipolar diffusion timescale is approximately (Maret & Bergin 2007)

$$\tau_{\rm ad} \sim 2 \times 10^{14} X(e^-) \text{ yr}, \tag{2.1}$$

and the free-fall timescale is given by:

$$\tau_{\rm ff} = \left(\frac{3\pi}{32 G \rho}\right)^{1/2} \sim 3.7 \times 10^7 (n_{\rm H_2}/\text{cm}^{-3})^{-1/2} \text{ yr}, \tag{2.2}$$

(using $\rho = n_{\rm H_2} m_{\rm H_2}$). Therefore, for a typical prestellar core density of 10^5 cm^{-3}, magnetic fields will be able to provide significant support for $X(e^-) \gtrsim 10^{-8}$ (at this point $\tau_{\rm ad} \gtrsim 10\tau_{\rm ff}$), assuming strong enough magnetic fields are present. The ionisation fraction is consequently a crucial factor in controlling the timescale for star formation (see Section 1.3). The ionisation fraction is strongly dependent on the chemical composition of the gas, because, for example, if the gas has a large fraction of low ionisation potential metals then these are easily ionised by cosmic rays, giving rise to a large electron fraction.

It is therefore extremely important to understand the chemical composition of the gas in molecular clouds in order to fully understand how stars form, as well as understanding which molecules can be used as tracers of particular physical and dynamical conditions.

2.2 Chemical processes

In the Earth's atmosphere, molecules such as O_2 and N_2 can easily form in the gas-phase via three body interactions. If one considers two atoms, X and Y, approaching each other, their energy of interaction can be described as in Figure 2.1. To conserve energy, when the distance between the atoms is that of the bottom of the potential well, the kinetic energy of the atoms will increase, and unless energy is removed from the system, the atoms will just bounce apart again. The chances that energy is removed from the system by a photon, i.e.

$$\text{A} + \text{B} \rightarrow \text{AB} + h\nu \tag{2.3}$$

are very small. This is because the time that the atoms are in contact is only $\sim 10^{-13}$ s (which is approximately the period of a vibrational oscillation in the molecule AB), which is much smaller

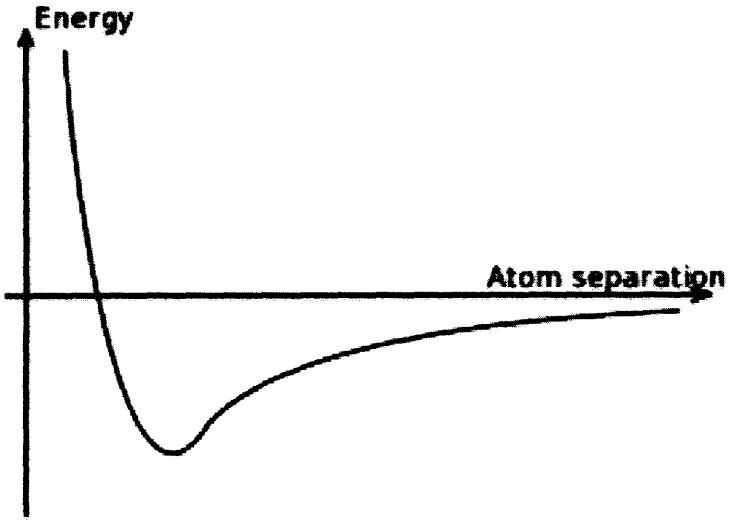

Figure 2.1: The interaction of two atoms.

than the timescale for the complex to radiate away a photon ($\sim 10^{-8}$ s) (Dyson & Williams 1997). This process is called radiative association, and is very slow in the conditions of the interstellar medium.

If, however, there is a third atom, Z, present, it may be able to remove some of the kinetic energy of the system, allowing atoms X and Y to remain at the bottom of the potential well to form the molecule XY. The chances of three atoms colliding in this way are high at the densities of the Earth's atmosphere (1.2 kg m^{-3} at sea level), but at the extreme low densities of the interstellar medium, ($n_{\rm H} \sim 10^4 - 10^6$ cm^{-3}, which corresponds to mass densities of $\sim 10^{-17} - 10^{-15}$ kg m^{-3} in 'dense' molecular clouds, which is lower density than can be achieved even with the latest ultra high vacuum chambers on Earth) this process is almost impossible (Hartquist & Williams 1995).

For reactions involving existing molecules, there is not a problem for energy stabilisation, because the unstable complex formed can dissociate into smaller products, which can carry off the excess energy of the complex as kinetic energy. So, for the general reaction

$$\mathrm{AB} + \mathrm{CD} \rightarrow \mathrm{ABCD}^* \rightarrow \mathrm{AC} + \mathrm{BD}, \tag{2.4}$$

the excess energy of the complex ABCD* is carried away by the kinetic energy of the products AC and BD. But how do molecules form initially in the interstellar medium?

Let us first assume that there is a substantial amount of molecular hydrogen already present (we will discuss the problem of H_2 formation in Section 2.2.1). The other elements present in the

molecular cloud (C, N, O, S, Fe, etc., which have been formed by nucleosynthesis in previous generations of stars) can react efficiently with molecular hydrogen if they have been ionised. For example, the reaction

$$O^+ + H_2 \rightarrow OH^+ + H \tag{2.5}$$

has a rate constant of $k = 1.70 \times 10^{-9}$ cm^3 s^{-1}, independent of temperature, which compared to the rate constant for the reaction of H_2 with neutral atomic oxygen ($k = 3.14 \times 10^{-17} \times e^{-350.0}$ cm^3 s^{-1} at 10 K $\sim$ 0.0 cm^3 s^{-1}), is extremely fast. This is because the ion can polarise the neutral molecule (in this case H_2), resulting in an electrostatic attraction between the species. According to classical theory, the cross-section for the interaction between the reactants is πb_0^2, with $b_0 = (\alpha e^2/\pi\varepsilon_0\mu v^2)^{1/4}$, where e is the charge on the ion, α is the polarisability of the molecule, ε_0 is the permittivity of free space, μ is the reduced mass of the reactants and v in the initial relative velocity. The rate coefficient is derived by $\langle v\pi b_0^2 \rangle$, which is independent of velocity and therefore explains why the rate for reaction (2.5) given above is independent of temperature.

Now we need to consider the sources of ionisation in molecular clouds. The interstellar medium is permeated by the interstellar radiation field (hereafter ISRF), which has contributions from the cosmic background radiation field at 2.7 K, galactic dust emission at 30 K, PAH (polycyclic aromatic hydrocarbon) emission, emission from cool stars and early-type (OB) stars, and emission by hot plasmas. The form of the ISRF for the solar neighbourhood is shown in Figure 2.2 (reproduced from Tielens 2005). The ionisation potentials of carbon, oxygen and nitrogen are $\sim 11 - 15$ eV, and so photons at ultraviolet (UV) wavelengths are required for ionisation ($\nu \sim 10^{15} - 10^{16}$ Hz). The contribution to the ISRF at these wavelengths comes from OB stars, and is capable of causing significant ionisation in the more diffuse regions of the interstellar medium.

Inside dark cores, however, the ISRF is heavily extinguished because of absorption and scattering by dust, so cosmic rays are the most important source of ionisation and therefore drive the chemical reaction network. Cosmic rays are energetic particles with various origins, such as rotating neutron stars and supernovae within the Galaxy, and are mostly made up of protons and electrons with energies of a few MeV. It is these energetic protons and electrons that are responsible for the ionisation in dark cores, simply because they are the most abundant form of cosmic rays. One of the most important ions in the interstellar medium is H_3^+, which is created by cosmic rays via the reactions:

$$H_2 + CR \rightarrow H_2^+ + e^- + CR \tag{2.6}$$

$$H_2^+ + H_2 \rightarrow H_3^+ + H. \tag{2.7}$$

Figure 2.2: The mean intensity of the ISRF in the solar neighbourhood in units of erg cm^{-1} s^{-1} Hz^{-1} sr^{-1}. *Source: Tielens (2005).*

Since H_2 has a low proton affinity, H_3^+ is more likely to react with species with a higher proton affinity such as carbon and oxygen. The H_3^+ ion therefore initiates chains of chemical reactions involving elements such as oxygen and carbon, giving rise to the rich number of chemical species that are seen.

Below is a brief summary of some of the many types of reactions that take place inside molecular clouds and dark cores:

Cosmic ray ionisation: e.g. $H_2 + CR \rightarrow H_2^+ + e^- + CR$. As mentioned above, cosmic rays drive the chemistry inside dark cores by creating H_3^+, but they also ionise other species such as He, C, N, O and CO. From the observed abundances of molecular ions inside dark cores, the ionisation rate of H_2 by cosmic rays has been estimated to be between 1×10^{-17} s^{-1} and 5×10^{-17} s^{-1} (Dalgarno 2006). In the chemical models used in this thesis we adopt the 'standard' cosmic ray ionisation rate for H_2 of 1.3×10^{-17} s^{-1}.

Photoionisation and photodissociation: e.g. $C + h\nu \rightarrow C^+ + e^-$; $HCN + h\nu \rightarrow CN + H$. As mentioned earlier, the UV component of the ISRF, originating from OB stars, is capable of ionising species such as C, N, O and H. The photoionisation rates are proportional to $e^{-\gamma A_v}$, where γ is a constant and A_v is the visual extinction caused by dust grains. For dark clouds, with $A_v \gtrsim 5$, the photoionisation rates are therefore highly suppressed. However, a small but significant UV field can be maintained in the interiors of dark clouds by cosmic rays (Prasad & Tarafdar 1983), so some degree of ionisation can be retained in dark cores. In this mechanism, UV radiation is produced by the decay of the Lyman and Werner states of molecular hydrogen, which has been excited by the energetic electrons emitted by cosmic

ray ionisation of H_2 (see Section 3.2.3 for more detail).

Exchange reactions: These can either be ion-molecule (e.g. $H_3^+ + CO_2 \rightarrow HCO_2^+ + H_2$), neutral-neutral (e.g. C + OH → CO + H), carbon insertion (e.g. $C + CH_2 \rightarrow C_2H + H$) or charge exchange (e.g. $N^+ + CO \rightarrow N + CO^+$). Neutral-neutral reactions are often slow because the forces between the reactants are weak, so they therefore have a much smaller cross-section than for ion-molecule reactions. Many neutral-neutral reactions also have an activation energy barrier, although they are difficult to predict theoretically and are often determined experimentally.

Radiative association: e.g. $C + O \rightarrow CO + h\nu$. As mentioned earlier, radiative association reactions are slow, so do not contribute significantly to the chemistry in molecular clouds.

Recombination: e.g. $H_3O^+ + e^- \rightarrow H_2O + H$ (dissociative); $O^+ + e^- \rightarrow O + h\nu$ (radiative). The initial product of recombination reactions is generally in an unstable, excited state, so it either has to dissociate or emit a photon. Dissociative recombination is generally an efficient process because of the strong attraction between the reactants, and the excess energy is carried off in the form of kinetic energy of the products. Radiative recombination, which occurs when atoms react with electrons, is less efficient because the resulting neutral atom is more likely to lose its newly acquired electron rather than emit a photon for stabilisation.

2.2.1 H_2 formation

We have explained above that if molecular hydrogen is present in molecular clouds, it can initiate a rich and complex chemistry. Now we have to answer the question of how molecular hydrogen can form in atomic conditions. The radiative association reaction

$$H + H \rightarrow H_2 + h\nu \tag{2.8}$$

is extremely unlikely at low temperatures, because the photon emitted must result from a forbidden transition (Gould & Salpeter 1963). Alternative gas-phase formation routes for H_2 are:

$$H + e^- \rightarrow H^- + h\nu \tag{2.9}$$

$$H^- + H \rightarrow H_2 + e^- \tag{2.10}$$

and also

$$H + H^+ \rightarrow H_2^+ + h\nu \tag{2.11}$$

$$H_2^+ + H \rightarrow H_2 + H^+. \tag{2.12}$$

These formation routes involve recombination and radiative association, which are slow and inefficient processes. In 1948, van de Hulst therefore postulated that H_2 formation could occur on dust grains, with the dust grain surface acting as a catalyst, and it is now widely accepted as the only viable formation route of H_2 under typical interstellar conditions. Three mechanisms for H_2 formation on dust grains have been proposed, and they are described below:

Langmuir-Hinshelwood (LH) mechanism: H atoms adsorb to the dust grain surface where they are thermalised. The H atoms diffuse over the surface, and can react when two H atoms meet. The newly formed H_2 molecule can then desorb from the surface of the dust grain, back into the gas-phase (Langmuir 1922).

Eley-Rideal (ER) mechanism: When an H atom collides with the dust grain, it reacts instantly with another H atom already adsorbed to the surface to form H_2 (Eley & Rideal 1940). This mechanism is more likely when the coverage of hydrogen atoms on the grain surface is high.

Hot atom mechanism: This mechanism is an intermediate between the LH and ER mechanisms. In this case, one hydrogen atom is adsorbed and in thermal equilibrium with the grain, whereas the other H atom is not yet thermalised and therefore at a higher temperature. The non-thermalised 'hot' atom can diffuse towards the thermalised H atom (Harris & Kasemo 1981).

In low mass star forming regions, it is possible that H_2 formation can occur via all three mechanisms, although the low H atom coverage means that the ER mechanism is the least likely.

The rate of H_2 formation on the grain surface depends on the probability of an H atom adsorbing to the grain surface (or to the ice mantle on the surface of the grain), the time spent on the grain before the H atom thermally desorbs, and the mobility of the H atom on the grain (Al-Halabi & van Dishoeck 2007). These factors are all dependent on the nature of the grain or the ice mantle covering the grain. For example, the binding energy of an H atom to an amorphous ice surface is likely to be higher than that for a crystalline ice surface, because in amorphous ice the porous surface is better at trapping H atoms.

Theoretical rates for H_2 formation are therefore complicated to calculate, but in order to account for the observed H_2 abundance seen in molecular clouds it must be a very efficient process, such that nearly every H atom that collides with a dust grain will leave as an H_2 molecule. The rate of formation of H_2 is therefore given by (in $cm^{-3}\ s^{-1}$):

$$R_{H_2} = \frac{1}{2}\pi\langle a_g^2 n_g\rangle v(H) n(H) S(H), \tag{2.13}$$

where $\pi\langle a_g^2 n_g\rangle$ is the average grain surface area per unit volume, $v(\mathrm{H})$ is the velocity of the hydrogen atoms, $n(\mathrm{H})$ is the gas-phase atomic hydrogen abundance, and $S(\mathrm{H})$ is the sticking coefficient of atomic hydrogen, which is a measure of the probability that an H atom will stick to the grain surface long enough for a reaction to take place. The factor of 1/2 in equation (2.13) is to take into account that for every H_2 molecule formed, two H atoms will be removed. The value of $\pi\langle a_g^2 n_g\rangle$ is rather uncertain, but has been estimated to be $\sim (2 \times 10^{-22} - 6 \times 10^{-22}) n_{\mathrm{H}}$ cm^{-1} (Rawlings *et al.* 1992). The velocity may be estimated by assuming thermal equilibrium, so $3/2kT = 1/2 m_{\mathrm{H}} v(\mathrm{H})^2$. Substituting these values into equation (2.13) gives:

$$R_{\mathrm{H_2}} \approx 10^{-17} S(\mathrm{H}) \sqrt{T} n(\mathrm{H}) n_{\mathrm{H}}, \tag{2.14}$$

with the exact value of the constant on the right hand side of this equation depending on the assumed grain size distribution.

In the models used in Chapter 3, the sticking coefficient is assumed to be unity, and in Chapters 4,5,6 and 7 the sticking coefficient is given by $(T/102.0 + 1)^{-2}$, which is the value estimated by Buch & Zhang (1991) using molecular dynamics simulations, also approximately unity at low temperatures ($\sim$ 10 K).

2.2.2 Freeze-out and surface chemistry

As well as dust grains acting as a catalytic surface for hydrogen formation, they also accrete gas-phase species, forming an icy mantle. This process is known as freeze-out, and it has a large effect on the overall chemistry inside a core by removing species from the gas-phase, and also by allowing surface reactions to occur on dust grains. Understanding freeze-out is essential for the theory of star formation, because if molecules such as CO are depleted this will have a large effect on the cooling rate of the gas. We also need to understand freeze-out to correctly interpret observations of the emission from molecules such as CO. For example, we cannot use the standard CO-H_2 conversion ratio to estimate the H_2 density from CO observations if CO is heavily depleted.

The evidence for freeze-out is very strong. Firstly, ices have been identified from infrared absorption spectra along the lines of sight towards several dark cores and YSOs. The bond stretch vibrations of molecules in the solid state, such as H_2O, CO and CO_2, and several others have been identified, and are found to be more abundant in the densest regions (e.g. Bergin *et al.* 2005). CO can have a fractional abundance of up to 10^{-4} in the ice phase, which is comparable to its abundance in the gas-phase in undepleted conditions (Pontoppidan 2006). Secondly, when comparing H_2 column densities of prestellar cores derived from dust continuum observations to those derived

from the CO column densities, it appears that those derived from CO data show a much flatter profile in the centre of the cores than those derived from the dust, indicating that CO is missing in the densest central regions. Bacmann *et al.* (2002) used this method to estimate the depletion in several nearby prestellar cores, and found CO to be depleted by a factor of 4–15 in the core centres.

Finally, interferometric observations of molecules such as CO, CS and N_2H^+ often reveal a ring-like structure around dense cores, again indicating that the molecules are missing in the dense central regions. Figure 2.3 shows the N_2H^+(1-0) integrated intensity map of the Class 0 object IRAM 04191+1552 taken from Belloche & André (2004), which clearly shows this ring-shaped structure around the central object.

Figure 2.3: $N_2H^+(1 \rightarrow 0)$ integrated intensity map of the Class 0 object IRAM 04191+1552. The contours vary from 0.16 to 2.1 in steps of 0.16 Jy beam^{-1} km s^{-1}, and the cross marks the central position of the object. *Source: Belloche & André (2004).*

The fact that freeze-out appears to be most severe in the densest regions of molecular clouds implies that the ISRF can prevent freeze-out by photodesorption. In fact, there appears to be a threshold visual extinction, $A_{v,\mathrm{crit}}$ below which no ice is detected on grain mantles. Observations of water ice in molecular clouds have shown that the opacity of the 3.1μm feature, which is a measure of the abundance of water ice, is related to the A_v by the relation

$$\tau_{3.1} = \alpha(A_v - A_{v,\mathrm{crit}}), \tag{2.15}$$

where α and $A_{v,\mathrm{crit}}$ are constants. For $A_v \leq A_{v,\mathrm{crit}}$, no water ice is detected. Values of $A_{v,\mathrm{crit}}$ range from $3-4$ mag in the Taurus and Corona Australis molecular clouds (Whittet *et al.* 1988; Chen & Graham 1993), to $5-6$ mag in the Serpens molecular cloud (Eiroa & Hodapp 1989).

The rate of accretion onto grains of species i is estimated by multiplying the rate of collisions of species i with the grain surface by the probability that it sticks to the grain [the sticking coefficient, $S(i)$] and a factor, $C(i)$, to take into account whether species is ionic and hence more attracted to the dust grains, which tend to be negatively charged. This gives the rate as:

$$\frac{dn(i)}{dt} = \pi\langle a_{\mathrm{g}}^2 n_{\mathrm{g}}\rangle v(i) n(i) S(i) C(i), \tag{2.16}$$

where $\pi\langle a_{\mathrm{g}}^2 n_{\mathrm{g}}\rangle$ and $v(i)$ have the same definitions as in Section 2.2.1. Equation (2.16) is a more generalised version of equation (2.13). The value of $C(i)$ is given by (Rawlings *et al.* 1992):

$$\begin{aligned} C &= 1 && \text{for neutral species,} \\ &= 1 + (16.71 \times 10^{-4}/a_{\mathrm{g}}T) && \text{for singly charged positive ions.} \end{aligned} \tag{2.17}$$

Assuming the velocity is given by $3/2kT = 1/2m(i)v(i)^2$ (thermal equilibrium), the freeze-out rate in $\mathrm{cm}^{-3}\ \mathrm{s}^{-1}$ becomes:

$$\frac{dn(i)}{dt} = 4.57 \times 10^4 \langle a_{\mathrm{g}}^2 n_{\mathrm{g}}\rangle T^{1/2} C S(i) m(i)^{-1/2} n(i). \tag{2.18}$$

The timescale for freeze-out of a heavy molecule such as CO is therefore $\sim 10^9/n_{\mathrm{H}} S(i)$ yrs, so at a typical dark core density of $10^5\ \mathrm{cm}^{-3}$ the freeze-out timescale in the absence of desorption is only 10^4 yr, which is much less than the typical dynamical and chemical timescales. Freeze-out is therefore a very efficient process, but there is still some debate as to whether freeze-out is complete, such that *all* of the heavy species such as CO will be removed from the gas-phase at high densities. It is possible that non-thermal desorption mechanisms may operate inside dark cores, maintaining significant abundances of gas-phase species, and this is the subject of Chapter 3.

Once molecules have frozen out, it is also likely that they can undergo further chemical reactions on the grain surface, as well as photoprocessing by the cosmic ray induced UV field inside dark cores (Ruffle & Herbst 2000*a*, 2001). The most likely types of chemical reactions that can occur are hydrogenation reactions, due to the high mobility of the hydrogen atom on the grain surface. It is therefore believed that hydrogen rich species, such as NH_3, CH_4, CH_3OH and H_2O are formed in significant quantities on grain surfaces, rather than only forming in the gas-phase.

In reality, the surface hydrogenation reactions to form these molecules will occur in a number of steps. For example, the formation of methanol on grain surfaces has been proposed to occur by

the following surface reactions, following the freeze-out of CO (Ruffle & Herbst 2000*a*):

$$\mathrm{H} + \mathrm{CO} \rightarrow \mathrm{HCO} \tag{2.19}$$

$$\mathrm{H} + \mathrm{HCO} \rightarrow \mathrm{H_2CO} \tag{2.20}$$

$$\mathrm{H} + \mathrm{H_2CO} \rightarrow \mathrm{CH_3O} \tag{2.21}$$

$$\mathrm{H} + \mathrm{CH_3O} \rightarrow \mathrm{CH_3OH}. \tag{2.22}$$

However, in the models in this thesis which include freeze-out, we simplify the surface chemistry by assuming that the hydrogenation occurs in one step. For CO, for example, we assume that one per cent of the CO that freezes-out will form CH_3OH in a single step, $CO_{(g)} \rightarrow CH_3OH_{(s)}$ (where the subscripts (g) and (s) denote species in the gas-phase and solid-phase respectively). The rest of the CO is assumed to remain as CO ice on the grain surface. We also assume that ions are neutralised when they freeze-out. A list of the surface reactions we have included (for the models used in Chapters 3, 4 and 8) is given in Table 2.1.

2.3 Modelling chemical networks

Much of the work in this thesis involves using models to predict chemical abundances inside prestellar cores and YSOs, to see how chemical abundances reflect the physical conditions of their environment. To do this we have to consider all the possible formation and destruction routes for each species.

The rate of production of a species C due to the chemical reaction, A + B $\rightarrow$ C + D, is given by:

$$\frac{dn(\mathrm{C})}{dt} = k_{\mathrm{p}}(T)n(\mathrm{A})n(\mathrm{B})\ \mathrm{cm^{-3}s^{-1}}, \tag{2.23}$$

where k_{p} is the rate coefficient in $\mathrm{cm^3\ s^{-1}}$, and whose value is often dependent on temperature. If the species C is destroyed by the reaction C + X $\rightarrow$ Y + Z, with a rate coefficient k_{d}, as well as being destroyed by photodissociation at a rate of $\beta(C)\ \mathrm{s^{-1}}$, and freezing out onto dust grains at a rate $k_{\mathrm{f}}(C)n_{\mathrm{H}}n(\mathrm{C})\ \mathrm{cm^{-3}\ s^{-1}}$, then the net rate of change of $n(\mathrm{C})$ is given by:

$$\frac{dn(\mathrm{C})}{dt} = k_{\mathrm{p}}(T)n(\mathrm{A})n(\mathrm{B}) - n(\mathrm{C})[k_{\mathrm{d}}n(\mathrm{X}) + \beta(\mathrm{C}) + k_{\mathrm{f}}(C)n_{\mathrm{H}}]\ \mathrm{cm^{-3}s^{-1}}. \tag{2.24}$$

In reality, the species C can be produced and destroyed by hundreds of chemical reactions, giving the total rate of change of $n(\mathrm{C})$ as:

$$\frac{dn(\mathrm{C})}{dt} = \sum_i \sum_j k_{\mathrm{ij}}n(i)n(j) - n(\mathrm{C})\left[\sum_j k_j n(j) + \beta(\mathrm{C}) + k_{\mathrm{f}}(C)n_{\mathrm{H}}\right]\ \mathrm{cm^{-3}s^{-1}}. \tag{2.25}$$

Table 2.1: Surface reactions included in the models used in Chapters 3, 4 and 8. The subscripts (g) and (s) denote the gas-phase and solid-phase respectively.

$C_{(g)}$	$\rightarrow CH_{4(s)}$	$HCS_{(g)}$	$\rightarrow H_2CS_{(s)}$
$CH_{(g)}$	$\rightarrow CH_{4(s)}$	$S_{(g)}$	$\rightarrow H_2S_{(s)}$
$OH_{(g)}$	$\rightarrow H_2O_{(s)}$	$S^+_{(g)}$	$\rightarrow H_2S_{(s)}$
$CH_{2(g)}$	$\rightarrow CH_{4(s)}$	$HS^+_{(g)}$	$\rightarrow H_2S_{(s)}$
$CH_{3(g)}$	$\rightarrow CH_{4(s)}$	$CS^+_{(g)}$	$\rightarrow CS_{(s)}$
$CH_{4(g)}$	$\rightarrow CH_{4(s)}$	$SO^+_{(g)}$	$\rightarrow SO_{(s)}$
$HCO_{(g)}$	$\rightarrow H_2CO_{(s)}$	$HCS^+_{(g)}$	$\rightarrow H_2CS_{(s)}$
$CN_{(g)}$	$\rightarrow HCN_{(s)}$	$SO^+_{2(g)}$	$\rightarrow SO_{2(s)}$
$C^+_{(g)}$	$\rightarrow CH_{4(s)}$	$NS^+_{(g)}$	$\rightarrow NS_{(s)}$
$NH_{(g)}$	$\rightarrow NH_{3(s)}$	$OCS^+_{(g)}$	$\rightarrow OCS_{(s)}$
$N^+_{(g)}$	$\rightarrow NH_{3(s)}$	$HNO^+_{(g)}$	$\rightarrow HNO_{(s)}$
$O^+_{(g)}$	$\rightarrow H_2O_{(s)}$	$H_2NO^+_{(g)}$	$\rightarrow HNO_{(s)} + H_{(g)}$
$C^+_{2(g)}$	$\rightarrow C_{2(s)}$	$O_2H^+_{(g)}$	$\rightarrow O_{2(s)} + H_{(g)}$
$O^+_{2(g)}$	$\rightarrow O_{2(s)}$	$H_3CO^+_{(g)}$	$\rightarrow H_2CO_{(s)} + H_{(g)}$
$N^+_{2(g)}$	$\rightarrow N_{2(s)}$	$NS^+_{(g)}$	$\rightarrow NS_{(s)}$
$CH^+_{(g)}$	$\rightarrow CH_{4(s)}$	$C_2H^+_{2(g)}$	$\rightarrow C_2H_{2(s)}$
$NH^+_{(g)}$	$\rightarrow NH_{3(s)}$	$H_3S^+_{(g)}$	$\rightarrow H_2S_{(s)} + H_{(g)}$
$OH^+_{(g)}$	$\rightarrow H_2O_{(s)}$	$H_2CS^+_{(g)}$	$\rightarrow HCS_{(s)} + H_{(g)}$
$CO^+_{(g)}$	$\rightarrow CO_{(s)}$	$HS^+_{2(g)}$	$\rightarrow S_{2(s)} + H_{(g)}$
$CN^+_{(g)}$	$\rightarrow HCN_{(s)}$	$H_2S^+_{2(g)}$	$\rightarrow HS_{2(s)} + H_{(g)}$
$NO^+_{(g)}$	$\rightarrow NO_{(s)}$	$S^+_{2(g)}$	$\rightarrow S_{2(s)}$
$CH^+_{2(g)}$	$\rightarrow CH_{4(s)}$	$H_3CS^+_{(g)}$	$\rightarrow H_2CS_{(s)}$
$NH^+_{2(g)}$	$\rightarrow NH_{3(s)}$	$HSO^+_{(g)}$	$\rightarrow SO_{(s)} + H_{(g)}$
$H_2O^+_{(g)}$	$\rightarrow H_2O_{(s)}$	$SO^+_{2(g)}$	$\rightarrow SO_{2(s)}$
$HCO^+_{(g)}$	$\rightarrow H_2CO_{(s)}$	$HOCS^+_{(g)}$	$\rightarrow OCS_{(s)} + H_{(g)}$
$HCN^+_{(g)}$	$\rightarrow HCN_{(s)}$	$Mg^+_{(g)}$	$\rightarrow Mg_{(s)}$
$C_2H^+_{(g)}$	$\rightarrow C_2H_{(s)}$	$NH^+_{4(g)}$	$\rightarrow NH_{3(s)} + H_{(g)}$
$NH^+_{3(g)}$	$\rightarrow NH_{3(s)}$	$HCNH^+_{(g)}$	$\rightarrow HCN_{(s)} + H_{(g)}$
$H_2CO^+_{(g)}$	$\rightarrow H_2CO_{(s)}$	$N_2H^+_{(g)}$	$\rightarrow N_{2(s)} + H_{(g)}$
$CH^+_{3(g)}$	$\rightarrow CH_{4(s)}$	$HNS^+_{(g)}$	$\rightarrow NS_{(s)} + H_{(g)}$
$H_3O^+_{(g)}$	$\rightarrow H_2O_{(s)} + H_{(g)}$	$C^+_{3(g)}$	$\rightarrow C_{2(s)} + C_{(g)}$
$HCO^+_{2(g)}$	$\rightarrow CO_{2(s)} + H_{(g)}$	$H_2S^+_{(g)}$	$\rightarrow H_2S_{(s)}$
$CH^+_{5(g)}$	$\rightarrow CH_{4(s)} + H_{(g)}$	$HSO2^+_{(g)}$	$\rightarrow SO_{2(s)} + H_{(g)}$
$CH^+_{4(g)}$	$\rightarrow CH_{4(s)}$	$CO_{(g)}$	$\rightarrow CH_3OH_{(s)}$
$NH_{2(g)}$	$\rightarrow NH_{3(s)}$	$C_3H^+_{5(g)}$	$\rightarrow CH_3CCH_{(s)} + H_{(g)}$
$N_{(g)}$	$\rightarrow NH_{3(s)}$	$C_2H_5OH^+_{2(g)}$	$\rightarrow C_2H_5OH_{(s)} + H_{(g)}$
$O_{(g)}$	$\rightarrow H_2O_{(s)}$	$CH_3H^+_{2(g)}$	$\rightarrow CH_3OH_{(s)} + H_{(g)}$
$HS_{(g)}$	$\rightarrow H_2S_{(s)}$	$CH_3CNH^+_{(g)}$	$\rightarrow H_4C_2N_{(s)}$
$CS_{(g)}$	$\rightarrow H_2CS_{(s)}$		

In order to solve for this equation we also need to know the number densities of all the other species involved, which will also be governed by equations of the form (2.25). Therefore, to calculate the abundance of any one species, we have to solve a network of hundreds, or even thousands, of coupled ordinary differential equations. In this thesis we use the code GEAR to solve these equations numerically (apart from in Chapter 8 where the more recent code LSODE is used). These codes are well-suited to solving sets of *stiff* differential equations[1], and are commonly used in astrochemical models.

In the chemical models used in this thesis, the gas-phase reactions are taken from the UMIST RATE06 and RATE99 databases for astrochemistry (Woodall *et al.* 2007; Le Teuff *et al.* 2000). These databases list more than 4000 reactions, along with the coefficients α, β and γ, which are used to calculate the rate coefficient for each reaction. For two-body reactions γ gives the value of the activation energy barrier, and the rate can be calculated using the modified Arrhenius equation:

$$k = \alpha(T/300)^{\beta} \exp(-\gamma/T) \text{ cm}^3 \text{ s}^{-1}. \tag{2.26}$$

The total list of reactions includes two-body reactions (including ion-molecule, neutral-neutral and carbon insertion exchange reactions, charge exchange reactions and radiative association), direct cosmic ray ionisation, cosmic ray induced photoreactions (from the UV field generated by cosmic rays) and recombination reactions (both dissociative and radiative). The calculation of the rate coefficient depends on the type of reaction, and can be calculated by the formulae given in Table 2.2.

Table 2.2: Calculation of the rate coefficients for reactions in the UMIST RATE99 and RATE06 databases. T is the *kinetic* temperature, ω is the dust grain albedo and A_v is the visual extinction.

Reaction type	**Rate constant**
Two body reactions	$k = \alpha(T/300)^{\beta} \exp(-\gamma/T)$ cm^{3}s^{-1}
Direct cosmic ray ionisation	$k = \alpha$ s^{-1}
Cosmic ray induced photoreactions	$k = \alpha(T/300)^{\beta}\gamma/(1-\omega)$ s^{-1}
Photoreactions	$k = \alpha \exp(-\gamma A_v)$ s^{-1}

Approximately one third of the values for α, β and γ are determined from experimental data, although for some reactions low temperature data is not available so the rate coefficients have to

[1]Differential equations are regarded as stiff if certain numerical methods for solving the equations are numerically unstable. In this case the equations are stiff because of the large variation in the rate constants and number densities.

be extrapolated. For reactions with no experimental data, values are calculated theoretically or estimated from the properties of the molecules and reaction type.

For some reactions, the values of α, β and γ are different for different temperature ranges. For the models of prestellar cores used in this thesis, the values for the lowest temperature ranges are used. For example, the reaction

$$O + OH \rightarrow O_2 + H \tag{2.27}$$

has $\alpha = 1.77 \times 10^{-11}$ and $\gamma = -178.0$ for $158 < T < 5000$ K, but $\alpha = 3.50 \times 10^{-11}$ and $\gamma = 0.0$ for $39 < T < 142$ K. For this work we take the second set of values, as using the first set would lead to large errors in abundances.

Reaction (2.27) is also an example of a reaction with a large negative activation energy. For these types of reaction, if no lower temperature values of the rate coefficients are available, the reaction must be removed from the network because the extremely large value of $\exp(-\gamma/T)$ at low temperatures is clearly unphysical and causes problems in the running of the code.

Surface reactions are not included in the UMIST databases, so these have to be added by hand. The formation of H_2 on grain surfaces, which is essential in models of dark cores, is added at the rate given by equation (2.14). In most of the models in this thesis, freeze-out is included at the rate given by equation (2.18), and it is assumed that species become fully hydrogenated once they stick to the grain, as described in Section 2.2.2.

CHAPTER 3

DESORPTION FROM INTERSTELLAR ICES

The work presented in this chapter is based on the paper by Roberts et al. *(2007).*

3.1 Introduction

In cold dark interstellar clouds, heavy molecules accumulate onto dust grains, forming icy mantles on their surfaces (see Section 2.2.2). This process, known as freeze-out, occurs on a timescale of a few times $10^9 n_{\rm H}^{-1}$ yr (where $n_{\rm H}$ is the total hydrogen nucleon number density) in the absence of desorption. This is much less than the expected lifetime of a typical molecular cloud so, if freeze-out was unlimited, we would expect the majority of observations to show no evidence for heavy gas-phase species. However, observations of molecules such as CO in dark clouds, for example L1689B, TMC1-CP and L134N (Lee *et al.* 2003; Smith *et al.* 2004; Wakelam *et al.* 2006*a*), indicate that desorption processes must be operating for mantle growth to be limited.

Although this conclusion has been accepted for over 20 years, it is still not fully understood how this desorption occurs. Many possible mechanisms have been proposed, most of which require impulsive heating of grains which can be caused by (a) direct impact of cosmic rays (Hasegawa & Herbst 1993; Hartquist & Williams 1990; Leger *et al.* 1985), (b) X-rays (Leger *et al.* 1985), (c) ultraviolet (UV) photons induced by cosmic rays (cosmic ray photodesorption) (Hartquist & Williams 1990; Duley *et al.* 1989), or (d) exothermic reactions occurring on the grain surface (Allen & Robinson 1975; Garrod *et al.* 2007), in particular the formation of molecular hydrogen (Willacy *et al.* 1994*b*; Duley *et al.* 1993). Molecules can either be desorbed by classical evaporation (Leger *et al.* 1985) or by chemical explosions (Shen *et al.* 2004; Shalabiea & Greenberg 1994; Leger *et al.* 1985). These chemical explosions can only occur if the mantle has previously been irradiated with

UV radiation which creates radicals. If the grain temperature is raised to $\sim$ 27 K, the radicals become mobile and then undergo explosive reactions capable of expelling the entire grain mantle. We will not consider chemical explosions in this chapter because in dark clouds with $A_v > 5$ magnitudes it is unlikely that the grain mantles will have received sufficient UV irradiation (Leger *et al.* 1985), and any radicals that do form are likely to be hydrogenated due to the high abundance of hydrogen atoms present (Willacy & Millar 1998).

Recent chemical models of dark clouds tend to include only desorption via thermal evaporation (which is negligible for dark clouds with temperatures of 10 K) and/or direct heating by cosmic rays, using the formulation given by Hasegawa & Herbst (1993) (hereafter HH93) (Ruffle & Herbst 2000*b*; Roberts *et al.* 2004). This chapter, therefore, aims to test the assumption that desorption via direct cosmic ray heating is the only effective non-thermal desorption mechanism relevant to dark molecular cores. In this study we adopt the model of a molecular cloud as being composed of an ensemble of dense (dark) cores in a more diffuse background (Garrod *et al.* 2006*a*). Ices are probably only present in the cores. We set out to test the desorption efficiencies, by including in an existing model of dark cloud chemistry three desorption mechanisms (desorption resulting from H_2 formation on grains, direct cosmic ray heating and cosmic ray photodesorption) that have been formulated in the literature, to find their relative importance in dark cores. We believe these three mechanisms are likely to be the most important in this situation, in the absence of any nearby X-ray sources in the molecular cloud.

We note that there already exist several other studies which model these three desorption mechanisms, for example Willacy *et al.* (1994*a*) (hereafter WRW94) performed a study very close to our own. However, our work differs to that of WRW94 because we try to take a simpler approach; by modelling a static cloud rather than a collapsing one we can easily see the effects of adding desorption to our chemical model. We also look further into the assumptions made about the ability of each desorption mechanism to desorb molecules with higher adsorption energies, such as H_2O and NH_3 (Section 3.4.3). Most importantly, we attempt to constrain the efficiency of each mechanism by comparing our results to observations of CO depletion in star-forming regions.

This chapter is structured as follows: In Section 3.2 we give a brief summary of these desorption mechanisms and in Section 3.3 we describe the model. The results are given in Section 3.4, and are discussed by comparing them to existing models in Section 3.5 and observations in Section 3.6. Concluding remarks are given in Section 3.7.

3.2 Desorption mechanisms

3.2.1 Desorption resulting from H_2 formation

It has long been suggested that the energy released from exothermic reactions on grain surfaces can release energy capable of desorbing mantle species (Allen & Robinson 1975). In particular, laboratory experiments on graphite substrates suggest that a non-negligible fraction, perhaps up to 40% (Creighan *et al.* 2006; Islam 2007) of the $\sim$ 4.5 eV released in the surface formation of molecular hydrogen is transferred to the grain surface. This leads to local heating which may thermally desorb weakly bound mantle species (Duley *et al.* 1993), although the extent to which the temperature rises transiently is not well determined, and depends on the local conductivity. In amorphous materials, the temperature rise may be relatively large.

Such a process may be *selective*, depending on the temperature achieved as a result of the energy deposition. In previous work (Duley *et al.* 1993; Willacy *et al.* 1994*b*,*a*), the conservative assumption was made that only the most volatile species (such as CO, N_2, NO, O_2, C_2 and CH_4) would be desorbed during the transient heating, corresponding to a threshold adsorption energy of $E_t = 1210$ K. Initially, we shall adopt the same threshold and range of volatile species, but we shall also consider the effects of variations from that value in Section 3.4.3.

The rate of desorption by this process for species i is given by:

$$R_{\rm hf} = \varepsilon R_{\rm H_2} M_{\rm s}(i,t) \quad {\rm cm^{-3}\ s^{-1}} \tag{3.1}$$

where $R_{\rm H_2}$ is the rate of H_2 formation on grains. $R_{\rm H_2}$ is proportional to the available grain surface area and the sticking/reaction probability to form H_2 (see Section 2.2.1). In this chapter we have used:

$$R_{\rm H_2} = 3.16 \times 10^{-17} n({\rm H}) n_{\rm H} \quad {\rm cm^{-3}\ s^{-1}} \tag{3.2}$$

where n(H) is the number density of atomic hydrogen and $n_{\rm H}$ is the total hydrogen nucleon density. This is equal to the rate given by equation 2.14 at a temperature of 10 K. $M_{\rm s}(i,t)$ is the fraction of the mantle consisting of species i, calculated self-consistently as a function of time. ε is an efficiency parameter such that $\varepsilon M_{\rm s}(i,t)$ gives the number of molecules of species i desorbing per H_2 molecule formed. The efficiency of this process is uncertain, but we can make a rough upper estimate as follows: If we assume that 40% ($\sim$ 2 eV) of the energy released during each H_2 formation is transferred to the grain, and given that the adsorption energies of the species we consider are $\sim$ 1000 K ($\sim 8.2 \times 10^{-2}$ eV), we would expect that a maximum of $\sim$ 20 molecules

could be desorbed every time an H_2 molecule is formed. It is likely, however, that this process is less efficient, because such a high value for ε would prevent the build-up of any mantle material until very late times (Willacy & Millar 1998). We therefore run our model with values of ε ranging from 0.01 to 1.0, and present results for $\varepsilon = 0.01$ and 0.1.

3.2.2 Desorption by direct cosmic ray heating

In this chapter, the rate of desorption by direct cosmic ray heating is calculated by simply considering the number of molecules capable of being desorbed per cosmic ray impact. This rate is different to that adopted in other models (see the discussion in Section 3.5.4).

As with desorption via H_2 formation, this process is believed to be selective (Willacy *et al.* 1994*a*), so only the volatile species (CO, etc.) are expected to be desorbed, at a rate given by:

$$R_{\rm cr} = F_{\rm cr}\langle \pi a_{\rm g}^2 n_{\rm g}\rangle \phi M_{\rm s}(i,t) \quad {\rm cm}^{-3}\ {\rm s}^{-1}. \tag{3.3}$$

where $F_{\rm cr}$ is the flux of cosmic rays, ϕ is an efficiency parameter such that $\phi M_{\rm s}(i,t)$ is the number of molecules released per cosmic ray impact, $a_{\rm g}$ is the grain radius and $n_{\rm g}$ is the number density of grains. We have used a value for the total grain surface area per cm^3, $\langle \pi a_{\rm g}^2 n_{\rm g}\rangle$, of $2.4 \times 10^{-22} n_{\rm H}$ cm^{-1}, consistent with Rawlings *et al.* (1992) if we use a value for the depletion coefficient of ~ 1.0.

Leger *et al.* (1985) showed that the iron nuclei component of cosmic rays should be the most effective in heating the grain, and therefore we adopt for the value for $F_{\rm cr}$ of 2.06×10^{-3} cm^{-2} s^{-1} which is an estimate of the iron fraction of the canonical cosmic ray flux. It is based on the proton cosmic ray flux in the interstellar medium given by Morfill *et al.* (1976), and the iron to proton ratio of 1.6×10^{-4} (estimated by Leger *et al.* 1985).

An estimate for ϕ can be taken from Leger *et al.* (1985) who worked out the evaporation rate of CO per grain resulting from both whole-grain and spot-grain heating by cosmic rays. For spot-grain heating, they calculated that 6×10^4 CO molecules would be released per cosmic ray impact, independent of grain size. For whole grain heating, however, the result was found to strongly depend on grain size, dominating spot-grain heating for $a_{\rm g} \leq 2500$ Å. We have tested this mechanism with values of ϕ ranging from 10^2 to 10^6, but we only present the results for $\phi = 10^5$ to be consistent with the lower estimate predicted by spot-grain heating. Since the volatile species make up approximately 40% of the grain mantle, using $\phi = 10^5$ implies that the number of molecules released per cosmic ray impact is $\phi M_{\rm s}(i) \approx 4 \times 10^4$.

3.2.3 Cosmic ray induced photodesorption

As cosmic rays travel through a molecular core, they ionise and excite the absorbing gas. Prasad & Tarafdar (1983) investigated the excitation of the Lyman and Werner systems of the hydrogen molecule, caused by collisions with either primary cosmic ray particles or secondary electrons released by cosmic ray ionisation. They found that emissions resulting from these excitations may be capable of maintaining a chemically significant level of UV photon flux in the interiors of dark clouds, where the interstellar UV radiation is heavily extinguished ($A_v \geq 5$).

When a UV photon impinges upon the mantle of a grain, it is most likely to be absorbed by H_2O which may then be dissociated into H and OH (Hartquist & Williams 1990). The energy of the dissociation products cause local heating, capable of desorbing nearby molecules. This process is non-selective, and proceeds at a rate given by:

$$R_{\rm crpd} = F_{\rm P}\langle \pi a_{\rm g}^2 n_{\rm g}\rangle Y M_{\rm s}(i,t) \quad {\rm cm}^{-3}\ {\rm s}^{-1}. \tag{3.4}$$

where $F_{\rm P}$ is the photon flux and Y is the yield per photon. Prasad & Tarafdar (1983) estimated $F_{\rm P}$ to be just 1350 cm^{-2} s^{-1}, but here we use a value of 4875 cm^{-2} s^{-1} taken from equation (21) of Cecchi-Pestellini & Aiello (1992) [1]. This value is much higher than the estimate of Prasad & Tarafdar (1983) because it explicitly includes the contribution to the excitation rate of H_2 by cosmic ray protons, not just the secondary electrons. We present the results for $Y = 0.1$, as estimated by Hartquist & Williams (1990), but as this value is uncertain we also ran the model with values of Y ranging from 1×10^{-3} to 100.

Obviously, the relative importance of these mechanisms depends upon the values used for ε, ϕ and Y, which can be treated as free parameters. In this chapter, we present the results for the values stated above, and in Section 3.6 we derive upper limits for these parameters based on observations.

3.3 The Model

In order to see clearly the relative importance of the various desorption mechanisms for the interstellar chemistry of molecular cores, we have used a simple one-point model of a static, isothermal dark cloud, at a density of $n_{\rm H} = 10^5$ cm^{-3} and a temperature of 10 K. The core has a visual extinction, A_v, of 10 magnitudes, and a radius of ~ 0.05 pc, implying a mass of 1 $M_\odot$.

[1] This is consistent with using a cosmic ray ionisation rate, ζ, of 1.3×10^{-17} s^{-1}.

3.3.1 The chemical model

The model, adapted from Viti *et al.* (2004), includes gas-phase reactions, freeze-out, surface reactions and desorption, with 127 gas-phase and 40 mantle species. The gas-phase species are listed in Table 3.1, and are made up of the elements H, He, C, O, N, S and Mg. The species and reactions are taken from the model as in Viti *et al.* (2004), which describes the rich chemistry of hot cores. The number of species and elements should therefore be more than sufficient to describe the low mass case in this chapter. The gas-phase reaction network consists of 1741 reactions from the UMIST RATE99 database (Le Teuff *et al.* 2000). Photoreactions are included, which take into account both the external interstellar radiation field and the internal cosmic ray induced UV field. Both direct and indirect ionisation by cosmic rays are also included, using a cosmic ray ionisation rate, ζ, of 1.3×10^{-17} s^{-1}. The hydrogen atom abundance (that drives the H_2 formation desorption mechanism) is determined self-consistently in the chemical network. Freeze-out and grain chemistry are described in Section 3.3.2.

The initial conditions are atomic, apart from carbon which is all singly ionised, and half the hydrogen nuclei are in the form of H_2. The initial elemental abundances are taken from Sofia & Meyer (2001) and are listed in Table 3.2.

3.3.2 Freeze-out and grain chemistry

The rate of accretion onto grains is given by equation (2.18). For the value of $\langle \pi a_g^2 n_g \rangle$, we have used the same value as in Section 3.2. Following WRW94, we have used $S(i) = 0.3$ for all species.

As described in Section 2.2.2, the only surface reactions that occur are hydrogenation of unsaturated species, and dissociative recombination of molecular ions. The list of surface reactions is given in Table 2.1. These reactions are assumed to occur instantly and the products remain on the grain surface until they are desorbed by one of the processes named above. H_2 is an exception in that it is assumed to desorb immediately because of the high exothermicity of the reaction, as is indicated by experimental studies (Creighan *et al.* 2006). We have also assumed that 1% of the CO that freezes-out forms CH_3OH on the grain surface, because gas-phase chemistry alone cannot reproduce the observed methanol abundances in star forming regions (Parise *et al.* 2006).

3.4 Results

By comparing the rate coefficients given for each of the desorption mechanisms, if we use $\varepsilon = 0.01$, $\phi = 10^5$ and $Y = 0.1$ at a density of $n_H = 10^5$ cm^{-3}, desorption via H_2 formation will dominate

Table 3.1: List of the gas-phase chemical species used in this model.

H	H_2	H_2^+	H_3^+	O
O^+	OH^+	OH	H^+	O_2
O_2^+	H_2O	H_2O^+	H_3O^+	O_2H^+
H_2CN	C	C^+	CH	CH^+
CH_2	CH_2^+	CH_3	CH_3^+	CH_4
CH_4^+	CH_5^+	C_2	C_2^+	C_2H
C_2H^+	$C_2H_2^+$	C_3^+	CO	CO^+
HCO	HCO^+	H_2CO	H_2CO^+	H_3CO^+
HCO_2^+	S	S^+	HS	HS^+
H_2S	H_2S^+	H_3S^+	OCS	OCS^+
S_2	S_2^+	HS_2	S_2H^+	$H_2S_2^+$
CS	CS^+	HCS	HCS^+	H_2CS
H_2CS^+	SO	HSO^+	SO_2	SO_2^+
HSO_2^+	H_3CS^+	$HOCS^+$	O_2H	CO_2
He	He^+	HeH^+	Mg	Mg^+
SO^+	N	N^+	NH^+	NH_2^+
NH_3^+	NH_4^+	NH	NH_2	NH_3
CN	CN^+	HCN^+	$HCNH^+$	HCN
N_2	N_2H^+	NS	NS^+	HNS^+
NO	NO^+	HNO	HNO^+	NO_2
H_2NO^+	N_2^+	OCN	CH_3OH	HNC
HC_3N	C_2H_2	CH_3CN	C_2H_4	CH_2CO
C_2H_5	C_2H_3	$C_3H_5^+$	C_3H_4	C_2H_5OH
$C_2H_7O^+$	$CH_3OH_2^+$	$H_5C_2O_2^+$	$HCOOCH_3$	C_2N
C_3N	C_2N^+	C_2NH^+	$C_2N_2^+$	C_4N^+
H_4C_2N	$H_4C_2N^+$			

Table 3.2: Initial elemental fractional abundances used in this model.

H	1.00
C	1.00×10^{-4}
O	2.14×10^{-4}
N	6.00×10^{-5}
S	1.30×10^{-6}
He	7.50×10^{-2}
Mg	7.00×10^{-9}

if the equilibrium atomic hydrogen density is greater than ~ 0.4 cm^{-3}. If ε is as high as 0.1 then this mechanism will always be dominant.

Figures 3.1 and 3.2 compare the effect of the different desorption mechanisms in a static cloud at a density of 10^5 cm^{-3} for selected observable molecules. In general, desorption has the most significant effect on gas-phase abundances after approximately 10^6 yr, which is when the molecules begin to freeze-out. Each of the desorption mechanisms are effective enough to be able to compete with freeze-out at late times, preventing full depletion of species onto grains. The exceptions are the sulphur bearing species, H_2S and CS, whose freeze-out is only prevented by the non-selective cosmic ray photodesorption. This mechanism is also able to enhance abundances of molecules such as NH_3 and H_2S at times as early as 10^5 yr. For the case of NH_3 this is because the NH_3 in the mantle builds up relatively quickly (compared to molecules like CO), so direct desorption by this mechanism can proceed close to its maximum rate. However, since the H_2 formation and direct cosmic ray heating mechanisms are not able to desorb NH_3 directly, desorption via these mechanisms can only affect NH_3 once enough NO has been desorbed to enhance the gas-phase production (via the reaction $NO + NH_3^+ \rightarrow NH_3 + NO^+$).

For most of the species shown in Figures 3.1 and 3.2, desorption via H_2 formation with $\varepsilon = 0.1$ is the most effective mechanism, being able to produce equilibrium abundances up to an order of magnitude greater than the other mechanisms. However, there are several molecules (NH_3, H_2S and CS), for which cosmic ray induced photodesorption is more effective, even though desorption via this mechanism proceeds at a rate more than ten times slower than H_2 formation with $\varepsilon = 0.1$. This is because we have assumed desorption via H_2 formation is selective, only being able to desorb molecules with adsorption energies less than 1210 K (CO, NO, N_2, O_2, C_2 and CH_4). Evidently, the higher gas-phase abundances of these molecules caused by selective desorption do not have a significant effect on the gas-phase chemistry of molecules like H_2S and CS, so their freeze-out is not prevented by selective mechanisms.

In the following subsections we look at the effectiveness of each mechanism under different conditions, by varying the density and the initial atomic hydrogen density. We also discuss further the effects of selectivity in Section 3.4.3.

3.4.1 Varying the density

When the model was run at a density of $n_{\rm H} = 10^6$ cm^{-3}, it was found that the equilibrium abundances of the desorbed species were reduced approximately by a factor of 10 compared to the equivalent runs at 10^5 cm^{-3}. Given that n(H) and $M_{\rm s}$ appear to show little variation in their

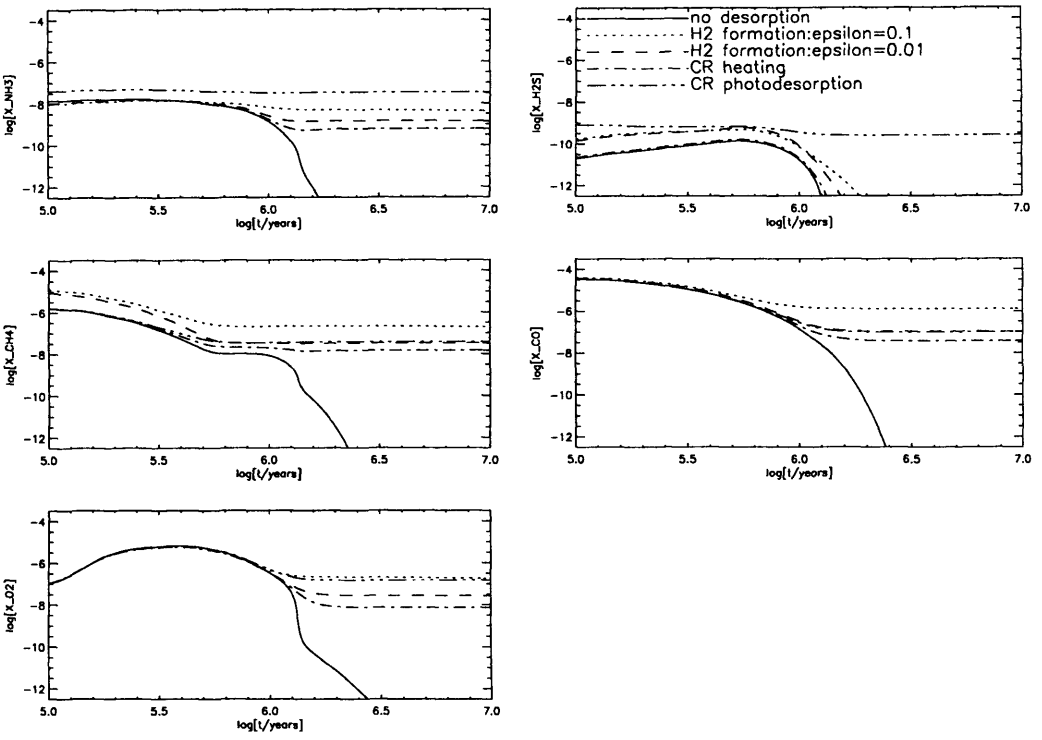

Figure 3.1: The time evolution of the molecules NH_3, H_2S, CH_4, CO and O_2 in a static cloud of density $n_H = 10^5$ cm^{-3}, $T = 10$ K, at a point with $A_v = 10$ mag. The abundances of species relative to hydrogen are shown as a function of time in years. The different curves compare the evolution of the species with no desorption, desorption via H_2 formation with $\varepsilon = 0.1$ and 0.01, desorption via direct cosmic ray heating and cosmic ray photodesorption (see key).

equilibrium values at different densities, the rates for each desorption mechanism should not depend on density. However, the rate for freeze-out has a direct linear dependence on density, so it is expected that the equilibrium abundances of desorbed species should scale roughly as n_H^{-1}, which would explain the reduction in equilibrium abundances found in the results.

3.4.2 Varying the initial atomic hydrogen density

Since desorption via H_2 formation depends on the abundance of atomic hydrogen, it would be expected that varying the initial ratio of atomic to molecular hydrogen could also influence how efficient this mechanism is. However, even when the model was run with all hydrogen in the form of H_2 initially, after 10^5 yr the abundance of atomic hydrogen had reached the same value ($n(H) \sim 0.4$ cm^{-3}) as in the previous runs (which had only half the hydrogen nuclei in H_2 initially), so there was no noticeable difference in the desorption via H_2 formation rate.

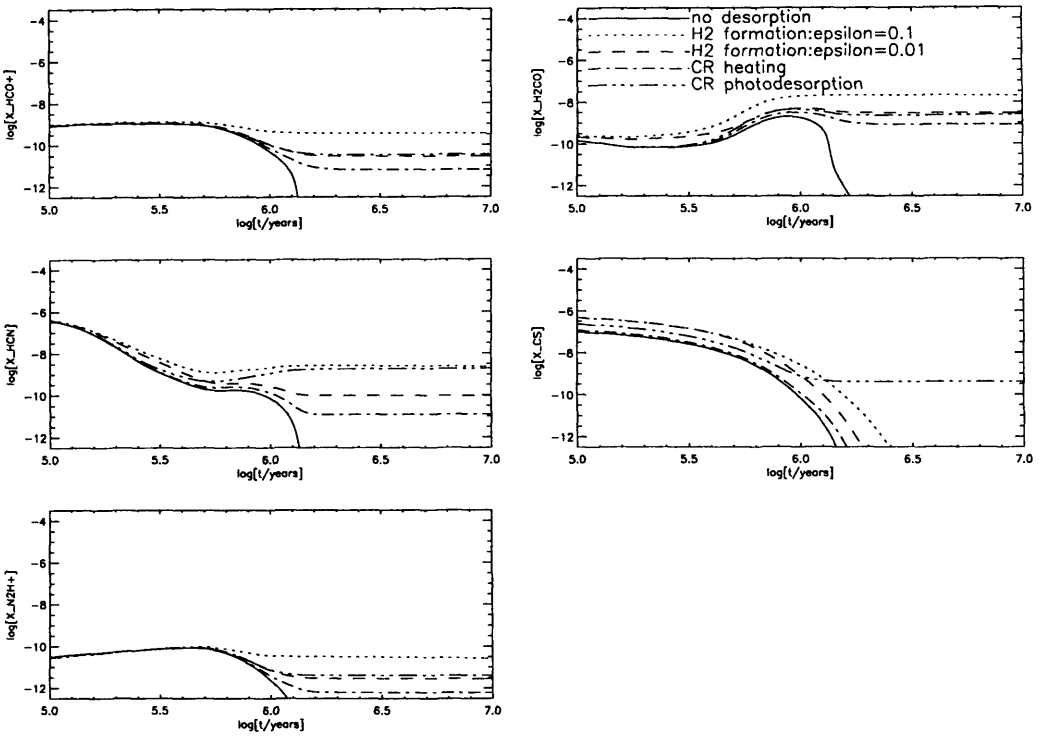

Figure 3.2: As in Figure 3.1 but for the molecules HCO^+, H_2CO, HCN, CS and N_2H^+.

3.4.3 Varying the threshold adsorption energy for selective mechanisms

So far we have assumed that the selective desorption mechanisms (H_2 formation and direct cosmic ray heating) are only capable of desorbing molecules with adsorption energies less than or equal to the value $E_t = 1210$ K. This number was chosen to be consistent with the study by WRW94, who assumed that only CO, N_2, C_2, O_2 and NO could be desorbed by these processes. CH_4 also has an adsorption energy of less than 1210 K, so we have also included CH_4 as a 'volatile' species. Although Leger *et al.* (1985) calculated that mantles composed *purely* of refractory ices such as CO_2, H_2CO, HCN, NH_3 and H_2O are unlikely to be affected by these mechanisms, they predicted that if these molecules are mixed with volatile species then spot heating processes may be able to raise the temperature of the grains enough to desorb these refractory molecules. Since the H_2 formation and direct cosmic ray heating mechanisms are both capable of spot-heating, we thought it was necessary to investigate the effect of varying E_t.

Figures 3.3 and 3.4 show the effect of varying E_t for the H_2 formation mechanism with $\varepsilon = 0.01$. The adsorption energies for each mantle species were taken from Aikawa *et al.* (1997), apart from H_2O which was taken from Fraser *et al.* (2001). Some of the molecules, such as CO,

CH_4 and H_2CO are relatively unaffected, even when E_t is so high (10 000 K) that all molecules can be desorbed. In the case of H_2CO which has an adsorption energy of 1760 K (Aikawa *et al.* 1997) this may seem rather surprising. The behaviour can be explained by the fact that, for the model and parameters that we have considered, gas-phase formation of H_2CO (via CH_3+O) dominates over desorption. On the other hand, molecules such as NH_3 and HCN show differences in abundances of more than one order of magnitude when they reach equilibrium. These differences can be explained as follows:

NH_3: The equilibrium fractional abundance of NH_3 increases from 1.4×10^{-9} to 2.5×10^{-8} when E_t increases from 3000 K to 4000 K. This change is simply because the adsorption energy of NH_3 is 3080 K, so for $E_t \geq 4000$ K, NH_3 can be desorbed directly. For $E_t \leq 4000$ K, the main production of NH_3 is through the reaction $NH_3^+ + NO \rightarrow NO^+ + NH_3$.

HCN: The equilibrium fractional abundance of HCN increases from 9.5×10^{-11} to 2.0×10^{-9} when E_t increases from 3000 K to 4000 K. The adsorption energy of HCN is actually greater than 4000 K, so this is not a consequence of direct HCN desorption. In fact, it is the direct desorption of NH_3 that produces the HCN via the reaction $NH_3 + CN \rightarrow HCN + NH_2$ when E_t is greater than 4000 K. Below this energy, the main route of production of HCN is the reaction $H + H_2CN \rightarrow HCN + H_2$.

For CS and H_2S, freeze-out is only prevented if E_t is greater than 2000 K. This is because at this energy both CS and H_2S can be directly desorbed. For CS if E_t is increased further from 2000 K to 3000 K, the equilibrium abundance of CS increases again by approximately an order of magnitude. This is due to the direct desorption of H_2CS at 2250 K, which can increase the CS abundance through the reaction $C^+ + H_2CS \rightarrow CS + CH_2^+$.

3.5 Comparison with existing models and formulations

We first of all compare our results to those of WRW94, which is the closest previous study to our own, then we consider two other studies, Willacy & Millar (1998) and Hartquist & Williams (1990) (hereafter WM98 and HW90 respectively), whose conclusions differed to ours. We also discuss various assumptions that are made in most chemical models of molecular clouds in which desorption is included, with particular reference to the formulation of desorption by direct cosmic ray heating by HH93.

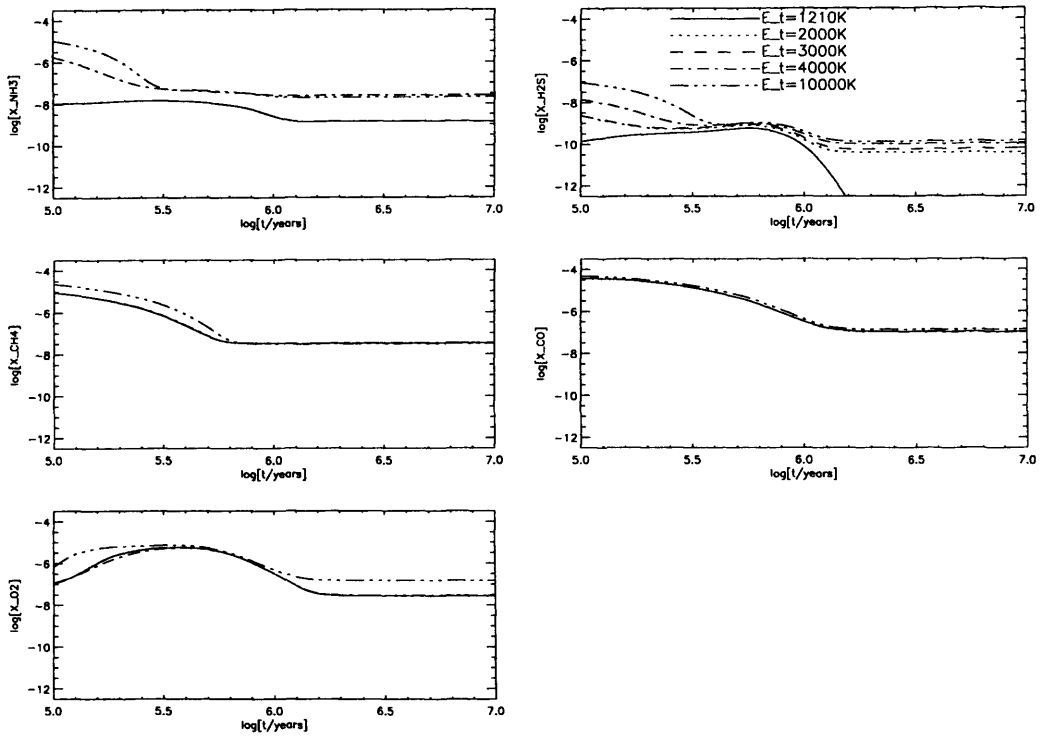

Figure 3.3: The effect of varying E_t for desorption via H_2 formation with $\varepsilon = 0.01$, in a static cloud of density $n_H = 10^5$ cm^{-3} at 10 K, for the molecules NH_3, H_2S, CH_4, CO and O_2

3.5.1 Comparison to WRW94

WRW94 investigated each of the desorption mechanisms discussed above, in the case of a collapsing cloud. They concluded that the only significant mechanism was desorption arising from H_2 formation on grains if it was assumed to be non-selective, using values for ε of 0.1 and 0.8. Since we have found that, for a static cloud, all desorption mechanisms are significant and can prevent complete freeze-out, it is therefore worth checking that our model agrees with that of WRW94 when it is run under similar conditions.

To simulate a collapse, as in WRW94, we have used a spherically symmetric, isothermal model, undergoing a free-fall collapse. The collapse is modified by a retardation factor B due to magnetic fields and other factors (Rawlings *et al.* 1992). The rate of change of density for the collapse is given by (4.7), and is discussed in more detail in Section 4.2. WRW94 used $B = 0.7$, a temperature of 10 K, an initial density, n_0, of 3×10^3 cm^{-3} and a final density of 10^6 cm^{-3}. The initial visual extinction of the cloud was 4.4 magnitudes. Figure 3.5 shows the results from our model when it was run with these parameters. We have plotted the abundances of the same molecules that appear

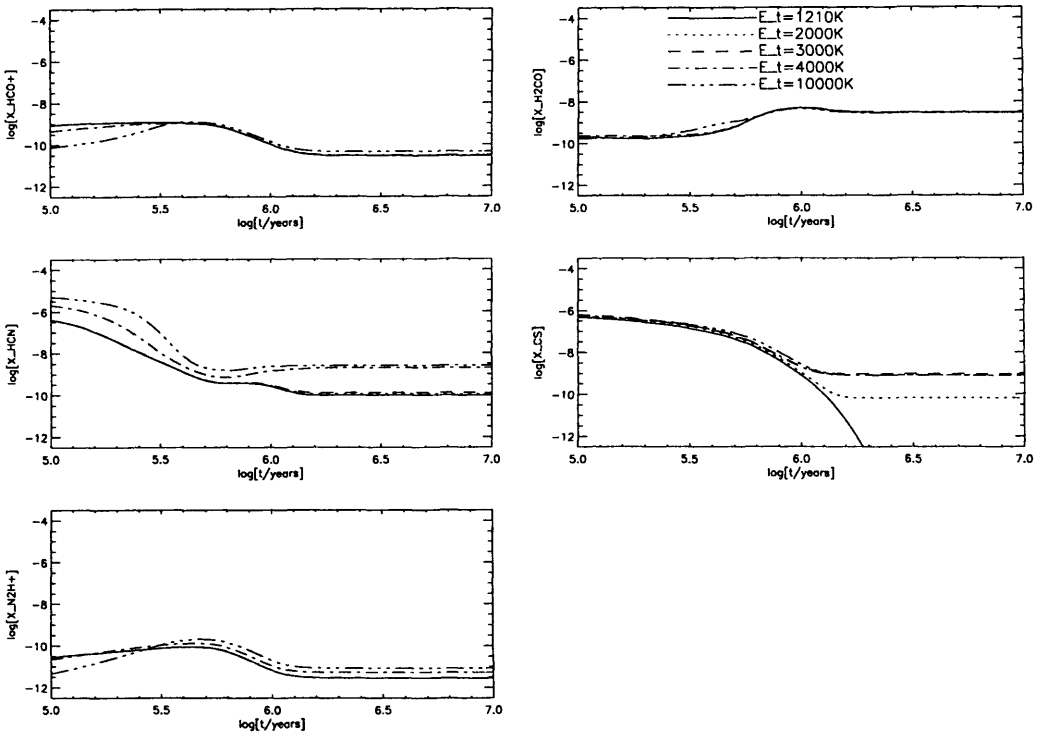

Figure 3.4: As in Figure 3.3 but for the molecules HCO^+, H_2CO, HCN, CS and N_2H^+.

in Figure 1 of WRW94, and have converted time to radius as they did to allow for easy comparison between our results and theirs. Even though the chemical reaction network in our model is much more complicated than in the WRW94 model, both models agree that desorption has the greatest effect on NH_3 and HCN. Also, under these conditions, we agree that the other mechanisms (direct cosmic ray heating and cosmic ray photodesorption) do not significantly affect the abundances of these molecules.

3.5.2 Comparison to WM98

WM98 carried out an investigation in which they tested the three desorption mechanisms used in our model, as well desorption by the explosive chemical reactions of radicals. Their model used similar physical conditions to ours, except that they adopted a lower density ($n_{\rm H} = 2 \times 10^4$ cm^{-3}). They found that models that include desorption by H_2 formation (with values of ε ranging from 0.1 to 1.0) gave the best agreement to the observed gas-phase abundances in TMC-1.

This actually agrees well with our model, since we also find that desorption by H_2 formation with $\varepsilon = 0.1$ is the most efficient mechanism. WM98 concluded, however, that desorption by direct

Figure 3.5: The variation of NH_3, CH, HCO^+ and HCN with radius for a cloud collapsing from $n_H = 3 \times 10^3$ cm^{-3} to 10^6 cm^{-3} at 10 K including non-selective desorption resulting from H_2 formation, as in Figure 1 of Willacy *et al.* (1994*a*).

cosmic ray heating and cosmic ray photodesorption were too inefficient because they generally under-predicted the gas-phase abundances. Thus, for example, CO, was found to be underabundant by approximately two orders of magnitude at an age of 5 Myr using the cosmic ray induced mechanisms. We agree that, when comparing the desorption mechanisms using our standard values of ε, ϕ and Y, desorption by H_2 formation can indeed maintain gas-phase abundances up to two orders of magnitude higher than the other mechanisms. But, since these parameters are so uncertain, we believe it is too early to confidently rule out cosmic ray heating and cosmic ray photodesorption as important desorption mechanisms.

3.5.3 Comparison to HW90

In their study, Hartquist & Williams (1990) carried out a purely theoretical analysis of cosmic ray induced desorption. They argued that direct cosmic ray heating would not be able to maintain significant gas-phase CO abundances because the desorbed CO would be destroyed by reactions with He^+ (leading to the formation of hydrocarbons). Their analytical calculation of the gas-phase

CO abundance at high densities gives the result

$$n_g(\mathrm{CO}) \propto e^{-\beta t}, \tag{3.5}$$

where β depends on the rates of the reactions

$$\mathrm{He}^+ + \mathrm{CO} \rightarrow \mathrm{C}^+ + \mathrm{O} + \mathrm{He} \tag{3.6}$$

$$\mathrm{CO(g)} \rightarrow \mathrm{CO(s)} \tag{3.7}$$

$$\mathrm{CO(s)} \rightarrow \mathrm{CO(g)} \tag{3.8}$$

$$\mathrm{He} + \mathrm{CR} \rightarrow \mathrm{He}^+ + \mathrm{e} + \mathrm{CR} \tag{3.9}$$

$$\mathrm{He}^+ + \mathrm{H}_2 \rightarrow \mathrm{H}^+ + \mathrm{H} + \mathrm{He}. \tag{3.10}$$

Reactions (3.6) to (3.8) are the main formation and destruction routes for CO, with reactions (3.7) and (3.8) referring to the freeze-out and desorption of CO. Reactions (3.9) and (3.10) are assumed to be the main formation and destruction routes of He^+ at high densities.

Hartquist & Williams (1990) calculated β to be

$$\beta^{-1} \approx 3 \times 10^6 \mathrm{yr}(n_\mathrm{H}/10^6 \mathrm{cm}^{-3}). \tag{3.11}$$

However, when we redo the calculation with the (updated) rate coefficients for these reactions used in our model, we obtain values of β^{-1} that are a factor almost six orders of magnitude larger. This implies that significant gas-phase CO abundances can be maintained over the lifetime of a typical cloud. The difference arises because we have used a much smaller desorption rate for CO [given by equation (3.3)]. So, in fact, using a *smaller* desorption rate allows for a more controlled release of CO into the gas-phase and thus enables the CO to remain in the gas-phase for a longer period of time.

Hartquist & Williams (1990) also concluded that cosmic ray induced photodesorption would only be effective in regions where the number density is 10^3 cm^{-3} or lower. They calculated the ratio at which heavy molecules desorb by cosmic ray induced photodesorption to the rate at which they freeze-out to be

$$R \approx \left(\frac{X_Z}{10^{-7}}\right)^{-1}\left(\frac{n_\mathrm{H}}{10^5 \mathrm{cm}^{-3}}\right)^{-1}\left(\frac{\zeta}{10^{-17}\mathrm{s}^{-1}}\right), \tag{3.12}$$

where X_Z is the fractional abundance of heavy molecules in the gas-phase and ζ is the cosmic ray ionisation rate. This expression implies that cosmic ray photodesorption will be more efficient at low densities. The rates we have used are consistent with this ratio, but our results clearly indicate

that the cosmic ray induced photodesorption mechanism can still maintain significant gas-phase abundances of heavy molecules at densities as high as 10^5 cm^{-3}, even though the efficiency of the process is not at its peak at this density.

3.5.4 Discussion of other formulations and assumptions

As mentioned earlier, other previous models that have included desorption in dark clouds tend to only include desorption by direct cosmic ray heating. One of the most commonly used formulations is that of HH93, who assumed that classical (~ 0.1 μm) grains are impulsively heated by relativistic nuclei with energies 20-70 MeV, depositing an average of 0.4 MeV per impact, raising the local (hot spot) temperature of the grain to 70 K. The subsequent (thermal) desorption rate is then calculated from the binding energies of the various molecular species and the cooling profile of the dust grain. In practice, the details of the cooling are simplified to a 'duty cycle' approach, so the desorption rate is proportional to the fraction of time spent by the grains in the vicinity of 70 K, $f(70\ \mathrm{K}) \sim 3.16 \times 10^{-19}$. The rate coefficient is then given by:

$$k_{\mathrm{cr-HH93}}(i) = f(70\ \mathrm{K})\nu_0(i)\exp[-E_{\mathrm{a}}(i)/70\ \mathrm{K}] \quad \mathrm{s}^{-1} \tag{3.13}$$

where $\nu_0(i)$ and $E_{\mathrm{a}}(i)$ are the characteristic adsorbate vibrational frequency and adsorption energy for species i respectively.

Flower *et al.* (2005) formulated a similar (but simpler) rate for cosmic ray desorption (in cm^{-3}s^{-1}) given by:

$$R_{\mathrm{crd-FPW05}} = M_s(i)\langle\pi a_{\mathrm{g}}^2 n_{\mathrm{g}}\rangle\gamma\exp\left[\frac{-(E_{\mathrm{a}}(i) - E_{\mathrm{a}}(\mathrm{CO}))}{70\ \mathrm{K}}\right] \tag{3.14}$$

where $\gamma = 70$ cm^{-2} s^{-1} gives the desorption rate of CO per unit area of dust grains as derived by Leger *et al.* (1985). This factor takes into account the cosmic ray flux, F_{cr}, and the efficiency parameter, ϕ, which were explicitly included in our rate. The above rate includes the same exponential factor as in HH93, but does not take into account variations in ν_0 for each species.

We decided not to use the above formulations because, bearing in mind the exponential sensitivity of the desorption rate to the ratio of the hot spot temperature to the binding energy, the resulting rates are extremely uncertain and strongly dependent on a number of very poorly constrained free parameters including the grain size and morphology, the molecular binding energies, the rate and energy/mass spectrum of the cosmic rays.

We can examine a few of these assumptions in a little more detail:

1. The formulations given above assume that interstellar dust grains can be thought of as homogeneous, symmetrical (spherical, spheroidal, or cylindrical) entities. In reality, we know that the grains may have very complex morphologies ('fluffy aggregates') with non-uniform thermal properties and composition. We can speculate that these grains therefore consist of poorly thermally connected sub-units, so that both the spot-heating and the whole grain heating rates may be quite different to what is derived for spherical, uniform dust grains.

2. Most of these studies also only consider the gas-grain interactions with large (~ 0.1 μm), classical grains. The justification given for this is that the equilibrium temperature of the (cosmic ray heated) smaller grains is too high to allow gas-phase species to freeze-out. However, this differentiation is not apparent in Leger *et al.* (1985) and there is no direct observational evidence of the universal presence of a population of warm dust grains. The smaller grains present a much larger surface area per unit volume of gas than the classical grains, so this is an important issue.

3. Concerning the desorption process itself, the assumption is usually made that the mantle ice is pure, so that the adopted binding/desorption energies correspond to the pure substance. Real ices are likely to have complex compositions and temperature-dependent morphologies. Laboratory work (Collings *et al.* 2003, 2004) shows that the desorption characteristics are drastically modified in such circumstances in a way that is very species-dependent. Thus, for example, in a mixed CO/H_2O ice, CO is desorbed in four distinct temperature bands (with $T \sim 25 - 100$ K).

4. Bringa & Johnson (2004) performed detailed molecular dynamics calculations of the thermal evaporation process driven by a cylindrical heat pulse, concentrating on a classical grain of ~ 0.1 μm, heated by a heavy cosmic ray ion. Even with the assumption of a single desorption energy/threshold for each species they still obtained very different results to HH93 – most notably the derived H_2O and CO desorption rates were found to be an order of magnitude higher and lower, respectively, as compared to HH93. However, even here, the calculations make very general assumptions about the cosmic ray energy spectrum and adopt a spherically symmetric grain with uniform thermal properties.

5. The issue of the surface chemistry is often not considered in many of the chemical models which use these desorption formulations. This would only be valid if one makes the seemingly unreasonable assumption that the surface residence timescale of adsorbed species is less than

the surface migration timescale for reactive species such as hydrogen atoms.

Because of these various uncertainties we must conclude that although approximate quantifications of the rate of desorption driven by cosmic ray grain heating are useful, the numerical details are very poorly constrained and anything more complicated or specific than our simple approach is very hard to justify.

The most important conclusion of this section, therefore, is that due to the considerable uncertainties in the microphysics of ice desorption which are, as yet, very poorly constrained by laboratory and/or theoretical studies, it is very difficult to make *qualitative* distinctions between different desorption mechanisms: Each of the desorption models discussed above has its own merits, but that there is insufficient information to discriminate or validate these models. However, we also make the point that, through empirically deduced values of the depletions, we *can* make well-constrained *quantitative* estimates of the desorption efficiencies. In the next section, we compare our models to observational results. Thus, by consideration of the deduced desorption efficiencies we are able to comment on the allowed values of the free parameter in each of the desorption models (ε, ϕ or Y) that are consistent with the observations.

3.6 Comparison with observations

As a consequence of our poor understanding of the theory of ice desorption, it is proposed that, rather than using desorption efficiencies as an input to the chemical models we invert the process and use whatever observations we can safely interpret to constrain, empirically, the nature and efficiencies of the desorption processes. We can then use that information to predict the chemical behaviours of other species and generate physical diagnostic indicators of the molecular clouds.

Observations of CO isotopomers in several prestellar cores provide strong evidence for the depletion of CO onto grains. For example, Redman *et al.* (2002) were able to estimate that at least 90 % of CO is depleted within 5000 AU of the centre of the prestellar core L1689B, by comparing their observations of the $C^{17}O$ $J = 2 \rightarrow 1$ line with models which included CO depletion in the centre of the core. Since L1689B is a typical prestellar core with a density of $n_{\rm H} = 1.2 - 1.4 \times 10^5$ cm^{-3} (Bacmann *et al.* 2000), it is an ideal candidate with which we can compare our results.

CO depletion has also been estimated in several other prestellar cores, such as L1544, L1709A, L310, L328, L429 and Oph D (Bacmann *et al.* 2002). In these cases, the CO depletion is estimated by comparing the observed ratio, X, of the $C^{17}O$ and H_2 column densities, to the 'canonical' abundance determined by Frerking *et al.* (1982) towards dark cores, $X_{\rm can} = 4.8 \times 10^{-8}$. The CO

depletion factor, f, is defined by $X_{\rm can}/X$, and was found to vary from 4.5 (in L1689B, which appears to be slightly less than the depletion estimated by Redman *et al.* 2002) to 15.5 in L429. Since $X_{\rm can}$ is the value of X obtained in undepleted conditions, and assuming that there is no selective depletion of different isotopomers of CO (so the fraction of $C^{17}O$ depleted onto grains is the same as the fraction of total CO depleted), then the fraction of CO depleted onto grains is given by $1 - 1/f$. This implies that CO depletion ranges from 78% to 94% in these cores. The densities of these cores are all of order $n(H_2) = 10^5$ cm^{-3} so it is also worth comparing these depletion fractions to our model.

Although our results have indicated that including desorption inhibits full freeze-out allowing abundances to reach an equilibrium, the percentage of CO frozen-out onto grains is actually greater than 98% ($f = 50$) for all of the mechanisms investigated, which is consistent with the observations above.

If we assume that L1689B is in a state of equilibrium, the values of ε, ϕ and Y needed to give the 90% freeze-out estimated in L1689B are approximately 0.5, 1.3×10^7 and 5.5 respectively. We calculated these values by assuming that freeze-out and desorption of CO are the main processes governing the CO abundance, so by equating these rates with 90% of CO on the grains and 10% remaining in the gas-phase we can predict the efficiencies needed. We then ran the model with these values of ε, ϕ and Y to confirm that the observed CO depletion is obtained. Since it is possible that L1689B is not in equilibrium and further freeze-out could be achieved, this gives us an upper limit for these parameters.

If we use the values estimated by Bacmann *et al.* (2002), for L1689B (in which they deduce that CO is depleted by 78%) we obtain even higher limits for ε, ϕ and Y of 1.4, 3.3×10^7 and 14.0 respectively. For L429, in which a CO depletion of 94% was deduced, the values for ε, ϕ and Y are reduced to 0.31, 7.5×10^6 and 3.2 respectively. The values for all the other cores studied by Bacmann *et al.* (2002) would lie in between the values for L1689B and L429.

These values are much higher than the estimates used in our model, indicating that if these desorption mechanisms operate then they are very efficient. However, using these observations it is not possible to determine which of the mechanisms is operating, or if it is a combination of all three.

3.7 Conclusions

There are two major conclusions from this study: Firstly, we have shown that the usual assumption that cosmic ray desorption is the the most effective desorption mechanism in dark molecular clouds is not always valid. All three desorption mechanisms that we have considered (desorption via H_2 formation on grain surfaces, direct cosmic ray heating and cosmic ray photodesorption) have been shown to have significant effects on the gas-phase abundances in quiescent dark molecular clouds and so should not be neglected in chemical models. These processes all operate on timescales of the order of $\sim 10^6$ yr. Each of the processes is capable of preventing total freeze-out, but in an equilibrium quiescent dark cloud of density 10^5 cm^{-3}, the predicted percentage of freeze-out is always greater than 98%. This figure is in good agreement with the observations (e.g. L1689B).

Addressing the specifics of the desorption processes, desorption via H_2 formation, if it is efficient ($\varepsilon = 0.1$), is the most effective mechanism. However the complete freeze-out of some species, such as CS and H_2S, can only be prevented by the cosmic ray photodesorption mechanism, which is non-selective. The relative importance of the three mechanisms appear to be insensitive to variations in the density and the initial atomic to molecular hydrogen ratio. For the selective desorption mechanisms, choosing the threshold adsorption energy, E_t, (such that molecules with adsorption energies less than E_t will be desorbed), can have a strong effect on the chemistry, particularly on molecules such as NH_3, HCN, CS and H_2S.

Secondly, our understandings of the chemical and physical structure of dust grains and the physical processes which drive desorption are, as yet, very incomplete and a purely theoretical approach to the problem is inadvisable. In this study we have investigated three particular desorption mechanisms (desorption via H_2 formation, direct cosmic ray heating and cosmic ray photodesorption) and have used the observed molecular depletions to constrain the poorly-determined free parameters in desorption processes. This is the first attempt at an empirical determination of the desorption efficiencies. Bearing in mind the huge uncertainties in these efficiencies, this empirical approach is the one that we recommend for use in future studies of interstellar chemistry where gas-grain interactions play an important role.

CHAPTER 4

INITIAL CONDITIONS OF STAR FORMATION

4.1 Introduction

The question we want to address is:

'Is star formation from the prestellar core stage a slow, quasi-static process, or is it dynamic, so that once a prestellar core has formed it immediately contracts and the gas is always dynamically evolving?'

The first scenario is the traditional picture of star formation where magnetic fields play an important role, as presented by Shu *et al.* (1987), and the second applies to the more recent rapid star formation models (see Elmegreen 2007 for a review). The evidence for and against these models is presented in Chapter 1, and in this and the following two chapters we see if chemical models can shed any more light on the answer to this question.

In this chapter we focus on the initial conditions of the chemical model. To clarify, the 'initial' stage refers to the point at which the prestellar core begins dynamically collapsing into a protostar. In the slow star formation (SSF) model, the prestellar core is subcritical and can only begin to collapse dynamically once the magnetic field has been sufficiently reduced (by ambipolar diffusion), and so the core remains approximately static for a period of time which depends on the strength of the magnetic field. In the rapid star formation (RSF) model, the core is initially supercritical or very close to the critical state, and so can begin collapsing instantaneously. The initial chemical conditions reflect the length of time the prestellar core has remained in quasi-static equilibrium. Here we investigate how the initial conditions reflect the chemical evolution of a core as it collapses, in order to understand the sensitivity of chemical models to their initial conditions and to find chemical diagnostics for the SSF and RSF models.

The initial conditions that we vary are:

1. The initial atomic to molecular hydrogen (H/H_2) ratio.

2. The initial degree of depletion.

Below we discuss these initial conditions in more detail.

4.1.1 The initial H/H_2 ratio

In chemical models of collapsing prestellar cores, it is routinely assumed that initially all (or nearly all) hydrogen will be in the form of H_2, but there is no direct evidence to show that this is the case; the molecular hydrogen content of prestellar/starless cores is difficult to measure directly because it lacks a permanent dipole moment and needs temperatures greater than that of dark cores in order to be detected. Indirect evidence comes from observations of molecules such as H_3^+, which forms from the cosmic ray ionisation of H_2 (Rawlings *et al.* 2002).

The atomic hydrogen content of dark clouds and prestellar cores can be measured using the HI narrow self-absorption technique (HINSA) (Li & Goldsmith 2003), where cold molecular hydrogen in dark cores in the foreground produce an absorption feature in the 21 cm HI emission from the Galactic background. Li & Goldsmith (2003) looked for HINSA in 31 dark clouds in the Taurus/Perseus region, and found that 77% of the clouds showed HINSA with an average [HI]/[H_2] ratio of 1.5×10^{-3}, which is slightly higher than the value expected with steady state equilibrium between H_2 formation on grains and cosmic ray destruction of H_2. In the dark core L134, van der Werf *et al.* (1988) used HI self-absorption to find that the H atom density in the coldest parts was an order of magnitude higher than the theoretical H/H_2 equilibrium value with a cosmic ray ionisation rate of 10^{-17} s^{-1}.

As mentioned earlier, the initial H/H_2 ratio is a measure of how long the core has been in its present dense state before it starts collapsing into a protostar, with the ratio likely to be higher for a core which has just formed from the diffuse interstellar medium than for a core which has remained static for a long period of time. Falle & Hartquist (2002) proposed a mechanism whereby cores are transient features, produced by density fluctuations associated with the excitation of slow-mode magnetohydrodynamical (MHD) waves due to the non-linear steepening of fast-mode waves. The dense cores will either disperse or collapse depending on whether they are gravitationally bound. Garrod *et al.* (2006*b*) used this idea to model a molecular cloud as an ensemble of transient dense cores, which form from a diffuse medium at a density of $n_{\rm H} = 10^3$ cm^{-3} to a peak density of 5×10^4 cm^{-3} and then disperse again over a total time of ~ 2 Myr, and found the maps generated

from these models were very well matched to observations of dark clouds such as L673. The timescale of H_2 formation in our models is $\sim 2.5 \times 10^9/n_H$ yr, but since the core will spend a large portion of time at low densities, it is possible that the H/H_2 ratio will be far from equilibrium when the core reaches its peak density. If such a core were to then go on to collapse further and form a protostar, the initial H/H_2 density could be much higher than for the slow star formation model, where the core remains approximately static at a high density for a substantial length of time.

Rawlings *et al.* (2002) investigated the effects of initially H-rich chemistry in a static dense core, of density 10^4 cm^{-3} and gas temperature 10 K, and found that starting with a high atomic hydrogen abundance led to enhanced early time abundances of OH, NH_3 and HNC, whereas molecules such as HCN and HCS favoured the H-poor (and so H_2-rich) conditions. We extend this work by modelling a collapsing core, specifically to attempt to find evidence for the H/H_2 ratio *at the time the core begins collapsing*, and in Chapter 5 we also generate line profiles for this model in both H-rich and H-poor conditions.

4.1.2 The initial degree of depletion

Depletion has been observed in a large number of prestellar cores (Bacmann *et al.* 2002; see Chapter 3 for more discussion), a number of which also show evidence for infall by the signature blue asymmetric line profiles (see Chapter 6, in particular Section 6.4.2.1 for a more discussion on how the blue asymmetric line profiles are produced). L1544, for example, was found to have a high level of depletion compared to other prestellar cores (Caselli *et al.* 1999; Bacmann *et al.* 2002), and is also believed to have extended inward motions signifying the collapse of the core (Tafalla *et al.* 1998). Lee *et al.* (2004) performed a survey to detect infall in 94 prestellar cores, and found strong evidence for both infall and depletion in 18 cores.

In some depleted prestellar cores, however, the line profiles are more ambiguous, and in some cases appear to show that the core is actually stable. Redman *et al.* (2006) interpreted the blue and red asymmetric line profiles of HCO^+ across the core B68 as evidence that the core is undergoing oscillations about a stable configuration. Both red and blue asymmetric line profiles were also detected across L1689B, and this has been shown to be consistent with a model of a rotating core without any infall (Redman *et al.* 2004).

If cores such as B68 and L1689B do ever undergo infall, it would be expected that they would suffer a significant degree of depletion before the collapse has started. Collapse in supposedly stable cores could occur if magnetic support, assuming it is significant in the first place, is lost through ambipolar diffusion. It is therefore essential to investigate the effect on the chemical

abundances inside a collapsing core starting with different levels of depletion, with the aim of providing diagnostic tests for the initial level of depletion and therefore the age of the core before its collapse.

4.2 The model

The model follows the chemical evolution of a single parcel of gas as it collapses towards the centre of the core. The chemical network is taken from the UMIST RATE06 database (Woodall *et al.* 2007), but is limited to the elements H, C, N, O, S, He and a representative metal, Na. The species list is the same as used in Chapter 3, given in Table 3.1 (apart from here we use Na instead of Mg as the representative metal), but since we use RATE06 instead of RATE99, the number of gas-phase reactions has increased to 1816. We have used the same initial elemental abundances as in the model of Federman *et al.* (1996), where the abundances are based on the observational estimates of Savage *et al.* (1992). Sodium is used as the representative low ionisation potential metal, so its abundance is the total estimated abundance of all the low ionisation potential metals.

The chemical network of gas-phase reactions includes two-body reactions, cosmic ray ionisation, at a rate of 1.30×10^{-17} s^{-1}, cosmic ray induced photoreactions, and interstellar photoreactions which take into account the extinction of the interstellar radiation field. H_2 is assumed to be fully self-shielded, completely suppressing its photodissociation.

H_2 formation on dust grains is included, the rate of which is given by the rate that hydrogen atoms stick to the grain surface (see Section 2.2.1):

$$R_{H_2} = 2.35 \times 10^{-17} S(\mathrm{H}) T^{1/2} n_{\mathrm{H}}, \tag{4.1}$$

where T is the gas temperature, n_{H} is the total number density of hydrogen nuclei, and S is the sticking probability of atomic hydrogen, given by $(T/102.0 + 1)^{-2}$ (Buch & Zhang 1991).

For the sample of 10 prestellar cores observed at 1.3 mm by Bacmann *et al.* (2000), the central densities ranged from $9 \times 10^4 - 6 \times 10^5$ cm^{-3}. Three of these cores (L1544, L1689B and L1709A[1]) had visual extinctions estimated in Myers *et al.* (1983), which ranged from $\sim 7 - 14$ mag. Since we are modelling a core collapsing from the beginning of the prestellar core phase, and it is likely that

[1]The visual extinctions of these cores are calculated from Table 6 of Myers *et al.* (1983) using $A_v = N(\mathrm{H_2})(\mathrm{cm}^{-2})/0.94 \times 10^{21}$ (Bohlin *et al.* 1978), except for L1709A which was not included in this table. For L1709A we have estimated the A_v from the value of N_{18}, the $C^{18}O$ column density, given in Table 3 of Myers *et al.* (1983), using the relation $A_v = 1.9 + 5.9 \times 10^{-15} N_{18}(\mathrm{cm}^{-2})$ which is given in the same paper

the cores in Bacmann *et al.* (2000) have undergone a degree of evolution, we have used a slightly lower initial density of 2×10^4 cm^{-3}, and an initial visual extinction, A_{v0}, of 4 magnitudes.

The one-dimensional radiation-hydrodynamics model of a collapsing prestellar core by Aikawa *et al.* (2008) predicted that the core temperature does not start to rise until the central density reaches $\gtrsim 10^6$ cm^{-3}, and that the increase is substantial for $n_{\rm H} \gtrsim 10^{11}$ cm^{-3}, so we therefore assume the collapse is isothermal until $n_{\rm H} \sim 10^7$ cm^{-3}, at which point we stop the collapse. The temperature is 10 K, which is a typical temperature for prestellar cores (Tafalla *et al.* 2004).

Once the collapse of the core begins, the rate of change of density is given by the modified free-fall collapse equation. This equation is derived from the energy conservation equation for a mass, m, on the surface of a self-gravitating sphere of radius r and mass M:

$$E_0 = \frac{1}{2}mv^2 - \frac{GMm}{r} = -\frac{GMm}{r_0}, \tag{4.2}$$

where E_0 is the total energy of the mass, m, and r_0 is the initial radius. This equation assumes that m is initially at rest, and neglects thermal and magnetic energy, which is appropriate for strongly supercritical cores. Rearranging for v gives:

$$v = \pm\left\{2\frac{GM}{r_0}\left(\frac{r}{r_0} - 1\right)\right\}^{1/2}. \tag{4.3}$$

Since we are considering infall we take the negative solution to this equation. Using mass conservation and assuming that the sphere is initially at a uniform mass density ρ_0 gives:

$$\frac{4}{3}\pi r^3\rho = M = \frac{4}{3}\pi r_0^3\rho_0, \tag{4.4}$$

so $r/r_0 = (\rho/\rho_0)^{1/3}$.

Differentiating equation (4.4) gives:

$$3\rho v + r\frac{d\rho}{dt} = 0. \tag{4.5}$$

Rearranging equation (4.5) and substituting for v using equation 4.3, and r/r_0 using equation 4.4, gives:

$$\frac{d\rho}{dt} = \left(\frac{\rho^4}{\rho_0}\right)^{1/3}\left\{18\frac{GM}{r_0^3}\left[\left(\frac{\rho}{\rho_0}\right)^{1/3} - 1\right]\right\}^{1/2}. \tag{4.6}$$

Finally, using equation 4.4 to substitute for $M/r_0^3 = \frac{4}{3}\pi\rho_0$, and $\rho \sim m_{\rm H}n_{\rm H}$, gives the equation of free-fall collapse:

$$\frac{dn_{\rm H}}{dt} = B\left(\frac{n_{\rm H}^4}{n_{\rm H0}}\right)^{1/3}\left\{24\pi G m_{\rm H} n_{\rm H0}\left[\left(\frac{n_{\rm H}^4}{n_{\rm H0}}\right)^{1/3} - 1\right]\right\}^{1/2} \quad n_{\rm H} > n_{\rm H0}. \tag{4.7}$$

As in Rawlings *et al.* (1992), we have multiplied this equation by a factor B, set equal to 0.7, to parametrise the retardation of the collapse due to magnetic fields, so this equation is more correctly referred to as the equation of *modified* free-fall collapse.

As the density of the core increases, the A_v also increases. We have approximated this increase using the relation:

$$A_v = A_{v0}(n_{\rm H}/n_{\rm H0})^{2/3}, \tag{4.8}$$

which is similar to that used by Ruffle *et al.* (1999) (with the contribution to the A_v from the interclump medium, A_v(ext), equal to zero). Strictly, this is only true for a point in the centre of a uniform density core. It is derived by assuming that the A_v is proportional to $rn_{\rm H}$, which is the column density of the core measured from the centre to the outer radius, r. According to equation (4.4), r is proportional to $n_{\rm H}^{1/3}$, and therefore $A_v \propto n_{\rm H}^{2/3}$.

The density is held constant once it reaches 10^7 cm^{-3}, because as mentioned above, this is approximately the density at which the core temperature starts to rise, which would increase the thermal pressure and cause the collapse to slow down. This happens 5.01×10^5 yr after the collapse has begun.

The freeze-out of gas phase species onto dust grains is included once the A_v rises above a certain value, $A_{v,\rm crit}$ (see Section 2.2.2). We have used $A_{v,\rm crit} = 5.0$ for the models in which we vary the initial H/H$_2$ ratio, and $A_{v,\rm crit} = 3.9$ for the models in which we vary the initial level of depletion, so freeze-out occurs at densities of $n_{\rm H} \gtrsim 2 - 2.8 \times 10^4$ cm^{-3}. The reasons we have used different values are discussed below, when we describe the two sets of models. Both the values of $A_{v,\rm crit}$ we have used are consistent with observed values of $A_{v,\rm crit}$ derived from observations of water ice (see Section 2.2.2).

Desorption is initiated once the total fractional abundance of species on the grain mantles is greater than 10^{-9}. This value was chosen simply to make the calculations run smoothly, as the chemical model has problems calculating the desorption rates when the mantle abundances are too low.

We use the desorption rate for cosmic ray heating of grains given in Chapter 3 in this thesis (which is based on the paper Roberts *et al.* 2007) with the number of molecules being desorbed per cosmic ray impact set to 10^5 (this parameter is called ϕ in Roberts *et al.* 2007). We note that other desorption mechanisms, such as desorption by H$_2$ formation on grains and desorption by the cosmic ray induced UV field may also operate in dark cores, but Roberts *et al.* (2007) have shown that these processes can have the same effect by simply varying the value of the efficiency

parameters, hence it is not necessary to include them all in this model.

As for the model used in Chapter 3, the only surface reactions that occur are hydrogenation of unsaturated species, and dissociative recombination of molecular ions. The list of surface reactions is given in Table 2.1. These reactions are assumed to occur instantly and the products remain on the grain surface until they are desorbed, apart from H_2 which is assumed to desorb immediately.

In this investigation we run two sets of models:

1. In the first set of models we vary the atomic to molecular hydrogen ratio at the beginning of the collapse. The initial abundances of atomic hydrogen are summarised in Table 4.2. In these models, $A_{v,\mathrm{crit}}$ is set to 5.0, so freeze-out only begins once the collapse is under way. We have chosen this value of $A_{v,\mathrm{crit}}$ so that freeze-out occurs once the density is $\gtrsim 3 \times 10^4$ cm^{-3}, because this is the density above which freeze-out has been observed to be dominant (Bergin & Tafalla 2007). All other elements are initially in neutral atomic form. By doing this we hope to isolate the effect of starting with initially H-rich cores, which is an indicator of the age of the core prior to collapse. The timescale of H_2 formation with this chemical model is $\sim 2.5 \times 10^9/n_{\mathrm{H}}$ yr, and the timescale of CO formation ranges from approximately 5.0×10^6 yr at $n_{\mathrm{H}} = 10^3$ cm^{-3} to 7.9×10^4 yr at $n_{\mathrm{H}} = 10^6$ cm^{-3}, so is longer than the H_2 formation timescale at a given density. This is because, as described in Section 2.2, there needs to H_2 present in order for other molecules to form. It is therefore reasonable to start with all other molecules in atomic form with varying degrees of H_2 formed.

2. In the second set of models, we investigate the effect of varying the initial amount of depletion of gas-phase species in the core, which is also a possible indicator of core age. To do this, we run the model in two stages:

   (i) All elements are initially in neutral atomic form, apart from hydrogen which starts in 90% molecular form (which is a standard assumption). The density is held constant at 2×10^4 cm^{-3}, and $A_{v,\mathrm{crit}}$ is set to 3.9, just below A_{v0}, so that freeze-out (and therefore desorption) can proceed at this density. This is slightly lower than the value used in the models varying the initial H/H_2 ratio but it is still consistent with the values of $A_{v,\mathrm{crit}}$ observed for water ice. The model is run for varying amounts of time so that different levels of gas-phase depletion can be achieved.

   (ii) In this stage, the initial molecular abundances are taken from output of stage (i) . The collapse proceeds as described above. The lengths of stage (i) range from $10^3 - 10^7$ yr

and are summarised in Table 4.3. For the shorter lengths of stage (i) ($< 10^5$ yr), freeze-out is not effective but the chemical abundances are still changing as they try to reach their gas phase equilibrium.

The estimated lengths of the prestellar stage deduced from observations vary tremendously. Ward-Thompson *et al.* (1994) estimated the length of the prestellar core stage to be 10^6 yr using the ratio of starless cores to cores with embedded point sources detected in the *IRAS* all-sky survey, consistent with the SSF theory. Hartmann *et al.* (2001), however, estimated that the entire lifetime of a molecular cloud is only $\sim 10^6$ yr, from the small age spread of the stellar population in molecular cloud complexes (see Section 1.3). This would mean that the formation of prestellar cores, the duration of the prestellar core phase, and the subsequent evolution to a protostar and then main sequence star, would *all* have to occur within this time, so the lifetime of a prestellar core would have to be $\ll 10^6$ yr. The models described above cover the possible range of lengths of the prestellar core phase, and so may help to distinguish between the SSF and RSF models.

Table 4.1: Elemental abundances

H	1.00
C	2.00×10^{-4}
N	7.94×10^{-5}
O	3.02×10^{-4}
S	8.00×10^{-6}
He	7.63×10^{-2}
Na	5.20×10^{-6}

4.3 Results

4.3.1 Varying the initial atomic to molecular hydrogen ratio

Figure 4.1 shows the evolution of the fractional abundances of HNC, OH, HCN, H_2CO, CH and NH_3 for varying initial fractional atomic hydrogen abundances (and therefore varying initial H/H_2 ratios). The results plotted are for models 1 to 9, with model 1 being the most H-poor model, and model 9 being the most H-rich. The arrow drawn on the plots for each molecule shows the direction

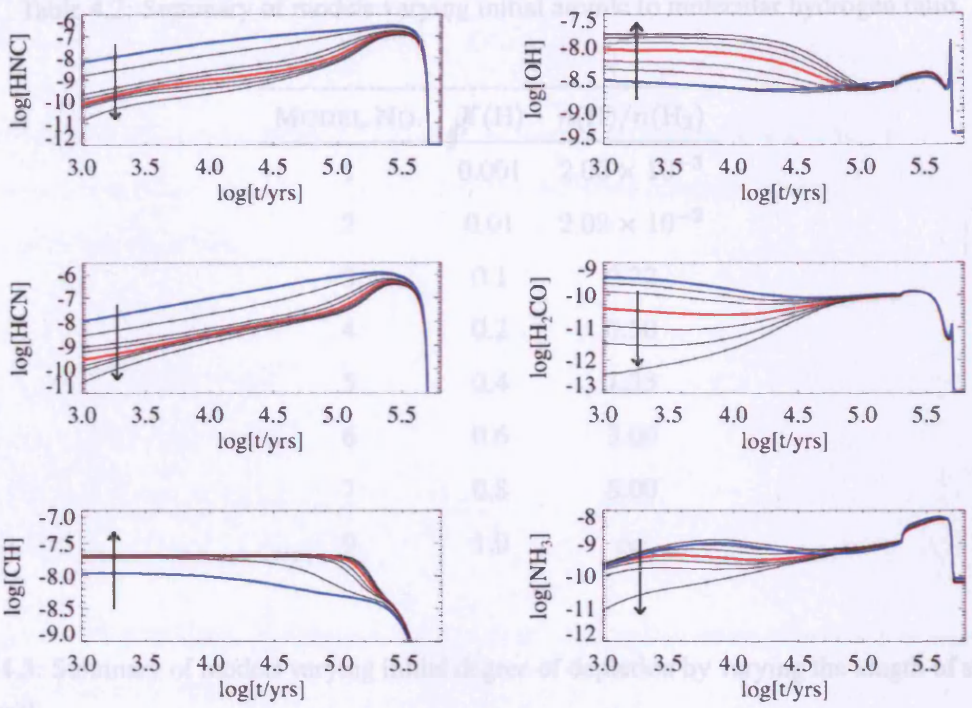

Figure 4.1: The evolution of the fractional abundances of HNC, OH, HCN, H_2CO, CH and NH_3 for varying initial fractional atomic hydrogen abundances (models 1 to 9). The direction of the arrow for each molecule indicates the direction of increasing initial atomic hydrogen abundance (and so increasing model number). The blue line shows the results from model 1 ($X(\mathrm{H}) = 0.001$) and the red line shows the results from model 5 ($X(\mathrm{H}) = 0.4$) (see Section 4.4.1).

HNC and HCN: These are mainly formed by the reaction of N with CH_2, where CH_2 is formed directly from H_2:

$$\mathrm{H_2 + C \rightarrow CH_2} + h\nu \tag{4.9}$$

$$\mathrm{N + CH_2 \rightarrow HNC + H} \tag{4.10}$$

$$\rightarrow \mathrm{HCN + H.} \tag{4.11}$$

Therefore, in the H-rich environment where the H_2 abundance is low, the CH_2 abundance falls, slowing down the production of HNC and HCN. In the absence of CH_2, HNC and HCN can be formed by the reaction between C and NH_2, which is not so affected by the H/H_2 ratio[2].

[2] This is because NH_2 is mainly produced by the dissociative recombination of NH_4^+ and NH_3^+, and although the NH_4^+ abundance decreases in H-rich conditions (see discussion on NH_3 below), the electron abundance is higher in the

Table 4.2: Summary of models varying initial atomic to molecular hydrogen ratio.

MODEL NO.	X(H)	n(H)/n(H_2)
1	0.001	2.00×10^{-3}
2	0.01	2.02×10^{-2}
3	0.1	0.22
4	0.2	0.50
5	0.4	1.33
6	0.6	3.00
7	0.8	8.00
9	1.0	∞

Table 4.3: Summary of models varying initial degree of depletion by varying the length of stage (i) (see text).

MODEL NO.	Stage (i) length (yr)
10	10^3
11	10^4
12	10^5
13	10^6
14	10^7

of increasing X(H). These plots show that HNC, HCN, H_2CO and NH_3 are more abundant in H-poor (H_2-rich) environments, but the opposite trend is shown for OH and CH.

These particular species are plotted because out of the species typically observed in dense cores, these are the ones which show the most sensitivity to the initial H/H_2 ratio. These species show very large variation in abundances at early times in the collapse ($< 10^5$ yr), with HCN, HNC and H_2CO having a difference of approximately three orders of magnitude. By $\sim 4 \times 10^5$ yr (log[t/yr] = 5.6) the models converge and the species become severely depleted due to freeze-out. Desorption is ineffective at maintaining significant gas-phase abundances at the final density ($n_H = 10^7$ cm^{-3}).

The molecules HNC, HCN, H_2CO and NH_3 are more abundant at early times for the H-poor (H_2-rich) models, for the reasons explained below:

H_2CO: The main production route for H_2CO is by the reaction:

$$CH_3 + O \rightarrow H_2CO + H. \tag{4.12}$$

In H-poor (H_2-rich) conditions, CH_3 can be formed by dissociative recombination of CH_5^+, which is itself produced by a series of fast H-abstraction reactions initiated by the cosmic ray ionisation of carbon:

$$C + CR \rightarrow C^+ + e^- \tag{4.13}$$

$$C^+ + H_2 \rightarrow CH^+ + H \tag{4.14}$$

$$CH^+ + H_2 \rightarrow CH_2^+ + H \tag{4.15}$$

$$\vdots \quad \vdots$$

$$CH_5^+ + e^- \rightarrow CH_3 + 2H. \tag{4.16}$$

In H-rich conditions, however, CH_3 is now formed by the much slower set of associative recombination reactions,

$$H + C \rightarrow CH + h\nu \tag{4.17}$$

$$H_2 + CH \rightarrow CH_3 + h\nu. \tag{4.18}$$

If there is sufficient H_2, reactions (4.13) to (4.16) are much faster than reactions (4.17) and (4.18) so CH_3 can be rapidly formed, in turn leading to a much higher H_2CO abundance.

NH_3: The production of NH_3 is initiated by the reaction:

$$He^+ + N_2 \rightarrow N^+ + N + He. \tag{4.19}$$

In H-poor (H_2-rich) conditions, N^+ can undergo a series of H-abstraction reactions (similar to reactions (4.14) and (4.15) but with a nitrogen instead of a carbon atom), eventually resulting in the production of an NH_4^+ ion:

$$NH_3^+ + H_2 \rightarrow NH_4^+ + H. \tag{4.20}$$

The NH_4^+ ion then dissociatively recombines with an electron to make NH_3:

$$NH_4^+ + e^- \rightarrow NH_3 + H. \tag{4.21}$$

As with the production of CH_3, NH_3 production is therefore reduced considerably when there is a lack of H_2.

H-rich conditions which means the rate of production of NH_2 by recombination of NH_3^+ can compensate for the loss in production by recombination of NH_4^+.

OH and CH, on the other hand, appear to favour H-rich conditions. Their increased abundances can be explained because when the H atom abundance is high enough, the reactions

$$H + O \rightarrow OH + h\nu \tag{4.22}$$

and

$$H + C \rightarrow CH + h\nu, \tag{4.23}$$

can compete with the faster H-abstraction and dissociative recombination route (similar to the CH_3 production route but with recombination happening at an earlier stage), significantly contributing the abundances of CH and OH.

In general, it appears that the hydrogen-rich species which are formed by dissociative recombination, such as CH_3 and NH_3, tend to favour a more H_2-rich environment, whereas unsaturated molecules such as OH and CH, which are formed by direct reactions with H atoms, favour atomic conditions.

It should be noted that our results disagree slightly with the findings of Rawlings *et al.* (2002), who found that NH_3 and HNC were more abundant in H-rich models. However, our results appear to be consistent with rates given in the RATE06 database so we are satisfied that the model is working correctly. For example, the reason HNC was more abundant in the H-rich models of Rawlings *et al.* (2002) was that in their model, HNC formed primarily by the reaction C + NH_2 $\rightarrow$ HNC + H, rather than the reaction N + CH_2, which is how HCN is formed. In RATE06, however, the reactions:

$$N + CH_2 \rightarrow HCN + H \tag{4.24}$$

$$\rightarrow HNC + H \tag{4.25}$$

have the same rate constant (= 1.13×10^{-10} cm^3 s^{-1} at 10 K), and the reactions,

$$C + NH_2 \rightarrow HCN + H \tag{4.26}$$

$$\rightarrow HNC + H \tag{4.27}$$

also have the same rate as each other, but this value (= 2.22×10^{-11} cm^3 s^{-1} at 10 K) is slightly less than for reactions (4.24) and (4.25). Therefore, in our model both HNC and HCN form by reactions (4.24) and (4.25), and are both more abundant in H-poor conditions.

Another interesting feature of these results is the behaviour of OH, H_2CO and NH_3 at late times; both OH and H_2CO show a 'spike' at $\log[t/\mathrm{yr}] \sim 5.7$, and NH_3 has a 'bump' around $\log[t/\mathrm{yr}] = 5.3 - 5.7$.

The spike in OH and H_2CO is due to the freeze-out of oxygen: OH and H_2CO are both destroyed by the reactions O + OH $\rightarrow$ O_2 + H and O + H_2CO $\rightarrow$ CO + OH + H, so when oxygen freezes out, OH and H_2CO can experience a brief enhancement until they themselves freeze-out. If the freeze-out of atomic oxygen is removed (by setting its rate to zero), the OH and H_2CO spikes disappear.

The bump in NH_3 is caused by desorption. In this model, desorption is 'switched on' once the total fractional abundance of mantle species is greater than 1.0×10^{-9}, so the NH_3 in the grain mantles is suddenly released at this time. The bump is particularly prominent in NH_3 because this species is saturated in hydrogen; since we have assumed when unsaturated species freeze-out they are hydrogenated on grain surfaces (see Section 2.2.2), saturated molecules are formed efficiently on grain surfaces an experience a large increase in abundance when they are desorbed. If this value is changed, the position of the bump changes. If desorption is removed entirely, the bump smooths and becomes a continuous line.

4.3.2 Varying the initial level of gas-phase depletion

Figure 4.2 shows the abundances of several observable species for stage (i) of the model, where the core is static with $n_H = 2 \times 10^4$ cm^{-3}. It is plotted on a logarithmic timescale so that the abundances at 10^3, 10^4, 10^5, 10^6 and 10^7 yr can clearly be seen, as these are the initial abundances taken for stage (ii) . It takes approximately 9×10^6 yr for most species to reach equilibrium.

The 'degree of depletion' can be given in terms of the depletion factor, $f = X_{can}/X$, as defined in Bacmann *et al.* (2002). Here X is the fractional abundance of CO in our model which includes freeze-out (and desorption), and X_{can} is the fractional abundance our model gives when freeze-out is not included. The values of f are summarised in Table 4.4. These are therefore initial values of f at the beginning of stage (ii) for each of the models.

It can be seen that even after 10^7 yr the core does not become fully depleted of heavy species. This is because at a density of 2×10^4 cm^{-3}, the freeze-out rates are much slower than the typical gas-phase chemistry rates of production for most species. For example, the main production route for CO at 10^7 yr is the reaction

$$HCO^+ + e^- \rightarrow CO + H, \tag{4.28}$$

which has a rate of $\sim 7 \times 10^{-15}$ cm^{-3} s^{-1}, whereas the freeze-out rate of CO at this time is still only 3×10^{-16} cm^{-3} s^{-1}. Even so, freeze-out still has a significant effect on chemical abundances; at 10^7 yr the fractional abundance of CO is only $\sim 5 \times 10^{-7}$, compared to $\sim 2 \times 10^{-4}$, the value it

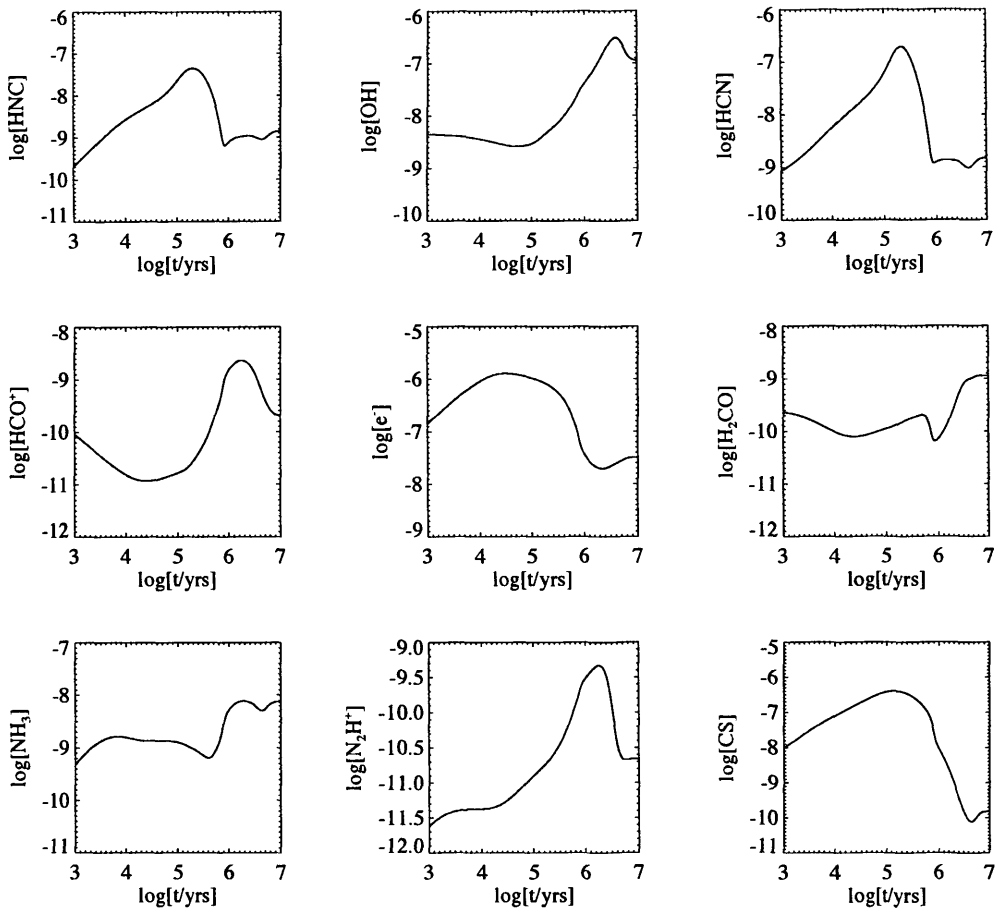

Figure 4.2: The evolution of several observable species in a static core of density 2.0×10^4 cm^{-3} (stage (i) of models 10-14).

Table 4.4: Depletion factors of CO ($f = X_{\rm can}/X$) at the end of stage (i) for the different models.

MODEL NO.	Length of stage (i) (yr)	f
10	10^3	1.00
11	10^4	1.00
12	10^5	1.12
13	10^6	3.80
14	10^7	418

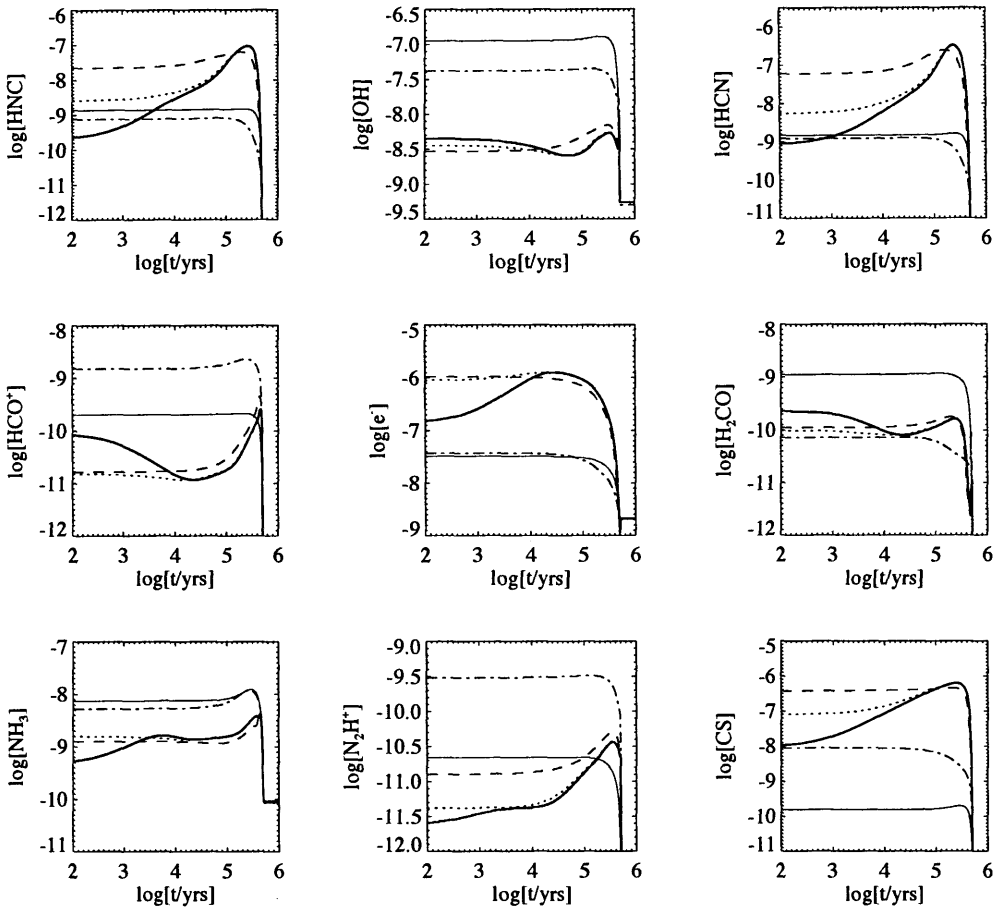

Figure 4.3: The evolution of the species which show the most difference in their qualitative behaviour due to different degrees of initial depletion in a collapsing core (stage (ii) of models 10-14). The thick solid line is model 10, the dotted line is model 11, the dashed line is model 12, the dot-dashed line is model 13, and the thin solid line is model 14. The time axis shows the time since collapse has begun.

would attain with pure gas-phase chemistry.

Desorption also prevents complete freeze-out from occurring, and this is responsible for the 'kinks' in molecules such as HNC, HCN, NH_3, N_2H^+ and CS at $\sim 5 \times 10^6$ yr ($\log t \sim 6.7$).

As demonstrated in Table 4.4, depletion begins to have an effect after 10^5 yr. Molecules such as OH, HCO^+, H_2CO and N_2H^+ experience a large increase in abundance because of depletion ('depletion enhancements'), peaking at $\sim 1.7 \times 10^6$ yr. This behaviour was also found by Rawlings *et al.* (1992), and is described below.

The increase in OH and H_2CO abundance is due to the freeze-out of atomic oxygen, since the major destruction pathway of these molecules is by reacting with atomic oxygen:

$$O + OH \rightarrow O_2 + H \tag{4.29}$$

$$O + H_2CO \rightarrow CO + OH + H. \tag{4.30}$$

The H_2CO abundance is also increased greatly by desorption. In this model, H_2CO is formed efficiently on grain surfaces because it is assumed that molecules such as HCO and HCO^+ will hydrogenate on the grain surface forming H_2CO. This surface production of H_2CO contributes significantly to the gas-phase H_2CO once it has been released from the grain mantle by desorption.

The increase in HCO^+ and N_2H^+ is partly explained by the depletion of H_2O, again because H_2O would usually destroy HCO^+ and N_2H^+ by the reactions

$$H_2O + HCO^+ \rightarrow CO + H_3O^+, \tag{4.31}$$

and

$$H_2O + N_2H^+ \rightarrow N_2 + H_3O^+. \tag{4.32}$$

N_2H^+ is also destroyed by CO, producing HCO^+ and H_2, so as CO freezes-out this would also allow an increase in N_2H^+. Furthermore, the electron abundance is lowest at the time when the HCO^+ and N_2H^+ peak, so at this point the destruction of these ions by recombination is also inhibited.

The depletion induced enhancement of molecules such as these then reflects on other molecules such as HNC and HCN, which begin to deplete but have a resurgence at the same time as the peak of OH, HCO^+ and N_2H^+. For HNC and HCN this can be explained by the increase in OH

abundance, which produces HNC and HCN in the following chain of reactions:

$$O + OH \rightarrow O_2 + H \tag{4.33}$$

$$CN + O_2 \rightarrow OCN + O \tag{4.34}$$

$$He^+ + OCN \rightarrow CN^+ + O + He \tag{4.35}$$

$$H_2 + CN^+ \rightarrow HCN^+ + H \tag{4.36}$$

$$H_2 + HCN^+ \rightarrow HCNH^+ + H \tag{4.37}$$

$$HCNH^+ + e^- \rightarrow HCN + H \tag{4.38}$$

$$\rightarrow HNC + H. \tag{4.39}$$

Figure 4.3 shows stage (ii) of models 10 to 14. The molecules plotted here are the ones which show the most difference in their qualitative behaviour throughout the collapse for the different models. The figure clearly illustrates that the length of stage (i) and the initial degree of depletion have a very large affect on the subsequent chemical abundances, especially during the early stages of collapse; the CS abundance varies by three orders of magnitude, and HNC, HCN and HCO^+ vary by two orders of magnitude.

For model 10 (stage (i) length 10^3 yr; thick solid line), the initial abundances start very far from chemical equilibrium, so their plots look quite similar to those for stage (i) in Figure 4.2. The density of the core does not begin changing rapidly until about 7×10^4 yr, so up until this point the results for model 10 are almost identical to the static core.

For models 11 and 12 (stage (i) lengths 10^4 and 10^5 yr; dotted and dashed lines respectively), the initial abundances of HNC, HCN, electrons, NH_3, N_2H^+ and CS all increase with respect to model 10, and for OH, HCO^+ and H_2CO the initial abundances decrease. By 10^5 yr, models 10, 11 and 12 converge. At this point the collapse is progressing; the density of the core is 2.18×10^4 cm^{-3} and the maximum velocity is 0.016 km s^{-1} (see Chapter 5 for the derivation of the velocity).

Models 13 and 14 (stage (i) lengths 10^6 and 10^7 yr; dot-dashed line and thin solid line respectively), however, do not converge with the other models until 5×10^5 yr, when the collapse has finished and the core density is 10^7 cm^{-3}. This is because once freeze-out has begun, it is irreversible in our model (although we have included desorption, it is not strong enough to desorb *everything* from the grain mantles, so once freeze-out has been initiated the gas-phase abundances will always suffer some degree of depletion), so models 13 and 14 can never reach the early stage abundances of models 10 to 12, which are effectively gas-phase only up until 5×10^5 yr.

The 'depletion enhancements' of OH, HCO^+, H_2CO, NH_3 and N_2H^+, experienced in stage (i)

of the models, can be seen by the high initial abundances for models 13 and 14 in stage (ii). For OH, H_2CO and NH_3, the highest initial abundance is for model 14. The high abundances of these molecules at 10^7 yr in stage (i) is primarily due to desorption; the simple grain surface chemistry in our model is effective at producing saturated molecules such as NH_3 and H_2CO on the grain surface, so when they are released by desorption they are able to have higher abundances than they would in gas-phase only chemistry (until they themselves freeze-out).

For models 10 to 12, the depletion enhancements occur at 5×10^5 yr. At this point the density is so high (10^7 cm^{-3}), that the enhancement is compressed into such a short amount of time that it only appears as a spike on the plots for OH and H_2CO. Despite this, It may still be observable (if it occurs), as the duration of the spike is still $\sim 2.3 \times 10^4$ yr.

In general, for the depletion enhanced molecules, if stage (i) lasts for $\geq 10^6$ yr, the effect of the depletion enhancement cannot be seen during the collapse phase. This may have important consequences for the observed line profiles (see Discussion below and Chapter 5).

4.4 Discussion

4.4.1 The initial atomic to molecular hydrogen ratio

Molecules such as HCN, HNC and H_2CO are very sensitive to the initial H/H_2 ratio, showing differences in abundances of up to three orders of magnitude, with the largest differences being at the early stage of collapse.

In reality, however, it would be unlikely that a core would begin collapsing with hydrogen in entirely atomic form ($X(\mathrm{H}) = 1.0$, as in model 9). A more plausible value for an H-rich core would be $X(\mathrm{H}) = 1/3$; at this value the H_3^+ generated is not too dissimilar to an H_2-rich model (Rawlings *et al.* 2002). This value lies in between models 4 and 5 ($X(\mathrm{H}) = 0.2$ and 0.4 respectively), so the most useful comparison to make is therefore between model 1 (H-poor model, $X(\mathrm{H}) = 0.001$) and models 4 and 5. Models 1 and 5 are marked in blue and red respectively on Figure 4.1. It shows that even for a modest degree of atomic hydrogen as in model 5, the abundances can still differ by up to two orders of magnitude compared to model 1 (e.g. for HNC, HCN). For these molecules at 10^3 yr the predicted abundances range from $X(\mathrm{HNC}) = 6.5 \times 10^{-9}$ and $X(\mathrm{HCN}) = 1.1 \times 10^{-8}$ in model 1 (H-poor) to $X(\mathrm{HNC}) = 7.6 \times 10^{-11}$ and $X(\mathrm{HCN}) = 2.6 \times 10^{-10}$ in model 5 (H-rich), so we propose that HNC and HCN could be used as indicators of the initial atomic hydrogen abundance in a collapsing core.

As a more robust diagnostic test, ratios of the molecules abundant in H-poor chemistry (HNC,

HCN, H_2CO, NH_3) to those abundant in H-rich chemistry (OH, CH) could be used as an indicator of the amount of atomic hydrogen in the core. For example, the ratio HNC:OH at 10^3 yr for model 1 is 2.14, but for model 5 at the same time it is 8.71×10^{-3}, three orders of magnitude smaller. By 3.16×10^5 yr ($\log[t/\mathrm{yr}] = 5.5$), the ratios become 85.1 (model 1) and 35.5 (model 5), when the two models have almost converged.

The CO:CS ratio, on the other hand, is insensitive to the initial H abundance; at 10^3 yr it is equal to $\sim$ 65 and at 3.16×10^5 yr it is $\sim$ 120 for both model 1 and model 5. Therefore, we propose that the CO:CS ratio could be used to indicate the age of the core, and then a ratio such as HNC:OH could indicate the initial H abundance.

We now compare the abundances predicted by the models to abundances estimated from observations for the dark core TMC1-CP, which has a density of $\sim 10^4$ cm^{-3} (Wakelam *et al.* 2006*b*). We note, however, that these abundances are likely to be averaged over the entire core, and may not represent the collapsing region that is the focus of our work. Furthermore, the core TMC1-CP may not even be collapsing at all; we have chosen it because its chemical composition has been very well studied and the abundances of over 50 molecules have been estimated, so we are able to make a direct comparison with the abundances from our model. We have used the abundances for TMC1-CP summarised in Table 3 of Smith *et al.* (2004).

This core has estimated HNC and HCN abundances of $\sim 2 \times 10^{-8}$, which, if the core is static or in the early stages of collapse, would indicate that TMC1-CP has already converted most of its hydrogen into molecular form before the onset of collapse. Alternatively, it could be a late time core ($t \gtrsim 10^5$ yr since the onset of collapse), which is well underway in its collapse (but before significant depletion has occurred), although this would not give us any information on the initial H abundance because by this time the H-rich and H-poor models have converged.

If we look at the observed abundance ratios, the CO/CS ratio is $\sim 2 \times 10^4$, which is much higher than the value stated above from our models, but agrees best with the predicted ratio for the late time core ($t = 3.16 \times 10^5$ yr). The HNC/OH ratio is ~ 0.1, which is much higher than the 8.71×10^{-3} predicted for an H-rich core at early times, therefore we infer that the core is poor in atomic hydrogen, consistent with the findings above.

It is difficult to draw any firm conclusions from the above comparison without knowing the dynamics of the core. Rather than looking only at the abundances, it would be more useful to study the line profile shapes which could give extra information on the dynamics and therefore also indicate the age of collapse. We do this in the following chapter.

4.4.2 The initial degree of depletion

The results from these models are quite difficult to interpret. For example, a CS abundance of $\sim 10^{-7} - 10^{-6}$ could mean that the core is in the final stages of collapse ($t \gtrsim 10^5$ yr since the onset of collapse) for a core which had a static phase [stage (i)] of only 10^3 yr, or it could mean that the core has been static for $\sim 10^5$ yr and is only in the early stages of collapse. The same can be said for HNC and HCN. Looking at the shape of the predicted line profiles would help to resolve this issue, giving us more information on the velocity structure of the core and therefore how advanced the collapse is.

For cores which have been static for $t \gtrsim 10^6$ yr the abundances are generally more depleted for the duration of the collapse phase. The abundances of species such as NH_3, N_2H^+ and HCO^+, however, actually remain relatively high throughout the collapse for models which have been static for long periods of time, because these are the 'depletion enhanced' species (see Section 4.3.2). Observations of starless cores have indeed revealed that NH_3 and N_2H^+ abundances can remain high even when molecules such as CO and CS are heavily depleted (Tafalla *et al.* 2002).

As for the models investigating the initial H/H_2 ratio, no firm conclusions can be drawn without considering the kinematics of the core and line profile shapes. Below we discuss how the predicted abundances might affect the observed line profiles.

For a collapsing parcel of gas starting at $n_H = 2\times10^4$ cm^{-3}, if it has been static for $\geq 10^6$ yr, the abundances of molecules such as OH, HCO^+, NH_3 and N_2H^+, which would usually experience an enhancement during collapse by the depletion of other molecules, no longer have this enhancement and their abundances simply fall.

If we consider a whole core to be made up of concentric shells, all with an initial density greater than 2×10^4 cm^{-3} and with the density increasing towards the centre (as has been observed in several prestellar cores), if the core has been static for $\geq 10^6$ yr, then the molecules OH, HCO^+, NH_3 and N_2H^+ would deplete in every shell, and the abundance profile of these molecules would show a depleted centre with abundances increasing towards the edge at all times since the initiation of the collapse.

Rawlings *et al.* (1992) identified several depletion enhanced species (including HCO^+ and N_2H^+), and therefore predicted that these molecules would be able to show broad emission lines in an infalling core, and could be used to diagnose the dynamics of protostar formation. This conclusion applies to a core undergoing collapse by the inside-out model, where the core is assumed to be strongly centrally condensed and the fastest moving material is in the centre (see Section 6.1.2).

The depletion enhancements of HCO^+ and N_2H^+ occur in the central dense, fast moving material, giving rise to broad emission lines.

Our findings reveal that if a dense core is static for long enough ($\geq 10^6$ yr for a core of initial density 2×10^4 cm^{-3}), the depletion enhancement of these molecules will not be seen in any part of the core, and they will not show broad emission lines.

In Chapter 5 we calculate the expected line profiles for an initially depleted and undepleted core which is undergoing modified free-fall collapse, to further investigate how the line profile shapes and intensities are affected by the initial degree of depletion, and whether they can be used to provide more robust diagnostics than the abundances on their own.

CHAPTER 5

GENERATING LINE PROFILES

In this chapter we test if the results from Chapter 4 would be observable in a collapsing core by calculating the line profiles of the molecules CS, H_2CO and HCO^+, using a spherical radiative transfer model.

To generate the line profiles, the velocity, density, temperature and abundance distribution need to be known. In this chapter we have assumed the simplest model for collapse, where the core remains at a uniform density throughout the collapse [with each point in the core collapsing by equation (4.7)]. Although most authors use the inside-out collapse model (see Chapter 6) for an infalling core (e.g. Rawlings *et al.* 1992; Evans *et al.* 1994; Weidenschilling & Ruzmaikina 1994), there is no conclusive evidence that this should be the case. In some observed infalling prestellar cores it has even been shown that the inside-out collapse model is not appropriate, for example Tafalla *et al.* (1998) found that the core L1544 has extended inwards motions which would only happen in the inside-out collapse model if it was highly evolved, which was shown not to be the case.

In Section 5.1 we discuss how we derived the abundance and velocity profiles, and in Section 5.2 we discuss the radiative transfer model we used to generate the line profiles. In Section 5.3 we give the results and the discussion and conclusions are given in Section 5.4.

5.1 Deriving the radial abundance and velocity profiles

To generate line profiles of a particular molecule, we need to know its spatial variation in abundance. In Chapter 4, the model used was a simple single point model, so more information is needed to know the spatial distribution. We therefore assumed that the chemical model in the previous chapter

referred to the chemical abundances in a shell at the outer radius of a core, and ran two more models at smaller radii to understand how the molecules behave inside the core. Three shells were assumed to be sufficient because, as mentioned above, the density of the core is assumed to be uniform at all times so the chemical abundances at different radii are unlikely to exhibit large differences in behaviour. The abundances for each shell are plotted in Figure 5.2 show that this is indeed the case.

The only difference between each collapsing shell was the A_v. Each shell collapsed according to equation (4.7) from a density of 2×10^4 cm^{-3}, until they reached 1×10^7 cm^{-3} (at $t = 5.01\times10^5$ yr), where the density was held constant until $t = 2 \times 10^6$ yr.

The initial A_v of each shell was approximated using the formula:

$$A_{\rm v}(t=0,R) = A_{\rm v}({\rm ext}) + 1.0 \times 10^{-21} \frac{n_{\rm H}(t=0)}{\rm cm^{-3}} \frac{d(t=0)}{\rm cm}, \tag{5.1}$$

where $A_{\rm v}$(ext) is a measure of the contribution to the A_v from the region outside the core, $n_{\rm H}(t=0)$ is the initial density (=2.0×10^4 cm^{-3} for all shells), and d is the depth into the cloud. This formula comes from the observation that 1 magnitude in A_v is equivalent to an increase in column density of 1.0×10^{21} cm^{-2} (Bohlin *et al.* 1978). With regards to calculating the photorates, this formula does not take into account the fact that the core is a sphere and can therefore be illuminated from all directions, so the extinction calculated here is a slight over-estimate. However, in these conditions the photoreactions are largely suppressed and do not play such a large role in the chemistry, so the extinctions calculated by equation (5.1) are adequate for our model. Since the chemical model from Chapter 4, which had $A_{v0} = 4.0$, is assumed to be for the shell at the outer radius (which has $d = 0.0$), this sets A_v(ext) $= 4.0$, consistent with Rawlings & Yates (2001).

We assigned the outer radius of the shell to be 1.0×10^{17} cm, which is a typical radius of the flat density profile regions of observed prestellar cores (Ward-Thompson *et al.* 1994; Bacmann *et al.* 2001). The inner shells were given radii of 5.5×10^{16} cm and 1.0×10^{16} cm, corresponding to visual extinctions of 4.9 and 5.8 respectively, using equation (5.1).

We ran two more chemical models, following the chemical evolution of the inner shells as they collapsed according to equation (4.7), with the A_v of each shell increasing according to equation (4.8).

The radius for each shell, as a function of time, was calculated using the condition that the mass enclosed within a particular shell is constant, i.e.

$$n(t)R^3(t) = \text{constant}. \tag{5.2}$$

The velocity of each shell was derived by differentiating equation (5.2):

$$v = \frac{dR}{dt} = -\frac{R}{3n}\frac{dn}{dt}. \tag{5.3}$$

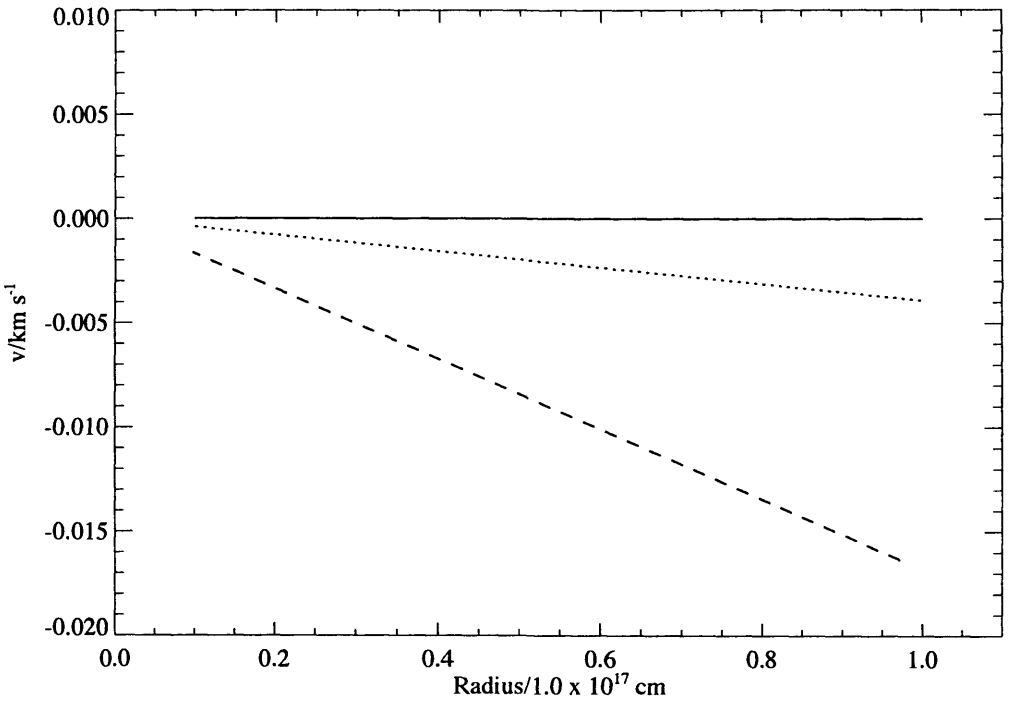

Figure 5.1: Infall velocity as a function of radius, at $t = 1.0 \times 10^3$ yr (solid line), $t = 1.0 \times 10^4$ yr (dotted line), $t = 1.0 \times 10^5$ yr (dashed line) and $t = 1.0 \times 10^6$ yr (dot-dashed line).

Figure 5.1 shows the radial dependence of the velocity. Since the core has a uniform density at all times, and dn/dt in equation (5.3) is a function of n only [see equation (4.7)], at any point in time the velocity is proportional to $-R$. This means that in this model the outer shells of the core have a higher velocity than the inner shells, which is the opposite to the standard inside-out collapse model (Shu 1977).

Figure 5.2 (bottom row) shows the radial dependence of the fractional abundances of CS and H_2CO, for the initially H-rich model (model 9) at different times. The solid line is for 10^3 yr, the dotted line is for 10^4 yr and the dashed line is for 10^5 yr. The diamond symbols represent the data from shell starting at $R = 1.0 \times 10^{17}$ cm, the triangles represent the data from the shell starting at $R = 5.5 \times 10^{16}$ cm, and the squares represent the data from the shell starting at $R = 1.0 \times 10^{16}$ cm. It shows that the abundance is approximately constant across the core, which is to be expected since the density is constant. The variation in A_v does not cause much change in the abundances across

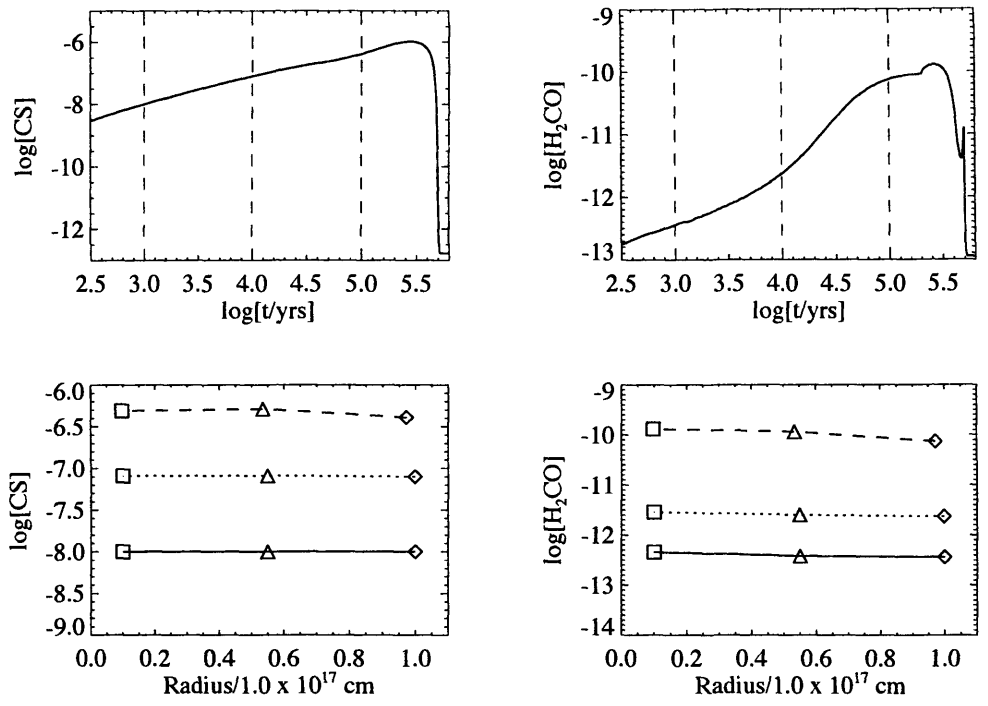

Figure 5.2: Top row: The time dependent evolution of CS and H_2CO for model 9, for the outer shell. The dashed lines show the times at which the data was taken for the radial profiles. Bottom row: The fractional abundances of CS and H_2CO as a function of radius, for the initially H-rich model (model 9). The solid line is for 10^3 yr, the dotted line is for 10^4 yr and the dashed line is for 10^5 yr. The diamond symbols represent the data from shell starting at $R = 1.0 \times 10^{17}$ cm, the triangles represent the data from the shell starting at $R = 5.5 \times 10^{16}$ cm, and the squares represent the data from the shell starting at $R = 1.0 \times 10^{16}$ cm.

the core, because even in the outer shell the A_v is high enough so that most of the photoreactions are already quenched. As the collapse progresses, the radius of each of the shells moves inwards. This cannot be seen very clearly on Figure 5.2 because by 10^5 yr the shells have only contracted to 97% their initial value.

The top row of Figure 5.2 shows the *time* dependent evolution of CS and H_2CO, also for model 9, for the outer shell. The dashed lines plotted show the times at which the data were taken for the radial profiles below. This is plotted just to show the points in the molecules' evolution at which we model the line profiles. A more full discussion of the time dependent evolution of the molecules is given in Chapter 4.

5.2 Radiative transfer model

The spherical radiative transfer code SMMOL ('Spherical Multi Mol') was used to generate the line profiles (Rawlings & Yates 2001). This is an approximate lambda-iteration code, which can be used for radiatively coupled clouds (as is likely to be the case here, see Section 5.3.1), where the standard large velocity gradient (LVG) models (which assume that clouds are radiatively *de*coupled) are not appropriate. SMMOL was benchmarked for accuracy by van Zadelhoff *et al.* (2002).

SMMOL requires input tables for each molecule giving the density, fractional abundance, gas temperature, dust temperature, infall velocity and turbulent velocity at different radii for a particular time. To generate the tables for each molecule, we took 100 evenly spaced values of the radius between the inner and outer shells (which began at $R_{\rm i} = 1.0 \times 10^{16}$ cm and $R_{\rm o} = 1.0 \times 10^{17}$ cm, but these radii decrease as the collapse progresses), and to get the abundances at each radii we interpolated between the data from the three test shells (shown in Figure 5.2). SMMOL assumes the material within the inner radius, $R_{\rm i}$, to be static and at a constant abundance equal to the abundance given at the inner radius. We tested that using 100 radial data points was sufficient by running the model with various grid sizes, and found that the resulting spectra were invariant for $\gtrsim 70$ radial grid points.

SMMOL works by assuming an input continuum radiation field and local thermodynamic equilibrium (LTE) populations, and then it can calculate the total radiation field and subsequent level populations. The new level populations then alter the total radiation field, so SMMOL then recalculates the total radiation field, checks for convergence and repeats the process until convergence is achieved. Following Rawlings & Yates (2001), we used a convergence criterion of $\Delta n_i/n_i \leq 10^{-4}$ (where n_i is the population of level i).

At each radial point in the core, SMMOL calculates the level populations and the line source functions. The emergent intensity distribution is convolved with the telescope beam, so the predicted line profiles are for a given source observed with a given telescope. The telescope beam is assumed to be Gaussian, and the beam is placed at the centre of the core. The characteristics of the telescope (half-power beam width and efficiency at particular frequencies) and distance to the source are free parameters in the code. The values we have chosen are summarised below.

The source was assumed to be at a distance of 140 pc, the distance of the Taurus Molecular Cloud. For the telescope beam we have used the characteristics of the IRAM 30m. These are listed in Table 5.1. At this distance the source has an angular diameter of $95.3''$ and the inner static core has a radius of $9.53''$. Figure 5.3 shows the part of the core which is sampled by a telescope with a

half-power beam width (HPBW) of w'', for outer and inner radii of R''_o and R''_i respectively. From Table 5.1 it can be seen that for frequencies above $\sim$ 226 GHz, the beam width is comparable to the size of the inner static core, but for lower frequencies the beam width is much larger so material in the centre of the core travelling transversely to the telescope is included in the resulting line profile. To determine the required frequency sampling, we tested the code using 100 and 150 frequency bins and found that the resultant spectra were invariant, indicating that using 100 bins is enough to ensure the line is sufficiently well sampled.

Because of the high densities in this model, we have assumed the gas and dust are thermally coupled and have equal temperatures (see Section 1.2.1.2). We have used a constant temperature of 10 K throughout the core, which has been observed in prestellar cores such as L1498 and L1517B (Tafalla *et al.* 2004). We also investigate other temperature profiles in Section 5.3.3. The infall velocity was calculated as explained in Section 5.1, and we used a constant turbulent velocity of 0.12 km s^{-1}, which was the value inferred from observations of the Class 0 infall candidate B335 (Zhou *et al.* 1993).

For the background radiation field we have used the standard interstellar radiation field (ISRF) of Mathis *et al.* (1983), supplemented by a black body at 2.7 K for the cosmic background radiation. The form of the ISRF at millimetre and submillimetre wavelengths is shown in Figure 5.4. The larger peak is due to the cosmic background continuum at 2.7 K, and the smaller peak is from the Galactic background dust emission at 30 K.

Table 5.1: Characteristics of the IRAM 30m telescope at the frequencies of the lines we generating, taken from the IRAM website (http://www.iram.fr/IRAMES/index.htm). HPBW is the half-power beam width, and η_a is the aperture efficiency.

Frequency (GHz)	HPBW (arcseconds)	η_a
89	27.5	0.61
98	25	0.60
141	17.5	0.55
147	16.5	0.55
226	11	0.42
245	10	0.39
268	9	0.36

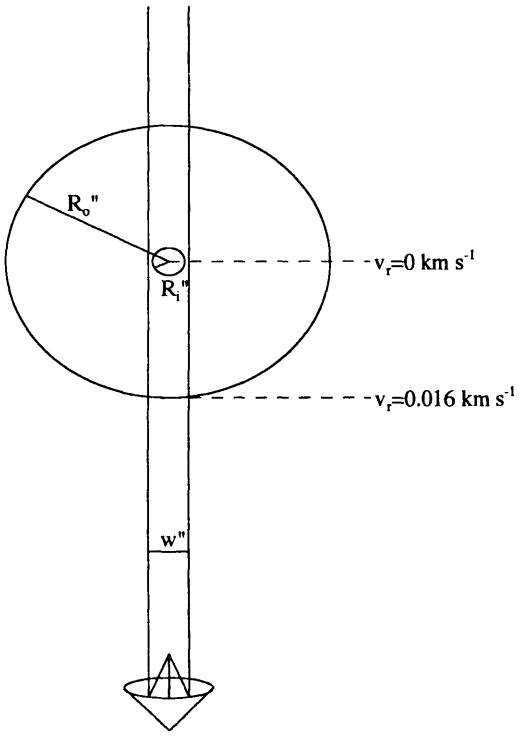

Figure 5.3: Diagram of model cloud in SMMOL. The velocities marked are for the core at $t = 1 \times 10^5$ yr.

The transitions we consider are CS $J = 5 \rightarrow 4$ at 244.94 GHz, CS $J = 3 \rightarrow 2$ at 146.97 GHz, CS $J = 2 \rightarrow 1$ at 97.98 GHz, ortho-H_2CO (hereafter o-H_2CO) $2_{12} \rightarrow 1_{11}$ at 140.84 GHz, o-H_2CO $3_{12} \rightarrow 2_{11}$ at 225.70 GHz, HCO^+ $J = 3 \rightarrow 2$ at 267.56 GHz, and HCO^+ $J = 1 \rightarrow 0$ at 89.19 GHz. These were chosen because these transitions are clearly detectable and are good tracers of the kinematics in protostellar infall sources (Zhou *et al.* 1993; Evans *et al.* 2005).

For each of the molecules above we had to chose to the maximum number of energy levels, $J_{\rm max}$, needed to accurately calculate the level populations. This was done by plotting the predicted level populations of each molecule using different values for $J_{\rm max}$, and finding the value of $J_{\rm max}$ for which the solutions converged. Figure 5.5 shows the level populations of CS in an initially H-rich core at $t = 10^5$ yr using $J_{\rm max} = 5, 6$ and 10. It shows that the level populations converge for $J_{\rm max} \geq 6$, so this is the value we chose to generate out final results. For HCO^+ and o-H_2CO the

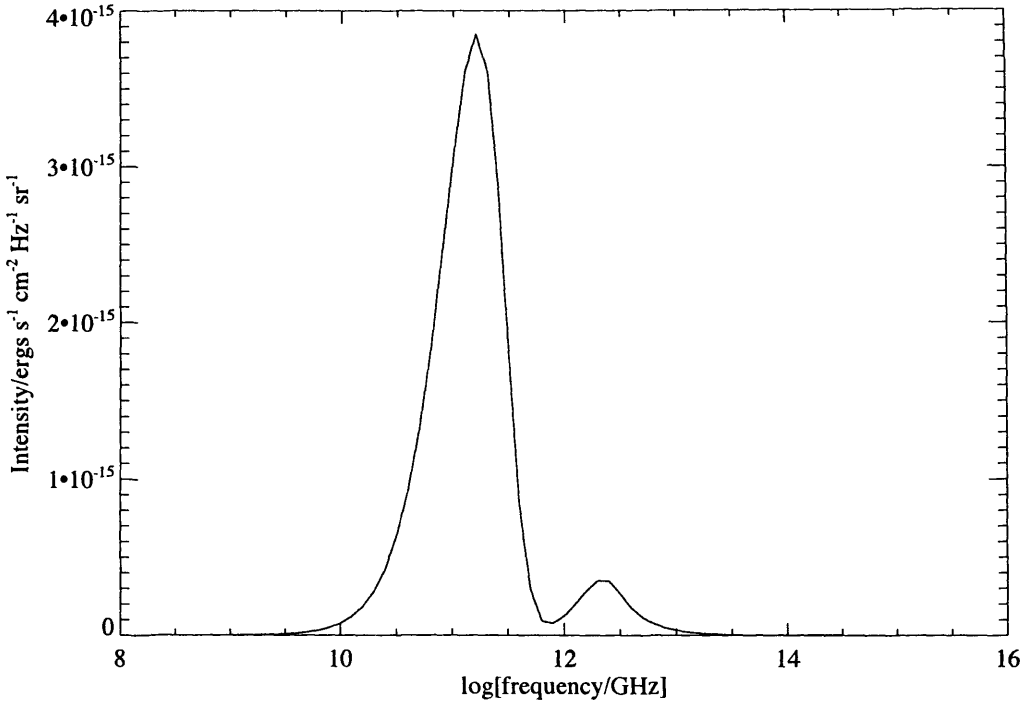

Figure 5.4: The background ISRF at millimetre and submillimetre wavelengths used in the radiative transfer model. We have used an ISRF similar to that of Mathis *et al.* (1983), supplemented by a black body at 2.7 K for the cosmic background radiation. The larger peak is due to the cosmic background continuum at 2.7 K, and the smaller peak is from the Galactic background dust emission at 30 K.

values of J_{max} required for convergence were 5 and 8 respectively.

We calculate the line profiles for both an H-poor and H-rich core (models 1 and 9 as described in Chapter 4), for CS $J = 5 \rightarrow 4$, $3 \rightarrow 2$ and $2 \rightarrow 1$, and o-H_2CO $2_{12} \rightarrow 1_{11}$ and $3_{12} \rightarrow 2_{11}$. H_2CO was chosen as an example of a molecule that is very sensitive to the initial H/H_2 ratio, and CS was chosen as a molecule that could possibly be more sensitive to the dynamics of the core. We also calculate the line profiles of the above molecules, as well as HCO^+ $J = 3 \rightarrow 2$ and $2 \rightarrow 1$ for a core that has been static for 10^3 yr (model 10) and 10^7 yr (model 14) before the onset of collapse.

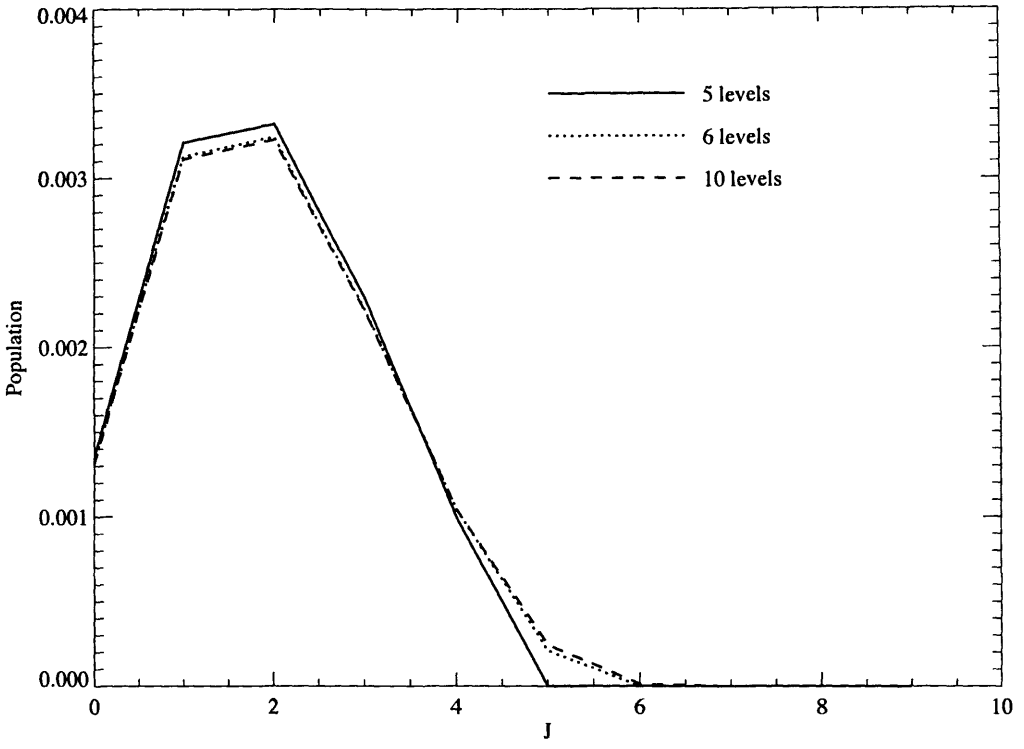

Figure 5.5: Plot of the level populations for CS in an initially H-rich core at $t = 10^5$ yr, for $J_{\rm max} = 5, 6$ and 10.

5.3 Results

5.3.1 Line profiles for models varying the initial atomic to molecular hydrogen ratio

In these models the line-width is dominated by turbulence; the turbulent velocity is $v_{\rm t} = 0.12\,{\rm km\,s^{-1}}$, but the maximum infall velocity is only $v_{\rm i} = 0.016$ km s^{-1}, and the thermal velocity is only $v_{\rm th} = \sqrt{3kT/m(i)} \sim 0.075$ km s^{-1} for CS at 10 K. Because of the low velocity gradient across the core, the cloud is essentially radiatively coupled, so a photon emitted at the back of the cloud can be absorbed by molecules in the front of the cloud.

Figure 5.6 shows the line profiles of CS $J = 5 \rightarrow 4$, $3 \rightarrow 2$ and $2 \rightarrow 1$ for the H-rich core (model 9) and the H-poor core (model 1) at $t = 10^3$, 10^4 and 10^5 yr. Although we mentioned in Section 4.4.1 that the most H-rich model (with $X({\rm H}) = 1.0$ initially) is unrealistic, we use it to derive the line profiles to gain a clearer understanding of how the hydrogen abundance affects the line profiles shapes. Obviously the effects predicted here for the H-rich model would be more

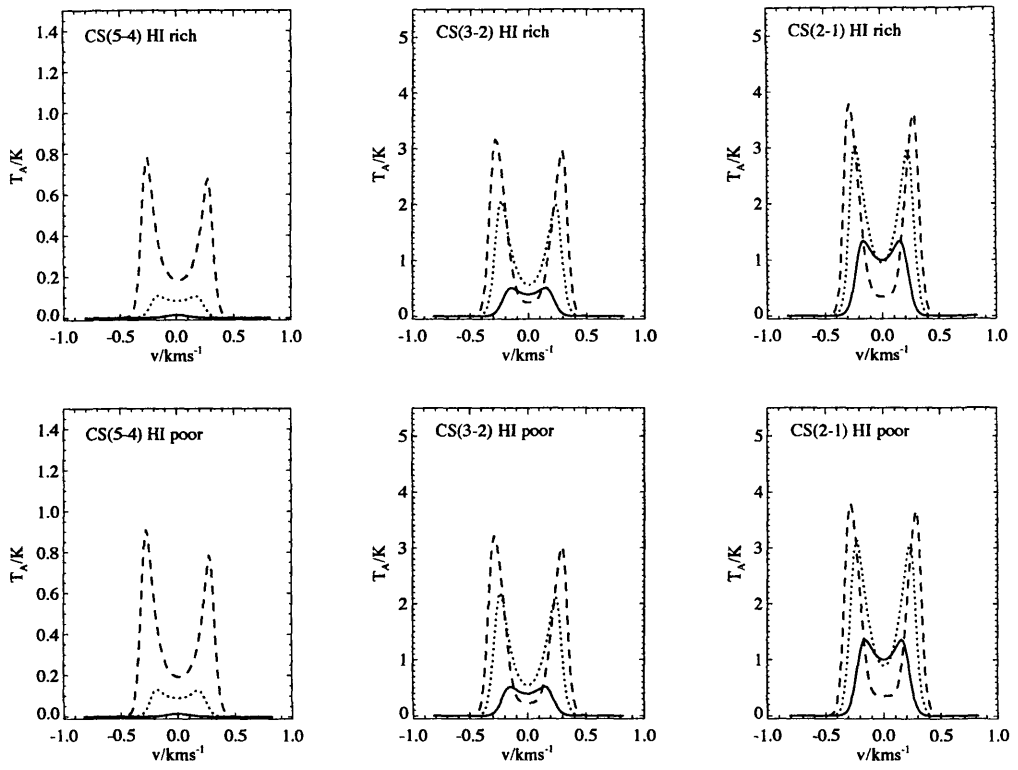

Figure 5.6: Line profiles of CS for transitions $J = 5 \rightarrow 4$, $3 \rightarrow 2$, $2 \rightarrow 1$ at $t = 1.0 \times 10^3$ yr (solid line), $t = 1.0 \times 10^4$ yr (dotted line) and $t = 1.0 \times 10^5$ yr (dashed line). The top row is for the H-rich model (model 9) and the bottom row is for the H-poor model (model 1). Note that CS($5 \rightarrow 4$) has a different T_A scale to the other lines.

understated for a more realistic H-rich core, such as those in models 4 and 5.

Both the H-rich and H-poor models show very similar line profiles. This is to be expected because CS is relatively unaffected by the H/H_2 ratio, and for both models its abundance profile follows that shown in Figure 5.2. The intensity of the line increases as time progresses, and for $t = 10^4$ and 10^5 yr, the line is strongly self-absorbed showing a double peaked profile. The peaks are located approximately 3σ [where σ is estimated by $(v_i^2 + v_t^2 + v_{th}^2)^{1/2}$] from the line centre, indicating that the emission is very optically thick. By 10^5 yr, a blue asymmetry appears in all transitions.

The blue asymmetry arises because of the velocity profile: the material responsible for the absorption is in the outer part of the core, closest to the observer, and this material has a higher velocity compared to the central material (see Figure 5.1). The outer (absorbing) material is therefore redshifted compared to the inner material, causing the absorption to be slightly off the

line centre (at ~ 0.01 km s^{-1}) and giving rise to the asymmetric profile. When the model was run with the velocity gradient removed, the line profiles were symmetric.

In these models the temperature is kept constant, at 10 K throughout the core, so it is interesting that the line profiles still show a blue asymmetry. In the inside-out collapse model (Shu 1977), however, a temperature profile with warm centre is needed to explain the asymmetry. This demonstrates the degeneracy of line profile shapes, and how extreme care must be taken when using line profile shapes to diagnose the physics of infall sources. These models show that although the CS does not give any information on the initial H/H_2 ratio, it does reveal valuable information on the collapse dynamics.

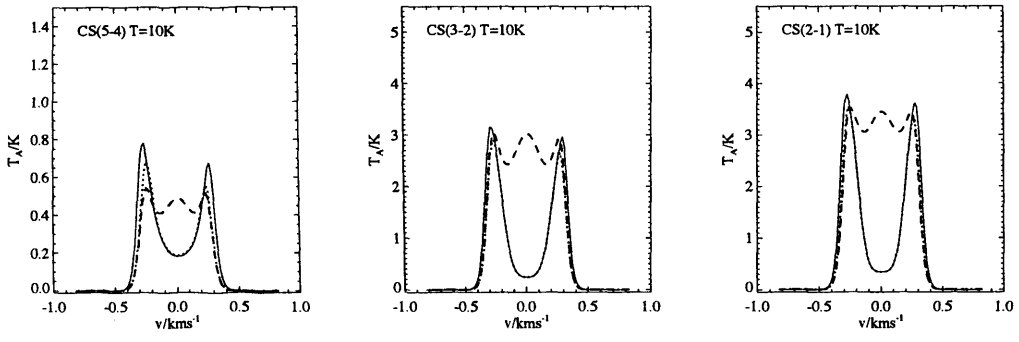

Figure 5.7: Line profiles of CS for transitions $J = 5 \rightarrow 4$, $3 \rightarrow 2$, $2 \rightarrow 1$ at $t = 1.0 \times 10^5$ yr for the initially H-rich model, with all material included (solid line), inner material removed (dotted line) and outer material removed (dashed line).

To test the origin of the CS line profile shape, we ran the radiative transfer code for a core with the same properties as the H-rich cores used for Figure 5.6 at $t = 10^5$ yr (i.e. with the same radius, velocity profile, abundance profile, temperature profile, etc.), except with no material within the inner half of the core (so the abundance of CS was set to 10^{-20} for $R \lesssim 5 \times 10^{16}$ cm), and also with no material in the outer half of the core (so the abundance of CS was set to 10^{-20} for $R \gtrsim 5 \times 10^{16}$ cm). These line profiles are shown in Figure 5.7, as well as the line profile for the core with all the material (solid line). The line profile for the core with no inner material (dotted line) looks very similar to the core with all the material, although slightly narrower, showing that the inner material contributes a small amount to the width of the line, but the shape of the line profile is mostly determined by the faster moving material in the outer half of the core. The line profile for the core with no outer material (dashed line) shows a central peak which must therefore come from the inner material, which gets absorbed when there is outer material present. These

tests are therefore consistent with the explanation above, that the absorption is caused by the faster moving outer parts of the core.

Figure 5.8 shows the line profiles for o-H_2CO for transitions $3_{12} \rightarrow 2_{11}$ and $2_{12} \rightarrow 1_{11}$ at $t = 10^3$, 10^4 and 10^5 yr for both the H-rich and H-poor models.

For the H-rich model, the $3_{12} \rightarrow 2_{11}$ would be undetectable at all times with current technology, and the $2_{12} \rightarrow 1_{11}$ only becomes marginally detectable by 10^5 yr (with $T_A \sim 0.02$ K). The H_2CO emission is optically thin, showing no signs of self-absorption and a much narrower line-width than for CS ($\Delta v \sim 0.2$ km s^{-1}, estimated by eye). At approximately this time, the abundance of H_2CO converges for both models (see Figure 4.1), so the intensities of the lines in both models are approximately the same. For the H-poor models, however, the intensities of the o-H_2CO lines decrease with time. Because of this property, o-H_2CO may be a good tracer of the initial H/H_2 ratio.

5.3.2 Line profiles for models varying the initial degree of depletion

Figures 5.9, 5.10 and 5.11 show the line profiles for transitions of CS, o-H_2CO and HCO^+ for both the initially undepleted model (model 10; stage (i) length 10^3 yr) and the initially depleted model (model 14; stage (i) length 10^7 yr). The line profiles of CS for an undepleted core are very similar to the line profiles for the H-rich and H-poor models (see Figure 5.6). For the depleted core, however, there is practically no emission from CS due to its low abundance at all times in the collapse.

o-H_2CO, on the other hand, has much stronger emission in the initially more 'depleted' core. This is because at the end of stage (i) for model 14, the abundance of H_2CO is relatively high, from a combination of H_2CO being produced on grain surfaces and then being desorbed, and also because the species that would normally destroy H_2CO are depleted [see Section 4.3.2]. The same trend is shown for the line profiles of HCO^+, whose abundance is kept high in the depleted core because of the depletion of water [see Section 4.3.2, equation (4.31)]. At 10^5 yr the intensity of the HCO^+ lines in the depleted core increase. The abundance of HCO^+ is actually approximately the same for the 10^4 and 10^5 yr, so the increase in intensity is down to the increase in the velocity gradient.

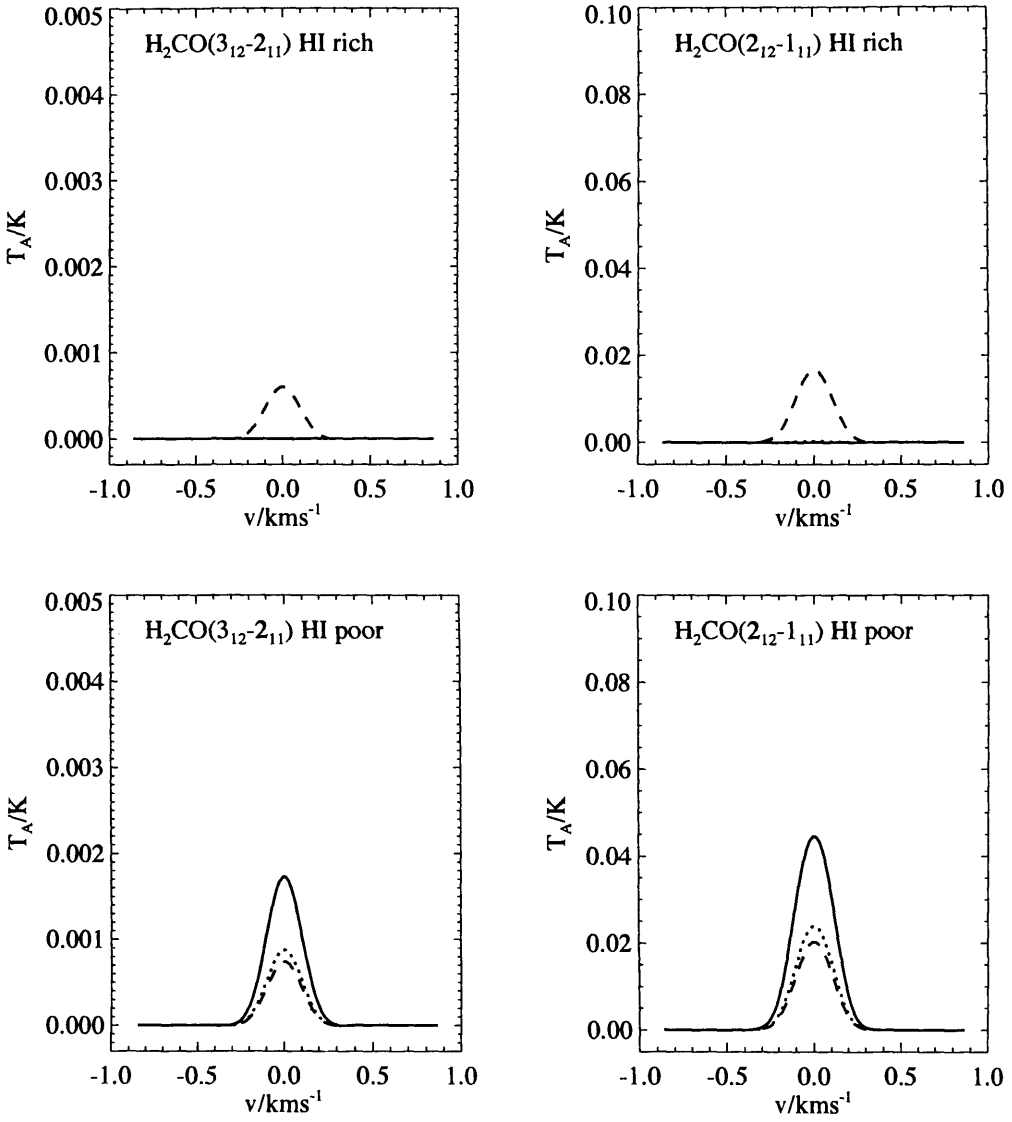

Figure 5.8: Line profiles of o-H_2CO for transitions $3_{12} \rightarrow 2_{11}$ and $2_{12} \rightarrow 1_{11}$ at $t = 1.0 \times 10^3$ yr (solid line), $t = 1.0 \times 10^4$ yr (dotted line) and $t = 1.0 \times 10^5$ yr (dashed line). The top row is for the H-rich model (model 9) and the bottom row is for the H-poor model (model 1). Note that the transitions have different T_A scales.

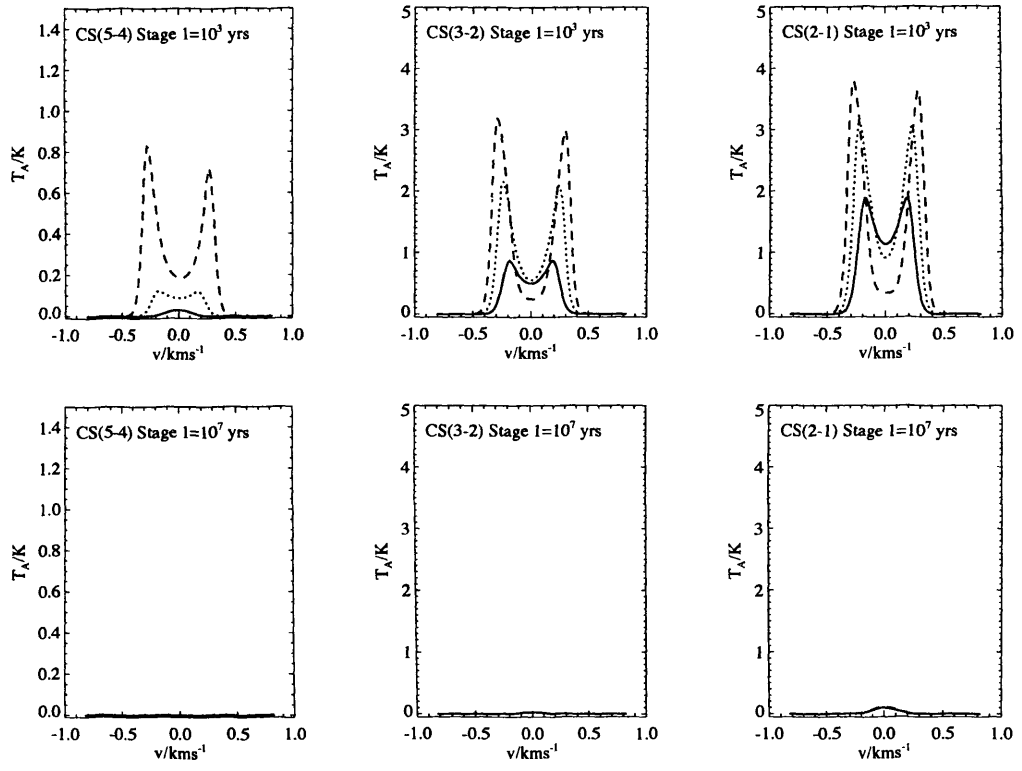

Figure 5.9: Line profiles of CS for transitions $J = 5 \rightarrow 4$, $3 \rightarrow 2$, $2 \rightarrow 1$ and $1 \rightarrow 0$ at $t = 1.0 \times 10^3$ yr (solid line), $t = 1.0 \times 10^4$ yr (dotted line), and $t = 1.0 \times 10^5$ yr (dashed line). The top row are for the undepleted core (model 10) in which stage (i) ran for 10^3 yr, and the bottom row are for the depleted core (model 14), in which stage 1 ran for 10^7 yr. Note that CS($5 \rightarrow 4$) has a different T_A scale to the other lines.

5.3.3 Testing the sensitivity of the line shapes to different temperature profiles

All the previous line profiles have been made by assuming a constant temperature of 10 K across the core, but now we look at how the line shapes are affected by other temperature profiles to test the robustness of our results.

The first temperature profile we model is the temperature profile deduced from dust continuum observations of the Class 0 source B335 (Zhou *et al.* 1990). The shape of this temperature profile comes from heating by the internal protostar in the centre and heating by the ISRF at the edge of the core. The radius has been normalised to 10^{17} cm, to fit the core that we are modelling.

Also, to understand more about the behaviour of the line profiles, we have tested two ad hoc linear temperature profiles, one of which is warm in the centre (12 K) and cold on the outside (8 K), and the other of which is cold (8 K) in the centre and warm (12 K) on the outside. The temperature

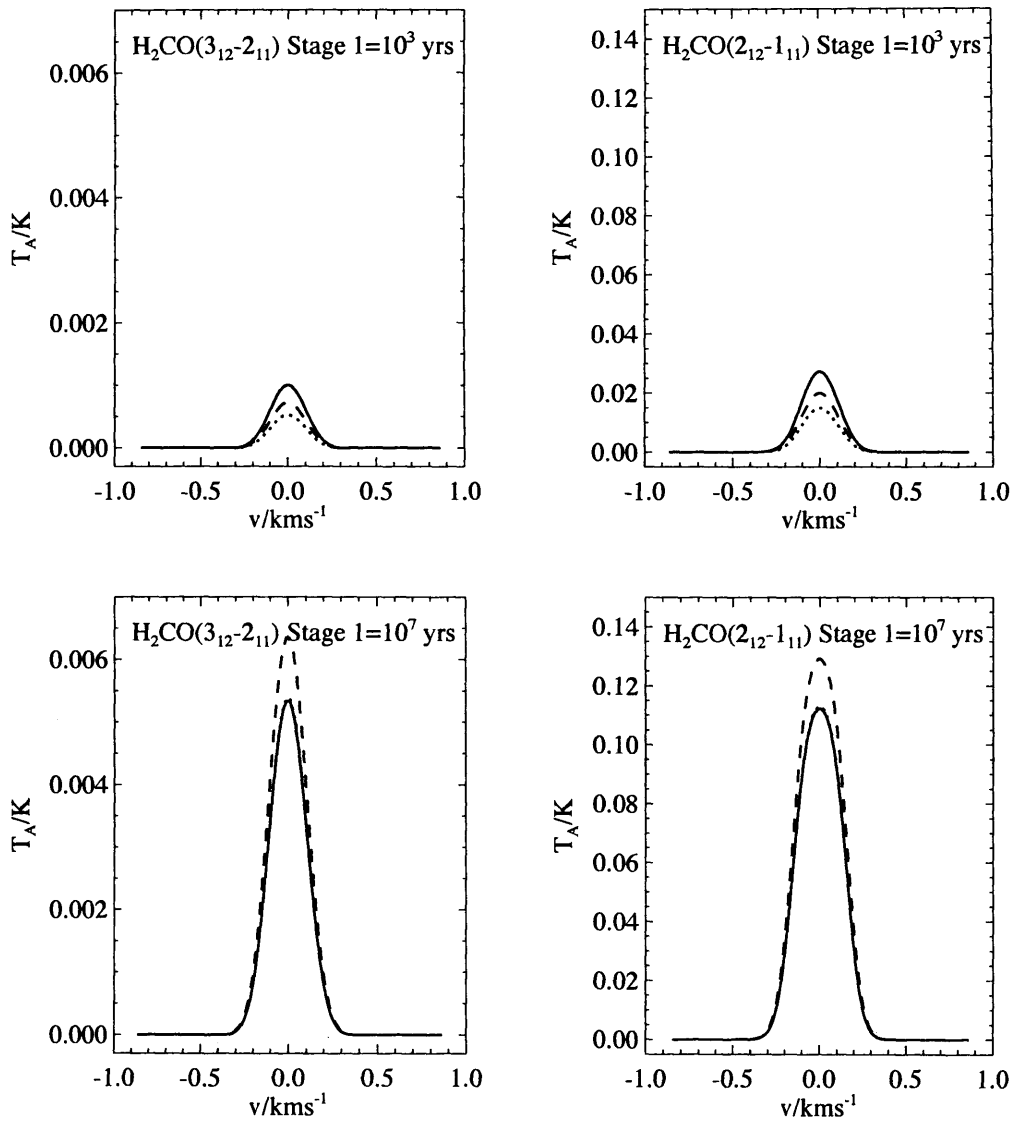

Figure 5.10: Line profiles of o-H_2CO for transitions $3_{12} \rightarrow 2_{11}$ and $2_{12} \rightarrow 1_{11}$ at $t = 1.0 \times 10^3$ yr (solid line), $t = 1.0 \times 10^4$ yr (dotted line), and $t = 1.0 \times 10^5$ yr (dashed line) . The top row are for the undepleted core (model 10) in which stage (i) ran for 10^3 yr, and the bottom row are for the depleted core (model 14), in which stage 1 ran for 10^7 yr. Note that the different transitions have different T_A scales.

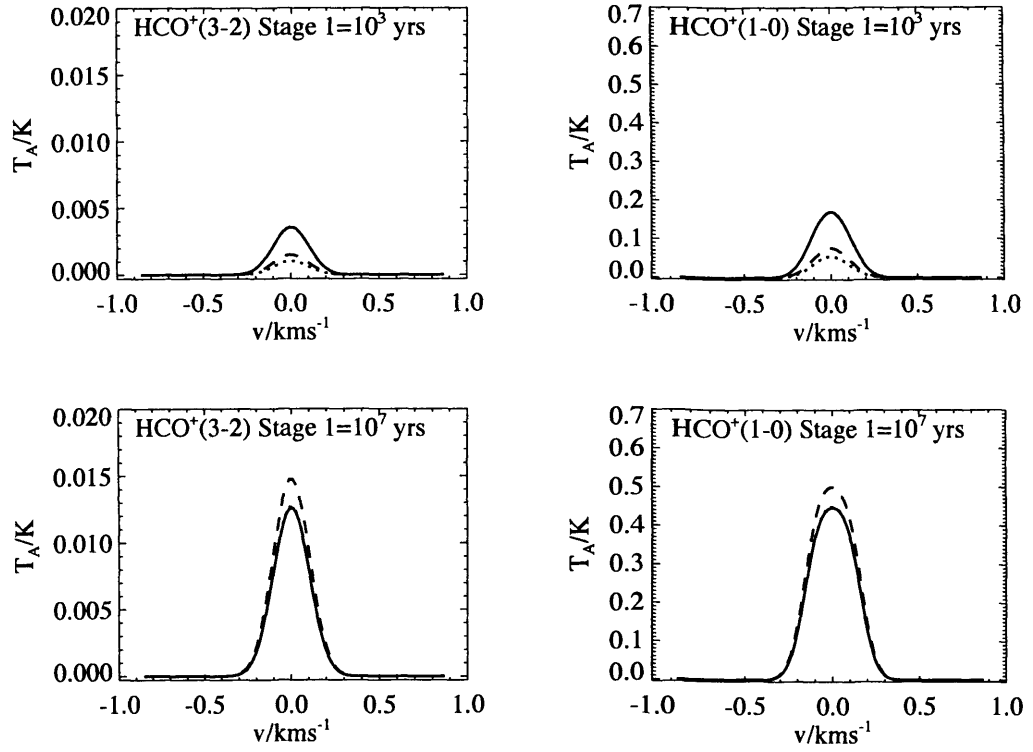

Figure 5.11: Line profiles of HCO^+ for transitions $J = 3 \rightarrow 2$ and $1 \rightarrow 0$ at $t = 1.0 \times 10^3$ yr (solid line), $t = 1.0 \times 10^4$ yr (dotted line) and $t = 1.0 \times 10^5$ yr (dashed line). The top row are for the undepleted core (model 10) in which stage (i) ran for 10^3 yr, and the bottom row are for the depleted core (model 14), in which stage (i) ran for 10^7 yr. Note that the different transitions have different T_A scales.

profiles are shown in Figure 5.12.

The line profiles for CS in an H-rich core using these temperature profiles are shown in Figure 5.13. The ratios of the blue to red peak intensities for each line are given in Table 5.2, as a measure of the line profile shape. The line profiles for the Class 0 temperature profile (second row), have a higher intensity due to the higher average temperature throughout the core, but the ratio of the blue to red peak intensities are approximately the same as for the constant 10 K profiles. The two linear temperature profiles have similar intensities to the 10 K lines, but the ratio of blue to red peak intensities is affected. In the core which is 12 K in the centre, the blue to red peak ratio is more than for the 10 K core. In the core which is 8 K in the centre, the opposite occurs, with a smaller blue to red ratio, and the CS($2 \rightarrow 1$) line actually has a stronger red peak. This could be because when the central regions are warm, the emission from the blue and red components arising

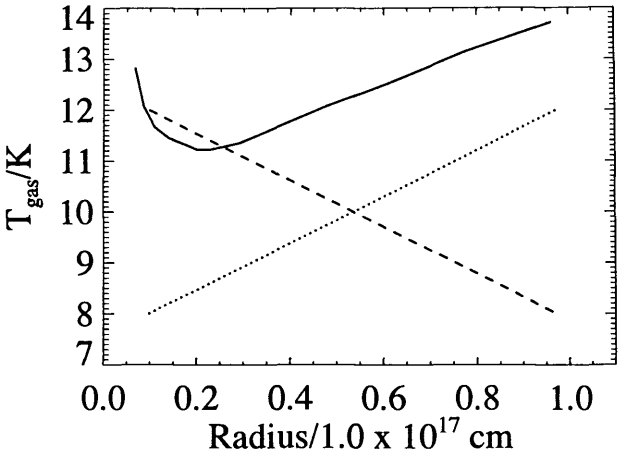

Figure 5.12: The temperature profiles tested. The solid line shows the temperature profile of the Class 0 source B335 (Zhou *et al.* 1993), normalised to 10^{17} cm. The dotted line shows a linear temperature profile which is colder in the centre (8 K) and warm on the outside (12 K), and the dashed line shows a linear temperature profile which is warmer in the centre (12 K) and colder on the outside (8 K).

from the centre of the core will increase, but since the absorption is due to the outer *redshifted* material, the emission from the red central regions is absorbed more than the emission from the blue central regions. The central blue emission is therefore less affected by absorption from the outer regions, which increases the strength of the blue peak relative to the red peak. Tsamis *et al.* (2008) found similar behaviour for the inside-out collapse model, where the predicted line profiles (also generated using SMMOL) gave stronger blue asymmetries for sources with Class 0 temperature profiles (which have warm centres) than for sources with pre-protostellar core temperature profiles (which are cold in the centre because there is no central source). We note, however, that the effects of the assumed temperature profile on the red:blue peak ratio are surprisingly small in our model compared to the results of Tsamis *et al.* (2008).

5.3.4 Line profiles at late times in the collapse

The previous line profiles were all given for times $\leq 10^5$ yr because these are the times for which the models show the most difference in chemical abundances. The maximum infall velocity at 10^5 yr is only 0.016 km s^{-1}, which is well below the sound speed of the gas, $v_s = \sqrt{kT/m(\mathrm{H_2})} =$ 0.2 km s^{-1}. It would therefore be interesting to see how the predicted line profile shapes change

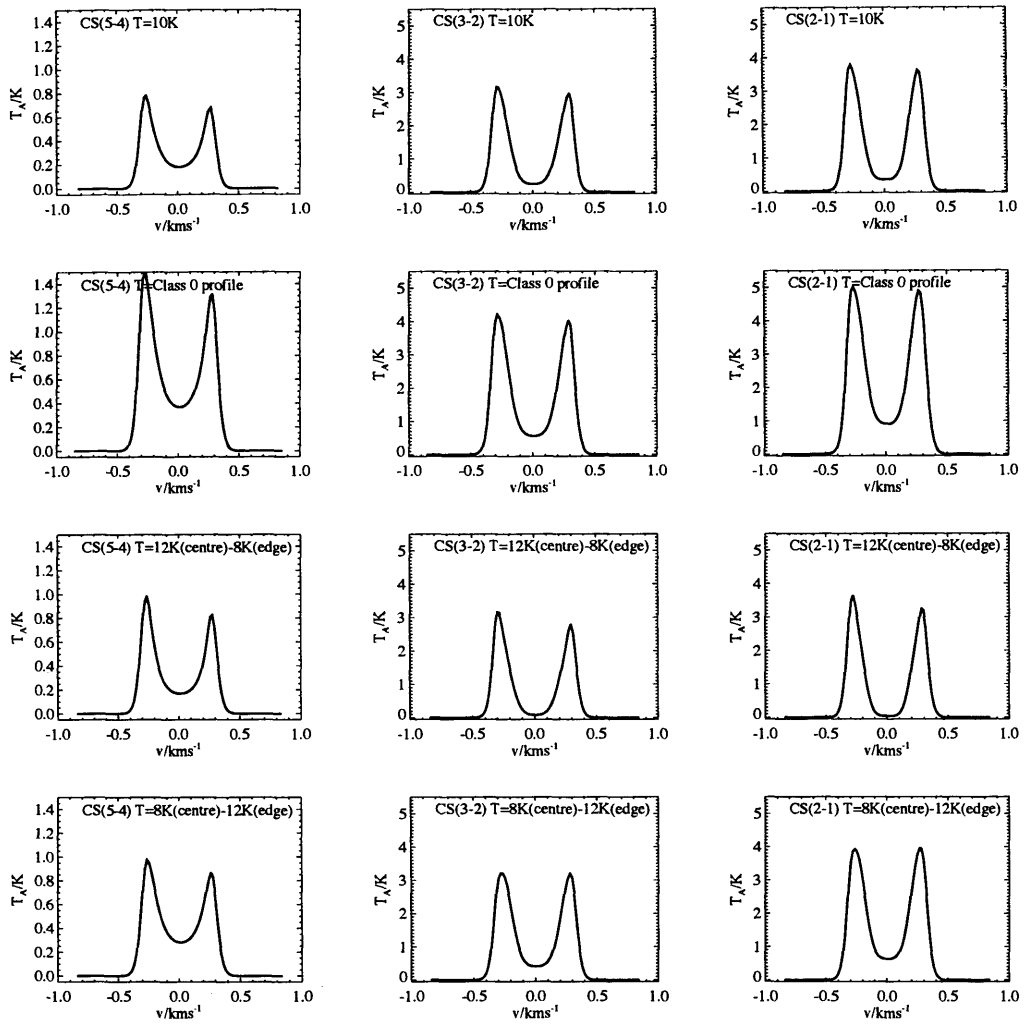

Figure 5.13: Line profiles of CS for transitions $J = 5 \rightarrow 4$, $3 \rightarrow 2$ and $2 \rightarrow 1$ for the H-rich model (model 9) with different temperature profiles at 1×10^5 yr. Top row: constant temperature (10K); second row: Class 0 temperature profile; third row: linear temperature profile which is 12 K in the centre and 8 K at the edge; bottom row: linear temperature profile which is 8 K in the centre and 12 K at the edge.

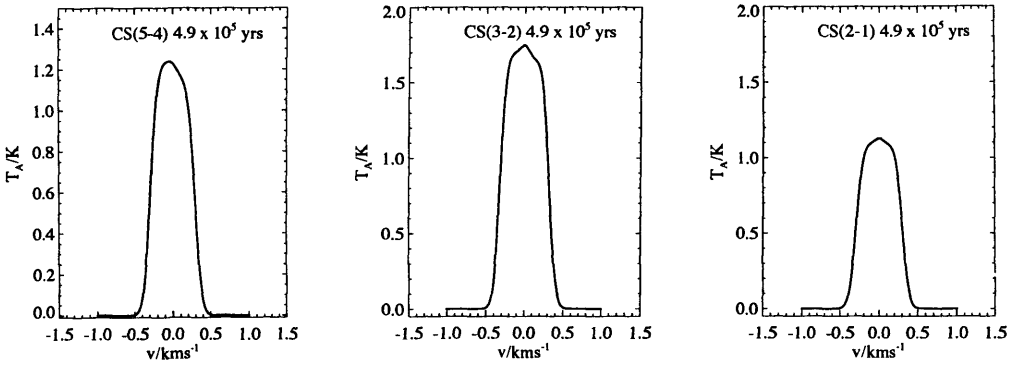

Figure 5.14: Line profiles of CS for transitions $J = 5 \rightarrow 4$, $3 \rightarrow 2$ and $2 \rightarrow 1$ for $t = 4.9 \times 10^5$ yr for an initially H-rich core (model 9). The maximum infall velocity at this time is $v_{\rm i} = 0.2$ km s^{-1}. Note that CS($5 \rightarrow 4$) has a different T_A scale to the other transitions.

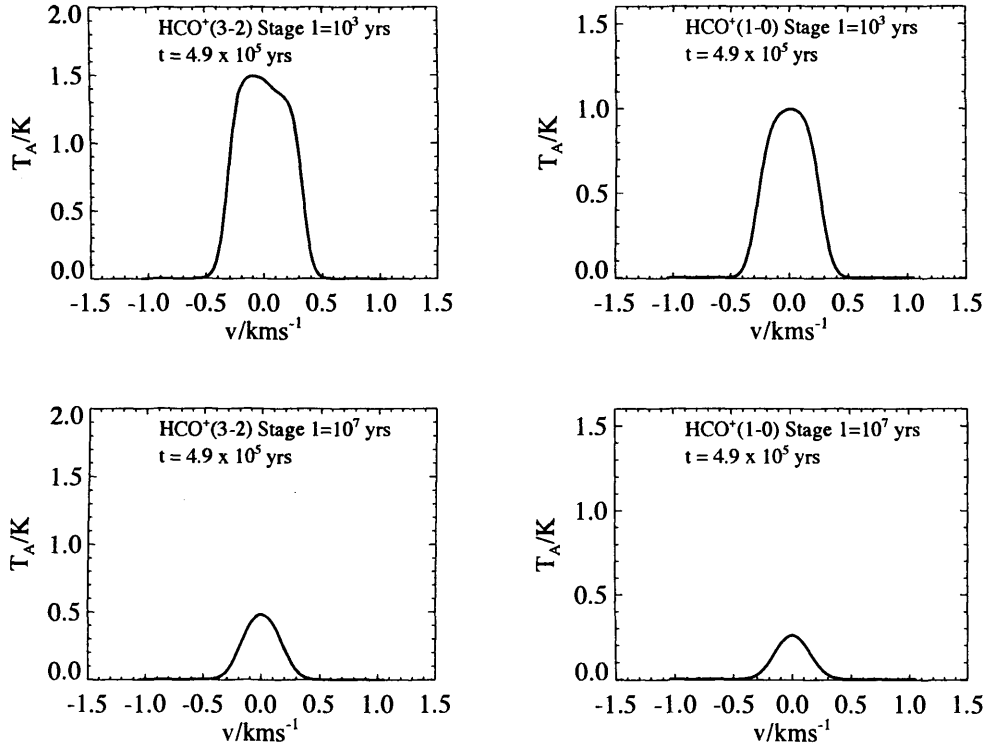

Figure 5.15: Line profiles of HCO^+ for transitions $J = 3 \rightarrow 2$ and $1 \rightarrow 0$ for $t = 4.9 \times 10^5$ yr. The top row is for the undepleted core (model 10) in which stage (i) ran for 10^3 yr, and the bottom row is for the depleted core (model 14), in which stage (i) ran for 10^7 yr. The maximum infall velocity at this time is $v_{\rm i} = 0.2$ km s^{-1}. Note that the different transitions have different T_A scales.

Table 5.2: The ratio of blue to red peak intensities for different temperature profiles.

Temp. profile	CS($5 \rightarrow 4$)	CS($3 \rightarrow 2$)	CS($2 \rightarrow 1$)
10 K	1.15	1.06	1.05
Class 0	1.14	1.04	1.02
12K centre - 8K edge	1.19	1.13	1.13
8K centre - 12K edge	1.12	1.00	0.99

when the infall speed becomes supersonic.

Figure 5.14 shows the line profiles for CS $J = 5 \rightarrow 4$, $3 \rightarrow 2$ and $2 \rightarrow 1$ for the initially H-rich core (model 9) at 4.9×10^5 yr, which is just before the end of the collapse. At this point the maximum infall speed (at the edge of the core) is just supersonic ($v_i = 0.2$ km s^{-1}), and the density is 3.2×10^6 cm^{-3}. The outer radius has contracted to 1.8×10^{16} cm (only 20 per cent of its original value), so for the telescope parameters we have chosen the source size is now comparable to the beam size.

By this time the CS has depleted by more than two orders of magnitude compared to its abundance at 10^5 yr. The lines are now single peaked, and the peak intensities of the $J = 3 \rightarrow 2$ and $2 \rightarrow 1$ lines have dropped by ~ 1.4 K and ~ 2.6 K respectively compared to the peak intensities at 10^5 yr. The peak intensity of the $J = 5 \rightarrow 4$ line, however, has increased from ~ 0.8 K at 10^5 yr, to ~ 1.2 K at 4.9×10^5 yr.

Figure 5.15 shows the line profiles for HCO^+ $J = 3 \rightarrow 2$ and $1 \rightarrow 0$ for the initially undepleted model (model 10; stage (i) length 10^3 yr) and the initially depleted model (model 14; stage (i) length 10^7 yr), also at 4.9×10^5 yr. In this figure the lines for the initially undepleted core (model 10) are now much stronger than for the initially depleted core (model 14), which is the opposite to the results at 10^5 yr (see Figure 5.11).

Furthermore, the line profiles for the initially undepleted core at 4.9×10^5 yr are much wider than for the depleted core ($\Delta v \sim 0.7$ km s^{-1} compared to ~ 0.4 km s^{-1}), and for the $J = 3 \rightarrow 2$ line in the undepleted core signs of asymmetry are beginning to appear.

This means that to see broad lines in HCO^+, the core needs to be initially undepleted, so that the 'depletion enhancement' of HCO^+ can occur during the later, faster stages of the collapse. If the core has been static for a long period of time ($\sim 10^6 - 10^7$ yr) before the collapse, the broad HCO^+ lines cannot be seen because the depletion enhancement has occurred too early, when the

infall velocities are low. This agrees with the conclusions drawn in Section 4.4.2, and shows that the core does not have be undergoing inside-out collapse for this effect to occur.

Another large difference for HCO^+ in the late stages of collapse is that now the $J = 3 \rightarrow 2$ line is stronger than the $1 \rightarrow 0$ line. As with CS, it seems that having a larger velocity gradient populates the higher rotational states, giving rise to increased intensities for the high-J lines.

5.4 Discussion and conclusions

We have used the radiative transfer code SMMOL to generate line profiles for the molecules CS, o-H_2CO and HCO^+ in a uniform density isothermal core undergoing modified free-fall collapse, with different initial chemical conditions.

The results have shown that the CS line profiles are insensitive to the initial H/H_2 ratio, but the line profile shapes are sensitive to the dynamics of the core. For example, the blue asymmetry of the CS lines increases as the collapse evolves, but then disappears at a few times 10^5 yr, because of depletion. Observations of CS could therefore be used to diagnose the 'age' of the collapse. However, the line profiles for the depletion models indicate that for an initially depleted core, or for a core in the late stages of collapse, the line profiles become more difficult to detect.

o-H_2CO, on the other hand, is more sensitive to the initial H/H_2 ratio, and for an early time core a high o-H_2CO intensity could imply an initially H-poor (H_2-rich) core. So, confirming our conclusions from Chapter 4, o-H_2CO could be used to identify the initial H/H_2 ratios in early stage collapsing cores.

With regards to the initial level of depletion in the core, for early time collapse ($\leq 10^5$ yr), the molecules o-H_2CO and HCO^+ have high intensities for cores which are initially 'depleted', because these molecules experience a brief depletion enhancement. However, at late times in the collapse, when v_i is supersonic, HCO^+ now has a high intensity for the initially undepleted core and a significantly lower intensity for the initially depleted core. The lines are very broad at this stage due to the high velocities, so if observations of collapsing cores reveal high intensity, broad lines for HCO^+, this would indicate late stage collapse for a core which has been static for $\lesssim 10^5 - 10^6$ yr prior to collapse. If observations showed narrow lines, this would imply the collapse is in its early stages, but that the core has already suffered some degree of depletion prior to collapse by remaining static for $\gtrsim 10^6 - 10^7$ yr.

Aside from the initial chemical conditions, one very important conclusion from this work is that the typical infall signature – double peaked line profiles with blue asymmetry – can be produced by

uniform density cores with constant temperature profiles undergoing modified free-fall collapse. The infall signature, therefore, does not necessarily imply inside-out collapse for a core with a non-constant temperature profile, as it is often interpreted (e.g. Zhou *et al.* 1993).

CHAPTER 6

THE DYNAMICS OF STAR FORMATION

In the previous chapter we investigated different initial chemical conditions that might be appropriate depending on the star formation regime (slow star formation [SSF] or rapid star formation [RSF]), and generated line profiles for these results assuming the simplest collapse model, modified free-fall collapse of a homogeneous sphere.

In this chapter we now look at two possibly more realistic models – the inside-out collapse model (Shu 1977) and a new ambipolar diffusion model (Stace & Rawlings 2008, hereafter SR08), to see if this has any effects on the chemical abundances during the collapse. We also generate line profiles for each model, to investigate the effect of the collapse dynamics and to find diagnostics of the collapse models, with the ultimate aim of finding evidence for either the SSF or RSF paradigms.

In Sections 6.1 and 6.2 we discuss the dynamical and chemical models, in Section 6.3 we discuss the results from the chemical models for each of the collapse regimes, and in Section 6.4 we give the line profiles from the models. Discussion and conclusions are given in Section 6.5.

6.1 The dynamical models

We have modelled two different types of core collapse: an ambipolar diffusion controlled collapse model from SR08, and the 'inside-out' collapse from the models of Shu (1977).

In both cases, we employ a 'semi-multipoint' model, following the chemical evolution of concentric test shells as they collapse inwards. The changes in density, radius and velocity that the shells experience depend on the collapse models used. Details of each of these models are given below:

6.1.1 Ambipolar diffusion controlled collapse

Ambipolar diffusion controlled collapse occurs in magnetically subcritical cores, where the magnetic field is strong enough to support the core. However, the neutrals do not directly feel the effect of the magnetic field, and so still tend to collapse towards the centre of the core, with the ions remaining tied to the magnetic field. The ions exert a drag force on the neutrals, slowing down their collapse. Eventually, in the centre of the core, enough mass will have built up so that the core becomes supercritical and begins to collapse on a dynamical timescale. This happens when the core mass to magnetic flux ratio, M/ϕ, is greater than $\sim 0.13G^{-1/2}$ (Mouschovias & Spitzer 1976).

We have taken the dynamical model from SR08 to couple with our chemical model. The results we have taken from this model are: (i) radius as a function of time, and (ii) density and velocity as a function of time and radius, for a set of 100 infalling shells making up a collapsing core (although we only run chemical models for six of these shells, spanning the core). This model takes into account the drag force from ions and negatively charged dust grains (which are assumed to have a charge of $-e$) using the following equations:

The total force exerted on a volume of gas, dV, with a hydrogen nucleon number density $n_{\rm H}$ is given by:

$$n_{\rm H} m_{\rm p} \left(\frac{1}{\tau_{\rm i}} + \frac{1}{\tau_{\rm g}}\right)(v_{\rm i} - v_{\rm n})dV \tag{6.1}$$

where $m_{\rm p}$ is the mass of a proton, and $\tau_{\rm i}$ is the mean time between collisions of the neutral gas with ions, $\tau_{\rm g}$ is the mean time between collisions of the neutral gas with dust grains, and $v_{\rm i} - v_{\rm n}$ is the ion-neutral drift velocity. $\tau_{\rm i}$ is given by Ciolek & Mouschovias (1993):

$$\tau_{\rm i} = \frac{1}{\omega_{\rm i}} = \frac{m_{\rm i} + 2m_{\rm p}}{m_{\rm i}} \frac{1.4}{n_{\rm i}\langle\sigma u\rangle} \tag{6.2}$$

where $\langle\sigma u\rangle$ is the collisional rate between ions of mass $m_{\rm i}$ and H_2 molecules of mass $2m_{\rm p}$, which is taken to be 1.7×10^{-9} cm^3 s^{-1} (which is the value for HCO^+ – H_2 collisions, so assumes that HCO^+ is the dominant ion). The factor of 1.4 takes into account the extra inertia of the gas provided by helium, assuming that helium makes up 10% of the gas.

$\tau_{\rm g}$ is given by:

$$\tau_{\rm g} = \frac{1}{\omega_{\rm g}} = \frac{m_{\rm n} + m_{\rm g}}{m_{\rm g}} \frac{1}{g_{\rm i}\langle\sigma v_{\rm g}\rangle n_{\rm g}} \sim \frac{1}{g_{\rm i}\langle\sigma v_{\rm g}\rangle n_{\rm g}} \tag{6.3}$$

where $m_{\rm n}$ is the average mass of neutral species, $m_{\rm g}$ is the mass of a dust grain ($m_{\rm g} \gg m_{\rm n}$), and $\langle\sigma v_{\rm g}\rangle$ is the collisional rate between dust grains and the neutral gas, given by:

$$\langle\sigma v_{\rm g}\rangle = \pi a^2 \sqrt{\frac{8kT}{\pi\mu m_{\rm p}}} \tag{6.4}$$

where a is the average dust grain radius, μ is the mean molecular mass, n_g is the number density of dust grains, T is the gas temperature and k is Boltzmann's constant. This value is derived by the product of the geometrical cross section of a grain and the mean random velocity of a neutral species.

The g_i factor in equation (6.3) gives the fraction of grains that are small enough to move with the magnetic field. The value of g_i used in this model is 1.0, which is appropriate for a distribution of small grains.

The drag force given in equation (6.1) is included to the force equation for an isothermal spherically symmetric cloud, collapsing under the influence of gravity, giving the following equation for the acceleration of the neutral gas:

$$\frac{dv_n}{dt} = -\frac{GM(r)}{r^2} + \Omega(v_i - v_n) - c_s^2 \frac{d\rho_n}{dr}\frac{1}{\rho_n} \tag{6.5}$$

where

$$\Omega = \omega_i + \omega_g = \frac{1}{\tau_i} + \frac{1}{\tau_g} \tag{6.6}$$

and G is the gravitational constant, $M(r)$ is the mass enclosed with radius r, c_s is the isothermal sound speed, and ρ_n is the neutral gas mass density.

$v_i - v_n$ is the ion-neutral drift velocity, given by:

$$v_i - v_n = -\frac{dB^2}{dr}\frac{1}{8\pi\Omega\rho_n} \tag{6.7}$$

where B is the magnetic field strength.

In SR08's model, they take into account how the changing chemical composition of the core affects its collapse equations; chemical reactions and freeze-out of ions onto dust grains affect the overall ionisation fraction of the gas, therefore the value of Ω varies over time. SR08 couple the chemical and dynamical equations to build a self-consistent model of ambipolar diffusion controlled collapse. The model follows the evolution of 100 infalling shells, in a core of mass 7.68 $M_\odot$, radius 8.54×10^{17} cm and magnetic field strength 8μG. The initial density distribution of the core is uniform, with $n_H = 2.8 \times 10^3$ cm^{-3}, and the collapse is isothermal with a gas temperature of 10 K.

In our model, we derive the chemical evolution of the shells numbered 1, 25, 50, 75, 91 and 100, from SR08's model, which have starting radii of 8.54×10^{17} cm, 7.37×10^{17} cm, 6.77×10^{17} cm, 5.41×10^{17} cm, 3.93×10^{17} cm and 1.82×10^{17} cm respectively. Shell 1 corresponds to the outer radius of the core. Shell 91 was included because this was the original shell we used to test the single point model.

Since the density is initially uniform, all shells begin with $n_{\rm H}(t = 0) = 2.8 \times 10^3$ cm^{-3}. The initial visual extinction of each shell, A_{v0} was calculated using equation (5.1), with $A_v(\text{ext}) = 1.0$. This value is lower than the $A_v(\text{ext})$ used in Chapter 5, but this makes sense because the core we are modelling here has a much larger size than the core in Chapter 5, therefore there is less contribution to the A_v from the foreground material.

We chose $A_v(\text{ext}) = 1.0$ so that freeze-out would occur at densities consistent with observations throughout the core; in the model the A_v of each shell varies according to $A_v(R_0, t = 0)(n_{\rm H}/n_{\rm H0})^{2/3}$, and since we have chosen $A_{\rm v,crit}$ to be 4.0 magnitudes (see Section 6.2), using equation (5.1) to give $A_v(R_0, t = 0)$ for each shell, this means that the range of densities each shell will begin to have freeze-out is from 3.3×10^3 cm^{-3} for the central shell [which has $A_v(R_0, t = 0) = 2.88$] and 1.6×10^4 cm^{-3} for the external shell [which has $A_v(R_0, t = 0) = 1.0$]. This is consistent with the range of densities above which freeze-out is observed, summarised in Bergin & Tafalla (2007).

Table 6.1: Table showing the initial radius (R_0), density ($n_{\rm H0}$) and A_v (A_{v0}) for each collapsing shell for which we derive the chemical evolution, for the ambipolar diffusion and inside-out collapse models.

AMBIPOLAR DIFFUSION			INSIDE-OUT		
Total mass 7.68 $M_\odot$			Total mass 0.96 $M_\odot$		
Outer radius 8.54×10^{17} cm			Outer radius 1.60×10^{17} cm		
R_0 (cm)	$n_{\rm H0}$ (cm^{-3})	A_{v0} (mag)	R_0 (cm)	$n_{\rm H0}$ (cm^{-3})	A_{v0} (mag)
1.82×10^{17}	2.8×10^3	2.88	1.0×10^{16}	4.7×10^6	47.13
3.93×10^{17}	2.8×10^3	2.29	2.5×10^{16}	7.5×10^5	18.85
5.41×10^{17}	2.8×10^3	1.88	5.0×10^{16}	1.9×10^5	9.43
6.77×10^{17}	2.8×10^3	1.50	7.4×10^{16}	8.7×10^4	6.39
7.73×10^{17}	2.8×10^3	1.23	1.6×10^{17}	1.8×10^4	2.95
8.54×10^{17}	2.8×10^3	1.00			

The initial physical parameters for each of the shells we have studied are summarised in Table 6.1. The physical evolution of the test shells is shown in Figure 6.1. It shows that the outer shell (black line) remains unperturbed by the collapse and remains at the same density and radius. The inner shell (purple line), however, collapses relatively quickly into the core, and before 10^6 yr

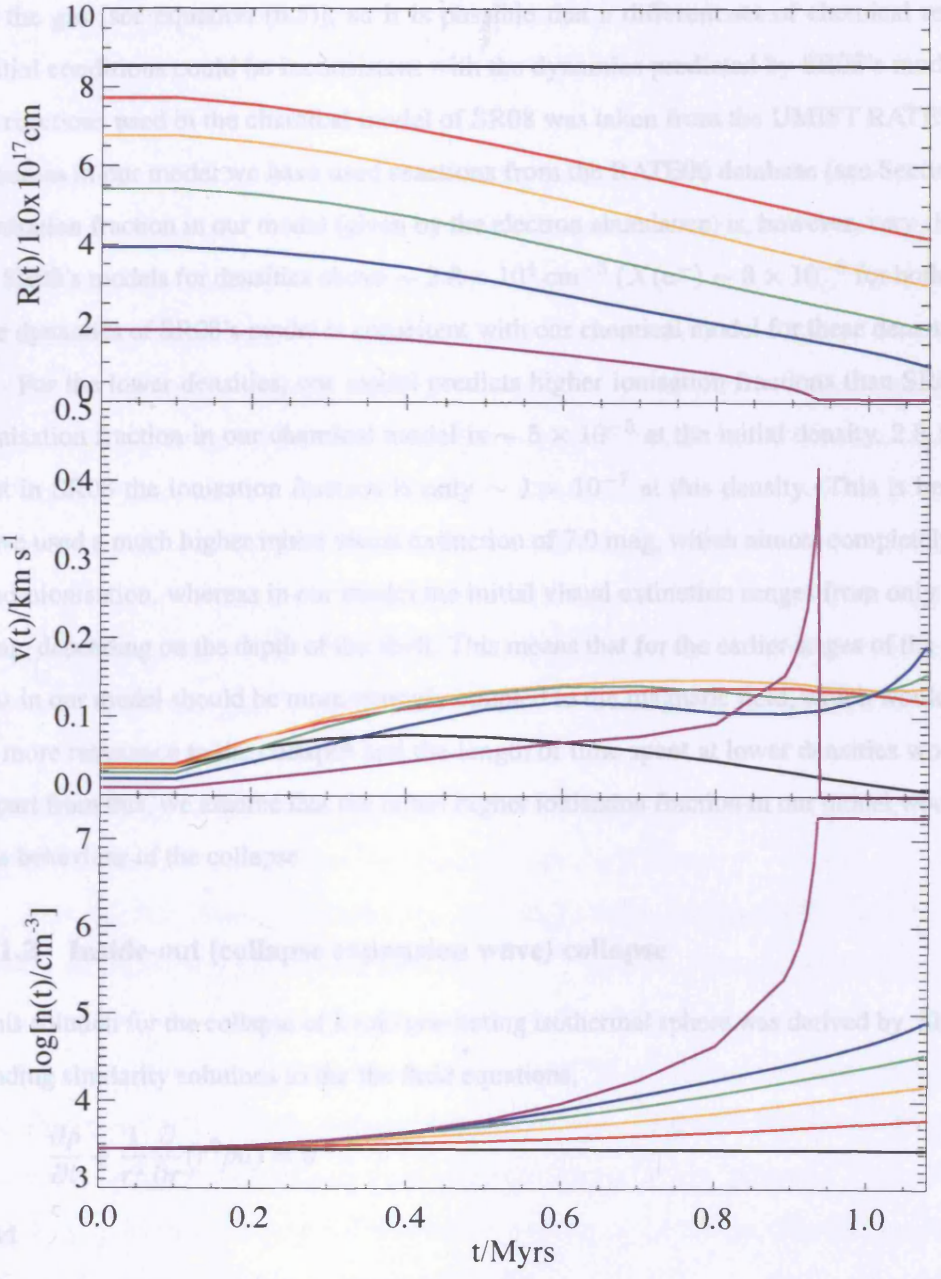

Figure 6.1: Physical evolution of the test shells in the ambipolar diffusion model. The black, red, yellow, green, blue and purple lines are for the shells beginning at $R_0 = 8.54 \times 10^{17}$, 7.73×10^{17}, 6.77×10^{17}, 5.41×10^{17}, 3.93×10^{17} and 1.82×10^{17} cm respectively.

it reaches its final density of $\sim 10^7$ cm^{-3} where the collapse halts and its velocity suddenly drops to zero.

The dynamics of SR08's model depend upon the chemistry, particularly the ionisation fraction of the gas [see equation (6.5)], so it is possible that a different set of chemical reactions and initial conditions could be inconsistent with the dynamics predicted by SR08's models. The set of reactions used in the chemical model of SR08 was taken from the UMIST RATE95 database, whereas in our model we have used reactions from the RATE06 database (see Section 6.2). The ionisation fraction in our model (given by the electron abundance) is, however, very similar to that in SR08's models for densities above $\sim 2.8 \times 10^4$ cm^{-3} ($X(\mathrm{e}^-) \sim 3 \times 10^{-8}$ for both models), so the dynamics of SR08's model is consistent with our chemical model for these densities.

For the lower densities, our model predicts higher ionisation fractions than SR08; the peak ionisation fraction in our chemical model is $\sim 5 \times 10^{-5}$ at the initial density, 2.8×10^3 cm^{-3}, but in SR08 the ionisation fraction is only $\sim 1 \times 10^{-7}$ at this density. This is because SR08 have used a much higher initial visual extinction of 7.0 mag, which almost completely suppresses photoionisation, whereas in our model the initial visual extinction ranges from only 1.00 to 2.88 mag, depending on the depth of the shell. This means that for the earlier stages of the collapse, the gas in our model should be more strongly coupled to the magnetic field, which would mean there is more resistance to the collapse and the length of time spent at lower densities would increase. Apart from this, we assume that the initial higher ionisation fraction in our model would not affect the behaviour of the collapse.

6.1.2 Inside-out (collapse expansion wave) collapse

This solution for the collapse of a self-gravitating isothermal sphere was derived by Shu (1977), by finding similarity solutions to the the fluid equations,

$$\frac{\partial \rho}{\partial t} + \frac{1}{r^2}\frac{\partial}{\partial r}(r^2 \rho u) = 0 \tag{6.8}$$

and

$$\frac{\partial u}{\partial t} + u\frac{\partial u}{\partial r} = -\frac{a^2}{\rho}\frac{\partial \rho}{\partial r} - \frac{GM}{r^2}. \tag{6.9}$$

where ρ is the mass density, r is the radial distance from the centre of the core, u is the fluid velocity, a is the isothermal sound speed and M is the mass enclosed within radius r at time t. Equation (6.8) is the continuity (mass conservation) equation, and equation (6.9) is the force equation for an ideal isothermal flow. Shu (1977) neglected the external pressure for the calculation, so the solution is

valid for the part of the flow which is far away from the core boundary, where internal pressures are much greater than the external pressure.

The collapse expansion wave (CEW) solution, is a particular solution to this problem, which starts with the initial density distribution of a singular isothermal sphere,

$$\rho(r,0) = \frac{a^2}{2\pi G} r^{-2}, \tag{6.10}$$

and the initial velocity is zero everywhere. The physical description of the solution is as follows:

Since the isothermal sphere configuration is in unstable equilibrium, a small perturbation at $t = 0$ in the core centre can cause the central regions to begin collapsing. The regions outside the collapsing centre have an unchanged density and gravitational field, so they can maintain hydrostatic equilibrium and are unaffected. Material immediately above the collapsing inner region begins to fall, once the material beneath it has given way. In this way, a 'collapse expansion wave' (CEW) is formed, where material inside the CEW is falling, and material outside is static. The CEW moves at the isothermal sound speed, a, which is the maximum speed that the collapsing inner regions can communicate with the static outer regions. The position of the head of the CEW is therefore given by $r = at$ at time t. The tail of the CEW is at the centre, where the material is approaching free-fall. For the region within the CEW, the density profile is approximately given by $\rho \propto r^{-3/2}$, associated with free-fall collapse.

This solution is valid for a singular isothermal sphere extending to infinity. For a bounded sphere, the solution breaks down once the CEW hits the boundary.

Although this solution starts with specific initial conditions, Shu (1977) argue that if the initial conditions are not very far removed from the $\rho \propto r^{-2}$ law, the cloud can readjust subsonically until it reaches this state as it tries to establish mechanical balance.

As in the numerical example given by Shu (1977), we have used a core mass of 0.96 $M_{\odot}$, a core radius 1.6×10^{17} cm and an isothermal sound speed of 0.2 km s^{-1}. These values are applicable to Bok globules which are possible candidates for star formation. The collapse finishes at $t = 2.5 \times 10^5$ yr, when the CEW hits the boundary of the sphere. The gas temperature of the core, used for the chemical calculations, is 10 K.

We ran the chemical model for a range 'test shells', starting at radii of 1.0×10^{16} cm, 2.5×10^{16} cm, 5.0×10^{16} cm, 7.4×10^{16} cm and 1.6×10^{17} cm.

We used the results given in Table 2 of Shu (1977) to derive the physical conditions of each shell. This table lists the solutions $\alpha(x)$ and $v(x)$, where x is the similarity variable $x = r/at$, and

$\alpha(x)$ and $v(x)$ are related to the density and velocity by

$$\rho(r,t) = \frac{\alpha(x)}{4\pi G t^2} \tag{6.11}$$

and

$$u(r,t) = av(x) \tag{6.12}$$

where ρ is the mass density and u is the velocity of the shell.

The shell will remain at its initial density and radius with zero velocity until the CEW, travelling at the sound speed of the gas, a, hits the shell. At this point we gave the shell a small initial velocity so we can work out its new position a small time δt later. At this new point, the dimensionless variable $x = r/at$ can be calculated, where r is the radius of the shell and t is the time since the collapse began. At this value of x the values of α and v can be calculated by interpolating between the values given in Table 2 of Shu (1977). To interpolate between the results we have used a spline interpolation routine.The shell now travels at its new velocity for a time δt, where its new x and hence α and v are recalculated.

Once the value of x drops below 0.05, which occurs once the shell gets close to the core centre, the density and velocity tend towards infinity and the solution is no longer valid. At this point, we stop the collapse by holding the density and radius constant and setting the velocity to zero.

The radius, density and velocity of each shell as a function of time is shown in Figure 6.2. The point when the collapse of each shell halts (when $x \leq 0.05$) is clearly seen by the sudden drop to zero in velocity. This point occurs once each shell reaches a distance of less than $\sim 1 \times 10^{16}$ cm from the centre of the core.

The outer shell, at 1.6×10^{17} cm remains static and at a constant density throughout the collapse. This is because the solution is no longer valid once the CEW has reached the outermost shell, so we stop the entire collapse at this point, which occurs at $\sim 2.5 \times 10^5$ yr.

As the shells collapse inwards, the changes in density and A_v have a large impact on chemical reaction rates, creating a large variation in chemical abundances across the core. The A_v was estimated by calculating the H_2 column density from the radius of the shell to the outer edge of the core, and then converting to A_v using $A_v = 10^{-21} N_{H_2}(\mathrm{cm}^{-2})$ mag (Bohlin *et al.* 1978).

The initial conditions for each shell are shown in Table 6.1.

It may seem inconsistent that the core mass and radius for the ambipolar diffusion model ($M = 7.68\ M_\odot$ and $R = 8.54 \times 10^{17}$ cm) are so much larger than that of the inside-out collapse model ($M = 0.96\ M_\odot$ and $R = 1.6 \times 10^{17}$ cm), but this is actually because the ambipolar diffusion

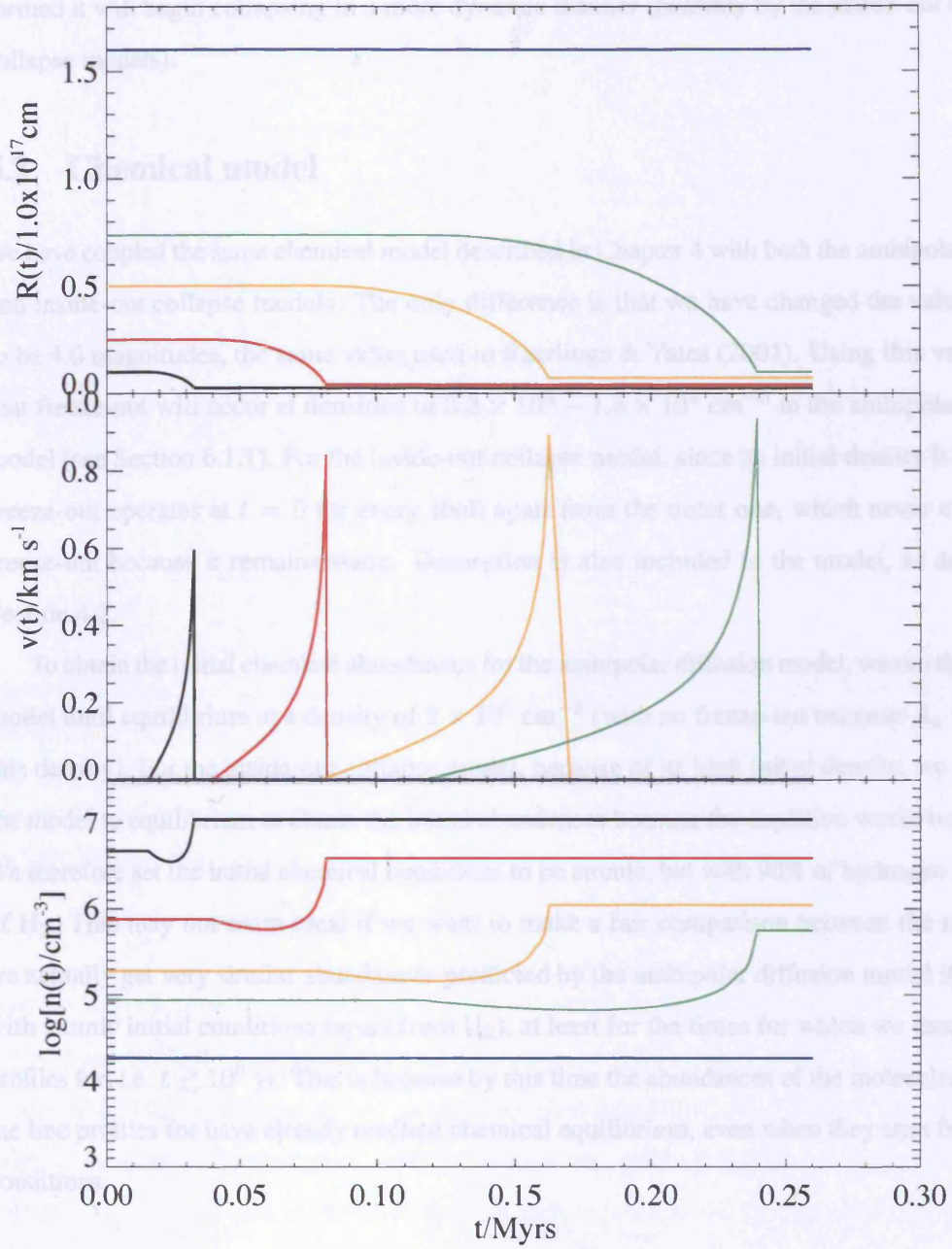

Figure 6.2: Physical evolution of the test shells in the inside-out collapse model. The blue, green, yellow, red and black lines refer to the shells which start at $R_0 = 1.6 \times 10^{17}$, 7.4×10^{16}, 5.0×10^{16}, 2.5×10^{16} and 1.0×10^{16} cm respectively.

model is starting from a much earlier, diffuse state, and not all of the mass of the ambipolar diffusion cloud would be expected to go into the protostar. In fact, the ambipolar diffusion model is evolving towards the initial state of the CEW model, and once a sufficiently centrally condensed core has formed it will begin collapsing in a more dynamic manner (possibly by the inside-out or free-fall collapse models).

6.2 Chemical model

We have coupled the same chemical model described in Chapter 4 with both the ambipolar diffusion and inside-out collapse models. The only difference is that we have changed the value of $A_{\rm v,crit}$ to be 4.0 magnitudes, the same value used in Rawlings & Yates (2001). Using this value means that freeze-out will occur at densities of $3.3 \times 10^3 - 1.6 \times 10^4$ cm^{-3} in the ambipolar diffusion model (see Section 6.1.1). For the inside-out collapse model, since its initial density is quite high, freeze-out operates at $t = 0$ for every shell apart from the outer one, which never experiences freeze-out because it remains static. Desorption is also included in the model, as described in Section 4.2.

To obtain the initial chemical abundances for the ambipolar diffusion model, we run the chemical model until equilibrium at a density of 2×10^3 cm^{-3} (with no freeze-out because $A_v < A_{v,\rm crit}$ at this density). For the inside-out collapse model, because of its high initial density, we cannot run the model to equilibrium to obtain the initial abundances because the depletion would be too severe. We therefore set the initial chemical conditions to be atomic, but with 90% of hydrogen in the form of H_2. This may not seem ideal if we want to make a fair comparison between the models, but we actually get very similar abundances predicted by the ambipolar diffusion model if we start it with atomic initial conditions (apart from H_2), at least for the times for which we model the line profiles for, i.e. $t \gtrsim 10^5$ yr. This is because by this time the abundances of the molecules we model the line profiles for have already reached chemical equilibrium, even when they start from atomic conditions.

6.3 Chemical results

6.3.1 Ambipolar diffusion model

Figure 6.3 shows the fractional abundances of CS, N_2H^+, H_2CO and HCO^+ for each test shell as they evolve with time, for the ambipolar diffusion model. These molecules were chosen because

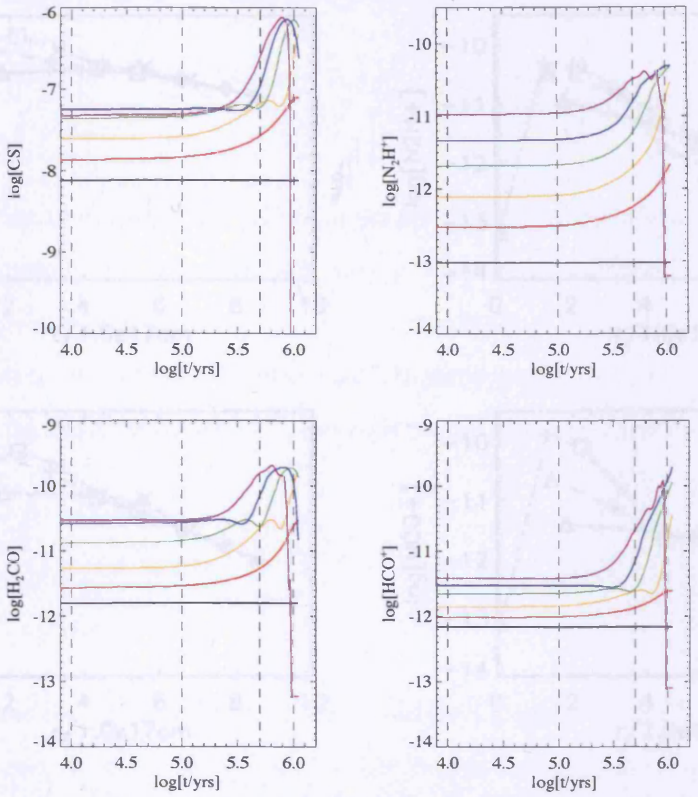

Figure 6.3: Fractional abundances of CS, N_2H^+, H_2CO and HCO^+ in each of the shells as a function time for the ambipolar diffusion model. The black, red, yellow, green, blue and purple lines are for the shells beginning at $R_0 = 8.54 \times 10^{17}$, 7.73×10^{17}, 6.77×10^{17}, 5.41×10^{17}, 3.93×10^{17} and 1.82×10^{17} cm respectively. The dashed lines mark the times for which we generate line profiles.

these are the molecules most commonly used to detect infall, so it will be useful to understand how they respond to different dynamics.

For all molecules, the abundances in the outer shell (black line; $R_0 = 8.54 \times 10^{17}$ cm) remain constant throughout the collapse. This is because the outer shell does not undergo infall and remains at a constant density and visual extinction (see Figure 6.1). For the inner shells, the abundances increase as time progresses and the density rises. The innermost shell (purple line; $R_0 = 1.82 \times 10^{17}$ cm), however, suffers from severe depletion; the final abundances in the inner shell for N_2H^+, H_2CO and HCO^+ falls by three orders of magnitude, and the depletion is even greater for CS. Depletion of CS also occurs in the second and third innermost shells (blue and green lines; $R_0 = 3.93 \times 10^{17}$ and 5.41×10^{17} cm respectively), and is beginning to occur for the second innermost shell for H_2CO. The depletion is not as severe for N_2H^+, H_2CO and HCO^+ because

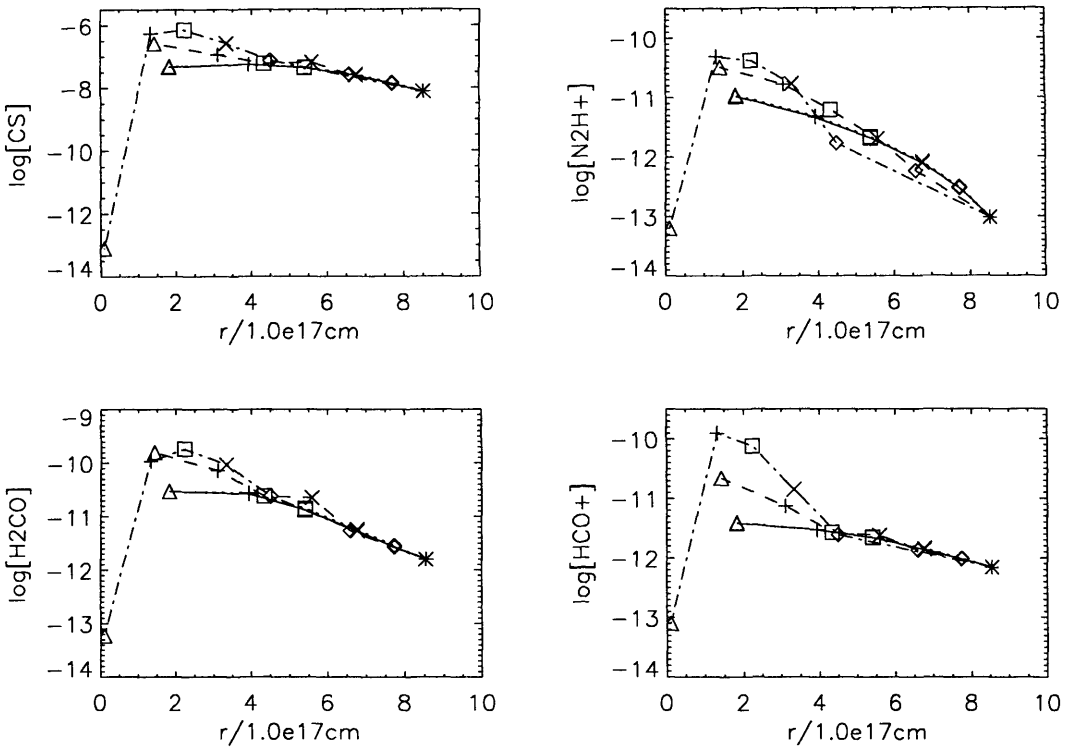

Figure 6.4: Fractional abundances CS, N_2H^+, H_2CO and HCO^+ of as a function of radius for the ambipolar diffusion model. The thick solid line is for 10^5 yr, the dashed line is for 5×10^5 yr, and the dot-dashed line is for 10^6 yr. A dotted line is also plotted for 10^4 yr, but this is indistinguishable from the line at 10^5 yr. The asterisks, diamonds, crosses, squares, pluses, and triangles refer to the shells which start at $R_0 = 8.54 \times 10^{17}$, 7.73×10^{17}, 6.77×10^{17}, 5.41×10^{17}, 3.93×10^{17} and 1.82×10^{17} cm respectively.

these are the initially 'depletion enhanced' species, as described in Section 4.3. By the time the collapse has finished, just after 10^6 yr, these molecules are still experiencing the enhancement from depletion.

For $t \leq 5.5$ Myr, the abundances of all the molecules increase as the initial radius of the shell decreases. Since the density is initially constant across the core, the increase in abundances is down to the decrease in A_v, which varies from 2.88 mag in the most central shell to 1.00 in the outer shell. The rate constant for photoreactions is proportional to $\exp(-A_v)$, so this results in the photoreactions being ~ 7 times slower in the central shell than in the outer shell.

The low abundance of CS in the outer shell is caused by direct photodissociation:

$$CS + h\nu \rightarrow C + S \tag{6.13}$$

$$\rightarrow CS^+ + e^-. \tag{6.14}$$

The low abundances of N_2H^+ and HCO^+ in the outer shells are actually caused by an increase in the rate of electronic recombination, which is a result of the increased electron abundance generated by photoionisation.

The low abundance of H_2CO in the outer shells is partly caused by direct photodissociation of H_2CO, but mainly by the reaction with C^+, which is highly abundant because of photoionisation:

$$C^+ + H_2CO \rightarrow CO + CH_2^+ \tag{6.15}$$

$$\rightarrow HCO^+ + CH \tag{6.16}$$

$$\rightarrow H_2CO^+ + C. \tag{6.17}$$

Figure 6.4 shows the radial distribution of the fractional abundances of CS, N_2H^+, H_2CO and HCO^+ across the core at 10^5 yr (solid line), 5×10^5 yr (dashed line) and 10^6 yr (dot-dashed line), for the ambipolar diffusion model. The abundance profile for 10^4 yr is also plotted (dotted line), but it is almost indistinguishable from the line at 10^5 yr. These abundance profiles were generated by taking the radius of each shell at a particular time from Figure 6.1, and taking the corresponding chemical abundance of the shells from Figure 6.3. The data taken from a particular shell is marked with a different symbol (see caption), for example, the triangle marks the evolution of the innermost shell. The plot demonstrates how the core is contracting, with the inner shells moving inwards as time progresses (seen most clearly by looking at the position of the triangle).

The plot shows the abundance profiles have quite a steep gradient, with the lowest abundances at the edge of the core, even at 10^5 yr when the density is practically uniform. This is a consequence of photodissociation at the edge of the core, as explained above.

By 5×10^5 yr, the collapse is well underway and so we begin to see the depletion enhancements of N_2H^+, H_2CO and HCO^+ in the inner shells, making the abundance gradient even steeper. The enhancement of HCO^+ in the inner shells is especially prominent, being enhanced by almost two orders of magnitude. The enhancement of CS in the inner regions is due to an increase in the rate of gas-phase reactions because of the density, rather than a depletion effect. By 10^6 yr the inner regions become extremely depleted.

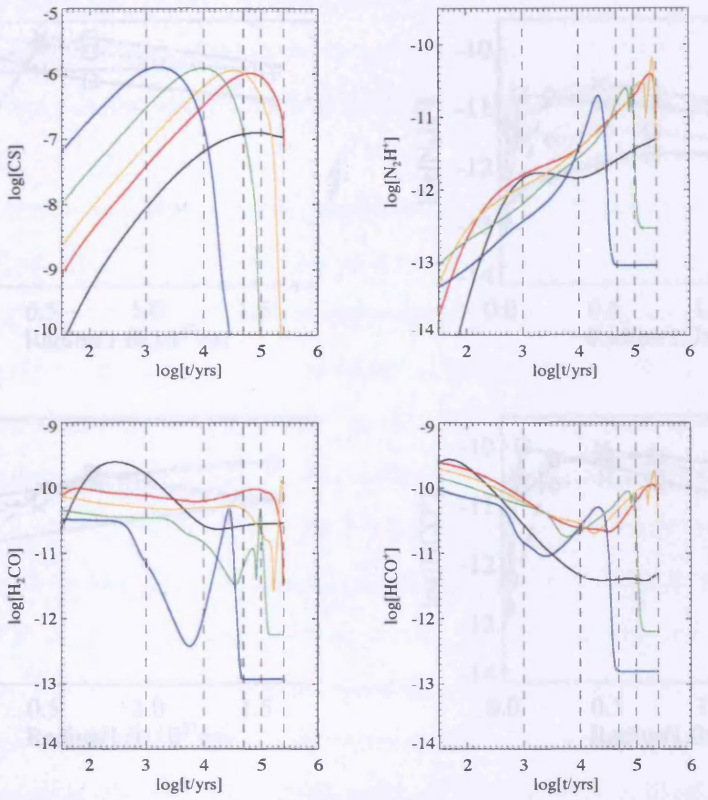

Figure 6.5: Fractional abundances of CS, N_2H^+, H_2CO and HCO^+ in each of the shells as a function time for the inside-out collapse model. The black, red, yellow, green and blue lines refer to the shells which start at $R_0 = 1.6 \times 10^{17}$, 7.4×10^{16}, 5.0×10^{16}, 2.5×10^{16} and 1.0×10^{16} cm respectively.

6.3.2 Inside-out collapse

Figure 6.5 shows the fractional abundances of CS, N_2H^+, H_2CO and HCO^+ for each test shell as they evolve with time, for the inside-out collapse model. The molecules appear to show much more complicated behaviour than for the ambipolar diffusion model for a number of reasons, such as: (i) the density of each shell actually experiences an initial *decrease* in density (see Figure 6.2), rather than monotonically increasing as in the ambipolar diffusion model; (ii) the initial density distribution is a singular isothermal sphere (rather than a uniform sphere in the ambipolar diffusion model), so the initial conditions of the shells cover a much larger range of densities and visual extinctions, and (iii) the chemical abundances do not start from equilibrium conditions.

The abundances in the outer shell (marked with pluses) show a very different evolution to the inner shells. This is because the outer shell does not collapse (the inside-out collapse solution

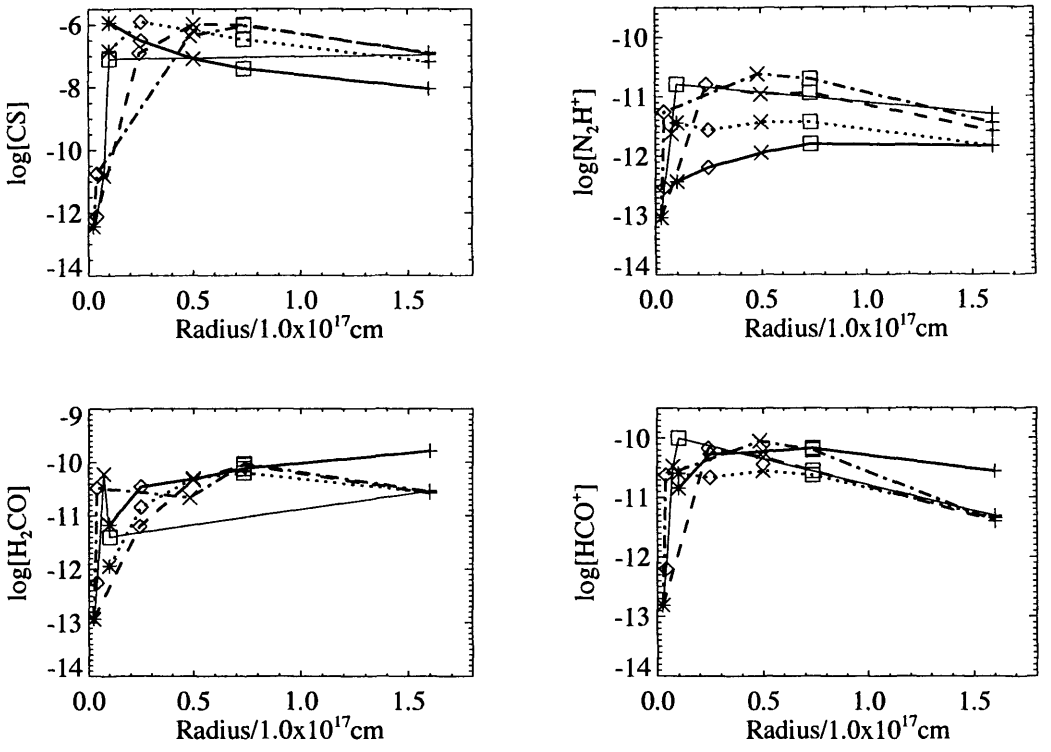

Figure 6.6: Fractional abundances of CS, N_2H^+, H_2CO and HCO^+ of as a function of radius for the inside-out collapse model at different times. The solid line is for 10^3 yr, the dotted line is for 10^4 yr, the dashed line is for 5×10^4 yr, the dot-dash line is for 10^5 yr and the thin solid line is for 2.5×10^5 yr. The pluses, squares, crosses, diamonds and asterisks represent the shells starting at 1.6×10^{17}, 7.4×10^{16}, 5.0×10^{16}, 2.5×10^{16} and 1.0×10^{16} cm respectively.

breaks down once the CEW hits the outer shell), so its A_v never exceeds the $A_{v,\mathrm{crit}}$ so that no freeze-out can occur in this shell. The profiles for the outer shell are therefore for pure gas-phase chemistry.

The inner shell, however, collapses very quickly and reaches its final density of $\sim 1.1 \times 10^7$ cm^{-3} at only $\sim 3.3 \times 10^4$ yr. It therefore remains at this high density for a long period of time and is able to reach equilibrium, but the molecular abundances are extremely depleted.

The depletion enhancements for the molecules N_2H^+, H_2CO for the inner shell are clearly seen by the sharp increase in abundance of these molecules just before they freeze-out. The enhancement in CS just before it freezes-out is not a depletion induced enhancement, as for the other molecules. In fact, when freeze-out is removed from the model CS is able to peak at a higher value at this time.

For the shells further out, the depletion enhanced peak occurs at later times. N_2H^+ and H_2CO

even show double peaks for the shells starting at 5×10^{16} and 2.5×10^{16} cm. The second peak occurs only when depletion is included in the model so is definitely due to the effects of depletion; the first peak occurs in gas-phase only chemistry but is not as high, so depletion is also a contributing factor to this peak.

Figure 6.6 shows the radial abundance distribution of the same species at 10^3, 10^4, 5×10^5, 10^5 and 2.5×10^5 yr. Most of the molecules peak in abundance towards the centre of the core, but N_2H^+ and H_2CO at 10^3 yr show a decrease towards the centre. As time increases, the peak abundance generally moves outwards, as the material in the centre of the core depletes. With the exception of the abundance profiles N_2H^+ at 10^3 and 10^4 yr, the peak abundance in the core remains approximately constant (although its position moves). For example, for HCO^+ the peak abundances are 7×10^{-11}, 3×10^{-11}, 7×10^{-11}, 9×10^{-11}, and 3×10^{-11} at 10^4, 5×10^5, 10^5 and 2.5×10^5 yr, which are all within one magnitude of each other. This is very different to the behaviour of HCO^+ in the ambipolar diffusion model, whose peak abundance is 4×10^{-12} at 10^5 yr and 1×10^{-10} at 10^6 yr, an increase of more than a factor of 30.

Another difference with the ambipolar diffusion model is that the abundance gradient is not as steep as in the ambipolar diffusion model (although note that the outer radii of the two models are different), which demonstrates the importance of photoreactions in the more diffuse core in the ambipolar diffusion model. These differences may have a large impact on the shapes and evolution of the line profiles, discussed in the next section.

6.4 Generating the line profiles

In this section we calculate the line profiles of CS, o-H_2CO and HCO^+ for the ambipolar diffusion and inside-out collapse models. N_2H^+ is also a commonly observed tracer for which we would like to generate line profiles, but because of its fine structure it is too complicated to model at this time.

As in Chapter 5, we use the radiative transfer model SMMOL to generate the line profiles, with the same telescope and source parameters as described in Section 5.2. At the adopted source distance of 140 pc, the model cores have angular sizes of $\sim 800''$ and $\sim 150''$ for the ambipolar diffusion model and inside-out model respectively, so are ~ 30 times and ~ 5 times larger than the largest beam size (which is $27.5''$ at 89 GHz). We have modelled the line profiles for beams going through the core centre only (i.e. we have not modelled any line profiles for beams offset from the core centre).

As before, SMMOL needs an input table giving the abundance, density, infall velocity, temper-

ature and turbulent velocity as a function of radius for a particular time. The abundance profiles are shown in Figures 6.4 and 6.6. To obtain the velocity and density profiles for the ambipolar diffusion model, we obtained the results from SR08. These are shown in Figure 6.7. As in Chapter 5, we have used a constant turbulent velocity of 0.12 km s^{-1} and a constant gas and dust temperature throughout the core of 10 K (see Section 5.2 for justification). For the inside-out collapse model, we derived the velocity and density at each radius using the results given in Table 2 of Shu (1977). These are shown in Figure 6.8.

6.4.1 Ambipolar diffusion line profiles

The line profiles for CS $J = 5 \rightarrow 4$, $3 \rightarrow 2$, $2 \rightarrow 1$, o-H_2CO $3_{12} \rightarrow 2_{11}$, $2_{12} \rightarrow 1_{11}$, and HCO^+ $J = 3 \rightarrow 2$ and $1 \rightarrow 0$ are shown in Figures 6.9, 6.10 and 6.11 for 1×10^5 yr, 5×10^5 yr and 1×10^6 yr. Note that the line profiles for 10^4 yr are not shown because they are the same as for 10^5 yr, because the abundances are so similar and the core is essentially static at these times.

In this model the turbulent velocity is 0.12 km s^{-1} and the thermal velocity is $v_{\rm th} = \sqrt{3kT/m(i)} \sim$ 0.075 km s^{-1} for CS at 10 K. At 1×10^5 yr the maximum infall velocity is 0.038 km s^{-1}, meaning that the line-width is dominated by turbulence and the core is essentially radiatively coupled. At 5×10^5 yr and 1×10^6 yr, however, the maximum infall velocity is 0.12 km s^{-1} and 0.31 km s^{-1} respectively. The infall velocity therefore begins to dominate the line-width, and at 10^6 yr the core centre and the core edge are radiatively decoupled because of the large velocity gradient. This can explain why the CS($5 \rightarrow 4$) line is only visible at 10^6 yr – it is only at this time that the photons emitted at this frequency can escape from the core centre without being absorbed by the outer material.

The line profiles for CS are very strongly self-absorbed. By 10^6 yr all transitions have an asymmetric profile with a stronger blue peak, which arises because the absorbing material (at the edge of the cloud, closest to the observer) is redshifted with respect to the inner material, therefore it preferentially absorbs the redshifted emission from the centre of the core rather than the blueshifted emission It can be seen that the absorption 'dip' is off centre, and it is most redshifted at 5×10^5 yr, where the minimum lies at ~ 0.1 km s^{-1}, which is approximately the velocity of the material in the outer regions of the core at this time (see Figure 6.7).

The depth of the dip remains approximately constant at all times because the CS abundance in the outer parts of the core ($R \gtrsim 5 \times 10^{17}$ cm), which is responsible for the absorption, is approximately constant as the core evolves.

For o-H_2CO, the line only becomes detectable at 10^6 yr. This is again possibly due to the fact

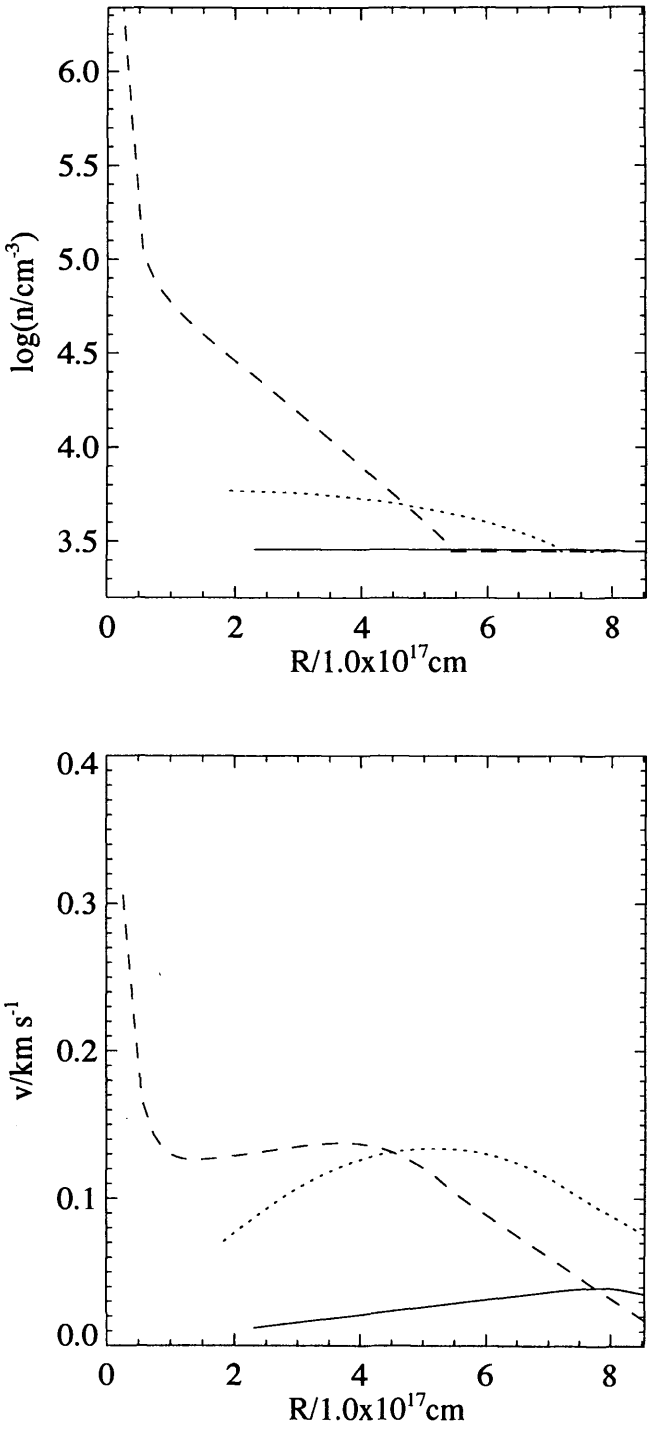

Figure 6.7: Density and velocity profiles for the ambipolar diffusion model at 1×10^5 yr (solid line), 5×10^5 yr (dotted line) and 1×10^6 yr (dashed line).

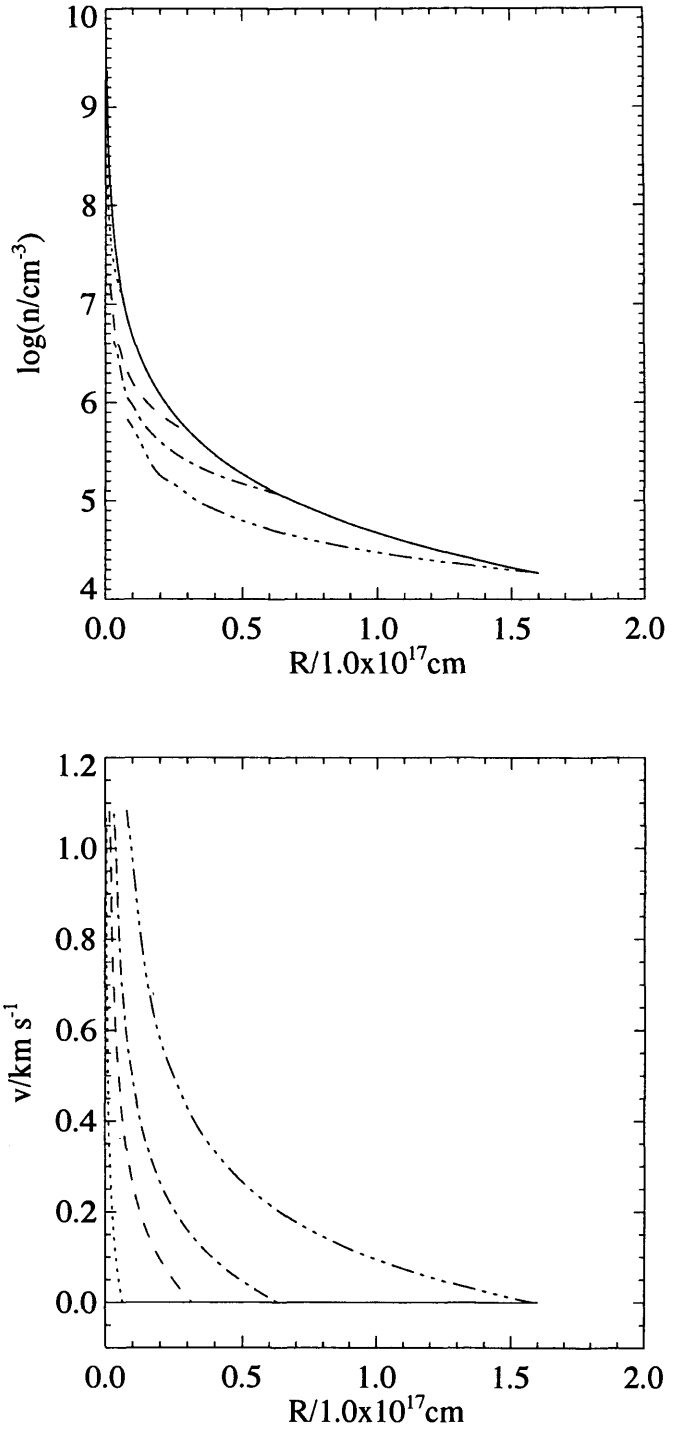

Figure 6.8: Density and velocity profiles for the inside-out collapse model at 1×10^3 yr (solid line), 10^4 yr (dotted line), 5×10^4 yr (dashed line) 1×10^5 yr (dot-dashed line) and 2.5×10^5 yr (triple dot-dashed line).

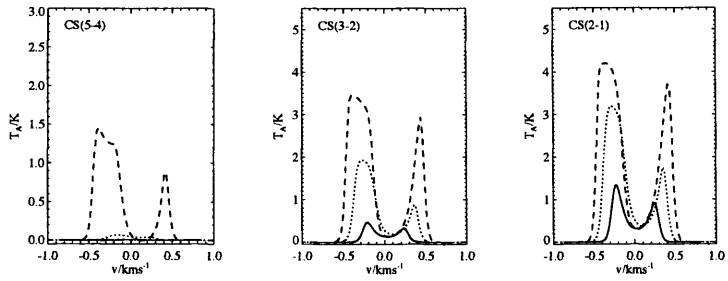

Figure 6.9: Line profiles of CS for transitions $J = 5 \rightarrow 4$, $3 \rightarrow 2$, and $2 \rightarrow 1$ for the ambipolar diffusion model at 1×10^5 yr (solid line), 5×10^5 yr (dotted line) and 1×10^6 yr (dashed line).

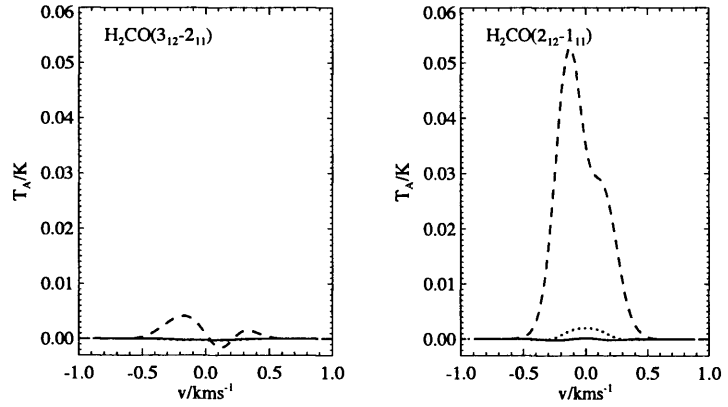

Figure 6.10: Line profiles of o-$H_2CO(3_{12} \rightarrow 2_{11})$ and $(2_{12} \rightarrow 1_{11})$ for the ambipolar diffusion model at 1×10^5 yr (solid line), 5×10^5 yr (dotted line) and 1×10^6 yr (dashed line).

that the core centre and edge are radiatively decoupled at this time, so the photons emitted from the centre of the core can escape. At this point the line is relatively broad for the transition $2_{12} \rightarrow 1_{11}$, with $\Delta v \sim 0.5$ km s^{-1} (estimated by eye). The H_2CO abundance at this time is very high in the centre of the core (see the thin solid line in Figure 6.4), and since the central material also has a high velocity (~ 0.3 km s^{-1}) this results in a broad line. The same behaviour is seen in the HCO^+ lines, although the predicted intensities at 10^6 yr are almost an order of magnitude higher for HCO^+ than for o-H_2CO. This implies that HCO^+ is a better tracer in these conditions than o-H_2CO, because it will be easier to detect.

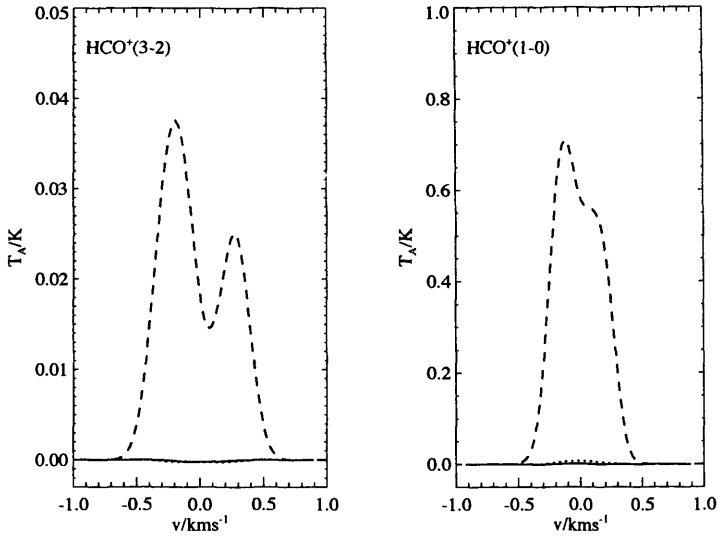

Figure 6.11: Line profiles for HCO^+ $J = 3 \rightarrow 2$ and $1 \rightarrow 0$ for the ambipolar diffusion model at 1×10^5 yr (solid line), 5×10^5 yr (dotted line) and 1×10^6 yr (dashed line).

6.4.1.1 Varying the temperature profiles for the ambipolar diffusion collapse

As in Section 5.3.3, we tested the effect of various different temperature profiles on the line profiles. The line profiles tested were (i) a typical temperature profile for a Class 0 source (taken from Zhou *et al.* (1990), see Section 5.13), (ii) a linear temperature profile which is warm in the centre (12 K) and cold on the outside (8 K), and (iii) a linear temperature profile which is cold (8 K) in the centre and warm (12 K) on the outside. The shape of the temperature profiles are shown in Figure 5.12, but note that we have scaled the temperature profiles to fit the core for this model, which has an outer radius of 8.54×10^{17} cm rather than 1.0×10^{17} cm, which was the core radius in the previous chapter. The results are shown in Figure 6.12 for the CS $J = 5 \rightarrow 4$, $3 \rightarrow 2$ and $2 \rightarrow 1$ lines at 5×10^5 yr.

For all the transitions with all the temperature profiles, the line profiles still show double peaks with blue asymmetries. The $J = 3 \rightarrow 2$ and $2 \rightarrow 1$ lines for the standard model (with a constant temperature profile at 10 K), and for temperature profiles (i) and (ii) all have similar peak intensities, but temperature profiles (i) and (ii) have slightly higher peak intensities for the $J = 5 \rightarrow 4$ lines than for the standard model. Temperature profile (iii) has noticeably lower intensities for all transitions compared to the other temperature profiles, especially for the blue peak whose peak intensity is approximately only 70% that of the other temperature profiles.

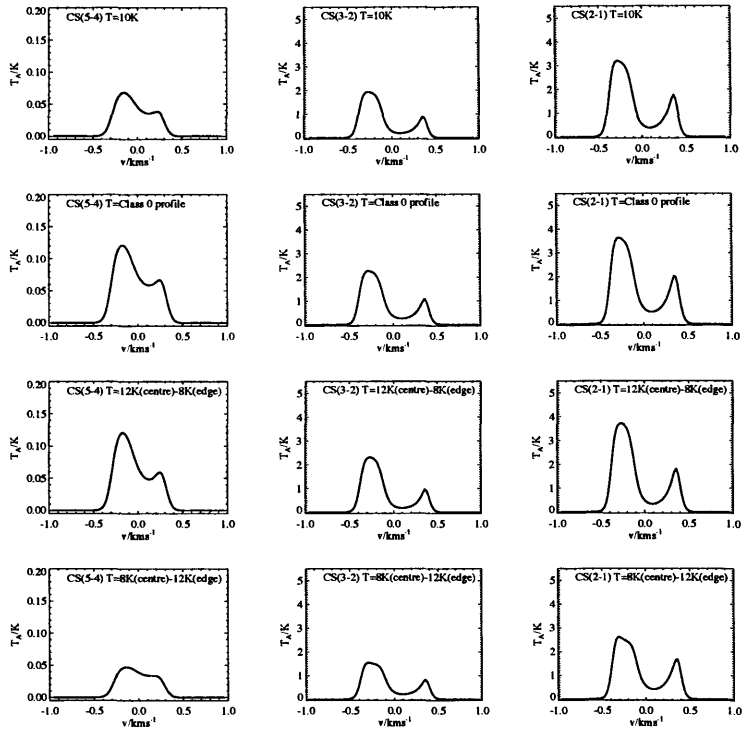

Figure 6.12: Plot of CS spectra at 5×10^5 yr for different temperature profiles, for ambipolar diffusion collapse. Top row: constant temperature (10K); second row: Class 0 temperature profile; third row: linear temperature profile which is 12 K in the centre and 8 K at the edge; bottom row: linear temperature profile which is 8 K in the centre and 12 K at the edge.

Table 6.2: The ratio of blue to red peak intensities for different temperature profiles for the ambipolar diffusion model at 5×10^5 yr.

Temp. profile	CS(5 → 4)	CS(3 → 2)	CS(2 → 1)
10 K	1.78	2.22	1.83
Class 0	1.81	2.11	1.81
12K centre - 8K edge	2.03	2.42	2.07
8K centre - 12K edge	1.40	1.89	1.57

This indicates that the central material contributes significantly to the emission in the blue peak, so when the temperature of the centre is reduced to 8 K as in temperature profile (iii), the intensity of the blue peak is drastically affected. The red peak appears to be less affected.

The ratios of the blue to red peak intensities are given in Table 6.2. The largest asymmetry for all lines is for the linear temperature profile which is 12 K in the centre, with an average blue to red ratio of 2.2, and the smallest asymmetry is for the linear temperature profile which is 8 K in the centre, which has an average blue to red ratio of only 1.6. Comparing this to Table 5.2, which gave the blue to red ratios for the modified free-fall collapse model in the previous chapter, it would appear that the ambipolar diffusion model in this chapter is much more sensitive to the temperature profiles than the modified free-fall collapse model. This is probably because the core centre in the ambipolar diffusion model is radiatively decoupled from the edge, so the resulting emission is much more dependent on the central temperatures.

6.4.2 Inside-out line profiles

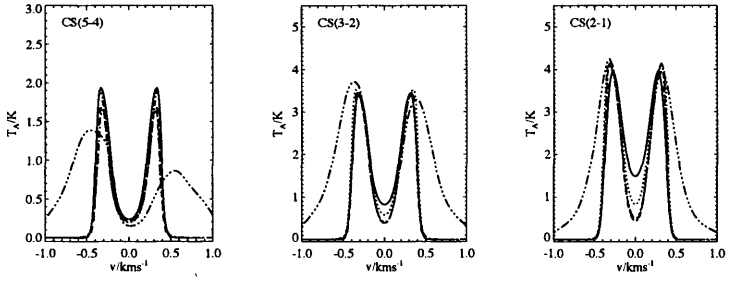

Figure 6.13: Line profiles of CS for transitions $J = 5 \rightarrow 4$, $3 \rightarrow 2$, and $2 \rightarrow 1$ for the inside-out collapse model at 1×10^3 yr (solid line), 1×10^4 yr (dotted line), 5×10^4 yr (dashed line), 1×10^5 yr (dot-dashed line) and 2.5×10^5 yr (triple dot-dashed line).

The line profiles are plotted for the same transitions as in Section 6.4.1, for the inside-out collapse model at 10^3, 10^4, 5×10^4, 10^5 and 2.5×10^5 yr. These are shown in Figures 6.13, 6.14 and 6.15.

As in Section 6.4.1, the turbulent velocity is 0.12 km s^{-1} and the thermal velocity is $v_{\rm th} \sim$ 0.075 km s^{-1} for CS at 10 K. At 1×10^3 yr the core is static (see Figure 6.8), and so turbulence dominates the line-width and the core is radiatively coupled. For $t \geq 10^4$ yr, the inner material in the core reaches velocities of $\sim$ 1.0 km s^{-1}, but the outer material remains static, meaning that the central regions of the core become radiatively decoupled from the outer static envelope.

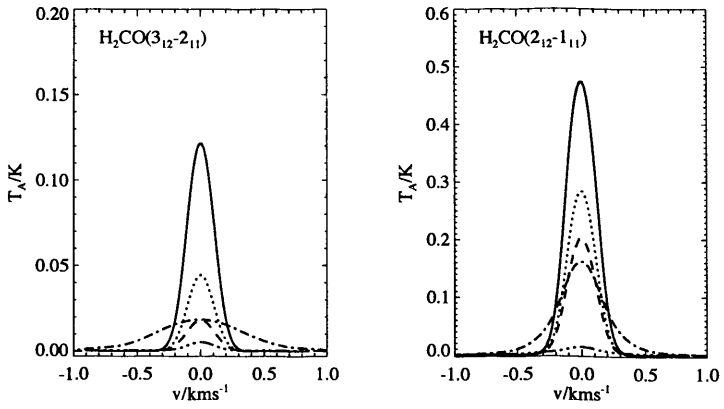

Figure 6.14: Line profiles of o-H_2CO for the transitions $3_{12} \rightarrow 2_{11}$ and $2_{12} \rightarrow 1_{11}$ for the inside-out collapse model at 1×10^3 yr (solid line), 1×10^4 yr (dotted line), 5×10^4 yr (dashed line), 1×10^5 yr (dot-dashed line) and 2.5×10^5 yr (triple dot-dashed line).

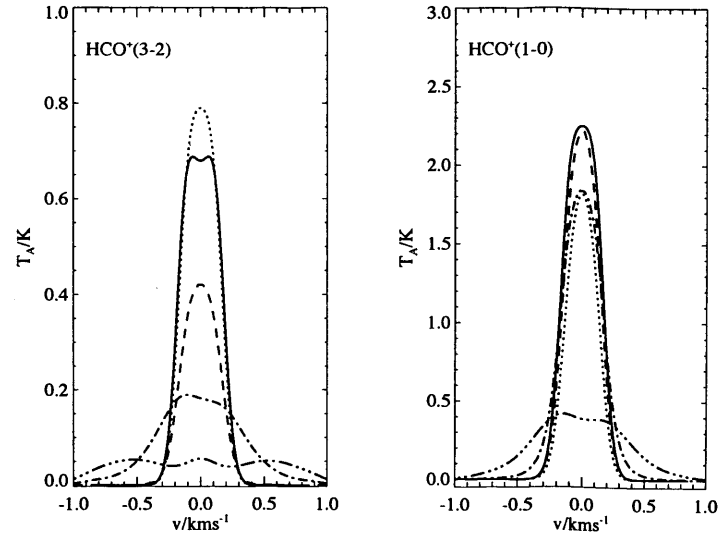

Figure 6.15: Line profiles of HCO^+ for the transitions $J = 3 \rightarrow 2$ and $1 \rightarrow 0$ for the inside-out collapse model at 1×10^3 yr (solid line), 1×10^4 yr (dotted line), 5×10^4 yr (dashed line), 1×10^5 yr (dot-dashed line) and 2.5×10^5 yr (triple dot-dashed line).

The line profiles for CS, plotted in Figure 6.13, show double peaked profiles which are approximately symmetric until the final time, 2.5×10^5 yr. The line-width remains approximately constant, with $\Delta v \sim 0.8$ km s^{-1} (this is approximately the total line-width, not the line-width for a single peak), also up until this time, but at 2.5×10^5 yr the line-width increases to $\Delta v \sim 1.0 - 1.5$ km s^{-1}, and the line profiles develop a blue asymmetry. This happens because at 2.5×10^5 yr the CEW has reached the boundary of the core, so there is no longer a static outer envelope. The outer material responsible for the absorption is now redshifted as it falls towards the core, causing more absorption of emission emanating from the central redshifted material than from the central blue shifted material. The minimum in the absorption dip is slightly redshifted at this time, at ~ 0.02 km s^{-1}, whereas for all the previous times it is exactly at 0.0 km s^{-1}, which supports this explanation.

Comparing this behaviour to the CS line profiles of the modified free-fall collapse model in Section 5.3 in the previous chapter, and the ambipolar diffusion model in Section 6.4.1, shows that if the outer material in the core is not static, strong blue asymmetries can appear without the need for a temperature gradient.

Another interesting feature of these lines is that the depth of the absorption dip in the $J = 3 \rightarrow 2$ and $2 \rightarrow 1$ lines increases as core evolves, up until 5×10^4 yr. After this time the depth remains approximately constant. This is because, as can be seen in Figure 6.6, the abundance of CS in the outer regions of the core ($R \gtrsim 5 \times 10^{16}$ cm) steadily increases from $\sim 10^{-8}$ to 10^{-7} up until this time, and so the amount of absorbing material increases.

The emission from o-H_2CO, shown in Figure 6.14 is single peaked at all times, and has a very narrow line-width ($\Delta v \sim 0.2 - 0.3$ km s^{-1}) up until 1×10^5 yr, where it increases to ~ 0.8 km s^{-1} for $3_{12} \rightarrow 2_{11}$ and ~ 0.4 km s^{-1} for $(2_{12} - 1_{11})$. This is because at this time a large proportion of the core is now infalling – the collapse expansion wave has reached a radius of 6.3×10^{16} cm, which is nearly half-way through the core. By 2.5×10^5 yr the o-H_2CO has depleted, so the predicted line intensities are very weak. It would appear that the 'depletion enhancement' of H_2CO at 2.5×10^5 yr, which can be seen in Figure 6.6 (plotted with the thin solid line), at a radius of $\sim 0.07 \times 10^{17}$ cm, is not enough to increase the line intensity.

The o-H_2CO emission in this model is generally much stronger than for the ambipolar diffusion model, shown in Figure 6.10. This is probably because the abundance of H_2CO at the edge of the core for the ambipolar diffusion model is only $\sim 10^{-12}$, but in the inside-out collapse model the abundance at the edge is much higher ($\sim 10^{-11} - 10^{-10}$). Since the line is probably optically thin with no self-absorption, the extra H_2CO in the outer radii of the core in the inside-out model can contribute to the emission (rather than absorption), making the line stronger. The reason for the

abundance difference at the edge of the cores in the two models is that the ambipolar diffusion core has a lower density at the edge, therefore a lower visual extinction, so photodissociation of H_2CO is more efficient than for the core in the inside-out collapse model.

The HCO^+ emission, shown in Figure 6.15, is also generally much narrower than the CS emission, with line-widths of $\sim 0.3 - 0.4$ km s^{-1} for both the $J = 3 \rightarrow 2$ and $1 \rightarrow 0$ lines, up until 1×10^5 yr. At this time the line-width of $HCO^+(3 \rightarrow 2)$ increases to ~ 0.7 km s^{-1}, and increases even further, to ~ 1.7 km s^{-1} at 2.5×10^5 yr. The line-width of $HCO^+(1 \rightarrow 0)$ is still narrow at 1×10^5 yr, but increases to ~ 0.9 km s^{-1} at 2.5×10^5 yr. This difference in behaviour could possibly be because the emission from the different transitions could be coming from different parts of the core, due to their different opacities.

As for the ambipolar diffusion model, the intensity of the HCO^+ lines are approximately an order of magnitude higher than the o-H_2CO lines. The HCO^+ lines tend to be single peaked, although $HCO^+(3 \rightarrow 2)$ at 10^3 yr shows a very small double peak, and signs of blue asymmetry start to appear in $HCO^+(3 \rightarrow 2)$ at 1×10^5 yr and $HCO^+(1 \rightarrow 0)$ at 2.5×10^5 yr. The peak intensities for both the HCO^+ transitions shown tend to decrease as the core evolves, although at 5×10^4 yr, the peak intensity of $HCO^+(1 \rightarrow 0)$ (plotted with the dashed line in Figure 6.15) increases to almost the original value it had at 1×10^3 yr (2.2 K). This increase is due to the depletion enhancement of HCO^+ experienced in three of the shells at this time (see Figure 6.6).

6.4.2.1 Varying the temperature profiles for the inside-out collapse

It is believed that in order to have asymmetric line profiles with a stronger blue peak for inside-out collapse, a temperature gradient is needed (Zhou *et al.* 1993). This is because, unlike in the modified free-fall collapse in Chapter 5 and the ambipolar diffusion collapse in Section 6.4.1, the outer regions of the core in the inside-out model are static and therefore not preferentially absorbing the red emission. If we consider the region inside the CEW, for purely radial infall, the red emission comes from the hemisphere which is closest to the observer and the blue emission comes from the hemisphere which is farthest. If there is a temperature gradient such that the material in the centre is warmest, then the observer will see the coolest side of the red hemisphere and the hottest side of the blue hemisphere, resulting in stronger blue emission.

The line profiles of CS in Figure 6.13 are all symmetric (apart from at 2.5×10^5 yr when there is no static envelope), which is to be expected for a constant temperature profile. However, we also found that when generating the CS line profiles for this model using the temperature profiles described in Section 6.4.1.1, the line profiles remained symmetric for all times $\leq 1 \times 10^5$ yr, even

when the core centre was 4 K hotter than the core edge [for temperature profile (ii)]. Rawlings & Yates (2001) also found that CS exhibited symmetric line profiles for inside-out collapse, and attributed this to the depletion of CS in the central regions, so this is probably also the case for our model .

We have also tested the effect of the temperature profiles listed in Section 6.4.1.1 for the CS $J = 5 \rightarrow 4$, $3 \rightarrow 2$ and $2 \rightarrow 1$ lines at 2.5×10^5 yr, when the lines profiles are asymmetric even for the constant temperature profile. The results are shown in Figure 6.16, and the ratios of blue to red peak intensities are given in Table 6.3. For the $3 \rightarrow 2$ and $2 \rightarrow 1$ lines, the blue to red ratio is highest for the linear temperature profile which is 12 K in the centre and 8 K at the edge [temperature profile (ii)], and for the $5 \rightarrow 4$ line the ratio is highest for the Class 0 temperature profile, which also has a temperature increase in the centre. For the linear temperature profile which is 8 K in the centre and 12 K at the edge, the $3 \rightarrow 2$ and $2 \rightarrow 1$ lines begin to show a red asymmetry. This shows that temperature profiles which have warmer centres can increase the blue asymmetry of the line profiles, whereas the asymmetry can be reversed for temperature profiles which are cooler in the centre.

Comparing Table 6.3 to Table 5.2 shows that inside-out collapse model at late times is more sensitive to the temperature profile than the modified free-fall collapse model, probably because, like the ambipolar diffusion model, the core centre is radiatively decoupled from the core edge, so the blue emission from the central regions is able to escape. However, comparing Table 6.3 to Table 6.2 shows the inside-out collapse model is less sensitive to the temperature profile than the ambipolar diffusion model. This is probably because at 2.5×10^5 yr, CS is more depleted in the inside-out collapse model than in the ambipolar diffusion model at 5×10^5 yr (which was the time for which we tested the temperature profiles in the ambipolar diffusion model).

Table 6.3: The ratio of blue to red peak intensities for different temperature profiles for the inside-out collapse at 2.5×10^5 yr.

Temp. profile	CS($5 \rightarrow 4$)	CS($3 \rightarrow 2$)	CS($2 \rightarrow 1$)
10 K	1.61	1.13	1.07
Class 0	1.68	1.11	1.00
12K centre - 8K edge	1.65	1.30	1.26
8K centre - 12K edge	1.33	0.88	0.85

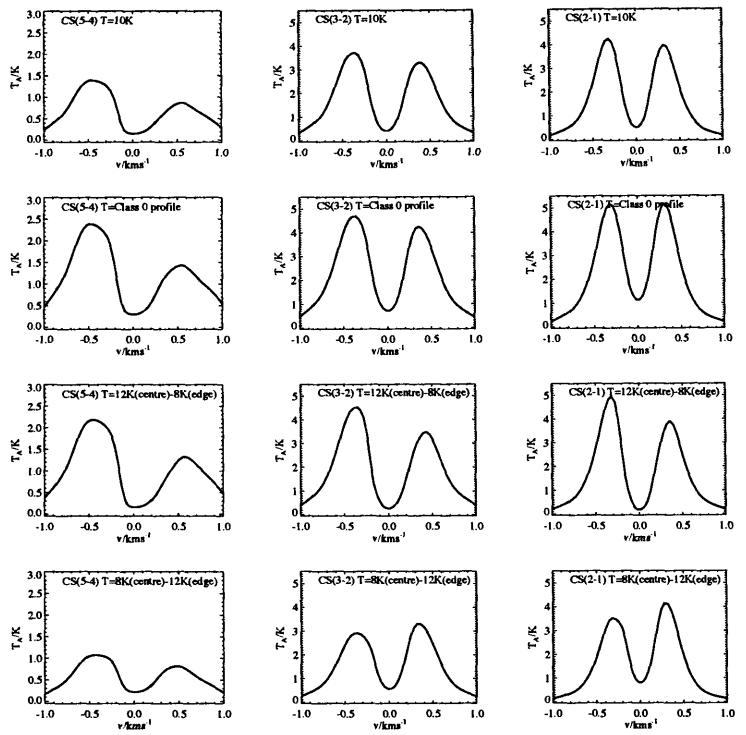

Figure 6.16: Plot of CS spectra for 2.5×10^5 yr for different temperature profiles, for inside-out collapse. Top row: constant temperature (10K); second row: Class 0 temperature profile; third row: linear temperature profile which is 12 K in the centre and 8 K at the edge; bottom row: linear temperature profile which is 8 K in the centre and 12 K at the edge.

6.5 Discussion and conclusions

In this chapter we have modelled the line profiles of several transitions of CS, o-H_2CO and HCO^+ at various times for core undergoing collapse by ambipolar diffusion and the inside-out collapse models, with the ultimate aim of finding observational diagnostics to discriminate between these collapse models. We have found that the shapes and intensities of the line profiles are strongly affected by many factors, such as the abundance profile of the molecule (which itself is strongly dependent of the density profile of the core), depletion, the initial chemical conditions, the velocity profile of the core, and the temperature gradient. Since many of these factors are poorly constrained, it is impossible to predict what the emission line for a particular molecule undergoing ambipolar diffusion or inside-out collapse at a particular time will look like. However, we have been able to draw some general conclusions, discussed below.

The transitions of CS which we have modelled only appear to show blue asymmetries if the core

has extended inward motions (which occur in the ambipolar diffusion model and at 2.5×10^5 yr for the inside-out collapse model, when the CEW has reached the core edge). It appears that the inside-out collapse model cannot produce blue asymmetries for CS even with large temperature gradients (apart from at 2.5×10^5 yr), because of the large degree of depletion in the core centre.

Previous studies (Zhou *et al.* 1993, e.g.) have claimed that observations of CS line profiles with blue asymmetries could be well fitted by the inside-out collapse model, but in these studies the CS abundance was assumed to be constant across the core. Since our models imply that extended infall motions are needed to produce the blue asymmetry for CS, this would mean that the inside-out model is actually *inconsistent* with these observations of CS. This is a very important conclusion, because it appears to overthrow a long accepted interpretation. It would be worth investigating whether the observations of CS from Zhou *et al.* (1993) could be reproduced by the ambipolar diffusion model instead, or even the modified free-fall collapse model from Chapter 5.

For both the ambipolar diffusion model and the inside-out collapse model, the predicted lines of o-H_2CO and HCO^+ fail to produce double peaks, whereas previous models of HCO^+ in cores collapsing by the inside-out model have been able to produce the double peaks (Rawlings & Yates 2001; Tsamis *et al.* 2008). This is because our chemical model predicts HCO^+ abundances of only $10^{-12} - 10^{-10}$, compared to $\sim 10^{-10} - 10^{-8}$ in Rawlings & Yates (2001). This could be due to a number of factors, for example, (i) we have used a lower temperature to Rawlings & Yates (2001), who used the temperature profile for a Class 0 source to work out the abundances in their chemical model; (ii) we have used a sodium abundance of 5.2×10^{-6}, whereas Rawlings & Yates (2001) only used a sodium abundance of 3.5×10^{-7}, which means that the electron abundance in our model may be higher (sodium has a low ionisation potential so is easily ionised), which could increase the rate of recombination of HCO^+; and (iii) we have used a reaction set taken from the RATE06 database, whereas Rawlings & Yates (2001) used a reaction set from the older UMIST astrochemistry databases, RATE90 and RATE95. This shows the sensitivity of the line profiles to the predicted abundances from the chemical model, and demonstrates the fact that when fitting a model core to observations, the full range of parameter space should be investigated before any model can be safely ruled out.

CHAPTER 7

DEUTERIUM CHEMISTRY IN COLLAPSING CORES

7.1 Introduction

The original motivation of the following work was to investigate whether the ion-neutral drift (ambipolar diffusion) associated with a core contracting in the presence of a magnetic field would have an observable effect upon the chemical abundances inside the core.

If this were to be the case, chemical abundances could be used as evidence as to whether ambipolar diffusion is occurring in star forming cores, helping to settle the debate on whether star formation is a slow process controlled by magnetic fields, or whether it is rapid and cores can collapse dynamically, bypassing the ambipolar diffusion phase.

The effect of the ion-neutral drift is to increase the rate of ion-neutral collisions, therefore increasing the rate of ion-neutral reactions. To quantify this non-thermal effect, we use the same method as employed in papers such as Draine (1980), Flower *et al.* (1985) and Federman *et al.* (1996), which is to define an effective temperature, $T_{\rm eff}$, to calculate the rate of ion-neutral reactions. The effective temperature is given by

$$\frac{3}{2}kT_{\rm eff} = \frac{3}{2}kT_{\rm kin} + \frac{1}{2}\mu v_{\rm d}^2 \tag{7.1}$$

where $T_{\rm kin}$ is the kinetic temperature of the gas, μ is the reduced mass of the ion and molecule involved in the reaction, $v_{\rm d}$ is the ion-neutral drift velocity and k is Boltzmann's constant. The factor of 3 multiplying the term on the left hand side and the first term on the right hand side of

equation (7.1) takes into account the fact that the thermal motions are three-dimensional whereas the ion-neutral drift is only in one dimension.

Previous studies of the diffuse interstellar medium have shown that ion-neutral drift can have a large effect on the molecule CH^+ (e.g. Federman *et al.* 1996). This is because the reaction

$$C^+ + H_2 \rightarrow CH^+ + H \tag{7.2}$$

has an energy barrier of $\Delta E = 4640$ K, so can be 'initiated' once the effective temperature reaches ~ 420 K, which corresponds to a drift velocity of 2.2 km s^{-1}.

However, in dark cores which are contracting through ambipolar diffusion, the evolution of the core is quasi-static, and drift velocities are expected to remain subsonic. CH^+, therefore, is unlikely to be affected in this situation.

One reaction that is more likely to be affected is the destruction of the species H_2D^+ by H_2, which has an energy barrier of only 220 K. As we explain later, this reaction has important consequences for the level of deuterium fractionation within dark cores. Because of this, deuterium chemistry seems the best place to start when looking for signatures of ambipolar diffusion in collapsing cores, which is why we have included chemical reactions involving molecules with deuterium atoms in our model. Below we discuss why deuterium chemistry is important in dark cores, and the significance of the H_2D^+ ion.

7.1.1 Deuterium chemistry in dark cores and the H_2D^+ ion

Although the interstellar ratio of deuterium to hydrogen atoms is only $\sim 1.5 \times 10^{-5}$, it has been observed that the degree of deuterium fractionation, which is the abundance ratio of a molecule containing a deuterium atom (XD) to the equivalent molecule with a hydrogen atom (XH), is extremely high in cold, dark cores. For example, in the dark cloud L134N, Tiné *et al.* (2000) found that $[NH_2D]/[NH_3] \sim 0.1$, $[N_2D^+]/[N_2H^+] \sim 0.35$ and $[DCO^+]/[HCO^+] \sim 0.18$. In the dense core TMC1-N, the same authors found the ratios to be $[NH_2D]/[NH_3] \sim 0.02$, $[N_2D^+]/[N_2H^+] \sim 0.08$ and $[DCO^+]/[HCO^+] \sim 0.02$, which are much less than in L134N but still well above the interstellar D/H ratio.

Furthermore, as a dense core evolves and heavy species such as CO freeze out onto dust grains, only molecules made up of the lighter atoms H, He and D can remain the in the gas-phase. The only species remaining which have rotational spectra in the submillimetre region and are therefore observable will be H_2D^+ and D_2H^+ (Roberts & Millar 2006). Deuterium chemistry, and the way it

responds to the physical environment, is therefore very important in dark cores, especially for the later stages in star formation when all other detectable molecules have frozen out.

The species H_2D^+ is the main ion responsible for transferring deuterium atoms into other molecules, causing the high levels of fractionation observed in dark cores. H_2D^+, like its analogue H_3^+, has a low proton affinity (see Section 2.2) and so is very important in ion-molecule reaction networks. In the same way that H_3^+ initiates chains of ion-molecule reactions, starting with the reaction

$$H_3^+ + X \rightarrow XH^+ + H_2, \tag{7.3}$$

H_2D^+ can initiate an equivalent chain of reactions, but now involving a deuterium atom:

$$H_2D^+ + X \rightarrow XD^+ + HD. \tag{7.4}$$

Further reactions of the molecular ion XD^+ with other neutral molecules spreads deuterium fractionation throughout the chemical network, leading to a wide range of abundant, deuterated molecules.

As mentioned above, deuterium chemistry in dark cores is very sensitive to temperature. This can be explained by considering the production and destruction of H_2D^+. H_2D^+ is produced by the reversible reaction

$$H_3^+ + HD \rightleftharpoons H_2D^+ + H_2, \tag{7.5}$$

where the forward reaction rate is $k_f = 1.7 \times 10^{-9}$ cm^3 s^{-1}, but the backwards rate has an activation energy barrier, ΔE, and is given by $k_b = k_f \exp(-\Delta E/T)$ cm^3 s^{-1}. ΔE has the value 220 K for $T < 100$ K, but falls to 130 K for $T > 100$ K (Roberts & Millar 2000*b*).

Because of the activation barrier for the backwards reaction of (7.5), the destruction of H_2D^+ at temperatures less than ~ 25 K is effectively quenched, so H_2D^+ can react with other molecules causing high deuterium fractionation throughout the core. However, once the temperature is above this value, H_2D^+ is rapidly destroyed by H_2, deuterium atoms become locked into the less reactive HD molecules, and deuterium fractionation is reduced.

If the ion-neutral drift velocity in the core is high enough, the increase in the effective temperature for reaction (7.5) in the backwards direction can overcome the activation energy barrier, causing the destruction of the H_2D^+ ion and drastically affecting deuterium fractionation. In this chapter we investigate the effect upon the deuterium chemistry in a core undergoing collapse in a magnetic field, in particular looking to see if ion-neutral drift can produce a detectable effect,

and to investigate whether deuterium chemistry can provide any information on the dynamics of the core collapse. In Section 7.2 we talk about the physical and chemical model we have used, in Section 7.3 we give the results and the discussion and conclusions are given in Section 7.4

7.2 The model

We have modelled the chemical evolution of a parcel of gas in a prestellar core as it collapses to form a protostar, with the collapse being hindered by magnetic fields. The density and the ion-neutral drift velocity of the gas as a function of time are taken from the results of the multipoint ambipolar diffusion collapse models of Stace & Rawlings (2008, hereafter SR08), which modelled the collapse of an 7.68 $M_{\odot}$ core with a total radius of 8.54×10^{17} cm. These models are described in more detail in Chapter 6 (see Section 6.1.1). Since we are using a single point model, we have tabulated the solutions for $n_{\rm H}(t)$ and $v_{\rm d}(t)$ for a single 'shell' which starts at a radius about halfway through the core.

The density and drift velocity as a function of time are shown with the solid line in Figure 7.1. The magnetic field strength in the 'standard' model was 8 μG, and for this model the density ranges from 2.8×10^3 cm^{-3} to 8.1×10^4 cm^{-3}. The initial A_v was 1.0 mag and varied according to equation (4.8). The final density was reached at 1.07 Myr.

Observations of magnetic fields in dark cores have shown that for ~ 1 $M_{\odot}$ cores, the magnetic field strength can be greater than $10^2 \mu$G. For example, the cores L183 ($M \sim 1.0$ $M_{\odot}$), L1544 ($M \sim 1.3$ $M_{\odot}$) and L43 ($M \sim 1.7$ $M_{\odot}$) have estimated magnetic field strengths of 80 μG, 140 μG and 160 μG respectively (Crutcher *et al.* 2004). The magnetic field in our model is only 8μG, which may seem inconsistent with the observations, but this is because we model the collapse starting from a much more diffuse state. By ~ 1 Myr when the core has evolved to a similar state to the observed cores, the magnetic field strength has increased to $\sim 48\mu$G.

We have also modelled the chemistry in a shell of gas collapsing at a higher initial magnetic field of 20μG. For this model we used the density and drift velocity (again from SR08's models) of the shell which enclosed a mass of ~ 1 $M_{\odot}$ (which also starts at a radius which is approximately half the outer radius), and whose final magnetic field strength was 80μG, to be consistent with the observations mentioned above. For this model, the final density is 3.5×10^5 cm^{-3} and the collapse takes 4.48×10^6 yr, much longer than for the 8 μG model. The density and drift velocity for this model are shown with the dotted line in Figure 7.1.

The gas-phase chemical model was based on the model used by Roberts & Millar (2000*b*), and

consists of 287 gas-phase species in a network of 5258 gas-phase reactions. The species are made up of the elements H, C, N, S, He, Fe, Si and contain up to six carbon atoms. Singly deuterated isotopes of each species are included, as well as the doubly deuterated species D_2CO and D_2CO^+. The full species list is given in Table 7.1. The initial elemental abundances and the initial HD abundance (the reservoir of deuterium) were also taken from Roberts & Millar (2000*b*), and are given in Table 7.2.

Table 7.1: List of species

H	H^+	D	D^+	He	He^+	C	C^+
N	N^+	O	O^+	H_2	HD	H_2^+	HD^+
CO	CO^+	Si	Si^+	CH	CH^+	CD	CD^+
NH	NH^+	ND	ND^+	OH	OH^+	OD	OD^+
C_2	C_2^+	NO	NO^+	O_2	O_2^+	CH_2	CHD
CH_2^+	CHD^+	NH_2	NH_2^+	NHD	NHD^+	H_2O	H_2O^+
HDO	HDO^+	HCO	DCO	HCO^+	DCO^+	HCN	HCN^+
DCN	DCN^+	HNC	DNC	C_2H	C_2H^+	C_2D	C_2D^+
C_3	C_3^+	CO_2	CH_3	CH_3^+	CH_2D	CH_2D^+	NH_3
NH_3^+	NH_2D	NH_2D^+	C_2H_2	C_2HD	H_2CO	H_2CO^+	HDCO
$HDCO^+$	C_3H	C_3D	C_3H^+	C_3D^+	CH_4	CH_3D	CH_4^+
CH_3D^+	C_2H_3	$C_2H_2^+$	C_2HD^+	C_2H_2D	$C_2H_3^+$	$C_2H_2D^+$	C_3H_2
C_3HD	$C_3H_2^+$	C_3HD^+	HC_3N	HC_3N^+	DC_3N	DC_3N^+	CH_3OH
H_3CO^+	CH_3OD	CH_2DOH	H_2DCO^+	CH_3CN	CH_3CN^+	CH_2DCN^+	CH_2DCN
CN	N_2	N_2^+	CN^+	CO_2^+	C_3N	C_3N^+	CH_2CO
CHDCO	CCN^+	CNC^+	H_2NC^+	$HDNC^+$	C_4^+	CH_2CO^+	$CHDCO^+$
C_4N^+	C_4H^+	C_4D^+	N_2H^+	N_2D^+	$HCNH^+$	$DCNH^+$	$HCND^+$
CH_3OH^+	CH_2DOH^+	CH_3OD^+	H_3^+	H_2D^+	H_3O^+	H_2DO^+	HCO_2^+
DCO_2^+	CH_5^+	CH_4D^+	$C_2H_4^+$	$C_2H_3D^+$	NH_4^+	NH_3D^+	$CH_3OH_2^+$
CH_3OHD^+	$CH_2DOH_2^+$	$C_3H_3^+$	CH_3CO^+	CH_2DCO^+	$H_2C_3N^+$	HDC_3N^+	$C_3H_2D^+$
CH_3CNH^+	CH_3CND^+	CH_2DCNH^+	HC_2O^+	DC_2O^+	C_2O	C_2O^+	Fe
Fe^+	CH_3CHO	CH_3CHO^+	CH_2DCHO	CH_2DCHO^+	CH_3OCH_3	$CH_3OCH_3^+$	$CH_3OCH_2D^+$
CH_3OCH_2D	$HCOOCH_3$	$HCOOCH_3^+$	$HCOOCH_2D^+$	$HCOOCH_2D$	$CH_3CH_2O^+$	$CH_2DCH_2O^+$	$CH_3OHCH_3^+$
$CH_3OHCH_2D^+$	$CH_2OOCH_3^+$	$CH_2OOCH_2D^+$	$C_2H_5^+$	$C_2H_4D^+$	C_2H_4	C_2H_3D	$COOCH_3^+$
$CH_2DOOCH_2^+$	C_2H_5	CH_3CHD	$C_2H_6^+$	$C_2H_5D^+$	C_2H_6	C_2H_5D	$C_2H_7^+$
$C_2H_6D^+$	$H_3OCH_2^+$	$CH_2DOCH_2^+$	$CH_2NH_2^+$	$CHDNH_2^+$	CH_2NHD^+	H_2NH	CHDNH
CH_2ND	S	S^+	S	HS^+	DS	DS^+	CS
S^+	SO	SO^+	SO_2	SO_2^+	H_2S	H_2S^+	HDS
HDS^+	OCS	H_2CS	H_2CS^+	HDCS	$HDCS^+$	HCS^+	CS^+
OCS^+	H_3CS^+	H_2DCS^+	$HOCS^+$	OCS^+	H_3S^+	H_2DS^+	HSO^+
DSO^+	HCS	DCS	HSO_2^+	DSO_2^+	C_2S	C_2S^+	HC_2S^+
DC_2S^+	C_4H_2	$C_4H_2^+$	C_4HD	C_4HD^+	$C_4H_3^+$	$C_4H_2D^+$	C_4H
C_4D	C_4	C_5H^+	C_5D^+	C_3H_4	C_3H_3D	$C_3H_5^+$	$C_3H_4D^+$
C_5N	HC_5N	DC_5N	C_5	C_6^+	HC_5N^+	DC_5N^+	$H_2C_5N^+$
HDC_5N^+	$C_5H_3^+$	$C_5H_2D^+$	C_5H	C_5D	C_5H_2	C_5HD	$C_5H_2^+$
C_5HD^+	C_5N^+	$C_3H_4^+$	$C_3H_3D^+$	C_3H_3	D_2CO	HD_2CO^+	

As in Chapters 3, 4 and 6, the chemical reaction network consisted of two body reactions, cosmic ray ionisation, at a rate of 1.3×10^{-17} s^{-1} for $H_2 \rightarrow H_2^+$, cosmic ray induced photoreactions and interstellar photoreactions which take into account the extinction of the interstellar radiation field. Both H_2 and HD formation on grains were included, at the rate given by equation (4.1).

Table 7.2: Initial abundances (taken from Roberts & Millar 2000*b*).

For HD the sticking probability is taken to be $(T/200.0 + 1)^{-2}$ (Buch & Zhang 1991). The kinetic temperature was kept at 10 K throughout the collapse. Freeze-out of species onto dust grains was included once the A_v was greater than $A_{\rm v,crit} = 4.86$ magnitudes, at the rate given by equation (2.2.2) with $S(i) = 0.3$. The value of $A_{\rm v,crit}$ was chosen so that freeze-out would occur for $n_{\rm H} \geq 3 \times 10^4$ cm^{-3}, which is roughly the density above which freeze-out is observed (Bergin & Tafalla 2007). This value is consistent with the values of $A_{v,\rm crit}$ deduced from observations for the Taurus, Corona Australis and Serpens molecular clouds (see Section 2.2.2). We have chosen not to include desorption in this model because we want to isolate the effects of ambipolar diffusion on the deuterium chemistry from the effects of surface chemistry.

Some of the chemical reactions we have included cannot be approximated by a single Arrhenius-type formula ($k = \alpha(T/300.0)^{\beta} \exp\{-\gamma/T\}$, see Section 2.3). Since we are particularly interested in how the chemistry responds to ion-neutral drift velocities, and hence different effective temperatures, we needed to make sure the correct values of the Arrhenius constants are used at a particular $T_{\rm eff}$. We have therefore updated the rates of these reactions to those given in the latest UMIST astrochemistry database, RATE06 (Woodall *et al.* 2007). The rates we have modified are summarised in Tables 7.3, 7.4 and 7.5.

The model was run in two stages; in the first stage the core was held static at a density of 2.8×10^3 cm^{-3} for 10^8 yr, until the species reached chemical equilibrium, and in the second stage the core collapsed according to the ambipolar diffusion models of SR08. Since $A_v < A_{v,\rm crit}$ for the first stage, there is no depletion at the beginning of the second stage. As discussed in Chapters 4 and 5, the initial abundances can affect the results of the model, but since we have already assumed

Table 7.3: Reaction rates which have been updated to the RATE06 values.

Reaction	α	β	γ	Temperature range
$O + HS \rightarrow SO + H$	0.00	0.00	0.0	$T < 298$
	8.25×10^{-11}	0.17	-254.0	$T \geq 298$
$O + DS \rightarrow SO + D$	0.00	0.00	0.0	$T < 298$
	8.25×10^{-11}	0.17	-254.0	$T \geq 298$
$OH + H_2CO \rightarrow H_2O + HCO$	0.00	0.00	0.0	$T < 200$
	2.22×10^{-12}	1.42	-416.0	$T \geq 200$
$OD + H_2CO \rightarrow HDO + HCO$	0.00	0.00	0.0	$T < 200$
	1.48×10^{-12}	1.42	-416.0	$T \geq 200$
$OD + H_2CO \rightarrow H_2O + DCO$	0.00	0.00	0.0	$T < 200$
	7.40×10^{-13}	1.42	-416.0	$T \geq 200$
$OH + HDCO \rightarrow HDO + HCO$	0.00	0.00	0.0	$T < 200$
	1.48×10^{-12}	1.42	-416.0	$T \geq 200$
$OH + HDCO \rightarrow H_2O + DCO$	0.00	0.00	0.0	$T < 200$
	7.40×10^{-13}	1.42	-416.0	$T \geq 200$
$O_2 + C_2H_3 \rightarrow H_2CO + HCO$	0.00	0.00	0.0	$T < 200$
	4.62×10^{-12}	0.00	-171.0	$T \geq 200$
$O_2 + C_2H_2D \rightarrow HDCO + HCO$	0.00	0.00	0.0	$T < 200$
	3.08×10^{-12}	0.00	-171.0	$T \geq 200$
$O_2 + C_2H_2D \rightarrow H_2CO + DCO$	0.00	0.00	0.0	$T < 200$
	1.54×10^{-12}	0.00	-171.0	$T \geq 200$
$S + O_2 \rightarrow SO + O$	0.00	0.00	0.0	$T < 200$
	4.74×10^{-13}	1.41	-439.0	$T \geq 200$
$C_2H_3^+ + e^- \rightarrow C_2H_2 + H$	0.00	0.00	0.0	$T < 1000$
	2.78×10^{-7}	-1.38	0.0	$T \geq 1000$
$C_2H_2D^+ + e^- \rightarrow C_2HD + H$	0.00	0.00	0.0	$T < 1000$
	1.86×10^{-7}	-1.38	0.0	$T \geq 1000$
$C_2H_2D^+ + e^- \rightarrow C_2H_2 + D$	0.00	0.00	0.0	$T < 1000$
	9.30×10^{-8}	-1.38	0.0	$T \geq 1000$
$C_2H_3^+ + e^- \rightarrow C_2H + H_2$	0.00	0.00	0.0	$T < 1000$
	5.75×10^{-8}	-1.38	0.0	$T \geq 1000$
$C_2H_2D^+ + e^- \rightarrow C_2D + H_2$	0.00	0.00	0.0	$T < 1000$
	1.92×10^{-8}	-1.38	0.0	$T \geq 1000$
$C_2H_2D^+ + e^- \rightarrow C_2H + HD$	0.00	0.00	0.0	$T < 1000$
	3.83×10^{-8}	-1.38	0.0	$T \geq 1000$
$H + NH_2 \rightarrow NH + H_2$	5.25×10^{-12}	0.79	2200.0	$T \leq 700$
	1.05×10^{-10}	0.00	-4450.0	$T > 700$
$D + NH_2 \rightarrow ND + H_2$	1.75×10^{-12}	0.79	2200.0	$T \leq 700$
	0.35×10^{-10}	0.00	-4450.0	$T > 700$
$D + NH_2 \rightarrow NH + HD$	3.50×10^{-12}	0.79	2200.0	$T \leq 700$
	0.70×10^{-10}	0.00	-4450.0	$T > 700$
$H + NHD \rightarrow ND + H_2$	1.75×10^{-12}	0.79	2200.0	$T \leq 700$
	0.35×10^{-10}	0.00	-4450.0	$T > 700$
$H + NHD \rightarrow NH + HD$	3.50×10^{-12}	0.79	2200.0	$T \leq 700$
	0.70×10^{-10}	0.00	-4450.0	$T > 700$
$C + O_2 \rightarrow CO + O$	4.70×10^{-11}	-0.34	0.0	$T \leq 300$
	2.48×10^{-12}	1.54	613.0	$T > 300$

Table 7.4: As for Table 7.3.

REACTION	α	β	γ	TEMPERATURE RANGE
$O + CH \rightarrow CO + H$	6.60×10^{-11}	0.00	0.0	$T \leq 2000$
	1.02×10^{-10}	0.00	-914.0	$T > 2000$
$O + CD \rightarrow CO + D$	6.60×10^{-11}	0.00	0.0	$T \leq 2000$
	1.02×10^{-10}	0.00	-914.0	$T > 2000$
$N + OH \rightarrow NO + H$	7.50×10^{-11}	-0.18	0.0	$T \leq 100$
	4.06×10^{-11}	0.05	78.0	$T > 100$
$N + OD \rightarrow NO + D$	7.50×10^{-11}	-0.18	0.0	$T \leq 100$
	4.06×10^{-11}	0.05	78.0	$T > 100$
$O + OH \rightarrow O_2 + H$	3.50×10^{-11}	0.00	0.0	$T \leq 150$
	1.77×10^{-11}	0.00	178.0	$T > 150$
$O + OD \rightarrow O_2 + D$	3.50×10^{-11}	0.00	0.0	$T \leq 150$
	1.77×10^{-11}	0.00	178.0	$T > 150$
$O + C_2 \rightarrow CO + C$	1.00×10^{-10}	0.00	0.0	$T \leq 4150$
	6.00×10^{-10}	0.00	0.00	$T > 4150$
$CH_4^+ + H_2 \rightarrow CH_5^+ + H$	3.40×10^{-11}	-1.35	23.0	$T \leq 300$
	3.30×10^{-11}	0.00	0.0	$T > 300$
$CH_3D^+ + H_2 \rightarrow CH_4D^+ + H$	3.40×10^{-11}	-1.35	23.0	$T \leq 300$
	3.30×10^{-11}	0.00	0.0	$T > 300$
$CH_4^+ + HD \rightarrow CH_4D^+ + H$	1.70×10^{-11}	-1.35	23.0	$T \leq 300$
	1.65×10^{-11}	0.00	0.0	$T > 300$
$CH_4^+ + HD \rightarrow CH_5^+ + D$	1.70×10^{-11}	-1.35	23.0	$T \leq 300$
	1.65×10^{-11}	0.00	0.0	$T > 300$
$NH_3^+ + H_2 \rightarrow NH_4^+ + H$	3.36×10^{-12}	0.00	-35.7	$T \leq 20$
	2.00×10^{-13}	0.00	0.0	$20 < T < 300$
	1.70×10^{-11}	0.00	-1044.0	$T \geq 300$
$NH_2D^+ + H_2 \rightarrow NH_3D^+ + H$	3.36×10^{-12}	0.00	-35.7	$T \leq 20$
	2.00×10^{-13}	0.00	0.0	$20 < T < 300$
	1.70×10^{-11}	0.00	-1044.0	$T \geq 300$
$NH_3^+ + HD \rightarrow NH_3D^+ + H$	1.68×10^{-12}	0.00	-35.7	$T \leq 20$
	1.00×10^{-13}	0.00	0.0	$20 < T < 300$
	0.85×10^{-11}	0.00	-1044.0	$T \geq 300$
$NH_3^+ + HD \rightarrow NH_4^+ + D$	1.68×10^{-12}	0.00	-35.7	$T \leq 20$
	1.00×10^{-13}	0.00	0.0	$20 < T < 300$
	0.85×10^{-11}	0.00	-1044.0	$T \geq 300$
$O^+ + N_2 \rightarrow NO^+ + N$	2.16×10^{-12}	-0.86	0.0	$T \leq 220$
	1.20×10^{-12}	0.00	0.0	$T > 220$
$He^+ + H \rightarrow H^+ + He$	1.20×10^{-15}	0.25	0.0	$T \leq 1000$
	8.20×10^{-16}	0.50	0.0	$T > 1000$
$He^+ + D \rightarrow D^+ + He$	1.20×10^{-15}	0.25	0.0	$T \leq 1000$
	8.20×10^{-16}	0.50	0.0	$T > 1000$
$H^+ + O \rightarrow O^+ + H$	7.31×10^{-10}	0.23	225.9	$T \leq 10000$
	3.04×10^{-10}	0.47	11.5	$T > 10000$
$D^+ + O \rightarrow O^+ + D$	7.31×10^{-10}	0.23	225.9	$T \leq 10000$
	3.04×10^{-10}	0.47	11.5	$T > 10000$

Table 7.5: As for Table 7.3.

Reaction	α	β	γ	Temperature range
$NH_2^+ + e^- \rightarrow N + H + H$	1.98×10^{-7}	-0.40	0.0	$T \leq 12$
	2.01×10^{-7}	-0.90	0.0	$12 < T < 310$
	1.74×10^{-7}	-0.80	0.0	$T \geq 310$
$NHD^+ + e^- \rightarrow N + D^+ H$	1.98×10^{-7}	-0.40	0.0	$T \leq 12$
	2.01×10^{-7}	-0.90	0.0	$12 < T < 310$
	1.74×10^{-7}	-0.80	0.0	$T \geq 310$
$NH_2^+ + e^- \rightarrow NH + H$	1.02×10^{-7}	-0.40	0.0	$T \leq 12$
	1.04×10^{-7}	-0.90	0.0	$12 < T < 310$
	9.02×10^{-8}	-0.80	0.0	$T \geq 310$
$NHD^+ + e^- \rightarrow ND + H$	5.10×10^{-8}	-0.40	0.0	$T \leq 12$
	0.52×10^{-7}	-0.90	0.0	$12 < T < 310$
	4.51×10^{-8}	-0.80	0.0	$T \geq 310$
$NHD^+ + e^- \rightarrow NH + D$	5.10×10^{-8}	-0.40	0.0	$T \leq 12$
	0.52×10^{-7}	-0.90	0.0	$12 < T < 310$
	4.51×10^{-8}	-0.80	0.0	$T \geq 310$
$NH_4^+ + e^- \rightarrow NH_2 + H + H$	3.19×10^{-7}	-0.47	0.0	$T \leq 620$
	4.69×10^{-7}	-1.00	0.0	$620 < T < 4460$
	6.04×10^{-5}	-2.80	0.0	$T \geq 4460$
$NH_3D^+ + e^- \rightarrow NHD + H + H$	1.59×10^{-7}	-0.47	0.0	$T \leq 620$
	4.69×10^{-7}	-1.00	0.0	$620 < T < 4460$
	3.02×10^{-5}	-2.80	0.0	$T \geq 4460$
$NH_3D^+ + e^- \rightarrow NH_2 + D + H$	1.59×10^{-7}	-0.47	0.0	$T \leq 620$
	4.69×10^{-7}	-1.00	0.0	$620 < T < 4460$
	3.02×10^{-5}	-2.80	0.0	$T \geq 4460$
$NH_4^+ + e^- \rightarrow NH_3 + H$	1.05×10^{-6}	-0.47	0.0	$T \leq 620$
	1.54×10^{-6}	-1.00	0.0	$620 < T < 4460$
	1.98×10^{-4}	-2.80	0.0	$T \geq 4460$
$NH_3D^+ + e^- \rightarrow NH_2D + H$	7.90×10^{-7}	-0.47	0.0	$T \leq 620$
	1.16×10^{-6}	-1.00	0.0	$620 < T < 4460$
	1.48×10^{-4}	-2.80	0.0	$T \geq 4460$
$NH_3D^+ + e^- \rightarrow NH_3 + D$	2.60×10^{-7}	-0.47	0.0	$T \leq 620$
	0.38×10^{-6}	-1.00	0.0	$620 < T < 4460$
	0.50×10^{-4}	-2.80	0.0	$T \geq 4460$
$C^+ + e^- \rightarrow C + h\nu$	4.67×10^{-12}	-0.60	0.0	$T \leq 7950$
	1.23×10^{-17}	2.49	21845.6	$7950 < T < 21140$
	9.62×10^{-8}	-1.37	-115786.2	$T \geq 21140$
$N^+ + e^- \rightarrow N + h\nu$	4.00×10^{-12}	-0.58	0.0	$T \leq 7950$
	3.78×10^{-15}	1.20	0.0	$T > 7950$
$H^+ + H \rightarrow H_2^+ + h\nu$	5.13×10^{-19}	1.85	0.0	$T \leq 4000$
	2.35×10^{-16}	0.24	-8500.0	$T > 4000$
$D^+ + H \rightarrow HD^+ + h\nu$	5.13×10^{-19}	1.85	0.0	$T \leq 4000$
	2.35×10^{-16}	0.24	-8500.0	$T > 4000$
$H^+ + D \rightarrow HD^+ + h\nu$	5.13×10^{-19}	1.85	0.0	$T \leq 4000$
	2.35×10^{-16}	0.24	-8500.0	$T > 4000$
$C + N \rightarrow CN + h\nu$	7.87×10^{-19}	0.06	96.0	$T \leq 2700$
	1.37×10^{-18}	0.13	-520.0	$T > 2700$
$HNC + H \rightarrow HCN + H$	1.00×10^{-15}	0.00	0.0	$T \leq 100$
	1.36×10^{-13}	4.48	0.0	$T > 100$
$DNC + H \rightarrow DCN + H$	5.00×10^{-16}	0.00	0.0	$T \leq 100$
	1.36×10^{-13}	4.48	0.0	$T > 100$
$DNC + H \rightarrow HCN + D$	5.00×10^{-16}	0.00	0.0	$T \leq 100$
	1.36×10^{-13}	4.48	0.0	$T > 100$
$HNC + D \rightarrow DCN + H$	5.00×10^{-16}	0.00	0.0	$T \leq 100$
	1.36×10^{-13}	4.48	0.0	$T > 100$
$HNC + D \rightarrow HCN + D$	5.00×10^{-16}	0.00	0.0	$T \leq 100$
	1.36×10^{-13}	4.48	0.0	$T > 100$
$H_2D^+ + H_2 \rightarrow H_3^+ + HD$	1.70×10^{-9}	0.00	220.0	$T \leq 100$
	1.70×10^{-9}	0.00	-130.0	$T > 100$

the collapse is slowed by magnetic fields and ambipolar diffusion, magnetic fields will have been able to support the core for a period of time prior to the collapse, allowing it to reach chemical equilibrium.

First of all, we tested how the chemistry behaved in the collapse with a field strength of 8 μG, imposing constant ion-neutral drift velocities ranging from $0.0 - 1.0$ km s^{-1} in increments of 0.1 km s^{-1}, to understand what values of $v_{\rm d}$ are needed to have an effect. The effect of the drift velocity was to modify the effective temperature of the ion-neutral reactions *only*, according to equation (7.1).

Since it is possible that dark cores can have temperatures up to $\sim$ 20 K (see Section 1.2.1.2), we also ran the model at kinetic temperatures of 15 K and 20 K, as it would be expected that a smaller ion-neutral drift velocity will be needed to affect the deuterium chemistry at these temperatures. Next we ran the model using the time dependent drift velocity predicted by SR08's models, shown in Figure 7.1, and finally we ran the model with the density and drift velocity taken from the collapse with a magnetic field strength of 20 μG.

7.3 Results

Figure 7.2 shows the fractional abundances of C^+, CH^+, OH and NH_3 for the collapsing stage of the model for the 8 μG field. The different lines show the results using drift velocities ranging from $0.0 - 1.0$ km s^{-1} in increments of 0.1 km s^{-1}, and the arrow shown on each plot shows the direction of increasing drift velocity.

C^+ and CH^+ are plotted because these species have been found to be affected by ion-neutral drift in previous investigations (e.g. Federman *et al.* 1996). In these investigations the CH^+ abundance was found to increase when a drift velocity was applied, because the reaction

$$C^+ + H_2 \rightarrow CH^+ + H, \tag{7.6}$$

which has an energy barrier $\Delta E = 4640$ K, could be initiated. In this model, however, it appears that these molecules are relatively unaffected, and they even show a slight decrease as the drift velocity increases. This is because the drift velocities are too low; the highest drift velocity we use is 1.0 km s^{-1}, but Federman *et al.* (1996) used velocities up to 4 km s^{-1}, which are more appropriate for the diffuse ISM. If we use drift velocities of this magnitude then the CH^+ abundance does indeed increase, but such high drift velocities are unlikely in prestellar cores; 4 km s^{-1} is highly supersonic (the sound speed is only $\sim$ 0.2 km s^{-1} in a 10 K dark cloud), and such high

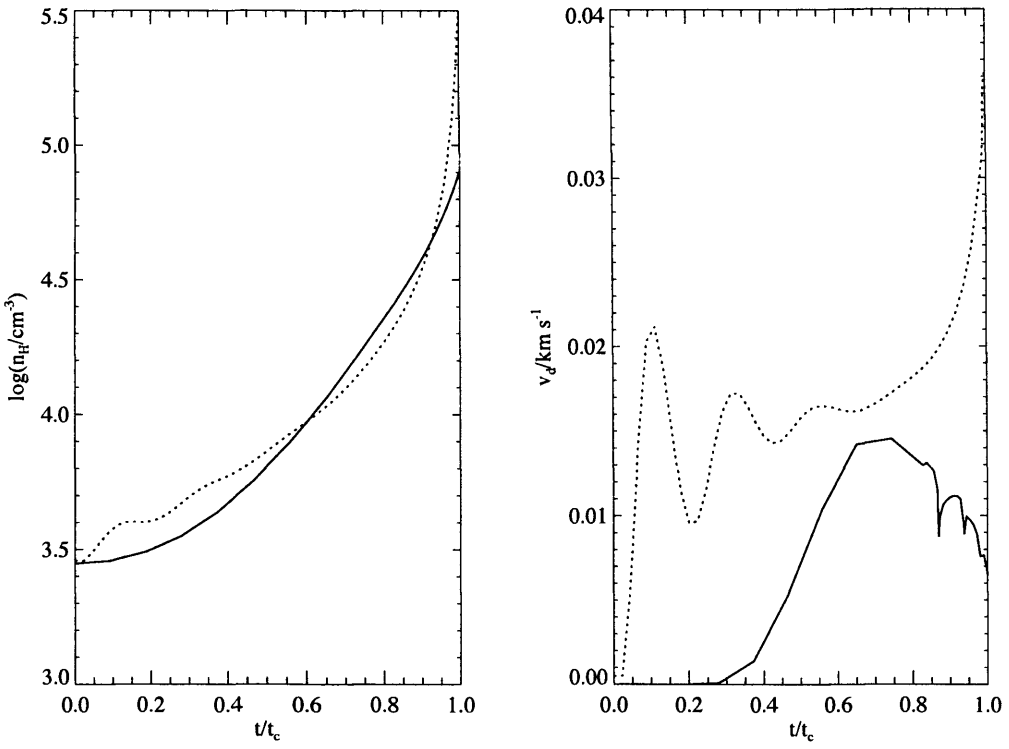

Figure 7.1: The density and drift velocity as a function of time used for our models. These results are taken from SR08. The solid line is for a core collapsing with ambipolar diffusion in an 8 μG magnetic field, and the dotted line is for a core collapsing in a 20 μG magnetic field. The time axis has been normalised by dividing by the collapse timescale, t_c, for each model, with $t_c = 1.07$ Myr for the 8 μG model, and $t_c = 4.48$ Myr for the 20 μG model.

drift velocities would generate shocks in the cloud which would dissipate the energy on a short timescale, so drift velocities of this magnitude could not be maintained in a dark cloud.

OH and NH_3 are plotted because they do show a slight response to drift velocities ≤ 1.0 km s^{-1}. The OH abundance is increased, especially at early times, when a drift velocity is included. This can be explained by looking at the destruction reaction:

$$C^+ + OH \rightarrow CO^+ + H. \tag{7.7}$$

This reaction has $k = 5.73 \times 10^{-9}(T_{\rm eff}/300.0)^{-1/2}$ cm^3 s^{-1}, so its rate actually decreases for higher drift velocities (and therefore higher effective temperatures), allowing more OH to survive.

The NH_3 abundance decreases as v_d increases, and there is an especially large 'jump' from using $v_d = 0.3$ km s^{-1} to 0.4 km s^{-1}. This can be explained by looking at the formation of NH_3

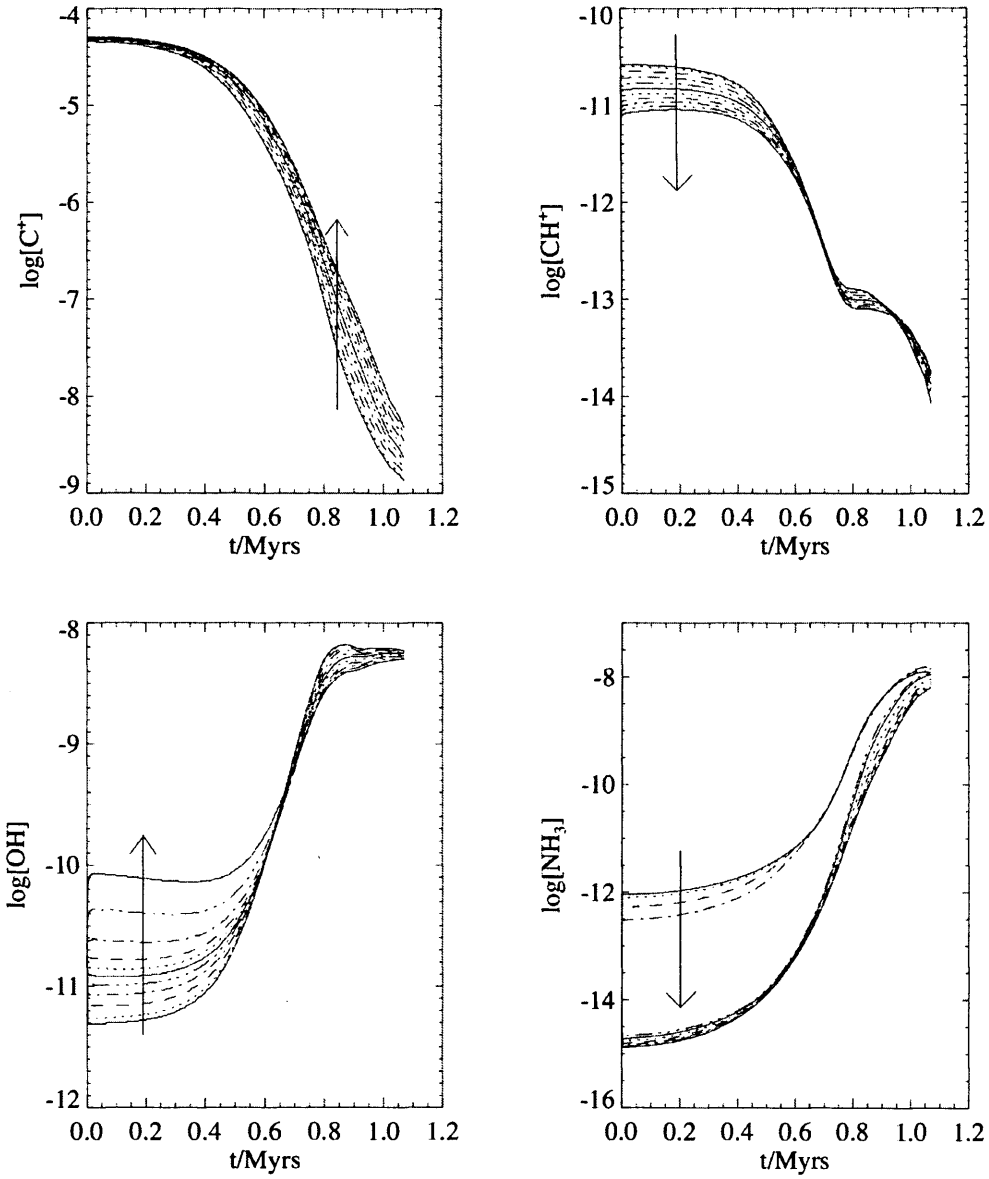

Figure 7.2: Fractional abundances of non-deuterated species for core collapsing with ambipolar diffusion for an 8μG magnetic field and kinetic temperature 10 K, for $v_d = 0.0$ to 1.0 km s^{-1} in increments of 0.1 km s^{-1}. The arrow on each plot shows the direction of increasing drift velocity.

by the reactions

$$NH_3^+ + H_2 \rightarrow NH_4^+ + H \tag{7.8}$$

$$NH_4^+ + e^- \rightarrow NH_3 + H. \tag{7.9}$$

Reaction (7.8) has a rate given by $k = 3.36 \times 10^{-12} \exp(37.5/T_{\rm eff})$ cm^3 s^{-1}, but for $20 \leq T_{\rm eff} \leq 300$ K, the rate becomes $k = 2.0 \times 10^{-13}$ cm^3 s^{-1}, independent of temperature. At $v_{\rm d} = 0.3$ km s^{-1}, the effective temperature is 16.5 K (using equation (7.1) with $\mu = 34/19$ a.m.u.), but for $v_{\rm d} = 0.4$ km s^{-1}, $T_{\rm eff}$ is 21.5 K, so the rate of NH_4^+ production has a sudden decrease to 2.0×10^{-13} cm^3 s^{-1}, having a 'knock-on' effect on the NH_3.

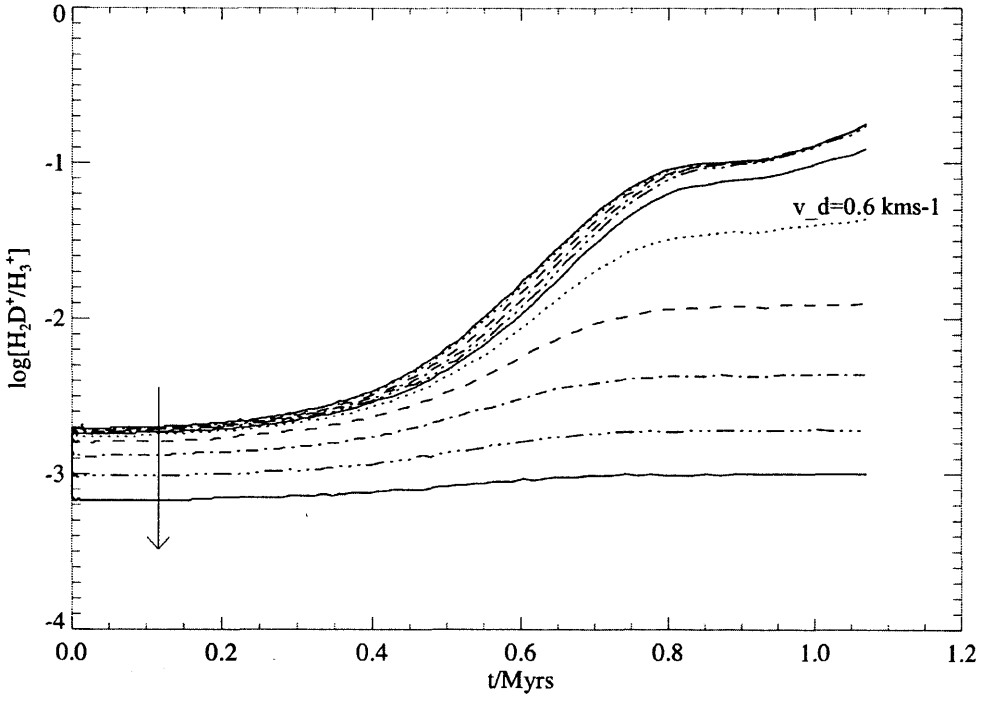

Figure 7.3: Ratio of H_2D^+/H_3^+ for the same models as in Figure 7.2. The arrow shows the direction of increasing drift velocity. Drift velocities of $\gtrsim 0.6$ km s^{-1} (labelled curve) are needed to have a significant effect on the H_2D^+/H_3^+ ratio.

Figure 7.3 shows the ratio of H_2D^+/H_3^+ for the same models as in Figure 7.2. The arrow shows the direction of increasing drift velocity. It shows that the H_2D^+ fractionation increases as the core collapses (apart from for $v_{\rm d} \gtrsim 0.9$ km s^{-1} where it remains approximately constant). One reason for this is that as the core collapses, the A_v increases therefore reducing the rate of photoionisation reactions in the core. This reduces the electron fraction inside the core which reduces the rate of

dissociative recombination of H_2D^+, which is one of the major destruction routes of H_2D^+. The reduction in electron abundance also means that there is more H_3^+ available to react with HD to form H_2D^+, so the ratio of H_2D^+ to H_3^+ increases.

Another factor contributing to the increase in H_2D^+/H_3^+ ratio is the freeze-out of CO once the A_v is greater than $A_{v,\mathrm{crit}}$. CO is another major destruction path for H_2D^+, through the reaction:

$$H_2D^+ + CO \rightarrow HCO^+ + HD \tag{7.10}$$

$$\rightarrow DCO^+ + H_2. \tag{7.11}$$

So when CO freezes out, H_2D^+ is able to remain in the gas-phase increasing the fractionation at late times. This behaviour was also found in previous models run by Roberts & Millar (e.g. Roberts & Millar 2000*a*).

As expected, the H_2D^+ fractionation decreases for higher drift velocities, although a drift velocity of $\gtrsim 0.6$ km s^{-1} is needed to have a significant effect. At this drift velocity, the effective temperature is $\sim$ 27 K, and the backwards reaction of (7.5) is now fast enough to dominate the other H_2D^+ destruction reactions.

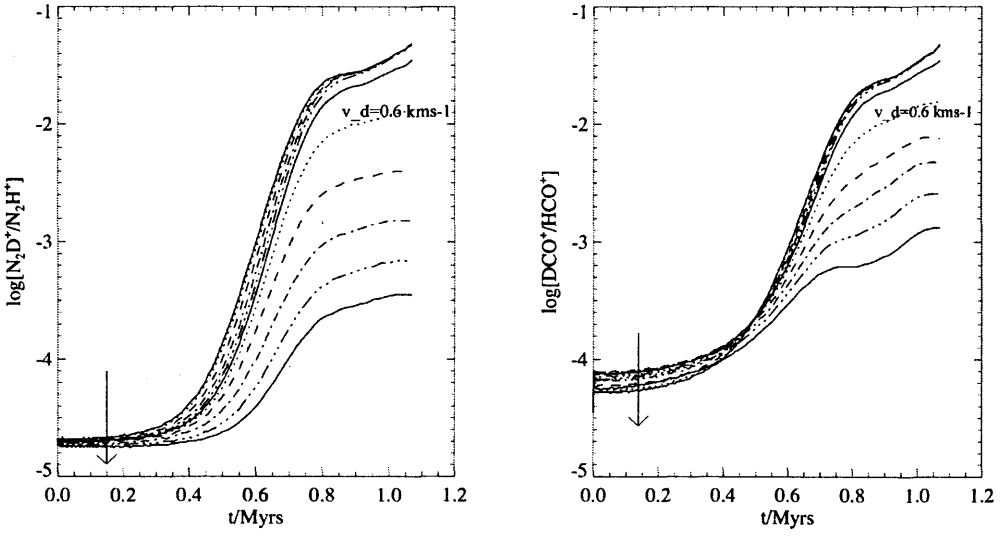

Figure 7.4: As in Figure 7.3 but for the abundance ratios N_2D^+/N_2H^+ and DCO^+/HCO^+.

Figure 7.4 shows the fractionation of N_2D^+ and DCO^+ for the same models. They both show the same behaviour as H_2D^+, with their fractionation decreasing noticeably for $v_d \gtrsim 0.6$ km s^{-1}. Other observable deuterated molecules (e.g. DCN, DNC, HDCO, D_2CO) also show the same trend. As explained in the introduction, this is because H_2D^+ is the primary deuterating ion, so when this

is destroyed it decreases the deuterium fractionation in most other molecules. For example, N_2D^+ is formed by:

$$H_2D^+ + N_2 \rightarrow N_2D^+ + H_2, \tag{7.12}$$

and so directly depends on the H_2D^+ abundance. Other 'deuterating' ions are CH_2D^+ and C_2HD^+ (Markwick *et al.* 2001), and they are also destroyed by high drift velocities, in a similar way to H_2D^+. CH_2D^+, for example, is destroyed by the reaction:

$$CH_2D^+ + H_2 \rightarrow CH_3^+ + HD, \tag{7.13}$$

which has an energy barrier of 370 K, so it becomes effective for $v_d \gtrsim 0.9$ km s^{-1}. CH_2D^+ is involved in the production of DCO^+ through the reaction

$$CH_2D^+ + O \rightarrow DCO^+ + H_2, \tag{7.14}$$

and so the decrease in CH_2D^+ contributes to the decrease in fractionation of DCO^+.

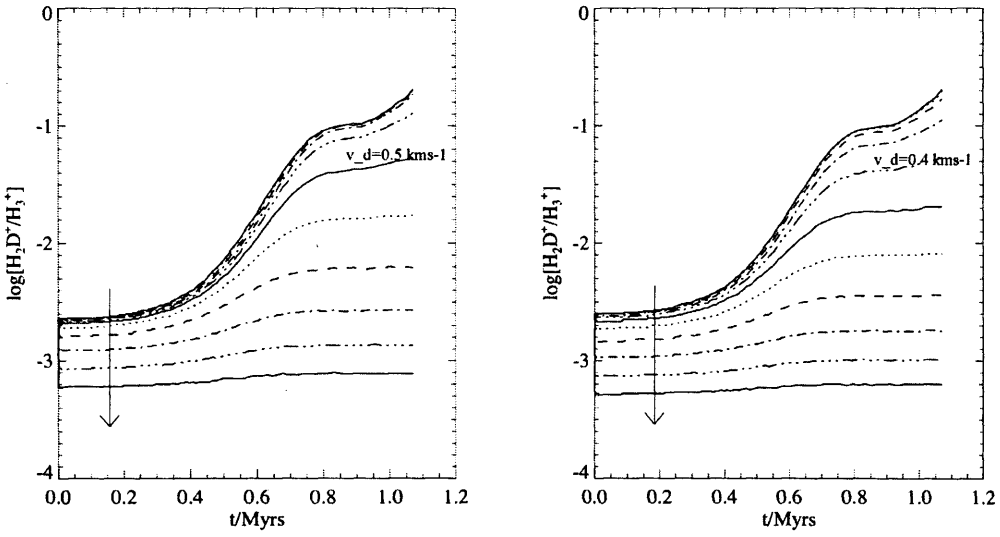

Figure 7.5: As in Figure 7.3 but for models with kinetic temperatures of 15 K and 20 K. Drift velocities of $\gtrsim 0.5$ km s^{-1} and $\gtrsim 0.4$ km s^{-1} at 15 K and 20 K respectively are needed to cause a significant decrease in the H_2D^+/H_3^+ ratios.

Looking at Figure 7.1, the drift velocities predicted by the ambipolar diffusion models do not go above 0.04 km s^{-1}, much less than the 0.6 km s^{-1} required to cause a difference in H_2D^+ fractionation. We therefore investigated the possibility that dark cores might have a higher kinetic

temperature than the 10 K we have used, which would mean a smaller drift velocity would be needed to activate the $H_2D^+ + H_2$ reaction.

Temperatures inside dark cores have been estimated to be up to 20 K (Bergin & Tafalla 2007) (see Section 1.2.1.2), so we ran models for the 8 μG ambipolar diffusion collapse with $T_{kin} = 15$ and 20 K, with $0.0 \leq v_d \leq 1.0$ km s^{-1}. These are shown in Figure 7.5. For $T_{kin} = 15$ K, $v_d \gtrsim 0.5$ km s^{-1} is needed to affect the H_2D^+ fractionation, and for 20 K, $v_d \gtrsim 0.4$ km s^{-1} is needed. These values are still well above the maximum drift velocity predicted by SR08's models.

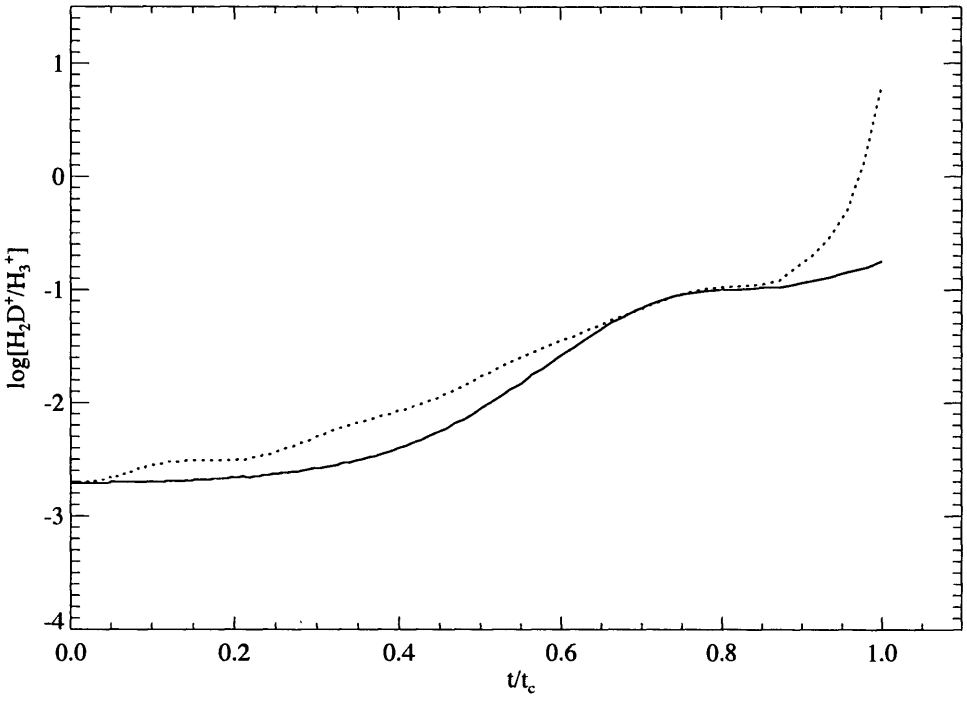

Figure 7.6: The H_2D^+/H_3+ ratio for ambipolar diffusion controlled collapse in an 8 μG magnetic field (solid line) and in a 20 μG magnetic field (dotted line). The time axis has been normalised by dividing by the collapse timescale, t_c, for each model, with $t_c = 1.07$ Myr for the 8 μG model, and $t_c = 4.48$ Myr for the 20 μG model.

Figure 7.6 compares the H_2D^+ fractionation for the 8 μG (solid line) and 20 μG (dotted line) collapses. The time has been normalised to the collapse timescale for each model ($t_c = 1.07$ Myr for the 8 μG model, and $t_c = 4.48$ Myr for the 20 μG model). These models use the drift velocities predicted by SR08's models, but the results are almost exactly the same as when the drift velocity is zero. This shows that even when the magnetic field is very strong (20 μG initially), the drift velocity is not high enough to affect the deuterium fractionation.

The main difference for these two models is the sharp increase in the fractionation for the 20 μG model at the end of the collapse, which is mainly due to the freeze-out of CO: In the 20 μG collapse the CO is depleted by more than two orders of magnitude compared to the 8 μG collapse, because of the higher final density (3.5×10^5 cm^{-3} compared to 8.1×10^4 cm^{-3}). As explained above, the freeze-out of CO results in an enhancement of H_2D^+, which can clearly be seen for the 20 μG collapse.

Since the shells modelled in the 8 μG and and 20 μG collapse both started at a radius of approximately half the outer radius of the core, it is interesting that the 20 μG model is able to reach significantly higher densities, and this indicates that the two models may have different radial density profiles. Since the H_2D^+/H_3^+ ratio appears to be so sensitive to the density, it could be worthwhile to perform a full multipoint model of the deuterium chemistry coupled to these two collapse models, to see how the radial distribution of the H_2D^+/H_3^+ ratio is affected by the different density distributions in each model. If the radial distribution of H_2D^+ (or other deuterated molecules which are produced by H_2D^+) could be observed, then this could potentially be used to diagnose if either of the two models we have investigated are realistic.

7.4 Discussion and conclusions

In collapsing cores, drift velocities of $\gtrsim 0.4$ km s^{-1} are needed to have an observable effect on the deuterium fractionation. An even higher drift velocity ($v_d \gtrsim 3$ km s^{-1}) is needed to affect the chemistry of non-deuterated molecules such as CH^+.

Such high drift velocities are not predicted by ambipolar diffusion controlled collapse models; even drift velocities of 0.4 km s^{-1} are highly supersonic, so would result in the generation of shocks and dissipation of the magnetic energy, meaning that such high drift velocities could not be maintained. Even if the drift velocities could be maintained somehow, then the star formation would be turbulence dominated and the ambipolar diffusion model used here would not be applicable.

However, although we have found that the drift velocities do not have an effect on the deuterium chemistry for realistic ambipolar diffusion models of collapsing cores, the deuterium chemistry has been found to be very sensitive to the density, and so the density profiles for different collapse models should produce different radial distributions of deuterated molecules. Following further investigation, this could potentially be used to help determine the density profile of collapsing cores and hence the collapse dynamics.

There are other situations in astrochemistry where very high drift velocities are present, for

which we could apply a similar model. For example, Markwick *et al.* (2001) have explained the gradient in deuterium fractionation along the TMC1 ridge as being due to the propagation of MHD waves, possibly originating from a nearby IRAS source, with drift velocities up to ~ 0.5 km s^{-1}.

Also, the magnetic precursor of C-shocks, which can arise when the outflows of young stellar objects interact with their surrounding medium, has predicted drift velocities of ~ 18 km s^{-1} for a shock speed of 30 km s^{-1} (e.g. Jiménez-Serra *et al.* 2008). These kinds of drift velocities should have a very large impact upon the chemistry of both deuterated and non-deuterated molecules. We investigate the chemistry of C-shocks in more detail in Section 8.4 of the next chapter.

CHAPTER 8

THE MAGNETIC PRECURSOR OF C-SHOCKS

The work presented in this chapter was done in collaboration with I. Jiménez-Serra of Leeds University, UK, and other collaborators at the Insituto de Estructura de la Materia, Spain. The JCMT observations were taken by myself and A. Rodriguez-Franco (Insituto de Estructura de la Materia), and the IRAM observations were taken by I. Jiménez-Serra. The raw data was reduced by I. Jiménez-Serra and the analysis was performed by myself.

8.1 Introduction

In this chapter we present studies on the interaction of molecular outflows of YSOs with their surrounding medium, in particular the outflow from the Class 0 object L1448-mm. The aim is to find observational evidence for the magnetic precursor of C-shocks in the surrounding medium of YSOs with outflows, and to identify other possible chemical signatures of the magnetic precursor interaction. The chapter is divided into two main sections: the first is observational work to measure the electron density enhancement in the magnetic precursor component of L1448-mm, and the second is a chemical model of precursor regions which takes into account the effect of ion-neutral drift in enhancing the rate of ion-neutral chemical reactions.

Molecular outflows are of great importance in star formation. They begin at the earliest protostellar phase (the Class 0 phase), while the protostar is still accreting large amounts of mass, and continue until the accretion disk surrounding the protostar disappears. The outflows are most energetic during the Class 0 phase, and there is strong evidence to suggest that they are powered by highly collimated disk winds (also known as jets) (Pudritz *et al.* 2007). The jets interact with the core and envelope of the protostar, entraining molecular material to create molecular outflows.

Although the origin of the jets is not completely clear, current theories suggest that they are driven by magnetic stresses in the disk-protostar system, and have been shown to be generated in simulations of the collapse of magnetized, rotating Bonner-Ebert spheres (e.g. Banerjee & Pudritz 2006). These accretion powered outflows can efficiently remove angular momentum from the protostar-disk system, and therefore play a crucial role in the evolution of the protostar.

The magnetic precursor constitutes an early stage of evolution of shocks, so in order to study it we need to observe a very young shock. The L1448 bipolar outflow, generated by the Class 0 object L1448-mm, is a typical example of a very young molecular outflow, and the subject of the observational section of this chapter. The chemical model in the second section can be also applied to the magnetic precursor in objects such as this. L1448-mm is at a distance of 300 pc, and is a compact submillimetre source with an angular diameter of only $\sim 5''$ (Curiel *et al.* 1990), which corresponds to $\sim$ 1450 AU at 300 pc. The outflow lobes, which are aligned $\sim$ 70 degrees to the line of sight, have a length projected on the sky of approximately 0.36 pc, and the jet speed is $\gtrsim 200$ km s^{-1} (Bachiller *et al.* 1995). The morphology of the outflow, based on the CO $J = 2 \rightarrow 1$ intensity maps taken by Bachiller *et al.* (1990), is shown in Figure 8.1. The points of L1448-mm observed for this work are marked with filled circles, and the points observed by Jiménez-Serra *et al.* (2006, hereafter JS06) are marked with stars.

The propagation of supersonic molecular outflows into the surrounding ambient material causes shocks, where the ambient material is rapidly heated, compressed and then cooled down again, producing a signature 'shock chemistry'. Understanding the chemical evolution of shocks can be used to provide information on the physics of the shocks, as well as to estimate the age of the shock and outflow.

One feature of shock chemistry is an enhanced SiO abundance of up to 10^6 times its typical value in an ambient medium, with a broad line-width centred around a velocity that is very different to the ambient cloud. This is believed to arise from the sputtering of atomic Si from dust grains, which occurs at shock speeds of $v_s \gtrsim 25$ km s^{-1} (Caselli *et al.* 1997; Jiménez-Serra *et al.* 2008). Enhanced abundances of CH_3OH, H_2CO and HCO^+ are also representative of shock chemistry (Arce *et al.* 2007).

Recently, a narrow (line-width $\sim 0.5 - 1.0$ km s^{-1}), low velocity component of SiO has been detected towards the NGC1333 and L1448-mm molecular outflows with an abundance of $\sim 10^{-10} - 10^{-11}$, which is about ten times the ambient abundance (Lefloch *et al.* 1998; Jiménez-Serra *et al.* 2004). The origin of this narrow SiO component is unclear, but it has been suggested that it is caused by sputtering of dust grains by the ion-neutral drift associated with the magnetic

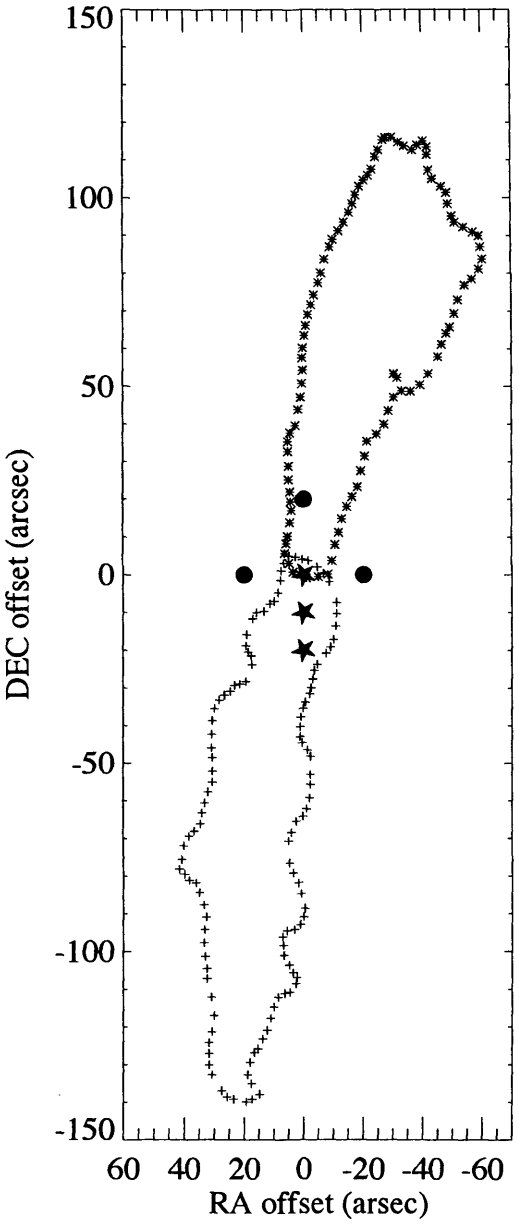

Figure 8.1: Morphology of the L1448 outflow originating from L1448-mm, based on the CO $J = 2 \rightarrow 1$ line intensity map of Bachiller *et al.* (1990). The blue shifted lobe is outlined in asterisks and the redshifted lobe is outlined in crosses. Offsets are given with respect to the central position of L1448-mm: $\alpha = 03^{h}25^{m}38^{s}.8$, $\delta = 30°44'05''.4$ (J2000).The points of L1448-mm observed for this work are marked with filled circles, and the points observed by Jiménez-Serra *et al.* (2006) are marked with stars.

precursor of C-shocks (Jiménez-Serra *et al.* 2004). In Part I (Section 8.3) of this chapter, we look at the comparative excitation of ions and neutral species in the submillimetre continuum L1448-mm (which has been observed to have this narrow SiO component), to find further evidence for the magnetic precursor and to estimate the enhanced electron density associated with it. In Part II (Section 8.4), we present a chemical model which makes further predictions on the chemistry of the magnetic precursor of C-shocks, in particular looking at the effect of ion-neutral drift on the enhancement of ion-neutral chemical reaction rates. We start by giving some background information on interstellar shocks, in order to explain the concept of the magnetic precursor.

8.2 Interstellar shocks and the magnetic precursor

Shocks arise in the interstellar medium when a pressure driven disturbance propagates through an ambient medium, affecting an irreversible change in the state of that medium. Following Draine (1980), we will use the word *shock wave* to mean the whole shock structure, moving through a medium, and *jump front* or *J-front* to mean the 'front' of the shock, where discontinuities in some or all of the flow variables (velocity, density, temperature, etc.) occur.

In the molecular envelopes surrounding young protostars, the ionisation fraction is low ($< 10^{-7}$ Guelin *et al.* 1982) although still highly influential on the shock structure. In order to accurately calculate the shock structure, the gas needs to be considered as being made up of at least two fluids, a neutral fluid and a charged fluid made up of ions and electrons (and possibly charged dust grains).

If one considers a one dimensional plane parallel disturbance propagating through an ambient medium with a velocity v_s, in the absence of a magnetic field, a shock will occur if v_s is greater than the neutral fluid sound speed, $(5kT/3m_n)^{1/2} \sim 0.08T^{1/2}$ km s^{-1}, where T is the gas temperature and m_n is the typical mass of a molecule in the neutral fluid (usually assumed to be the mass of H_2). This is because the neutral fluid at the disturbance is unable to 'communicate' with the gas ahead of the disturbance, so the gas ahead of the disturbance receives a 'surprise' once the disturbance arrives, resulting in discontinuities in the fluid variables.

If, however, there is a magnetic field $\mathbf{B_0}$ perpendicular to the direction of the shock flow, the charged fluid is able to support fast magnetosonic waves which propagate at a speed $v_f \sim v_A$, where v_A is the Alfvén speed of the charged fluid. The Alfvén velocity is given by $B_0/(4\pi\rho_i)^{1/2}$, where ρ_i in the mass density of the charged fluid, and this is approximately equal to $100(X(e^-)/10^{-4})^{-1/2}$ km s^{-1} (for the ion fluid, so neglecting charged dust grains), where $X(e^-)$ is the fractional abundance of electrons (equal to the ionisation fraction, assuming the ions are all singly charged)(Draine

& McKee 1993). For $X(e^-) \sim 10^{-7}$, the typical ionisation fraction in dense cores, this gives $v_f \sim v_A \sim 3000$ km s^{-1}.

If $v_s < v_f$, the fast magnetosonic wave in the charged fluid can 'out-run' the shock, and the charged fluid is 'aware' of the shock before the arrival of the J-front. In this case, the magnetic field ahead of the J-front becomes compressed over a length L, which is the damping length of the magnetosonic wave, and this region is known as the *magnetic precursor* (Draine 1980). The ions are accelerated in the magnetic precursor and, through collisions with the neutral fluid, the neutral fluid also becomes heated and compressed ahead of the J-front. If the magnetic field is increased, the damping length L becomes longer and there are more ion-neutral collisions, leading to more exchange of momentum between the ion and neutral fluid so that the neutral fluid can reach higher velocities.

If the magnetic field is greater than a certain value B_{crit} (or v_s is less than a critical velocity v_{crit}, if the magnetic field is fixed), the effect of the precursor on the neutral fluid becomes so pronounced that the neutral fluid flow variables become continuous everywhere and the J-front is 'quenched'. In this case the shock is called a 'C-shock' (where the 'C' stands for 'continuous'). For $B_0 < B_{crit}$ (or $v_s > v_{crit}$), the shock is known as a 'J-shock'. Schematic illustrations of the structure of shocks for increasing magnetic fields are shown in Figure 8.2 (reproduced from Draine 1980).

Le Bourlot *et al.* (2002) calculated that C-shocks can exist for shock velocities of up to 70 km s^{-1}, using the standard relation $B = b[n_H(\mathrm{cm}^{-3})]^{1/2}$ with $b = 1$ (Draine 1991), and a pre-shock density of $n_H = 10^4$ cm^{-3}. H_2 collisionally dissociates above this velocity which results in a sonic point in the flow which gives rise to discontinuities, causing the shock to become a J-shock. Molecular outflows associated with star formation can have velocities ranging from ten to hundreds of km s^{-1} (Draine & McKee 1993), so both types of shock should be prevalent in the interstellar medium.

8.3 Part I: Observational work

Previous observations of L1448-mm at various offsets have revealed narrow SiO emission (line-width ~ 0.5 km s^{-1}) with a fractional abundance of 10^{-11}, slightly redshifted compared to the velocity of the ambient cloud, which has been interpreted as evidence for a magnetic precursor (Jiménez-Serra *et al.* 2004). If this interpretation is correct, there should also be an electron density enhancement of ~ 100 times observed at the same velocity component as the narrow SiO emission (Flower *et al.* 1996). The enhancement arises from UV fluorescence generated by collisional

Figure 8.2: Schematic illustration of shock structures for increasing values of B_0. In this figure $v_{\rm ims}$ is the velocity of the fast magnetosonic wave in the charged fluid ($v_{\rm f}$ in the text). The velocity is velocity relative to the shock front. *Source: Draine (1980).*

excitation of H_2 in the magnetic precursor. Here we use multiline observations of ionic and neutral species to measure the electron density enhancement at various positions around L1448-mm, to constrain the spatial extent of the electron density enhancement. This will help to reveal whether the electron enhancement is due to the precursor, or if it is actually due to some other mechanism, for example UV illumination or opacity effects (see Section 8.3.3).

JS06 made the first measurements of the electron density enhancement in L1448-mm, by comparing the excitation of $H^{13}CO^+$, $HN^{13}C$ and $H^{13}CN$. They observed several transitions (from $J = 1 \rightarrow 5$) of these molecules, as well as SiO, at offsets (0,0), (0,-10) and (0,-20). Narrow SiO emission (~ 0.6 km s^{-1}) was detected at a velocity ~ 5.2 km s^{-1} at each position, which is believed to be due to the precursor. The line profiles of $H^{13}CO^+$, $HN^{13}C$ and $H^{13}CN$ all showed double peaks, made up of an ambient component at 4.7 km s^{-1} (4.7 km s^{-1} being the ambient velocity of the cloud) and a precursor component at ~ 5.2 km s^{-1}.

In the ambient gas, the ion ($H^{13}CO^+$) and neutral ($HN^{13}C$ and $H^{13}CN$) fluids showed similar excitation conditions, with an H_2 density of $\sim 10^5$ cm^{-3} and a kinetic temperature of 21 K. In the precursor component, however, $H^{13}CO^+$ appeared to be over-excited, requiring an H_2 density ten times that of $HN^{13}C$ and $H^{13}CN$ in the precursor, assuming that collisional excitement is by H_2 collisions only.

The discrepancies in the H_2 densities could be explained if there is an extra contribution to the excitement of $H^{13}CO^+$. JS06 calculated that an electron density enhancement of 500 times in the precursor component could provide this contribution. The electrons selectively excite ionic species, such as $H^{13}CO^+$, whilst leaving the neutrals relatively unaffected because because the collisional cross section of electrons with $H^{13}CO^+$ is more than a factor of ten larger than that for e^- – $HN^{13}C$ and e^- – $H^{13}CN$ collisions at low temperatures (see examples given in JS06). For the typical electron densities in the ambient gas (where the fractional abundance of electrons is less than 10^{-7}), electrons are unable to contribute to the excitation of these molecules.

In Part I of this chapter we first re-evaluate the predicted line intensities of $HN^{13}C$ and SiO for the observations from JS06 using new electron-HCN and election-SiO collisional coefficients (Faure *et al.* 2007; Faure 2008) to check that the conclusions drawn in JS06 are still valid with the new data. In Section 8.3.2 we describe the new observations taken for this work, which include observations of different isotopes of HCO^+ and HNC at positions (0,0) and (0,-10) , as well as observations of rotational transitions of SiO, $H^{13}CO^+$ and $HN^{13}C$ at new positions (0,20), (20,0) and (-20,0) towards L1448-mm. The observations of the different isotopes are to verify that the emission is optically thin, to justify the use of an excitation model using the large velocity gradient

(LVG) approximation in JS06[1], and to rule out the possibility that the over-excitement of ions is due to opacity effects (Cernicharo *et al.* 1984). The observations of SiO, $H^{13}CO^+$ and $HN^{13}C$ at the new positions are to understand the extent of the over-excitation of $H^{13}CO^+$. If we find that there is *not* a significant over-excitation of $H^{13}CO^+$ (and therefore no electron density enhancement is required to explain the observations) in these new positions it will show that the phenomenon is confined to a relatively small region, and therefore less likely to be produced by UV radiation and opacity effects, which would produce more widespread effects.

In Section 8.3.3 we present the results of the opacity calculations from the isotope observations, and in Section 8.3.4 we investigate if there is an electron density enhancement at the new positions observed. Conclusion are given in Section 8.3.5.

8.3.1 Using new collisional data to analyse the results from JS06

Since JS06 was published, new data for the collisional coefficients of electrons with SiO and HNC have been released (Faure *et al.* 2007; Faure 2008). In JS06 it was concluded that in the precursor component at positions (0,0), (0,-10) and (0,-20), the observed line intensities could be produced using an H_2 number density of $\sim 3 \times 10^5$ cm^{-3} and an enhanced electron fractional abundance of $\sim 5 \times 10^{-5}$. We now need to check that this conclusion still stands when we use the new collisional coefficients in our excitation model based on the LVG approximation. The LVG model is the same as that used in JS06 (apart from the new collisional coefficients for SiO and HNC). The collisional coefficients for H_2 with SiO, $H^{13}CO^+$ and $HN^{13}C$ are taken from Turner *et al.* (1992), Flower (1999) and Green & Thaddeus (1974) respectively, and the collisional coefficients for electrons with $H^{13}CO^+$ were taken from Faure & Tennyson (2008).

We have recalculated the expected intensities of the $J = 5 \rightarrow 4, 3 \rightarrow 2$ and $2 \rightarrow 1$ lines of SiO and the $J = 4 \rightarrow 3, 3 \rightarrow 2$ and $1 \rightarrow 0$ lines of $HN^{13}C$ using the LVG excitation model of JS06, in the precursor component with a kinetic temperature of 21 K, an H_2 number density of 3×10^5 cm^{-3} and an electron fractional abundance of both 5×10^{-5} and 1×10^{-8}. If the conclusions of JS06 are correct, then the enhanced electron abundance of $X(e^-) = 5 \times 10^{-5}$ should not affect the excitation of $HN^{13}C$, so the predicted intensities using both electron fractions

[1]The LVG approximation assumes that two emitted photons are only locally radiatively coupled, therefore an emitted photon has a high probability of escaping rather than being absorbed or scattered by the surrounding gas. This can be the case either if there is a large velocity gradient within the gas, so that two non-local points emit and absorb at different frequencies, or if the emission is optically thin so that very little absorption or scattering of an emitted photon can take place. For more details see Grinin (2001).

should be approximately equal, and should agree with the observed intensities.

The line-widths used were 0.6 km s^{-1} for SiO and 0.8 km s^{-1} for $HN^{13}C$, and the column densities used for the molecules at each position were taken from Table 3 of JS06. The observed and predicted intensities (using both $X(e^-) = 5 \times 10^{-5}$ and 1×10^{-8}) are given in Table 8.1. The observed intensities were taken from Table 1 of JS06 and converted to main beam temperatures. All main beam temperatures were converted to the same beam size (28″, which is the largest beam size for these observations), to correct for beam dilution effects.

Table 8.1 shows that the predicted intensities using $X(e^-) = 5 \times 10^{-5}$ and $X(e^-) = 1 \times 10^{-8}$ do not differ by more than a factor of ~ 1.7. This demonstrates the electrons do not contribute significantly to the excitement of $HN^{13}C$ and SiO using the new collisional coefficients, meaning that the new collisional coefficients are consistent with the theory behind this work, i.e. that the electrons selectively excite the ion fluid whilst leaving the neutral fluid relatively unaffected.

The predicted intensities also agree well with the observations, except SiO $J = 3 \rightarrow 2$ at (0,0) where the observed intensity is 1.6 times lower than the prediction. Also, the $HN^{13}C$ $J = 3 \rightarrow 2$ predictions are a factor of ~ 3 too high, but this was found to be the case in the JS06 paper. Given the uncertainties in the observed data, the data are still consistent with an electron enhancement in the precursor component using the new electron collisional coefficients.

8.3.2 Observations

We observed the $J = 3 \rightarrow 2$ and $J = 1 \rightarrow 0$ transitions of $H^{13}CO^+$ and $HN^{13}C$ at offsets (0,20), (20,0) and (-20,0) with respect to the central position of L1448-mm ($\alpha = 03^h25^m38^s.8$, $\delta = 30°44'05''.4$ [J2000]). To measure the opacity we observed the $J = 3 \rightarrow 2$ transition of several isotopes of HCO^+ and HNC, namely HCO^+, $HC^{18}O^+$, $H^{13}C^{18}O^+$ and $H^{15}N^{13}C$ at offsets (0,0) and (0,-10), and $H^{15}NC$ at (0,0).

The $J = 3 \rightarrow 2$ transitions were observed with the James Clerk Maxwell Telescope (JCMT) at Mauna Kea (Hawaii), using the position switch observing mode, with the reference (off) position at an offset of (800,0) arcseconds with respect to the central position. The beam size was 21″ and the main beam efficiency was 0.69 at the frequency of the $J = 3 \rightarrow 2$ transitions, $\sim$ 260 GHz. The ACSIS spectrometer provided a spectral resolution of 31 kHz, which corresponds to a velocity resolution of ~ 0.04 km s^{-1} in the A3 receiver. The system temperatures ranged from 400 K. to 700 K.

The observations for the $J = 1 \rightarrow 0$ transitions of $H^{13}CO^+$ and $HN^{13}C$ ($\nu \sim 90$ GHz) and the $J = 2 \rightarrow 1$ transition of SiO (also $\nu \sim 90$ Ghz) at offsets (0,20), (20,0) and (-20,0), were taken by

Table 8.1: Comparison of observed and predicted line intensities for positions (0,0), (0,-10) and (0,-20) towards L1448-mm. Observed values are taken from Table 1 of JS06 and converted to a main beam temperature with a beam size of 28″, and predicted line intensities are calculated from an LVG excitation model (input parameters given in the text).

LINE	OBSERVED T_{mb} AT 28″	PREDICTED T_B FOR $X(e^-) = 5 \times 10^{-5}$	PREDICTED T_B FOR $X(e^-) = 1 \times 10^{-8}$
		(0,0)	
SiO(2 → 1)	0.130	0.13	0.12
SiO(3 → 2)	0.087	0.14	0.09
SiO(5 → 4)	0.051	0.02	0.01
$HN^{13}C(1 \rightarrow 0)$	0.439	0.36	0.36
$HN^{13}C(3 \rightarrow 2)$	<0.070	0.10	0.06
$HN^{13}C(4 \rightarrow 3)$	...	0.01	0.01
		(0,-10)	
SiO(2 → 1)	0.134	0.12	0.11
SiO(3 → 2)	0.106	0.14	0.08
SiO(5 → 4)	<0.039	0.02	0.01
$HN^{13}C(1 \rightarrow 0)$	0.866	1.27	1.24
$HN^{13}C(3 \rightarrow 2)$	<0.077	0.38	0.24
$HN^{13}C(4 \rightarrow 3)$	<0.047	0.06	0.04
		(0,-20)	
SiO(2 → 1)	0.122	0.13	0.11
SiO(3 → 2)	0.112	0.14	0.08
SiO(5 → 4)	<0.025	0.02	0.01
$HN^{13}C(1 \rightarrow 0)$	0.829	1.08	1.06
$HN^{13}C(3 \rightarrow 2)$	<0.078	0.32	0.20
$HN^{13}C(4 \rightarrow 3)$	<0.043	0.05	0.03

I. Jiménez-Serra, with the IRAM (Insituto de Radioastonomía Milimétrica) 30 m telescope at Pico Veleta (Spain). The SIS receivers were tuned to a single sideband with image rejections $\geq$ 10 dB. Observations we done in frequency-switching and wobbler-switching modes with frequency and position throws of 7.2 MHz and 240″ respectively. A spectral resolution of $\sim$ 40 kHz was achieved with the autocorrelators, which corresponds to a velocity resolution of $\sim$ 0.14 km s^{-1} at 90 GHz. Typical system temperatures ranged from $\sim$ 150 – 400 K. The beam size and main beam efficiency at 90 Ghz were 28″ and 0.82 respectively.

All the intensities were calibrated in units of antenna temperature (T_A^*), and converted to main beam temperature ($T_{\rm mb}$) using the main beam efficiencies given above.

8.3.3 Calculation of opacities

Although the over-excitation of the ion fluid in the precursor component can be explained by the electron density enhancement produced by the precursor, it may be possible that these differences in excitation could be produced by opacity effects. Cernicharo *et al.* (1984) reported anomalies in the ratios of the intensities of the hyperfine components of HCN $J = 1 \rightarrow 0$ line in the Heiles Cloud 2 (HCL2) in the Taurus Molecular Cloud, and suggested that this was because the emission from the HCL2 core was being absorbed by a low density envelope, and then re-emitted over a large volume. This effect requires the lines to be optically thick, so if we can prove that the emission lines from $H^{13}CO^+$ and $HN^{13}C$ are optically thin for the positions observed in JS06, then we can rule out the possibility that the over-excitation of $H^{13}CO^+$ is an opacity effect. We also need to prove that the emission is optically thin to justify the use of an LVG excitation model.

Using the observations we have of the $J = 3 \rightarrow 2$ transitions of the different isotopes of HCO^+ and HNC at (0,0) and (0,-10) (described in Section 8.3.2), we can estimate the opacities of the $H^{13}CO^+$ and $HN^{13}C$ $J = 3 \rightarrow 2$ transitions. The observed line profiles are shown in Figure 8.3, and Table 8.2 shows the observed parameters of these lines.

Below we describe two methods we have used to estimate the opacities. The first method assumes that the isotopes $HC^{18}O^+$, $H^{13}C^{18}O^+$, $H^{15}NC$ and $H^{15}N^{13}C$ are optically thin, which is likely to be the case seeing as the lines were not detected above the 3σ noise level. The second method does not assume that the isotopes are optically thin, but requires that the upper limits for the intensities of the isotopes which are expected to have small opacities are less than the intensities (or upper limits of intensities) of the isotopes which are expected to have larger opacities. This is not always the case, for example, one would expect the intensity of $HC^{18}O^+$ to be less than that of $H^{13}CO^+$ because ^{18}O is a rarer isotope than ^{13}C, yet the upper limit of the intensity of $HC^{18}O^+$

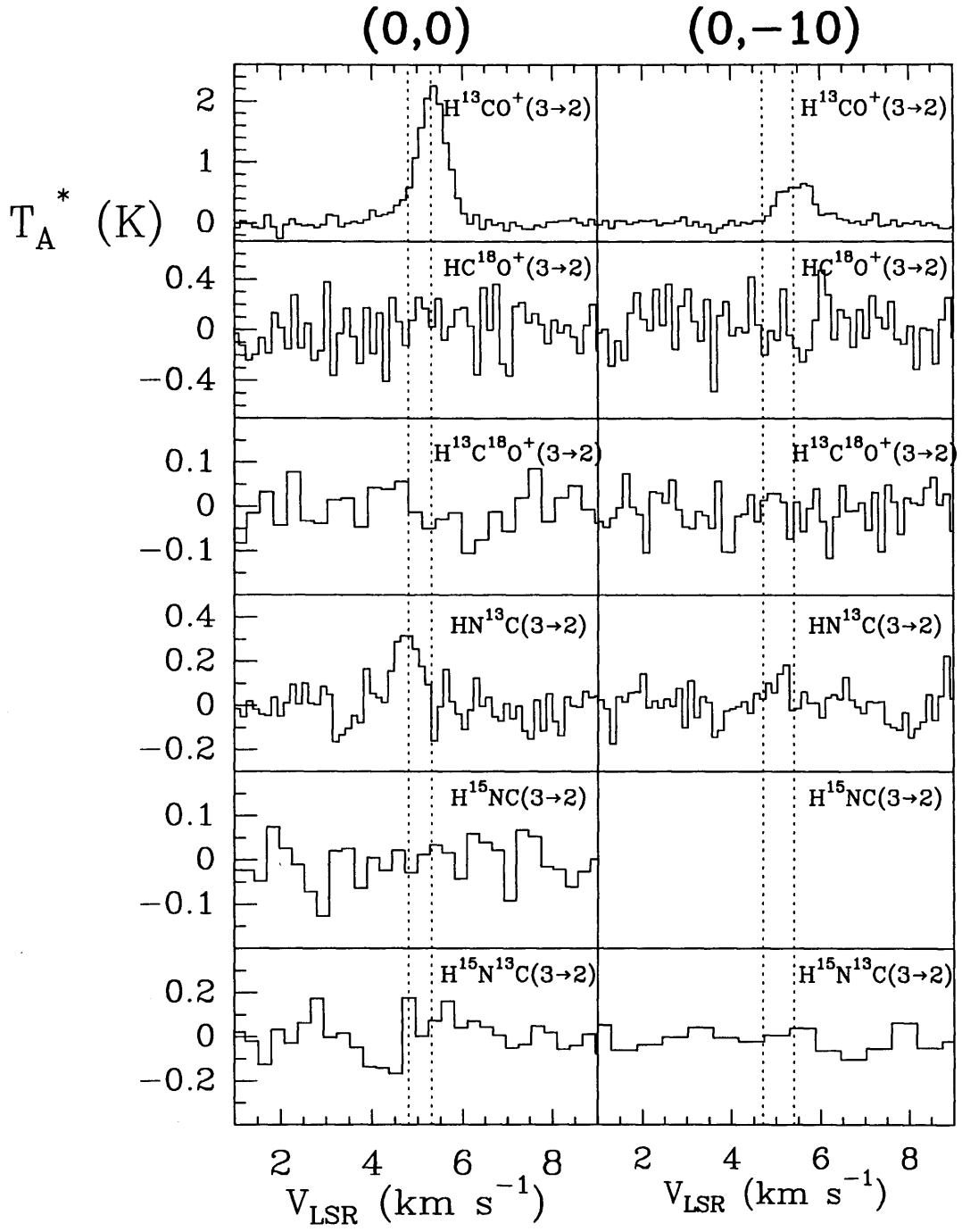

Figure 8.3: Observations of isotopes to calculate the opacity of $H^{13}CO^+$ and $HN^{13}C$. Offsets in arcseconds are shown in the upper part of the columns. The vertical dotted lines show the ambient gas at 4.7 km s^{-1} and the precursor component at 5.2 km s^{-1}. Figure generated by I. Jiménez-Serra.

Table 8.2: Observed parameters of the HCO^+, $H^{13}CO^+$, $HC^{18}O^+$, $H^{13}C^{18}O^+$, $HN^{13}C$, $H^{15}NC$ and $H^{15}N^{13}C$ $J = 3 \rightarrow 2$ lines. The upper limits of the line intensities correspond to the 3σ noise level. The upper limits of the integrated intensities are calculated by $3\sigma\sqrt{\Delta v \delta v}$, where Δv is the expected line-width (we have used ~ 0.8 km s^{-1} for all the isotopes in this table, assuming that they follow the line-widths of $H^{13}CO^+$ and $HN^{13}C$ in JS06), and δv is the spectral resolution. All the molecules were observed with the JCMT which has a beam size of 21″ and beam efficiency of 0.69 at $\sim$ 260 GHz, apart from those marked by *, which were observed with the IRAM 30m telescope, which has a beam size of 10″ and beam efficiency 0.52.

	(0,0)				(0,-10)			
	V_{LSR}	Δv	T_A^*	$\int T_A^* dv$	V_{LSR}	Δv	T_A^*	$\int T_A^* dv$
LINE	(km s^{-1})	(km s^{-1})	(K)	(K km s^{-1})	(km s^{-1})	(km s^{-1})	(K)	(K km s^{-1})
HCO^+	4.238	0.624	1.931	1.282	...	...	...	...
	5.674	0.856	3.381	3.079	...	...	...	...
*$H^{13}CO^+$	4.463	0.949	0.227	0.230	5.083	0.220	0.176	0.041
	5.350	0.712	2.207	1.674	5.522	0.900	0.646	0.619
$HC^{18}O^+$	$\sim$ 4.7	...	$\leq$ 0.423	$\leq$ 0.204	$\sim$ 4.7	...	$\leq$ 0.297	$\leq$ 0.201
	$\sim$ 5.2	...	$\leq$ 0.423	$\leq$ 0.204	$\sim$ 5.2	...	$\leq$ 0.297	$\leq$ 0.201
$H^{13}C^{18}O^+$	$\sim$ 4.7	...	$\leq$ 0.106	$\leq$ 0.052	$\sim$ 4.7	...	$\leq$ 0.189	$\leq$ 0.065
	$\sim$ 5.2	...	$\leq$ 0.106	$\leq$ 0.052	$\sim$ 5.2	...	$\leq$ 0.189	$\leq$ 0.065
*$HN^{13}C$	4.751	0.621	0.354	0.234	$\sim$ 4.7	...	$\leq$ 0.264	$\leq$ 0.087
	$\sim$ 5.2	...	$\leq$ 0.178	$\leq$ 0.088	$\sim$ 5.2	...	$\leq$ 0.264	$\leq$ 0.087
$H^{15}NC$	$\sim$ 4.7	...	$\leq$ 0.135	$\leq$ 0.063	...	...	...	....
	$\sim$ 5.2	...	$\leq$ 0.135	$\leq$ 0.063	...	...	...	....
$H^{15}N^{13}C$	$\sim$ 4.7	...	$\leq$ 0.273	$\leq$ 0.131	$\sim$ 4.7	...	$\leq$ 0.201	$\leq$ 0.136
	$\sim$ 5.2	...	$\leq$ 0.273	$\leq$ 0.131	$\sim$ 5.2	...	$\leq$ 0.201	$\leq$ 0.136

at (0,0) in the ambient component is 0.423 K on the T_A^* scale (which is 0.61 K on the T_{mb} scale), which is greater than the observed intensity of $H^{13}CO^+$ for the same position and component (0.227 K on the T_A^* scale, which is 0.099 K on the T_{mb} scale, having corrected for beam dilution), so we cannot calculate the opacity of $H^{13}CO^+$ using the observation of $H^{13}C^{18}O^+$.

The first method is described below:

Assuming that the rare isotopes of $H^{13}CO^+$ (i.e. $HC^{18}O^+$ and $H^{13}C^{18}O^+$) that we have observed are optically thin, then the column density of the upper level for these isotopes, N_u (cm^{-2}), can be estimated by (Rohlfs & Wilson 2000):

$$N_u = 1.93 \times 10^3 \frac{\nu^2}{A_{ul}} \int T_B dv \tag{8.1}$$

where ν is the frequency of the transition in GHz [equal to 255.48 GHz for $HC^{18}O^+(3 \rightarrow 2)$ and 247.92 GHz for $H^{13}C^{18}O^+(3 \rightarrow 2)$], A_{ul} is the Einstein A coefficient which gives the rate of

spontaneous transitions, and $\int T_{\rm B} dv$ is the integrated intensity of the brightness temperature, in K km s^{-1}. In this case, however, the source size and morphology are unknown, so we cannot work out the intrinsic brightness temperature of the source, and instead we have to use the main beam temperature ($T_{\rm mb}$), which is calculated from the antenna temperature, T_A^*, by $T_{\rm mb} = T_A^*/\eta_{\rm mb}$ (where $\eta_{\rm mb}$ are the main beam efficiencies given in Section 8.3.2). For a particular beam size the main beam temperature is related to the brightness temperature by $T_{\rm mb} = fT_{\rm B}$, where f is the beam filling factor. In these observations the source is smaller than the beam size, so f is less than unity and the integrated intensities will be an underestimate.

The value of A_{ul} for $HC^{18}O^+(3 \rightarrow 2)$ is 1.2756×10^{-3} s^{-1}, taken from the Leiden Atomic and Molecular Database (Schöier *et al.* 2005). The value for $H^{13}C^{18}O^+(3 \rightarrow 2)$ was not listed in this database, so we estimated it to be 1.3×10^{-3} s^{-1}, which is approximately the value for $HC^{18}O^+(3 \rightarrow 2)$ and $H^{13}CO^+(3 \rightarrow 2)$.

The column density of the lower level, N_l (cm^{-2}), can be calculated from N_u using:

$$\frac{N_u}{N_l} = \frac{g_u}{g_l} \exp\left(-\frac{h\nu}{kT_{\rm ex}}\right) \tag{8.2}$$

where g_u and g_l are the statistical weights of the upper and lower level, equal to 7 and 5 respectively for the $(3 \rightarrow 2)$ transitions (Schöier *et al.* 2005), and $T_{\rm ex}$ is the excitation temperature of the line. We have assumed that the excitation temperatures of $HC^{18}O^+$ and $H^{13}C^{18}O^+$ are the same as for $H^{13}CO^+$, which can be derived from the observations of JS06 using the LVG excitation model used in Section 8.3.1. Using the column densities and H_2 number densities given in table 3 of JS06, a kinetic temperature of 21 K (Curiel *et al.* 1999), a line-width of 0.8 km s^{-1} and an electron fractional abundance of 10^{-8} in the ambient component and 5×10^{-5} in the precursor component (see JS06), the LVG model calculates the excitation temperature of $H^{13}CO^+(3 \rightarrow 2)$ at (0,0) and (0,-10) to be 6 K in the ambient component and 9 K in the precursor component. These are the values we have adopted for the excitation temperatures of $HC^{18}O^+$ and $H^{13}C^{18}O^+$.

The column density of the lower level of $H^{13}CO^+$ can be calculated from the column density of the lower level of $HC^{18}O^+$ using:

$$N_l(H^{13}CO^+) = RN_l(HC^{18}O^+), \tag{8.3}$$

where R is the abundance ratio of $[H^{13}CO^+]/[HC^{18}O^+] = [^{13}C]/[^{12}C] \times [^{16}O]/[^{18}O]$, observed for the local interstellar medium. $N_l(H^{13}CO^+)$ can also be derived from $N_l(H^{13}C^{18}O^+)$, using the appropriate isotope ratio for R. We have derived the values of R using the elemental isotope ratios for the local interstellar medium from Wilson (1999), and these are summarised in Table 8.3.

Table 8.3: Isotope abundance ratios for the local interstellar medium taken from Wilson (1999)

The opacity of $H^{13}CO^+$ can now be calculated from N_l using the equation:

$$\tau\Delta v = \frac{g_{ul}c^3}{8\pi\nu^3}A_{ul}N_l\left[1-\exp\left(-\frac{h\nu}{kT_{\rm ex}}\right)\right] \tag{8.4}$$

where Δv is the line-width (we have used $\Delta v = 0.8$ km s^{-1} which is approximately the value found in JS06 for $H^{13}CO^+$), $g_{ul} = g_u/g_l = 7/5$ is the statistical-weight ratio of of the molecules in the upper and lower levels, ν is the frequency of the $H^{13}CO^+(3 \rightarrow 2)$ transition, equal to 260.26×10^9 Hz, and c, h and k are the speed of light, Planck's constant and Boltzmann's constant respectively. We have used the same values for $T_{\rm ex}$ as given above.

Since we have observed two isotopes of $H^{13}CO^+$ ($HC^{18}O^+$ and $H^{13}C^{18}O^+$), using this method we can derive two estimates for the opacity for both the ambient and precursor components at each position. We have also derived estimates of the opacity of $HN^{13}C$ at the same positions from the observations of $H^{15}N^{13}C$ and $H^{15}NC$ by this method, using the following values for the calculations: $\nu[H^{15}NC(3 \rightarrow 2)] = 266.59$ GHz, $\nu[H^{15}N^{13}C(3 \rightarrow 2)] = 255.77$ GHz, $\nu[HN^{13}C(3 \rightarrow 2)] = 261.26$ GHz, $A_{ul} = 7.6835 \times 10^{-4}$ s^{-1} (for all the isotopes of $HN^{13}C$), $T_{\rm ex} = 5$ K for the ambient component and 6 K for the precursor component, and $\Delta v = 0.8$ km s^{-1}. Since the value of A_{ul} was not listed in the Leiden Atomic and Molecular Database for all the isotopes of $HN^{13}C$ that we have observed, we have used the value of A_{32} for HNC and assumed that it will be the same for each isotope. The values of $T_{\rm ex}$ were calculated from the data in JS06 using an LVG model, as described above. The value of Δv was also estimated from the JS06 observations of $HN^{13}C$.

The derived opacities are summarised in Table 8.4. The upper limits for the opacity of $H^{13}CO^+$ and $HN^{13}C$ using the isotopes $H^{13}C^{18}O^+$ and $H^{15}N^{13}C$ respectively at both positions are rather high and do not help us very much to constrain the real values. However, the opacity of $H^{13}CO^+$ for the precursor component at both positions calculated from the $HC^{18}O^+$ emission is $\lesssim 0.7$, so it is definitely optically thin. The opacity of $HN^{13}C$ at (0,0) derived from the $HN^{15}C$ observations is

also optically thin in both components ($\tau \leq 0.6$ and ≤ 0.4 in the ambient and precursor components respectively).

Table 8.4: Opacities of $H^{13}CO^+$ and $HN^{13}C$ derived from observations of isotopes using the first method described in the text. The isotope used to calculate the opacities is given in column 2.

SPECIES	ISOTOPE USED	COMPONENT	τ
	(0,0)		
$H^{13}CO^+$	$HC^{18}O^+$	Amb.	≤ 1.7
		Pre.	≤ 0.74
	$H^{13}C^{18}O^+$	Amb.	≤ 26
		Pre.	≤ 11
$HN^{13}C$	$HN^{15}C$	Amb.	≤ 0.63
		Pre.	≤ 0.39
	$H^{15}N^{13}C$	Amb.	≤ 75
		Pre.	≤ 48
	(0,-10)		
$H^{13}CO^+$	$HC^{18}O^+$	Amb.	≤ 1.7
		Pre.	≤ 0.72
	$H^{13}C^{18}O^+$	Amb.	≤ 32
		Pre.	≤ 14
$HN^{13}C$	$H^{15}NC$	Amb	...
		Pre.	...
	$H^{15}N^{13}C$	Amb.	≤ 78
		Pre.	≤ 49

The second method used to calculate the opacities, which does not assume the emission from the rarer isotopes is optically thin, is described below:

The brightness temperature of a source which is attenuated by a medium of opacity τ, with the background emission subtracted, is given by:

$$T_B = [J(T_{ex}) - J(T_{bg})](1 - \exp(-\tau)), \tag{8.5}$$

where

$$J(T) = \frac{h\nu/k}{\exp(h\nu/kT) - 1}, \tag{8.6}$$

ν is the frequency of the transition, $T_{\rm ex}$ is the excitation temperature and $T_{\rm bg}$ is the background temperature.

As mentioned above, if the source is observed with a particular beam size, so that the source has a beam filling factor f, the observed main beam temperature is $fT_{\rm B}$. If we observe two different isotopes of a particular molecule (for the same transition so that the frequency is approximately the same), which have main beam temperatures $T_{\rm mb,1}$ and $T_{\rm mb,2}$, assuming the sources have the same morphology (and therefore the same f), and the same $T_{\rm ex}$, then we can take the ratio of the observed main beam temperatures to get:

$$\frac{T_{\rm mb,1}}{T_{\rm mb,2}} = \frac{1 - e^{-\tau_1}}{1 - e^{-\tau_2}}. \tag{8.7}$$

The ratio of the opacities, τ_1/τ_2 can be estimated using:

$$\frac{\tau_1}{\tau_2} = \frac{[1]}{[2]} = R \tag{8.8}$$

where R is the observed isotope abundance ratio in the local interstellar medium, given in Table 8.3.

Using this ratio, we can now solve for τ_1 and τ_2:

$$\frac{T_{\rm mb,1}}{T_{\rm mb,2}} = \frac{1 - e^{-R\tau_2}}{1 - e^{-\tau_2}}. \tag{8.9}$$

Because we observed several isotopes of $H^{13}CO^+$ and $HN^{13}C$, different estimates of τ for these molecules can be derived by using different isotope ratios. The results are summarised in Table 8.5.

As mentioned earlier, we cannot use this method if upper limits for the intensities of the isotopes which are expected to have small opacities are greater than the intensities (or upper limits of intensities) of the isotopes which are expected to have larger opacities. This is because if $\frac{T_{\rm mb,1}}{T_{\rm mb,2}}$ is less than unity, but $R = [1]/[2]$ is greater than unity (so we expect species '1' to have a larger opacity than species '2', because it is a more common isotope), then equation (8.9) does not have a solution. There were no detections for the rare isotopes of HNC, and since the RMS noise for the rare isotopes were greater than for $HN^{13}C$, no opacity could be estimated for $HN^{13}C$.

For $H^{13}CO^+$, reasonable estimates of the opacity could be obtained at (0,0) for both the ambient and precursor component, using the $H^{13}CO^+/HCO^+$ ratio. The estimates in both the precursor and ambient component are small, reassuring us that the $H^{13}CO^+$ emission is optically thin in this position, and that the over-excitation of $H^{13}CO^+$ in the precursor is *not* due to an opacity effect.

Using these two methods to calculate the opacity, we have shown that the $H^{13}CO^+$ emission at (0,0) and (0,-10) is definitely optically thin in the precursor component, and the second method reveals that it is also optically thin in the ambient component at (0,0). The first method shows that the $HN^{13}C$ emission is also optically thin at (0,0). Since $H^{13}CO^+$ is the line showing the over-excitation, and we have shown it to be optically thin, this shows that the over-excitation observed in this line is *not* due to opacity effects, and this supports our claim that the over-excitation is due to the magnetic precursor. The results also justify the use of a large velocity gradient approximation model to analyse the excitation of the molecules (which requires the emission to be optically thin).

Table 8.5: Opacities of $H^{13}CO^+$ derived from observations of isotopes using the second method described in the text.

RATIO USED	COMPONENT	T^1_{mb}/T^2_{mb}	$\tau(H^{13}CO^+)$	T_{ex}/K
	(0,0)			
$H^{13}CO^+/HCO^+$	Ambient	0.0353	0.0319	7.9
	Precursor	0.196	0.219	10.0
$HC^{18}O^+/H^{13}CO^+$	Ambient	< 6.205	...	...
	Precursor	< 0.637	< 8.47	> 4.9
$H^{13}C^{18}O^+/H^{13}CO^+$	Ambient	< 2.330	...	...
	Precursor	< 0.239	< 158	> 4.8
	(0,-10)			
$HC^{18}O^+/H^{13}CO^+$	Ambient	< 5.612	...	...
	Precursor	< 1.528	...	...
$H^{13}C^{18}O^+/H^{13}CO^+$	Ambient	< 3.571	...	...
	Precursor	< 0.972	< 207	> 3.5

8.3.4 Excitation differences between ion and neutral molecular species

Figure 8.4 shows the line profiles of SiO $J = 2 \rightarrow 1$, and the $J = 3 \rightarrow 2$ and $1 \rightarrow 0$ transitions of $H^{13}CO^+$ and $HN^{13}C$ measured at offsets (0,20), (20,0) and (-20,0) towards L1448-mm. The lines were fitted with double gaussians with $V_{LSR} \sim 4.7$ and 5.2 km s^{-1}, corresponding to the ambient and precursor components, the parameters of which are given in Table 8.6. The ambient and precursor component velocities are marked with dashed lines on Figure 8.4.

Narrow SiO($2 \rightarrow 1$) emission is detected at (-20,0), and very faintly at (20,0), with a line-width of ~ 0.5 km s^{-1} centred on ~ 5.2 km s^{-1}. The $J = 1 \rightarrow 0$ lines of $H^{13}CO^+$ and $HN^{13}C$ do not show double peaks as clearly as they do at the positions observed in JS06, but they are still well fitted by double gaussians centred on ~ 4.7 and ~ 5.2 km s^{-1}, with an average line-width of $\sim 0.7 - 0.8$ km s^{-1}. The $H^{13}CO^+(1 \rightarrow 0)$ lines peak in the ambient component at (0,20) and (20,0), but in the precursor component at (-20,0), where the detection of narrow SiO is more clear. The $HN^{13}C(1 \rightarrow 0)$ lines all have their peaks at the ambient velocity.

The $H^{13}CO^+(3 \rightarrow 2)$ lines at (20,0) and (0,-20) show single peak emission at ~ 5.2 km s^{-1}, whereas at (0,20) a double gaussian can be fitted. At (-20,0), the precursor components, where detected, have a slightly higher V_{LSR} than at the other positions, especially for $HN^{13}C(1 \rightarrow 0)$, which has $V_{LSR} \sim 5.6$ km s^{-1}. JS06 also reported a progressive redshift in the precursor components of $H^{13}CO^+$ in $HN^{13}C$ from 5.2 km s^{-1} at (0,0), to 5.4 km s^{-1} at (0,-10) and 5.6 km s^{-1} at (0,-20), and suggested that this may be due to an evolutionary effect of the shock, where the ion and neutral fluids may have slipped to larger velocities at later flow times within the shock. No signal was detected for $HN^{13}C(J = 3 \rightarrow 2)$ at any position above the 3σ noise level.

Table 8.6: Observed parameters of the SiO, $H^{13}CO^+$ and $HN^{13}C$ lines. The upper limits of the line intensities correspond to the 3σ noise level.

	(0,20)			(20,0)			(-20,0)		
	V_{LSR}	Δv	T_A^*	V_{LSR}	Δv	T_A^*	V_{LSR}	Δv	T_A^*
LINE	(km s^{-1})	(km s^{-1})	(K)	(km s^{-1})	(km s^{-1})	(K)	(km s^{-1})	(km s^{-1}	(K)
SiO($2 \rightarrow 1$)	4.751	0.809	0.030	~ 4.7	...	≤ 0.030	~ 4.7	...	≤ 0.036
	~ 5.2	...	≤ 0.027	5.069	0.477	0.037	5.289	0.512	0.060
$H^{13}CO^+(1 \rightarrow 0)$	4.597	0.625	0.748	4.645	0.590	0.737	4.606	0.869	0.485
	5.126	0.816	0.568	5.254	0.892	0.678	5.318	0.721	0.846
$H^{13}CO^+(3 \rightarrow 2)$	4.598	0.526	0.196	~ 4.7	...	≤ 0.213	~ 4.7	...	≤ 0.132
	5.328	0.681	0.361	5.1934	1.009	0.225	5.331	0.269	0.279
$HN^{13}C(1 \rightarrow 0)$	4.625	0.799	0.516	4.589	0.784	0.567	4.888	0.856	0.839
	5.224	0.795	0.145	5.242	0.854	0.399	5.579	0.633	0.212
$HN^{13}C(3 \rightarrow 2)$	~ 4.7	...	≤ 0.105	~ 4.7	...	≤ 0.111	~ 4.7	...	≤ 0.132
	~ 5.2	...	≤ 0.105	~ 5.2	...	≤ 0.111	~ 5.2	...	≤ 0.132

If there is an enhanced electron abundance in the precursor component, then the high excitation lines of $H^{13}CO^+$ should be much brighter than for $HN^{13}C$, because the electrons are able to selectively excite ions. The emission should be optically thin (see Section 8.3.3), so the line intensity ratio between different transitions is directly related to the excitation temperature of

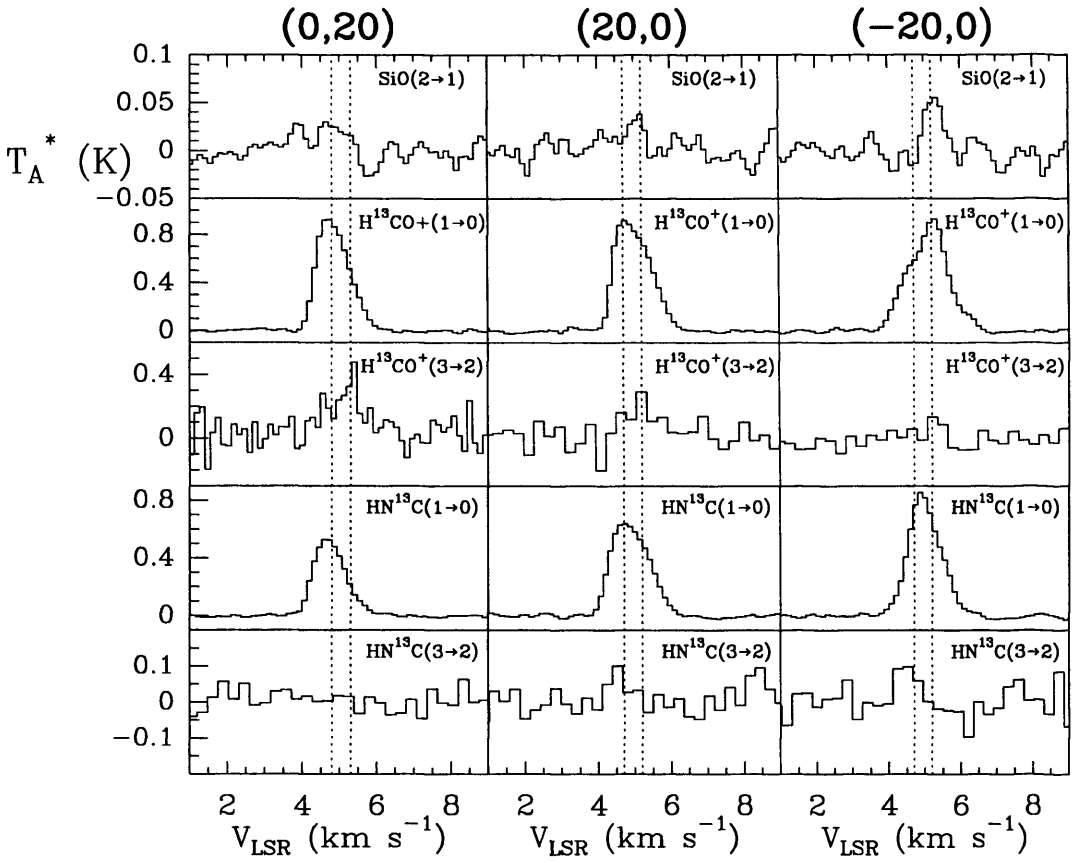

Figure 8.4: Observations of SiO(2 → 1) and the $J = 3 \rightarrow 2$ and $1 \rightarrow 0$ lines of $H^{13}CO^+$ and $HN^{13}C$. Offsets in arcseconds are shown in the upper part of the columns. The vertical dotted lines show the ambient gas at 4.7 km s^{-1} and the precursor component at 5.2 km s^{-1}. Figure generated by I. Jiménez-Serra.

the molecule. The integrated intensity ratios of the $(3 \rightarrow 2)/(1 \rightarrow 0)$ for $H^{13}CO^+$ and $HN^{13}C$ are given in Table 8.7. For all positions apart from (-20,0), the line ratio for *both* $H^{13}CO^+$ and $HN^{13}C$ is greater in the precursor component. Unlike the observations in JS06, the line ratio for the precursor component at each position is not substantially higher for $H^{13}CO^+$ than for the upper limits of $HN^{13}C$. This behaviour is expected because we believe the magnetic precursor interaction is restricted to the southern part of the outflow where very young shocks have been reported by Girart & Acord (2001).

This is also qualitatively shown by the H_2 gas densities derived from the intensity ratios in Table 8.8, which assume collisional excitation by H_2 only. As the excitation model for these molecules, we used the large velocity gradient (LVG) approximation excitation model discussed in Section 8.3.1. The kinetic temperature was assumed to be 21 K, and we used a line-width of

0.8 km s^{-1} for both molecules.

For $H^{13}CO^+$, the precursor component requires an H_2 density which is only $\sim 1.2 - 3$ times greater than for the ambient component, which is not a significant difference, especially when compared to the results of JS06 who found that the required H_2 density in the precursor component was ≥ 10 times higher than in the ambient component at the positions they observed. For $HN^{13}C$, the derived upper limits for the H_2 density from this molecule are consistent with those calculated by JS06 for the (0,0), (0,-10) and (0,-20) positions.

These results imply that there is no over-excitation of $H^{13}CO^+$ at (0,20), (20,0) and (-20,0), and therefore no extra mechanism in the precursor component is required to explain the observations.

Table 8.7: Integrated line intensity ratios $(3 \rightarrow 2)/(1 \rightarrow 0)$ (in T_A^* units)

	(0,20)		(20,0)		(-20,0)	
MOLECULE	Ambient	Precursor	Ambient	Precursor	Ambient	Precursor
$H^{13}CO^+$	0.220	≤ 0.530	0.218	0.375	≤ 0.139	0.123
$HN^{13}C$	≤ 0.113	≤ 0.404	≤ 0.111	≤ 0.145	≤ 0.074	≤ 0.437

Table 8.8: Derived H_2 number densities and column densities for $H^{13}CO^+$ and $HN^{13}C$.

	H_2 DENSITY (cm^{-3})		COLUMN DENSITY (cm^{-2})	
MOLECULE	Ambient	Precursor	Ambient	Precursor
		(0,20)		
$H^{13}CO^+$	7.9×10^4	2.3×10^5	6.3×10^{11}	4.4×10^{11}
$HN^{13}C$	$\leq 1.9 \times 10^5$	$\leq 9.5 \times 10^5$	$\leq 1.1 \times 10^{12}$	$\leq 2.3 \times 10^{11}$
		(20,0)		
$H^{13}CO+$	$\leq 9.1 \times 10^4$	1.1×10^5	$\leq 6.3 \times 10^{11}$	5.6×10^{11}
$HN^{13}C$	$\leq 1.8 \times 10^5$	$\leq 3.2 \times 10^5$	$\leq 1.2 \times 10^{12}$	$\leq 7.0 \times 10^{11}$
		(-20,0)		
$H^{13}CO^+$	$\leq 8.5 \times 10^4$	1.1×10^5	$\leq 4.2 \times 10^{11}$	7.1×10^{11}
$HN^{13}C$	$\leq 1.0 \times 10^5$	$\leq 7.9 \times 10^5$	$\leq 2.6 \times 10^{12}$	$\leq 3.3 \times 10^{11}$

8.3.5 Conclusions

The observations for positions (0,20), (20,0) and (-20,0) do not show evidence for an electron density enhancement, implying that the magnetic precursor is not present in these positions. Furthermore, the SiO($2 \rightarrow 1$) line at these positions is also quite weak, compared to the SiO emission at (0,0), (0,-10) and (0,-20) in JS06. Looking at Figure 8.1, it shows that the regions where the precursor is confirmed (the positions observed in JS06, marked with stars) extend down into the redshifted lobe of the outflow. At the positions marked with circles (the observations for this work), the precursor is not observed.

Girart & Acord (2001) detected very young shocks (with a dynamical age $\leq$ 90 yr) at approximately (0,-10) towards L1448-mm, and since our results have shown the over-excitation of ions is also confined to this region, this is strong evidence to suggest that the over-excitation is produced by the electron density enhancement in the magnetic precursor associated with these young shocks. Furthermore, the confinement of the over-excitation of ions also means that the effect is unlikely to be caused by UV illumination, as this is expected to be a large scale effect.

We have also confirmed that the over-excitation of ions is not due to an opacity effect, as observed by Cernicharo *et al.* (1984) for the hyperfine components of HCN. This effect would require the emission to be optically thick, but we have shown that the $H^{13}CO^+$ emission is optically thin at (0,0) and (0,-10), and the $HN^{13}C$ emission is optically thin at (0,0). In addition, since the HCN hyperfine anomalies reported by Cernicharo *et al.* (1984) were a result of the re-emission of the radiation from the dense regions of the cores in HCL2 over a large volume, they were therefore observed over a large area. If a similar effect is responsible for the over-excitation of $H^{13}CO^+$ in L1448-mm, then we would also expect the emission to be observed on large scales, and not confined to a small region as we have observed.

By re-analysing the observations of JS06 using new collisional coefficients for e^- – SiO and e^- – $HN^{13}C$ (Faure *et al.* 2007; Faure 2008), we have shown that the predicted intensities from the LVG model using an electron density enhancement of approximately 500 times in the precursor compared to the ambient gas are still consistent with the old observations. There is therefore compelling evidence for an electron density enhancement of $\sim$ 500 times in the precursor component of the gas, and this is very likely a result of the early interaction of C-type shocks with the ambient gas.

In order to fully understand the extent of the magnetic precursor, high spatial resolution observations of the high excitation lines of $H^{13}CO^+$ and $HN^{13}C$, taken with interferometers such as the Submillimeter Array (SMA), would be highly desirable. It is also necessary to search for signs

of the electron density enhancement in other young outflows where narrow SiO has been detected, such as L1448-IRS3, NGC1333-IRS4 and NGC1333-IRS2, in order to investigate whether the electron density enhancement is a common phenomenon in this type of object, and if it is always associated with narrow SiO emission.

8.4 Part II: C-shock model

In this next section we present the preliminary results from a chemical model, in which a molecular cloud is subjected to the propagation of a C-shock. This is to simulate the conditions experienced by the gas in a young molecular outflow source, such as L1448-mm. In the model we include the non-thermal enhancement of ion-neutral reaction rates due to ion-neutral drift in the magnetic precursor of the shock, to see if we can identify any chemical tracers of the precursor interaction. This will help to confirm whether the narrow SiO and selective excitement of ions observed in L1448-mm are indeed a result of the magnetic precursor.

The chemistry of C-shocks was investigated in a series of papers some 20 years ago (Flower *et al.* 1985; Pineau des Forets *et al.* 1986*a*,*b*, 1987, 1989). The models used in these papers *did* include the enhancement of the ion-neutral drift reactions owing to ambipolar diffusion, but the reaction sets were limited and included fewer than 300 chemical reactions. They also neglected to include gas-grain interactions; the 'injection' of species released from the mantles of dust grains by sputtering in a shock have the potential to drastically alter the gas-phase chemistry.

In the model presented here, we use reaction sets with nearly 2000 gas-phase chemical reactions. The model includes freeze-out of species onto dust grains during a collapse phase prior to the propagation of the shock, and unsaturated species are assumed to hydrogenate on the grain surface as described in Section 2.2.2. Sputtering by dust grains is also included. We specifically investigate the effect of ambipolar diffusion on ion-neutral reactions. We discuss the physical and chemical model in Section 8.4.1, the results in Section 8.4.2 and the discussion and conclusions in Section 8.4.3.

8.4.1 The model

Our model is based on the model developed by Jiménez-Serra & Viti (2008). This is a single point model which approximates the C-shock structure using parametric equations (Jiménez-Serra *et al.* 2008). The ion and neutral velocities, in the frame of the pre-shock gas, are given by:

$$v_{\mathrm{n,i}} = (v_{\mathrm{s}} - v_0) - \frac{v_{\mathrm{s}} - v_0}{\cosh[(z - z0)/z_{\mathrm{n,i}}]}, \tag{8.10}$$

where v_s is the shock velocity, z is the spatial coordinate, z_n/z_i is a measure of the ion-neutral decoupling, z_0 corresponds to the distance at which the ion and neutral fluids decouple, and v_0 is the final downstream velocity of the ion and neutral fluids in the frame of the shock. The temperature of the neutral fluid is given by:

$$T_n = T_0 + \frac{[a_T(z - z_0)]^{b_T}}{\exp[(z - z_0)/z_T] - 1} \tag{8.11}$$

where b_T is an integer, and a_T and z_T depend on the maximum value of T_n ($T_{n,max}$) at the distance $z_{n,max}$. The temperature of the ion fluid is calculated by $T_i = T_n + mv_d^2/3k$, where $v_d = v_i - v_n$ is the ion-neutral drift velocity. The values used for these parameters are given in Table 8.9, and are the same as those used in Jiménez-Serra *et al.* (2008) for a shock velocity of 30 km s^{-1}. These parameters were chosen to reproduce the physical structure of a shock of this velocity generated by MHD modelling (see Section 4.1 of Jiménez-Serra *et al.* 2008 for more details).

We model the time dependent evolution of a single parcel of gas as it passes through the C-shock described above. The 'time' referred to is the *neutral fluid flow time*, and can be considered as the characteristic dynamical time across the shock. It is related to the distance along the shock by:

$$t = \int \frac{\mathrm{d}z}{v_s - v_n} \tag{8.12}$$

Table 8.9: Parameters of C-shock model

PARAMETER	VALUE
v_s	30.0 km s^{-1}
a_T	2.0×10^{-15}
b_T	6.0
T_0	10 K
v_0	4.34 km s^{-1}
z_n/z_i	4.5
z_0	0

The model is run in two stages. The first stage starts from a diffuse medium (with n_H = 100 cm^{-3}) in atomic form apart from hydrogen, which is 50% molecular (by number), and undergoes free-fall collapse until the typical densities of the ambient gas surrounding molecular outflows are reached ($n_H = 10^5$ cm^{-3}, see Part I of this chapter). The temperature during this

stage is held constant, at 10 K. Freeze-out of gas-phase species onto dust grains is included in this stage, according to equation (2.18). Species are assumed to hydrogenate when they freeze-out, as described in Section 2.2.2. The final abundances of the first stage are then used as the initial abundances of the second stage, the C-shock, where the physical conditions in the shock are governed by the above equations. The physical conditions of the gas during this stage are shown in Figure 8.5.

The reason we have adopted a two-stage model is so that the ice mantle composition in the second stage is is derived by a time dependent computation of the chemical evolution of the gas-dust interaction process, rather than simply assuming an initial mantle composition. By the end of the first stage, 50% of CO has frozen out onto dust grains, which is the same degree of freeze-out as used in Jiménez-Serra & Viti (2008).

The initial elemental abundances for this model are given in Table 8.10, and are taken from Viti & Williams (1999).

Table 8.10: Initial elemental abundances.

H	1.00
C	1.79×10^{-4}
O	4.45×10^{-4}
N	8.52×10^{-5}
S	1.43×10^{-6}
He	7.50×10^{-2}
Mg	5.12×10^{-6}

The chemical reaction network is the same as in Chapter 3. The initial visual extinction is 0.0135 mag at $n_{\rm H} = 100$ cm^{-3}, which increases to 12.15 mag at $n_{\rm H} = 10^5$ cm^{-3}.

Freeze-out is halted in the second stage of the model, and instantaneous evaporation of the grain mantles occurs once $t > t_{\rm sat} = 4.4$ yr. $t_{\rm sat}$ is the *saturation time*, and is a measure of the time taken for the shock to evaporate all the grain mantle species by sputtering. Jiménez-Serra *et al.* (2008) calculated values of $t_{\rm sat}$ for shocks with velocities ranging from 10 km s^{-1} to 40 km s^{-1} and densities ranging from $10^4 - 10^6$ cm^{-3}, by calculating the yield of silicon sputtered from the grain mantles and cores by considering collisions with the species H_2, He, C, O, Si, Fe and CO, and the value we have used ($t_{\rm sat} = 4.4$ yr) is taken for a shock with a $v_{\rm s} = 30$ km s^{-1} and $n_{\rm H} = 10^5$ cm^{-3}.

For higher densities the saturation time decreases as $\propto n^{-1}$ (see Jiménez-Serra *et al.* 2008).

The fundamental difference between our model and the model of Jiménez-Serra *et al.* (2008) is that we include the 'enhancement' of ion-neutral reactions due to ambipolar diffusion. As described in Chapter 7, we define an effective temperature $T_{\rm eff}$, given by:

$$\frac{3}{2}kT_{\rm eff} = \frac{3}{2}kT_{\rm n} + \frac{1}{2}\mu v_{\rm d}^2, \tag{8.13}$$

which is used instead of the kinetic temperature to calculate the rates of the temperature dependent ion-neutral reactions *only*. This is to take into account the increased rate of collisions between ion and neutral species by the streaming of ions through the neutral species. The remaining temperature dependent reaction rates are calculated using the neutral gas temperature. We refer to the use of $T_{\rm eff}$ instead of $T_{\rm n}$ as the non-thermal 'enhancement' of the rates, even though the rates of some ion-neutral reactions actually decrease. The rates which decrease with increasing temperature are generally those for which the neutral species has a large, permanent dipole moment, so 'dipole locking' effects occur at low temperatures, resulting in a temperature dependence of $T^{\sim -0.5}$. For example, the reaction:

$$\rm H^+ + HCN \rightarrow HCN^+ + H \tag{8.14}$$

has a rate constant $k = 1.05 \times 10^{-8} \times (T/300)^{-0.13}$ cm^3 s^{-1}, because HCN has a strong permanent electric dipole moment of 2.98 Debye (Le Teuff *et al.* 2000). Once the temperature is greater than $\sim$ 300 K, the dipole locking is no longer effective, so for $T_{\rm eff} > 300.0$ (and for $T > 300.0$ when we run the model without the non-thermal rate enhancements), we set $\beta = 0.0$ for these reactions.

The maximum ion-neutral drift velocity in this model is $v_{\rm i} - v_{\rm n} = 18.2$ km s^{-1}, so the effective temperature can be more than 13,400 K higher than the kinetic temperature (which is 123 K at this time), which is likely to cause a large perturbation to the gas-phase chemistry.

8.4.2 Results

Figure 8.6 shows examples of the abundances during the collapse phase of the model, as a function of time. It shows that at $\sim 3 \times 10^6$ yr, the abundances of these molecules begin to increase. This is because the density of the core begins to rapidly increase around this point, which increases the rate of collisions and therefore the rate of formation of molecules, and also decreases the rate of destruction of molecules by photoreactions, because of the increase in visual extinction. By the time the core reaches its final density of 10^5 cm^{-3}, 50% of CO has depleted onto dust grains, so the gas-phase is still relatively molecule rich.

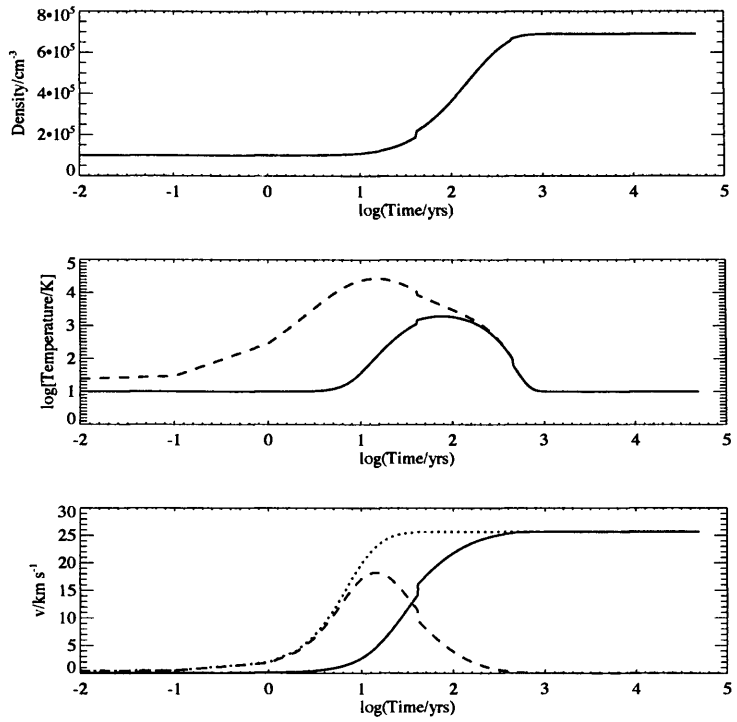

Figure 8.5: The physical structure of the C-shock used in this model, using the parametrised equations as described in Section 8.4.1. Top panel: The density of the neutral fluid; middle panel: the temperature of the neutral fluid (solid line) and ion fluid (dashed line); bottom panel: the velocity of the neutral fluid (solid line), the velocity of the ion fluid (dotted line), and the ion-neutral drift velocity (dashed line). The velocities are given relative to a frame co-moving with pre-shock gas.

Figures 8.7 to 8.10 show the evolution of the fractional abundances of the species which appear to be most sensitive to the inclusion of the non-thermal rate enhancements of ion-neutral reactions. The solid line shows the results of the model without the enhancement of the ion-neutral rates (so the temperature used to calculate the rates of all reactions is T_n), and the dotted line shows the results of the model *with* the enhancement of ion-neutral reaction rates due to ambipolar diffusion (so the ion-neutral reaction rates are calculated using T_{eff} rather than T_n).

Because of the complicated behaviour of the molecules and their highly time dependent nature, it is impossible to generate meaningful diagnostics from these figures. Instead, we focus on the differences between the results with and without the non-thermal rate enhancements. The behaviour of the molecules, in particular the sulphur chemistry, is discussed in more detail in Jiménez-Serra & Viti (2008).

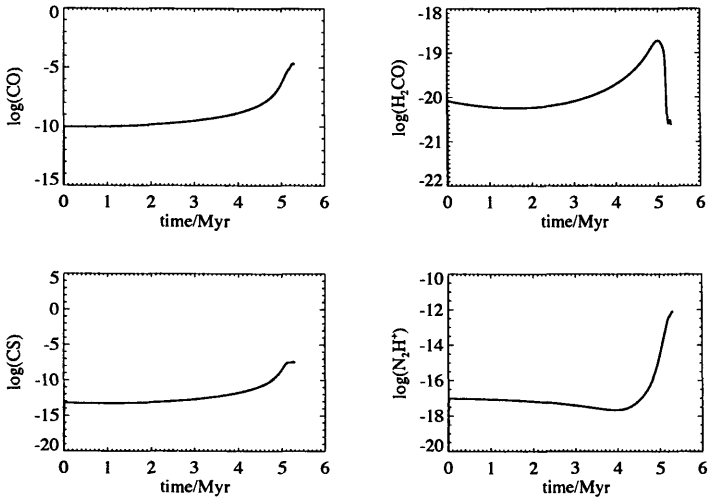

Figure 8.6: Fractional abundances of CO, H_2CO, CS and N_2H^+ in stage (i) (the collapse phase) of the model.

For most of the species plotted, the point at which the mantles are evaporated, just after $t_{sat} = 4.4$ yr, can clearly be seen by a sharp increase in gas-phase abundances. There are a few species, however, whose abundances decrease. These are H^+, C^+, S^+, N^+ and C_2N^+. The reasons that these abundances decrease are as follows:

H^+: Any H^+ on the grain surface is assumed to hydrogenate other species, so when the grain mantles are released, all the hydrogen from the grain surface is locked up in larger species. Ionic hydrogen, therefore, is not released into the gas-phase at this point so its abundance does not increase. The H^+ already in the gas-phase is then destroyed by the species that have just been released, particularly CH_4 and H_2O.

C^+, S^+ and N^+: When these ions freeze-out onto grain surfaces, they are assumed to hydrogenate instantly to form CH_4, H_2S and NH_3 respectively. Therefore, like H^+, these ions are not released from the grain mantles when the evaporation takes place. Furthermore, as the temperature of the gas increases due to the shock, the following endothermic reactions can be initiated:

$$C^+ + H_2 + \Delta E_1 \rightarrow CH^+ + H \tag{8.15}$$

$$S^+ + H_2 + \Delta E_2 \rightarrow HS^+ + H \tag{8.16}$$

$$N^+ + H_2 + \Delta E_3 \rightarrow NH^+ + H, \tag{8.17}$$

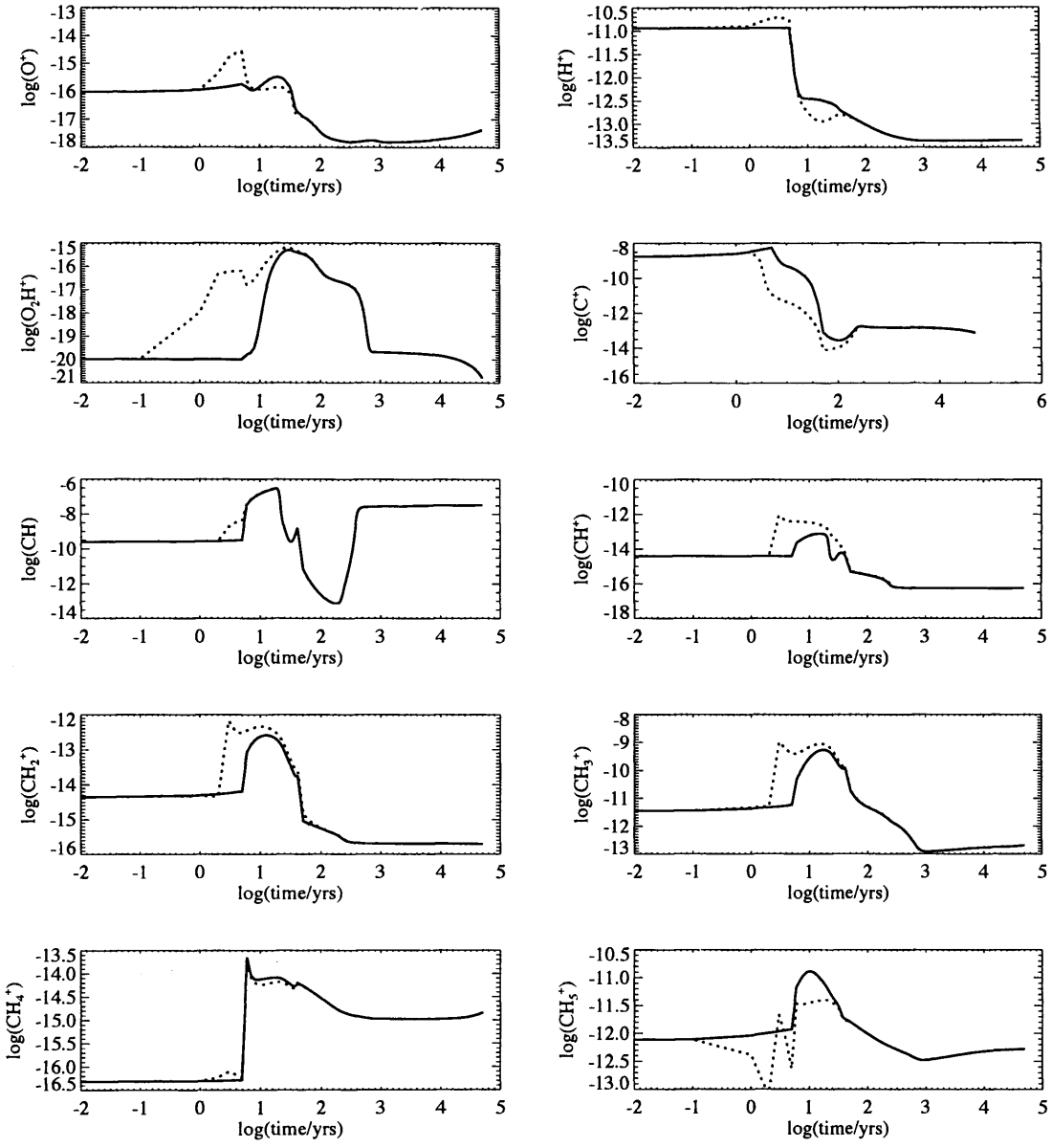

Figure 8.7: The evolution of molecules in a C-shock. The dotted and solid lines show the results from the model with and without the non-thermal rate enhancements due to ion-neutral drift in the precursor respectively.

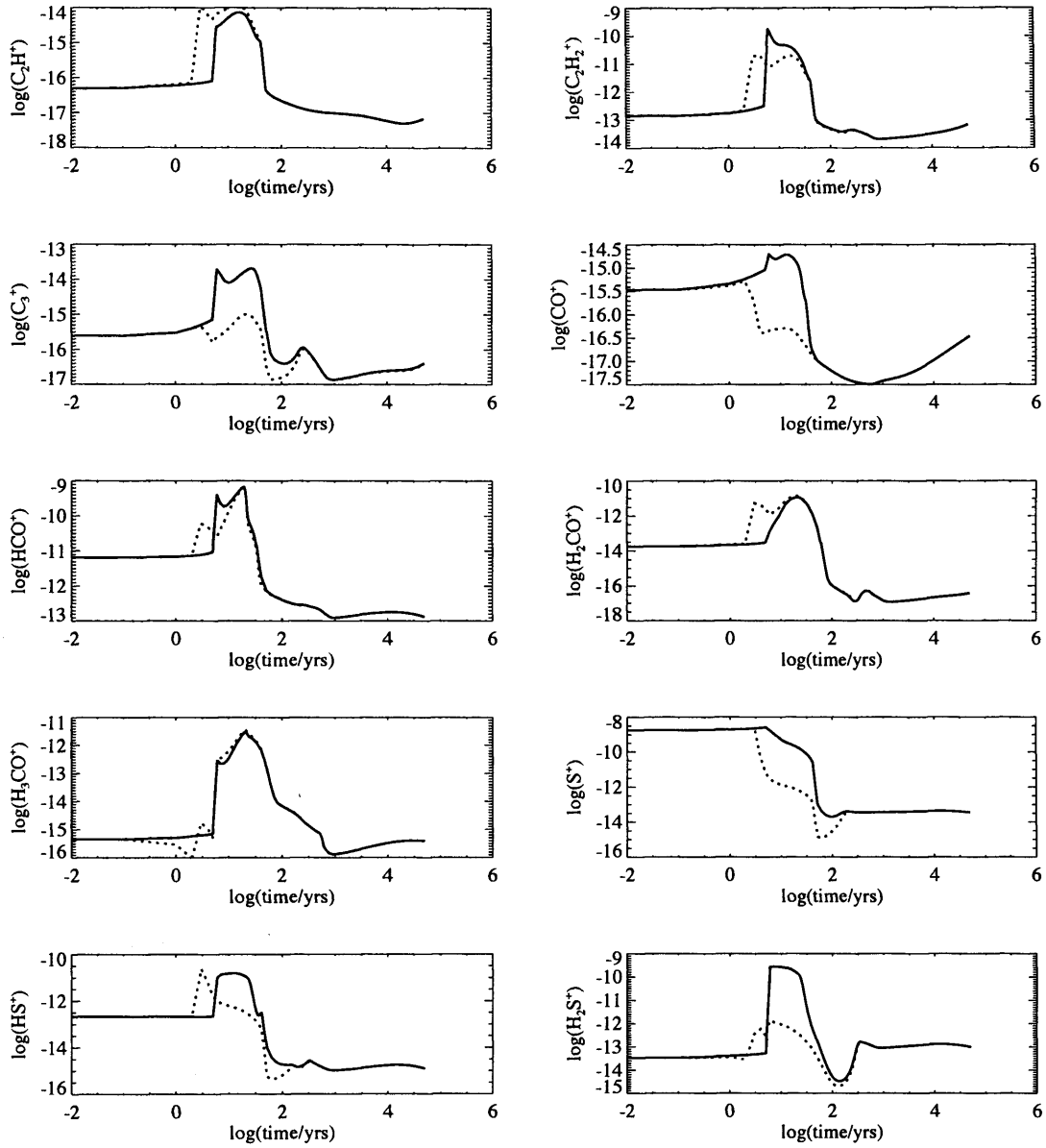

Figure 8.8: As in Figure 8.7, but for different molecules.

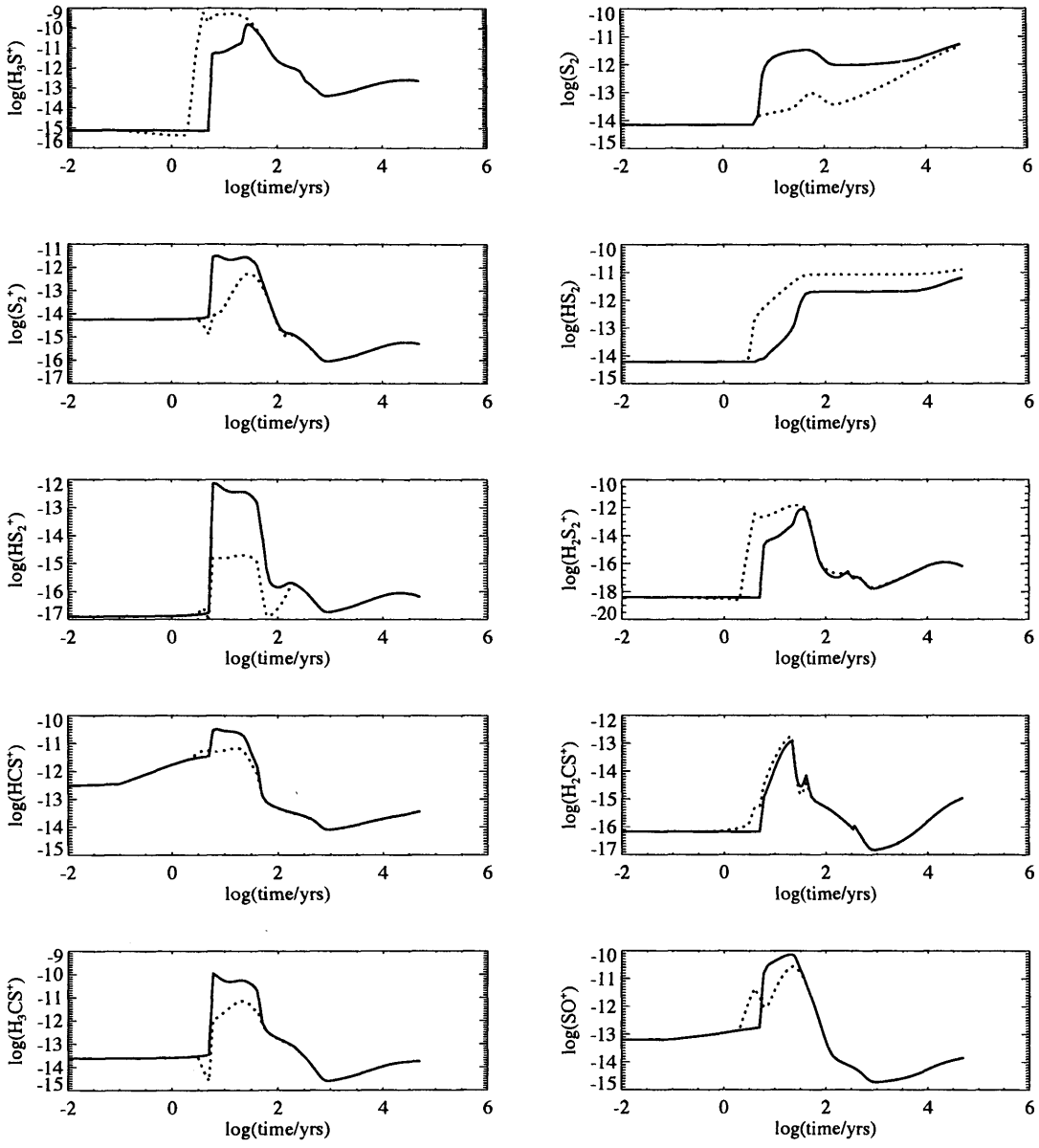

Figure 8.9: As in Figure 8.7, but for different molecules.

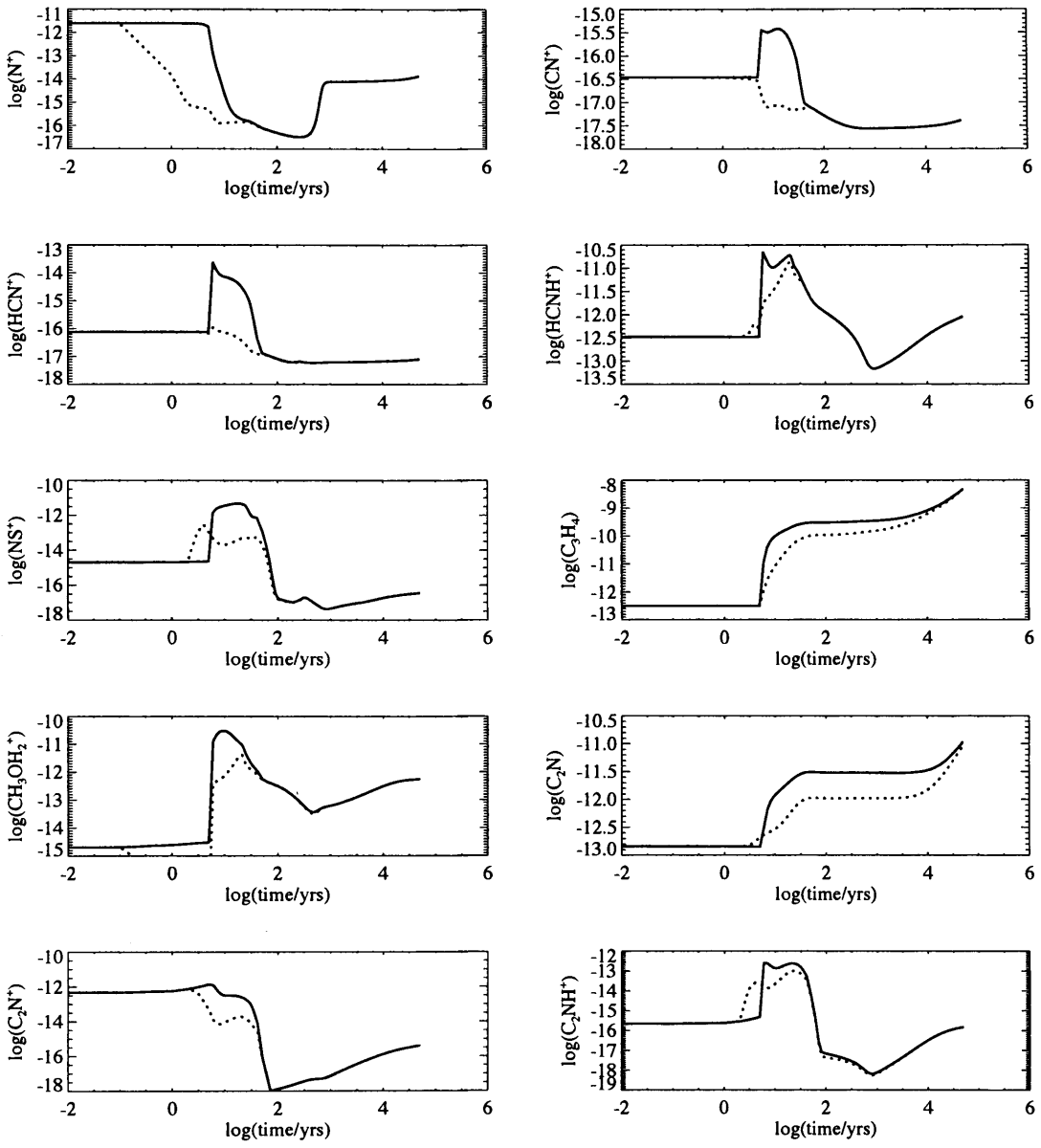

Figure 8.10: As in Figure 8.7, but for different molecules.

where $\Delta E_1 = 4640$ K, $\Delta E_2 = 9860$ K and $\Delta E_3 = 85.0$ K. This also explains why the abundances of C^+, S^+ and N^+ are even lower when the non-thermal enhancement of ion-neutral reaction rates is included (see Figures 8.7 to 8.10).

C_2N^+: Large amounts of NH_3 are released when the grain mantles evaporate, because NH_3 is a saturated species and so forms efficiently on the grain surfaces. The newly released NH_3 then destroys C_2N^+ by the reaction

$$NH_3 + C_2N^+ \rightarrow HCNH^+ + HCN, \tag{8.18}$$

resulting in a decrease in the C_2N^+ abundance.

The results in Figures 8.7 to 8.10 show that many molecules have a large response to the non-thermal rate enhancements in the magnetic precursor, and show significant changes in abundance *before* the mantle evaporation takes place. Examples of such species are O^+, CH^+, CH_2^+ and CH_3^+. Some molecules, such as O_2H^+, CH_5^+ and N^+ respond to the precursor at times as early as 10^{-1} yr. Other molecules, such as S_2 and HS_2^+ only respond to the precursor once the mantles have been evaporated. For these species, they can only form efficiently once the H_2S has been released from the grain mantles, so we can only see their response to the precursor after H_2S has been released.

The two models (with and without the non-thermal ion-neutral rate enhancements) converge after $\sim 10^2$ yr for most molecules. At this point, the ion-neutral drift velocity is only ~ 3.8 km s^{-1}, giving rise to effective temperatures of $T_n + 580\mu$ K, where μ is the reduced mass of the reactants. T_n, the neutral gas temperature, is ~ 1850 K at this point, and so dominates the contribution to T_{eff}.

Molecules such as S_2, HS_2, C_3H_4 and C_2N retain their 'memory' of the ion-neutral drift in the magnetic precursor for up to 10^4 yr. This is because the gas-phase reactions involving these species are relatively slow, so it takes them longer to 'catch-up' to the abundances in the model without the non-thermal rate enhancements.

It is clear that the species most affected by the enhanced ion-neutral rates are molecular ions, as we would expect. The abundances can both increase and decrease with respect to the model without non-thermal rate enhancements. We discuss some of the molecules in more detail below.

CH^+: The reaction

$$H_2 + C^+ \rightarrow CH^+ + H \tag{8.19}$$

has an energy barrier of 4640 K. After ~ 3 yr, this reaction becomes 'activated' in the model with the non-thermal enhancements. At this point the kinetic temperature of the gas is only

10.3 K, but the drift velocity is 6.1 km s^{-1}, making the effective temperature of this reaction $\sim$ 2800 K. It is therefore able to proceed at a much earlier time, when the non-thermal reaction rates are taken into consideration, causing an increase in CH^+ abundance and a decrease on C^+.

O_2H^+: The main formation route of O_2H^+ is the reaction:

$$H_3^+ + O_2 \rightarrow O_2H^+ + H_2, \tag{8.20}$$

which has an energy barrier of 150 K. At early times ($\lesssim$ 10 yr), when the neutral temperature is still $\lesssim$ 40 K, the effective temperature is already $\sim$ 30000 K, so this reaction can proceed at its maximum rate. Without the non-thermal rate enhancements, the O_2H^+ does not increase until the neutral temperature reaches $\sim$ 150 K, which occurs at $\sim$ 18 yr.

CO^+: The CO^+ abundance actually decreases when the non-thermal rate enhancements are included, even though the rate of the production reaction

$$O^+ + CO \rightarrow CO^+ + O, \tag{8.21}$$

which has an activation energy barrier of 4580 K, increases. This is because reaction (8.21) is only a minor production route for CO^+. The main production route for CO^+ is

$$C^+ + OH \rightarrow CO^+ + H, \tag{8.22}$$

the rate of which is independent of temperature. Since the C^+ abundance decreases when the non-thermal rate enhancements are included [see reaction (8.19)], this results in an overall decrease in the abundance of CO^+.

Sulphur chemistry: The reactions

$$H_2 + S^+ \rightarrow HS^+ + H \tag{8.23}$$

$$H_2 + HS^+ \rightarrow H_2S^+ + H \tag{8.24}$$

$$H_2 + H_2S^+ \rightarrow H_3S^+ + H \tag{8.25}$$

have activation energy barriers of 9860 K, 6380 K and 2900 K respectively, which can be overcome earlier with the inclusion of the non-thermal enhancements. This causes the abundances of S^+, HS^+, H_2S^+ to fall, but the abundance of H_3S^+ increases, because it is the final product of the above reactions. One would also expect the abundance of H_2S to

increase, by the reaction $H_3S^+ + e^- \rightarrow H_2S + H$, but this is not the case. The abundance of H_2S is unaffected by the inclusion of the non-thermal rate enhancements, because in this model the primary route of production of H_2S is on the grain surfaces. When H_2S is released from the grain mantles it dwarfs the extra gas-phase production due to the ion-neutral drift.

8.4.3 Discussion and conclusions

To draw any meaningful conclusions from our models, we have to consider if the differences between the models with and without the non-thermal enhancement of ion-neutral rates would be observable with current technology.

If we consider single-dish telescopes such as the JCMT and IRAM 30m, a typical beam size is $\sim 20''$ at ~ 200 GHz (with smaller beam sizes for higher frequencies and larger beam sizes for lower frequencies). At the distance of L1448-mm (300 pc), this corresponds to a size of 0.03 pc.

Since we are using a steady state shock model, the abundances as a function of time can be converted to the abundances as a function of distance using $dz = (v_s - v_n)dt$. Using this formula, a distance of 0.03 pc from the 'shock front'[2] corresponds to a time of approximately 6.3×10^3 yr. Looking at Figure 8.5, the duration of the precursor (i.e. the time for which there is significant ion-neutral decoupling) is $\sim$ 100 yr, which corresponds to a size of $\sim$ 0.001 pc, therefore the precursor itself would not be resolvable with single-dish observations. Instead, if the precursor was observed by such a single-dish telescope, the abundances would be averaged over the $20''$ (0.03 pc) beam (corresponding to the average abundances for $t \lesssim 6.3 \times 10^3$ yr on Figures 8.7 to 8.10). In Table 8.11, we estimate the average fractional abundances over a $20''$ beam (0.03 pc) centred on the precursor for the models both with and without the non-thermal enhancements of ion-neutral reaction rates using $\langle X(i) \rangle = \int X(i)dz/0.03$ pc. The ratio of the predicted fractional abundances from each model, $\langle X(i)_{\text{enhanced rates}} \rangle / \langle X(i)_{\text{standard rates}} \rangle$ is given in the third column. The molecules in Table 8.11 were selected because they all show differences between the two models of factors greater than two.

Given the uncertainties in determining fractional abundances from observations, we estimate that differences in abundances of a factor $\gtrsim 5$ would be needed to distinguish observationally between each model. The molecules which show differences of this magnitude are CH^+, C_3^+, CO^+, HS^+, H_2S^+, H_3S^+, HS_2^+, HCN^+, NS^+ and $H_4C_2N^+$. Some of these species are not directly observable so we cannot use all of them as tracers of the precursor. CH^+ and CO^+, however, are

[2]The term 'shock front' does not really apply to C-shocks, so here what we actually mean is the point (in time or space) where the pre-shock gas first feels the effect of the approaching shock.

Table 8.11: The predicted fractional abundances, $\langle X(i) \rangle$, averaged over a 20″ beam for selected molecules using both the standard and enhanced ion-neutral rates. The ratio in column three is given by $\langle X(i)_{\text{enhanced rates}} \rangle / \langle X(i)_{\text{standard rates}} \rangle$.

SPECIES	$\langle X(i)_{\text{standard rates}} \rangle$	$\langle X(i)_{\text{enhanced rates}} \rangle$	RATIO
C^+	3.15×10^{-11}	9.76×10^{-12}	0.31
CH^+	9.94×10^{-16}	6.18×10^{-15}	6.22
CH_2^+	3.89×10^{-15}	7.95×10^{-15}	2.05
$C_2H_2^+$	1.02×10^{-12}	4.08×10^{-13}	0.40
C_3^+	4.32×10^{-16}	4.28×10^{-17}	0.10
CO^+	3.82×10^{-17}	8.07×10^{-18}	0.21
S^+	2.24×10^{-11}	8.85×10^{-12}	0.40
HS^+	2.30×10^{-13}	4.36×10^{-14}	0.19
H_2S^+	3.65×10^{-12}	1.15×10^{-13}	0.03
H_3S^+	2.38×10^{-12}	1.19×10^{-11}	4.99
S_2	1.30×10^{-12}	3.28×10^{-13}	0.25
S_2^+	7.22×10^{-14}	1.09×10^{-14}	0.15
HS_2	2.04×10^{-12}	8.33×10^{-12}	4.09
HS_2^+	1.08×10^{-14}	9.16×10^{-17}	0.01
$H_2S_2^+$	1.08×10^{-14}	3.25×10^{-14}	3.01
HCS^+	5.10×10^{-13}	1.57×10^{-13}	0.31
SO^+	1.19×10^{-12}	4.43×10^{-13}	0.37
N^+	2.21×10^{-14}	1.03×10^{-14}	0.46
CN^+	8.73×10^{-18}	3.27×10^{-18}	0.37
HCN^+	1.24×10^{-16}	7.93×10^{-18}	0.06
NS^+	8.11×10^{-14}	2.04×10^{-15}	0.03
$C_3H_5^+$	9.44×10^{-13}	4.38×10^{-13}	0.46
C_3H_4	4.37×10^{-10}	2.42×10^{-10}	0.55
$CH_3OH_2^+$	4.49×10^{-13}	1.78×10^{-13}	0.40
$H_5C_2O_2^+$	3.90×10^{-18}	1.87×10^{-18}	0.48
$HCOOCH_3$	9.06×10^{-16}	4.08×10^{-16}	0.45
C_2N	2.97×10^{-12}	1.07×10^{-12}	0.36
C_2N^+	1.26×10^{-14}	3.09×10^{-15}	0.25
C_2NH^+	5.07×10^{-15}	1.93×10^{-15}	0.38
$H_4C_2N^+$	6.17×10^{-13}	1.26×10^{-13}	0.20

commonly observed molecules, so we propose that these molecules would be the best tracers. We find that the CH^+ abundance is substantially increased, which is consistent with previous models which have included the enhancement of the rate of ion-neutral reactions due to ambipolar diffusion (e.g. Pineau des Forets *et al.* 1986*a*).

If molecules such as CH^+ and CO^+ were to be observed towards L1448-mm at approximately the (0,-10) offset, where there is already strong evidence for a magnetic precursor from the electron density enhancement and narrow SiO emission, then a high CH^+/CO^+ ratio ($\gtrsim 500$) would be further evidence for the presence of the magnetic precursor, since CH^+ is expected to be enhanced by the precursor, but CO^+ is expected to decrease. If, on the other hand, the ratio was found to be low ($\lesssim 50$, as predicted by the model without the non-thermal enhancement of the ion-neutral reaction rates), then because there is already such strong evidence for the presence of a magnetic precursor in this position, it could indicate a problem with the chemical modelling. For example, the use of an effective temperature to account for the enhancement of ion-neutral reactions due to ambipolar diffusion could be a vast over-simplification.

Ideally, we would like to use this model to infer properties about shocks, such as the shock speed, from observations. Since we have shown that the CH^+/CO^+ ratio is sensitive to the enhancement of ion-neutral reactions, it is possible that for different shock speeds this ratio could be altered. In the future we would therefore like to fully explore the parameter space of this model, so we can fully exploit its capabilities in interpreting observational data.

We are also currently working on including deuterium chemistry into this model, because, as demonstrated in Chapter 7, the degree of deuterium fraction in a core can be greatly affected for ion-neutral drift velocities $\gtrsim 0.4$ km s^{-1}. Drift velocities well above this magnitude are predicted by the shock model in this chapter, so it will be interesting to see how the deuterium chemistry is affected.

In summary, we have presented the results of an up-to-date chemical model coupled with a parametrised C-shock model, which includes both the sputtering of ice mantles from dust grains and the enhancement of ion-neutral reactions due to ambipolar diffusion. In Part I of this chapter we presented strong evidence that there is a magnetic precursor in the southern lobe of the outflow from the source L1448-mm, so comparisons between the predictions of this model and observations of magnetic precursor in L1448-mm would tell us if this model is an accurate description of the chemistry in C-shocks, and may also give us more information on the degree of ion-neutral decoupling in the shocks associated with this source.

CHAPTER 9

DISCUSSION AND CONCLUSIONS

The aim of this thesis has been to gain a clearer understanding of how a pre-protostellar (prestellar) core evolves into a protostar. The majority of the work has involved developing models of the chemical kinetics inside prestellar cores, in order to predict molecular abundances throughout the core as a function of time. Using these models, we can identify molecular tracers of different physical conditions and processes.

In Chapter 3, we investigated the desorption of interstellar ices by non-thermal desorption mechanisms that become important inside dark cores, where the IRSF is heavily extinguished. These desorption processes are very poorly understood, and can potentially have a considerable effect on the predicted gas-phase abundances. The desorption mechanisms considered were desorption resulting from exothermic H_2 formation on grain surfaces, cosmic ray heating of grains, and heating by UV photons induced by the cosmic ray excitation of H_2 molecules. The results showed that, surprisingly, the H_2 formation mechanism is the most efficient, which challenges the commonly made assumption that cosmic ray heating of grains is the dominant non-thermal desorption mechanism.

However, because of the uncertainty in the parameters used in the desorption rates, we concluded that theoretical estimates of desorption rates are subject to huge errors. For the first time, therefore, we attempted to constrain these parameters using observed depletions in the dark core L1689B. It is hoped that these estimates will help constrain our theories of desorption.

The results of this desorption study were used to include desorption in the chemical models in the following chapters (apart from Chapter 7 which does not include desorption, and Chapter 8 where the only desorption mechanism is sputtering due to the passage of a C-shock).

In Chapters 4, 5, 6 and 7 we focussed on how the chemistry is affected during the dynamical evolution of a core as it collapses to form a protostar. In Chapter 4, we investigated the initial chemical conditions of a prestellar core at the onset of collapse, in order to find chemical signatures for a core which has been static for a long period of time before collapse, or a core which collapses almost as soon as it has formed. The first of these cases represents the traditional star formation model, where prestellar cores are initially magnetically subcritical, and contract in quasi-static equilibrium through the process of ambipolar diffusion, over a time period of $\sim$ 10 Myr. Eventually the centre of the core becomes dense enough that it is supercritical, and the collapse commences on a dynamical timescale. The second case represents the more recent rapid star formation models, where either magnetic fields are insignificant, or turbulence can accelerate the collapse.

The initial conditions we varied were the initial ratio of atomic to molecular hydrogen and the initial degree of depletion onto dust grains. By following the evolution of molecules in the subsequent collapse of the core, we found that species such as HCN, HNC and H_2CO, and to a lesser extent OH, CH and NH_3, are very sensitive to the initial atomic to molecular hydrogen ratio, especially during the earliest stages of collapse. If a core could be observed during these early stages, then the abundance ratios such as HNC:OH could indicate the initial amount of molecular hydrogen. With regards to the initial degree of depletion, the most important finding was that if a core has been static for $\gtrsim 10^6$ yr (for an initial density of $\sim 10^4$ cm^{-3}), then the 'depletion enhancement' of molecules such as HCO^+ and N_2H^+ will not occur as the core collapses, so these molecules will *not* show broad emission lines, which has been predicted by previous models (e.g. Rawlings *et al.* 1992). Overall, however, we concluded that it is difficult to draw any conclusions from chemical models by looking at the chemical abundances alone because there is no information on the dynamics of the core.

Therefore, in Chapter 5, we calculated the line profiles of the molecules CS, H_2CO and HCO^+ for the chemical models of Chapter 4, using the spherical radiative transfer code SMMOL. For simplicity, we assumed the core remained at a uniform density (spatially) throughout the collapse, and collapsed according to the modified free-fall collapse equation. We found that CS was insensitive to the initial chemical conditions of the core, but since its line profile shape changed considerably during the collapse, it could possibly be used to diagnose the age of the collapse. The line profiles of H_2CO and HCO^+ were found to be sensitive to the initial atomic to molecular hydrogen ratio and the initial degree of depletion respectively, so could be useful tracers for the initial chemical conditions.

The most surprising conclusion from Chapter 5 was that the collapse model we had assumed,

modified free-fall with a uniform density core, could produce the typical infall signature (double peaked line profiles with a blue asymmetry) using a constant temperature profile. This infall signature, therefore, does not necessarily imply inside-out collapse for a core with a non-uniform temperature profile, as it is often interpreted.

In Chapter 6 we investigated how different dynamical models of collapse affected the abundances inside the core and the resulting line profiles. The collapse models we investigated were the iniside-out collapse model and the new ambipolar diffusion collapse model of Stace & Rawlings (2008). As expected, we found the shapes of line profiles were strongly affected by many factors, such as the abundance profile of the molecule, depletion, the initial chemical conditions and the temperature gradient.

The most important conclusion from this study is that for the CS transitions we have modelled, a blue asymmetry can only be produced for cores which have extended inward motions (i.e., no static envelope). We believed this is because of the depletion of CS in the core centre. This is a significant result because it implies that previously observed line profiles of CS with blue asymmetries are actually inconsistent with the inside-out collapse model, if the effects of depletion are considered.

One problem with the models in both Chapters 5 and 6 is that the predicted lines of o-H_2CO and HCO^+ fail to produce double peaks, whereas observed line profiles of HCO^+ in prestellar cores typically do have double peaks (e.g. Evans *et al.* 2005). Previous models using the same radiative transfer code have not had this problem. We believe this may be due to the initial conditions we have chosen (for example the initial elemental abundances), although, since the initial conditions we have adopted are all within observational constraints, it could be that another dynamic effect, such as rotation, is needed to produce double peaked profiles. Further study is needed to find the reason for this discrepancy.

In Chapter 7 we investigated the effect of ambipolar diffusion on deuterium fractionation in collapsing dark cores, again to determine observational diagnostics for a core collapsing through ambipolar diffusion, as in the traditional star formation model. We found that for drift velocities $\gtrsim 0.4$ km s^{-1}, the energy barrier for the destruction of H_2D^+ by H_2 could be overcome. This results in a significant decrease in the H_2D^+ abundance and therefore also in the degree of deuterium fractionation throughout the core, but such high drift velocities are not predicted for cores undergoing collapse by ambipolar diffusion (Stace & Rawlings 2008). We did, however, find that the deuterium fractionation is very sensitive to density, and therefore the spatial distribution of H_2D^+ and other deuterated molecules could be used to determine the density profiles of collapsing cores and hence constrain the collapse dynamics.

In Chapter 8, we focussed on a later phase in star formation, and presented studies on the interaction of molecular outflows of YSOs with their surrounding medium, in particular the outflow from the Class 0 submillimetre source L1448-mm. In Part I of this chapter we presented firm observational evidence for the presence of a magnetic precursor associated with a young shock in the southern lobe of the L1448-mm outflow. The detection of the magnetic precursor is very important in understanding the physical structure of interstellar shocks and how they interact with their environment. In Part II, we presented the results of a chemical model for the magnetic precursor which included both sputtering of ice mantles and the enhancement of ion-neutral reaction rates due to the ion-neutral drift associated with the magnetic precursor. We found that observable molecules such as CH^+ and CO^+, whose abundances are significantly enhanced and diminished respectively, could be used to distinguish between the models with and without the inclusion of the non-thermal ion-neutral rate enhancement. Observations of these molecules should therefore give an indication of the degree of ion-neutral decoupling, and hence give information on the nature of the shock.

We plan to follow up the work presented in this thesis by conducting further work on the following points:

1. Most of the models in this thesis have been purely theoretical. It is therefore necessary to compare our models with new or existing observations in order to constrain our models and draw conclusions about the physical conditions in star forming regions.

2. The discrepancy between the predicted line profiles of HCO^+ in Chapters 4 and 5, which do not show double peaks, and observed line profiles of HCO^+, which do tend to show double peaks, needs to be investigated further. We hope to ascertain whether the discrepancy is caused by the initial conditions of the chemical model, or whether the observed double peaks in HCO^+ could actually be due to another dynamical mechanism which we have not considered, such a rotation or pulsation.

3. Since the results in Chapter 7 suggested that the H_2D^+/H_3^+ ratio, and also fractionation of other deuterated molecules which are produced by H_2D^+, are very sensitive to the density, we propose carrying out a full multipoint model of the deuterium chemistry in cores collapsing by various different collapse models (inside-out collapse, ambipolar diffusion collapse with different magnetic field strengths, free-fall collapse, etc.), which predict different density profiles as a function of time. The predicted distribution of fractionation could possibly be used as a diagnostic to distinguish between the different collapse models.

4. We are currently working on a model similar to that presented in Part II of Chapter 8, but including deuterium chemistry. We predict that the deuterium chemistry will be very sensitive to the presence of ion-neutral drift, and may be used to provide further observational diagnostics for the presence of a magnetic precursor in shocks associated with young outflows.

The overall conclusion from this thesis is that while chemical models are an important tool for interpreting astronomical observations, they are still subject to a large number of uncertainties, and many different physical models can often result in the same chemical abundances or line profile shapes.

There is, however, much hope for the future of star formation research. The JCMT Gould Belt Survey (GBS), which is currently underway, will map large areas of nearby molecular clouds (which all appear to lie within the Gould Belt) in submillimetre continuum emission and CO line emission, and will help to answer many questions in star formation, such as the relative timescales of the prestellar core phase and each of the protostellar phases, and the relative importance of magnetic fields and turbulence in providing cloud support. Furthermore, the Atacama Large Millimetre/submillimetre array (ALMA), which is due to be fully operational in 2012, will be able to produce high resolution maps of the chemical abundance inside molecular clouds, which will give us more insight into the initial chemical conditions for star formation. With the extra information provided from ALMA and surveys such as the JCMT GBS, we hope to constrain our models and improve their accuracy in predicting the chemical abundances inside star forming regions.

Bibliography

Aguti, E. D., Lada, C. J., Bergin, E. A., Alves, J. F. & Birkinshaw, M., 2007, *ApJ*, **665**, 457

Aikawa, Y., Umebayashi, T., Nakano, T. & Miyama, S. M., 1997, *ApJL*, **486**, L51

Aikawa, Y., Wakelam, V., Garrod, R. T. & Herbst, E., 2008, *ApJ*, **674**, 984

Al-Halabi, A. & van Dishoeck, E. F., 2007, *MNRAS*, **382**, 1648

Allen, M. & Robinson, G. W., 1975, *ApJ*, **195**, 81

Alves, J. F., Lada, C. J. & Lada, E. A., 2001, *Nature*, **409**, 159

André, P., Basu, S. & Inutsuka, S., 2008, *ArXiv e-prints*, 0801.4210

Andre, P., Ward-Thompson, D. & Barsony, M., 1993, *ApJ*, **406**, 122

Andre, P., Ward-Thompson, D. & Motte, F., 1996, *A&A*, **314**, 625

Arce, H. G., Shepherd, D., Gueth, F., Lee, C.-F., Bachiller, R., Rosen, A. & Beuther, H., 2007, in B. Reipurth, D. Jewitt & K. Keil (eds.), *Protostars and Planets V*, pp. 245–260

Bachiller, R., Guilloteau, S., Dutrey, A., Planesas, P. & Martin-Pintado, J., 1995, *A&A*, **299**, 857

Bachiller, R., Martin-Pintado, J., Tafalla, M., Cernicharo, J. & Lazareff, B., 1990, *A&A*, **231**, 174

Bacmann, A., André, P., Puget, J.-L., Abergel, A., Bontemps, S. & Ward-Thompson, D., 2000, *A&A*, **361**, 555

Bacmann, A., André, P. & Ward-Thompson, D., 2001, in T. Montmerle & P. André (eds.), *From Darkness to Light: Origin and Evolution of Young Stellar Clusters*, volume 243 of *Astronomical Society of the Pacific Conference Series*, pp. 113–124

Bacmann, A., Lefloch, B., Ceccarelli, C., Castets, A., Steinacker, J. & Loinard, L., 2002, *A&A*, **389**, L6

Ballesteros-Paredes, J. & Hartmann, L., 2007, *Revista Mexicana de Astronomia y Astrofisica*, **43**, 123

Banerjee, R. & Pudritz, R. E., 2006, *ApJ*, **641**, 949

Basu, S., Ciolek, G. E., Dapp, W. & Wurster, J., 2008, *ArXiv e-prints*, 0810.0783

Basu, S. & Mouschovias, T. C., 1995, *ApJ*, **453**, 271

Belloche, A. & André, P., 2004, *A&A*, **419**, L35

Bergin, E. A., Maret, S., van der Tak, F. F. S., Alves, J., Carmody, S. M. & Lada, C. J., 2006, *ApJ*, **645**, 369

Bergin, E. A., Melnick, G. J., Gerakines, P. A., Neufeld, D. A. & Whittet, D. C. B., 2005, *ApJL*, **627**, L33

Bergin, E. A. & Tafalla, M., 2007, *ArA&A*, **45**, 339

Bianchi, S., Gonçalves, J., Albrecht, M., Caselli, P., Chini, R., Galli, D. & Walmsley, M., 2003, *A&A*, **399**, L43

Bohlin, R. C., Savage, B. D. & Drake, J. F., 1978, *ApJ*, **224**, 132

Bonnor, W. B., 1956, *MNRAS*, **116**, 351

Bringa, E. M. & Johnson, R. E., 2004, *ApJ*, **603**, 159

Buch, V. & Zhang, Q., 1991, *ApJ*, **379**, 647

Burke, J. R. & Hollenbach, D. J., 1983, *ApJ*, **265**, 223

Caselli, P., Hartquist, T. W. & Havnes, O., 1997, *A&A*, **322**, 296

Caselli, P., Walmsley, C. M., Tafalla, M., Dore, L. & Myers, P. C., 1999, *ApJL*, **523**, L165

Cecchi-Pestellini, C. & Aiello, S., 1992, *MNRAS*, **258**, 125

Cernicharo, J., Castets, A., Duvert, G. & Guilloteau, S., 1984, *A&A*, **139**, L13

Chen, W. P. & Graham, J. A., 1993, *ApJ*, **409**, 319

Ciolek, G. E. & Mouschovias, T. C., 1993, *ApJ*, **418**, 774

Collings, M. P., Anderson, M. A., Chen, R., Dever, J. W., Viti, S., Williams, D. A. & McCoustra, M. R. S., 2004, *MNRAS*, **354**, 1133

Collings, M. P., Dever, J. W., Fraser, H. J., McCoustra, M. R. S. & Williams, D. A., 2003, *ApJ*, **583**, 1058

Creighan, S. C., Perry, J. S. A. & Price, S. D., 2006, *J. Chem. Phys.*, **124**, 114701

Crutcher, R. M., Nutter, D. J., Ward-Thompson, D. & Kirk, J. M., 2004, *ApJ*, **600**, 279

Curiel, S., Raymond, J. C., Moran, J. M., Rodriguez, L. F. & Canto, J., 1990, *ApJL*, **365**, L85

Curiel, S., Torrelles, J. M., Rodríguez, L. F., Gómez, J. F. & Anglada, G., 1999, *ApJ*, **527**, 310

Dalgarno, A., 2006, in P. Earis (ed.), *Chemical evolution of the Universe*, volume 133 of *Faraday Discussions*, pp. 9–25

Dobashi, K., Uehara, H., Kandori, R., Sakurai, T., Kaiden, M., Umemoto, T. & Sato, F., 2005, *PASJ*, **57**, 1

Draine, B. T., 1980, *ApJ*, **241**, 1021

Draine, B. T., 1991, in E. Falgarone, F. Boulanger & G. Duvert (eds.), *Fragmentation of Molecular Clouds and Star Formation*, volume 147 of *IAU Symposium*, pp. 185–196

Draine, B. T. & McKee, C. F., 1993, *ArA&A*, **31**, 373

Duley, W. W., Jones, A. P., Taylor, S. D. & Williams, D. A., 1993, *MNRAS*, **260**, 415

Duley, W. W., Jones, A. P., Whittet, D. C. B. & Williams, D. A., 1989, *MNRAS*, **241**, 697

Dyson, J. E. & Williams, D. A., 1997, *The physics of the interstellar medium* (The graduate series in astronomy, Institute of Physics Publishing, ISBN: 0750303069)

Eiroa, C. & Hodapp, K.-W., 1989, *A&A*, **210**, 345

Eley, D. D. & Rideal, E. K., 1940, *Nature*, **17**, 621

Elmegreen, B. G., 2007, *ApJ*, **668**, 1064

Evans, II, N. J., Lee, J.-E., Rawlings, J. M. C. & Choi, M., 2005, *ApJ*, **626**, 919

Evans, II, N. J., Rawlings, J. M. C., Shirley, Y. L. & Mundy, L. G., 2001, *ApJ*, **557**, 193

Evans, II, N. J., Zhou, S., Koempe, C. & Walmsley, C. M., 1994, *ApSS*, **212**, 139

Falle, S. A. E. G. & Hartquist, T. W., 2002, *MNRAS*, **329**, 195

Faure, A., 2008, private communication

Faure, A. & Tennyson, J., 2008, In preparation

Faure, A., Varambhia, H. N., Stoecklin, T. & Tennyson, J., 2007, *MNRAS*, **382**, 840

Federman, S. R., Rawlings, J. M. C., Taylor, S. D. & Williams, D. A., 1996, *MNRAS*, **279**, L41

Flower, D. R., 1999, *MNRAS*, **305**, 651

Flower, D. R., Pineau des Forets, G., Field, D. & May, P. W., 1996, *MNRAS*, **280**, 447

Flower, D. R., Pineau des Forets, G. & Hartquist, T. W., 1985, *MNRAS*, **216**, 775

Flower, D. R., Pineau Des Forêts, G. & Walmsley, C. M., 2005, *A&A*, **436**, 933

Fraser, H. J., Collings, M. P., McCoustra, M. R. S. & Williams, D. A., 2001, *MNRAS*, **327**, 1165

Frerking, M. A., Langer, W. D. & Wilson, R. W., 1982, *ApJ*, **262**, 590

Garrod, R. T., Wakelam, V. & Herbst, E., 2007, *A&A*, **467**, 1103

Garrod, R. T., Williams, D. A. & Rawlings, J. M. C., 2006*a*, *ApJ*, **638**, 827

Garrod, R. T., Williams, D. A. & Rawlings, J. M. C., 2006*b*, *ApJ*, **638**, 827

Girart, J. M. & Acord, J. M. P., 2001, *ApJL*, **552**, L63

Goldsmith, P. F. & Li, D., 2005, *ApJ*, **622**, 938

Gould, R. J. & Salpeter, E. E., 1963, *ApJ*, **138**, 393

Green, S. & Thaddeus, P., 1974, *ApJ*, **191**, 653

Grinin, V. P., 2001, *Astrofizika*, **44**, 402

Guelin, M., Langer, W. D. & Wilson, R. W., 1982, *A&A*, **107**, 107

Harris, J. & Kasemo, B., 1981, *Surface Science*, **105**, L281

Hartmann, L., Ballesteros-Paredes, J. & Bergin, E. A., 2001, *ApJ*, **562**, 852

Hartmann, L., Stauffer, J. R., Kenyon, S. J. & Jones, B. F., 1991, *AJ*, **101**, 1050

Hartquist, T. W. & Williams, D. A., 1990, *MNRAS*, **247**, 343

Hartquist, T. W. & Williams, D. A., 1995, *The Chemically Controlled Cosmos: Astronomical Molecules from the Big Bang to Exploding Stars* (Cambridge University Press, ISBN: 0521419832)

Hasegawa, T. I. & Herbst, E., 1993, *MNRAS*, **261**, 83

Henyey, L. G., Lelevier, R. & Levee, R. D., 1988, *PASP*, **100**, 1467

Heyer, M. H. & Brunt, C., 2007, in B. G. Elmegreen & J. Palous (eds.), *Triggered Star Formation in a Turbulent ISM*, volume 237 of *IAU Symposium*, pp. 9–16

Islam, F., 2007, private communication

Jessop, N. E. & Ward-Thompson, D., 2000, *MNRAS*, **311**, 63

Jiménez-Serra, I., Caselli, P., Martín-Pintado, J. & Hartquist, T. W., 2008, *A&A*, **482**, 549

Jiménez-Serra, I., Martín-Pintado, J., Rodríguez-Franco, A. & Marcelino, N., 2004, *ApJL*, **603**, L49

Jiménez-Serra, I., Martín-Pintado, J., Viti, S., Martín, S., Rodríguez-Franco, A., Faure, A. & Tennyson, J., 2006, *ApJL*, **650**, L135

Jiménez-Serra, I. & Viti, S., 2008, In preparation

Johnstone, D., Di Francesco, J. & Kirk, H., 2004, *ApJL*, **611**, L45

Kirk, J. M., Ward-Thompson, D. & André, P., 2007, *MNRAS*, **375**, 843

Lada, C. J., 1987, in M. Peimbert & J. Jugaku (eds.), *Star Forming Regions*, volume 115 of *IAU Symposium*, pp. 1–17

Lada, C. J. & Wilking, B. A., 1984, *ApJ*, **287**, 610

Langmuir, I., 1922, *Trans. Faraday Soc*, **146**, 401

Le Bourlot, J., Pineau des Forêts, G., Flower, D. R. & Cabrit, S., 2002, *MNRAS*, **332**, 985

Le Teuff, Y. H., Millar, T. J. & Markwick, A. J., 2000, *A&AS*, **146**, 157

Lee, C. W. & Myers, P. C., 1999, *ApJS*, **123**, 233

Lee, C. W., Myers, P. C. & Plume, R., 2004, *ApJS*, **153**, 523

Lee, J.-E., Evans, II, N. J., Shirley, Y. L. & Tatematsu, K., 2003, *ApJ*, **583**, 789

Lefloch, B., Castets, A., Cernicharo, J. & Loinard, L., 1998, *ApJL*, **504**, L109

Leger, A., Jura, M. & Omont, A., 1985, *A&A*, **144**, 147

Li, D. & Goldsmith, P. F., 2003, *ApJ*, **585**, 823

Lynds, B. T., 1962, *ApJS*, **7**, 1

Maret, S. & Bergin, E. A., 2007, *ApJ*, **664**, 956

Markwick, A. J., Charnley, S. B. & Millar, T. J., 2001, *A&A*, **376**, 1054

Masunaga, H., Miyama, S. M. & Inutsuka, S.-I., 1998, *ApJ*, **495**, 346

Mathis, J. S., Mezger, P. G. & Panagia, N., 1983, *A&A*, **128**, 212

Morfill, G. E., Voelk, H. J. & Lee, M. A., 1976, *J. Geophys. Research*, **81**, 5841

Mouschovias, T. C. & Spitzer, Jr., L., 1976, *ApJ*, **210**, 326

Mouschovias, T. C., Tassis, K. & Kunz, M. W., 2006, *ApJ*, **646**, 1043

Myers, P. C., Linke, R. A. & Benson, P. J., 1983, *ApJ*, **264**, 517

Parise, B., Ceccarelli, C., Tielens, A. G. G. M., Castets, A., Caux, E., Lefloch, B. & Maret, S., 2006, *A&A*, **453**, 949

Pineau des Forets, G., Flower, D. R., Hartquist, T. W. & Dalgarno, A., 1986*a*, *MNRAS*, **220**, 801

Pineau des Forets, G., Flower, D. R., Hartquist, T. W. & Millar, T. J., 1987, *MNRAS*, **227**, 993

Pineau des Forets, G., Roueff, E. & Flower, D. R., 1986*b*, *MNRAS*, **223**, 743

Pineau des Forets, G., Roueff, E. & Flower, D. R., 1989, *MNRAS*, **240**, 167

Pontoppidan, K. M., 2006, *A&A*, **453**, L47

Prasad, S. S. & Tarafdar, S. P., 1983, *ApJ*, **267**, 603

Prialnik, D., 2000, *An Introduction to the Theory of Stellar Structure and Evolution* (Cambridge University Press, ISBN: 052165937X)

Pudritz, R. E., Ouyed, R., Fendt, C. & Brandenburg, A., 2007, in B. Reipurth, D. Jewitt & K. Keil (eds.), *Protostars and Planets V*, pp. 277–294

Rawlings, J. M. C., Hartquist, T. W., Menten, K. M. & Williams, D. A., 1992, *MNRAS*, **255**, 471

Rawlings, J. M. C., Hartquist, T. W., Williams, D. A. & Falle, S. A. E. G., 2002, *A&A*, **391**, 681

Rawlings, J. M. C. & Yates, J. A., 2001, *MNRAS*, **326**, 1423

Redman, M. P., Keto, E. & Rawlings, J. M. C., 2006, *MNRAS*, **370**, L1

Redman, M. P., Keto, E., Rawlings, J. M. C. & Williams, D. A., 2004, *MNRAS*, **352**, 1365

Redman, M. P., Rawlings, J. M. C., Nutter, D. J., Ward-Thompson, D. & Williams, D. A., 2002, *MNRAS*, **337**, L17

Roberts, H., Herbst, E. & Millar, T. J., 2004, *A&A*, **424**, 905

Roberts, H. & Millar, T. J., 2000*a*, *A&A*, **364**, 780

Roberts, H. & Millar, T. J., 2000*b*, *A&A*, **361**, 388

Roberts, H. & Millar, T. J., 2006, *Royal Society of London Philosophical Transactions Series A*, **364**, 3063

Roberts, J. F., Rawlings, J. M. C., Viti, S. & Williams, D. A., 2007, *MNRAS*, **382**, 733

Roberts, W. W., 1969, *ApJ*, **158**, 123

Rohlfs, K. & Wilson, T. L., 2000, *Tools of radio astronomy* (Astronomy and astrophysics library, Springer, ISSN0941-7834)

Ruffle, D. P., Hartquist, T. W., Caselli, P. & Williams, D. A., 1999, *MNRAS*, **306**, 691

Ruffle, D. P. & Herbst, E., 2000*a*, *MNRAS*, **319**, 837

Ruffle, D. P. & Herbst, E., 2000*b*, *MNRAS*, **319**, 837

Ruffle, D. P. & Herbst, E., 2001, *MNRAS*, **322**, 770

Savage, B. D., Cardelli, J. A. & Sofia, U. J., 1992, *ApJ*, **401**, 706

Schöier, F. L., van der Tak, F. F. S., van Dishoeck, E. F. & Black, J. H., 2005, *A&A*, **432**, 369

Scoville, N. Z., Solomon, P. M. & Sanders, D. B., 1979, in W. B. Burton (ed.), *The Large-Scale Characteristics of the Galaxy*, volume 84 of *IAU Symposium*, pp. 277–282

Shalabiea, O. M. & Greenberg, J. M., 1994, *A&A*, **290**, 266

Shen, C. J., Greenberg, J. M., Schutte, W. A. & van Dishoeck, E. F., 2004, *A&A*, **415**, 203

Shirley, Y. L., Evans, II, N. J., Rawlings, J. M. C. & Gregersen, E. M., 2000, *ApJS*, **131**, 249

Shu, F. H., 1977, *ApJ*, **214**, 488

Shu, F. H., Adams, F. C. & Lizano, S., 1987, *ArA&A*, **25**, 23

Smith, I. W. M., Herbst, E. & Chang, Q., 2004, *MNRAS*, **350**, 323

Sofia, U. J. & Meyer, D. M., 2001, *ApJL*, **554**, L221

Stace, H. A. W. & Rawlings, J. M. C., 2008, In preparation [SR08]

Stone, J. M., Ostriker, E. C. & Gammie, C. F., 1998, *ApJL*, **508**, L99

Tafalla, M., Mardones, D., Myers, P. C., Caselli, P., Bachiller, R. & Benson, P. J., 1998, *ApJ*, **504**, 900

Tafalla, M., Myers, P. C., Caselli, P. & Walmsley, C. M., 2004, *A&A*, **416**, 191

Tafalla, M., Myers, P. C., Caselli, P., Walmsley, C. M. & Comito, C., 2002, *ApJ*, **569**, 815

Tassis, K. & Mouschovias, T. C., 2004, *ApJ*, **616**, 283

Tielens, A. G. G. M., 2005, *The Physics and Chemistry of the Interstellar Medium* (Cambridge University Press, ISBN: 0521826349)

Tiné, S., Roueff, E., Falgarone, E., Gerin, M. & Pineau des Forêts, G., 2000, *A&A*, **356**, 1039

Tsamis, Y. G., Rawlings, J. M. C., Yates, J. A. & Viti, S., 2008, *MNRAS*, **388**, 898

Turner, B. E., Chan, K.-W., Green, S. & Lubowich, D. A., 1992, *ApJ*, **399**, 114

van de Hulst, H. C., 1948, in *Centennial Symposia*, pp. 73–86

van der Werf, P. P., Goss, W. M. & van den Bout, P. A., 1988, *A&A*, **201**, 311

van Zadelhoff, G.-J., Dullemond, C. P., van der Tak, F. F. S., Yates, J. A., Doty, S. D., Ossenkopf, V., Hogerheijde, M. R., Juvela, M., Wiesemeyer, H. & Schöier, F. L., 2002, *A&A*, **395**, 373

Viti, S., Collings, M. P., Dever, J. W., McCoustra, M. R. S. & Williams, D. A., 2004, *MNRAS*, **354**, 1141

Viti, S. & Williams, D. A., 1999, *MNRAS*, **305**, 755

Wakelam, V., Herbst, E. & Selsis, F., 2006*a*, *A&A*, **451**, 551

Wakelam, V., Herbst, E. & Selsis, F., 2006*b*, *A&A*, **451**, 551

Ward-Thompson, D., 1996, *ApSS*, **239**, 151

Ward-Thompson, D., Di Francesco, J., Hatchell, J., Hogerheijde, M. R., Nutter, D., Bastien, P., Basu, S., Bonnell, I., Bowey, J., Brunt, C., Buckle, J., Butner, H., Cavanagh, B., Chrysostomou, A., Curtis, E., Davis, C. J., Dent, W. R. F., van Dishoeck, E., Edmunds, M. G., Fich, M., Fiege, J., Fissel, L., Friberg, P., Friesen, R., Frieswijk, W., Fuller, G. A., Gosling, A., Graves, S., Greaves, J. S., Helmich, F., Hills, R. E., Holland, W. S., Houde, M., Jayawardhana, R., Johnstone, D., Joncas, G., Kirk, H., Kirk, J. M., Knee, L. B. G., Matthews, B., Matthews, H., Matzner, C., Moriarty-Schieven, G. H., Naylor, D., Padman, R., Plume, R., Rawlings, J. M. C., Redman, R. O., Reid, M., Richer, J. S., Shipman, R., Simpson, R. J., Spaans, M., Stamatellos, D., Tsamis, Y. G., Viti, S., Weferling, B., White, G. J., Whitworth, A. P., Wouterloot, J., Yates, J. & Zhu, M., 2007, *PASP*, **119**, 855

Ward-Thompson, D., Motte, F. & Andre, P., 1999, *MNRAS*, **305**, 143

Ward-Thompson, D., Scott, P. F., Hills, R. E. & Andre, P., 1994, *MNRAS*, **268**, 276

Weidenschilling, S. J. & Ruzmaikina, T. V., 1994, *ApJ*, **430**, 713

Whittet, D. C. B., Bode, M. F., Longmore, A. J., Adamson, A. J., McFadzean, A. D., Aitken, D. K. & Roche, P. F., 1988, *MNRAS*, **233**, 321

Willacy, K. & Millar, T. J., 1998, *MNRAS*, **298**, 562

Willacy, K., Rawlings, J. M. C. & Williams, D. A., 1994*a*, *MNRAS*, **269**, 921

Willacy, K., Williams, D. A. & Duley, W. W., 1994*b*, *MNRAS*, **267**, 949

Williams, D. A. & Viti, S. W., 2002, *Annu. Rep. Prog. Chem., Sect. C*, **98**, 87

Wilson, T. L., 1999, *Reports of Progress in Physics*, **62**, 143

Wolkovitch, D., Langer, W. D., Goldsmith, P. F. & Heyer, M., 1997, *ApJ*, **477**, 241

Woodall, J., Agúndez, M., Markwick-Kemper, A. J. & Millar, T. J., 2007, *A&A*, **466**, 1197

Zhou, S., Evans, II, N. J., Butner, H. M., Kutner, M. L., Leung, C. M. & Mundy, L. G., 1990, *ApJ*, **363**, 168

Zhou, S., Evans, II, N. J., Koempe, C. & Walmsley, C. M., 1993, *ApJ*, **404**, 232

ACKNOWLEDGEMENTS

First of all, I would like to thank my supervisor, Jonathan Rawlings, for all the advice, support and guidance he has given me over the last three years. I am similarly grateful to Serena Viti and David Williams, for always having the time to help me out when I've needed extra support. I am especially grateful for all the time they put in to proof read my chapters during the final weeks of writing-up. Their help and kindness made the final stages of this thesis much more bearable!

I would also like to thank Izaskun Jiménez-Serra for giving me the opportunity to go observing (in Hawaii!), and for teaching me everything I know about C-shocks, and Jeremy Yates for all his help on the radiative transfer work in Chapters 5 and 6.

To my friends from the Wirral, I cannot thank you enough for your unwavering friendship, support and reassurance during these past three years. You have been the best friends anyone could ever ask for, and I don't know where I'd be without you. To my parents also, thank you putting up with all my moaning, and for all the love and encouragement you have given me. And of course I'd like to give a massive thank you to my boyfriend - even though you're thousands of miles away you've always been there for me, and I couldn't have done this without you.

And finally, thank you to everyone in Group A at UCL for being so friendly and making studying at UCL one of the happiest and most fulfilling times of my life!